



# Online Approach for Parameter Identification and Temperature Estimation in Permanent Magnet Synchronous Machines

Luis Guillermo Ayala Ramirez

Vollständiger Abdruck der von der TUM School of Engineering and Design der  
Technischen Universität München zur Erlangung des akademischen Grades eines

**Doktors der Ingenieurwissenschaften (Dr.-Ing.)**

genehmigten Dissertation.

**Vorsitzender:**

Prof. Dr. sc.techn. Andreas Herkersdorf

**Prüfende der Dissertation:**

1. Prof. Dr.-Ing. Dr. h. c. Ralph Kennel
2. Prof. Dr.-Ing. Mario Pacas,  
Universität Siegen

Die Dissertation wurde am 10.01.2022 bei der Technischen Universität München  
eingereicht und durch die TUM School of Engineering and Design am 19.09.2022  
angenommen.



# Abstract

The online parameter estimation of permanent magnet synchronous machines has been broadly reported in the literature. However, the parameters estimation accuracy might suffer due to deficient machine models that neglect saturation and cross-coupling effects. Furthermore, the availability of the estimated parameters might be subject to the machine's excitation. Conversely, the superimposition of signals to improve the estimation adds acoustic noise or torque pulsations that in some applications are unacceptable.

In this work, a polynomial based nonlinear Permanent Magnet Synchronous Machine (PMSM) model is introduced. The validity of the proposed expressions is demonstrated based on finite element analysis simulation results, but also on experimental data by means of a fast and simple measurement procedure. A solution to the rank deficient problem reported in the literature for online parameter identification approaches is provided. Where the polynomial formulation of the saturation and cross-coupling effects with respect to the dq-axes currents leads to an identification scheme that over several operating points forms an overdetermined system of equations with a unique solution. Additionally, an equivalent dq-axes voltage model with two sets of iron loss resistors is presented to model the influence of the iron losses on the flux-linkages. On the other hand, the temperature dependency of the permanent magnet flux-linkage and the average winding resistance is modeled with a lumped-parameter thermal network, which is derived through a model reduction approach, in order to generate a thermal network that can be implemented on an embedded system.

To conclude, a hybrid online parameter setup is presented, which comprises the equivalent dq-axes voltage circuit based on the proposed flux-linkage expressions and the thermal model. The hybrid arrangement delivers average winding and magnet temperature estimates, as well as flux-linkage coefficients and average winding resistance estimates. A parameter identification algorithm based on constrained optimization in conjunction with the machine's thermal model enables the parameter estimation at any load condition, as the thermal model takes over the estimation at machine's operating regions with insufficient current or speed excitation an vice-versa.



# Kurzfassung

Die Online-Parameteridentifikation von Permanentmagnet-Synchronmaschinen (PMSM) wurde relativ oft in der Literatur untersucht. Jedoch leidet die Genauigkeit der geschätzten Parameter, wenn nichtlineare Effekte in den Maschinenmodellen vernachlässigt werden. Darüber hinaus ist die Verfügbarkeit der Parameterschätzungen abhängig von der Maschinenerregung. Andererseits können kontinuierliche Erregungen durch überlagerte hochfrequente Signale zu Geräuschentwicklung und unerwünschtem Drehmomentrippel führen, die in manchen Anwendungen nicht zulässig sind.

In der vorliegenden Arbeit wird ein nichtlineares Polynom-basierendes PMSM-Modell vorgestellt. Das aufgestellte Flussverkettung-Modell wird anhand von Finite-Elementen-Simulationsergebnissen und Messdaten validiert. Eine Lösung zu den in der Literatur oftmals berichteten unbestimmten Gleichungssystemen in der Online-Parameteridentifikation wird vorgeschlagen. Die polynomische Beschreibung der stromabhängigen Sättigungs- und Kopplungseffekte ermöglicht ein Identifikationsschema, das über mehrere Arbeitspunkte ein überbestimmtes Gleichungssystem mit einer eindeutigen Lösung bildet. Zusätzlich dazu wird ein dq-Ersatzschaltbild mit Eisenverlust-Ersatzwiderständen vorgeschlagen, um den Einfluss von Eisenverlusten auf die Flussverkettungen über der Frequenz zu modellieren. Außerdem wird die mittlere Temperaturentwicklung in den Maschinenwicklungen und Magneten mittels einem thermischen Netzwerkmodell bestimmt. Das thermische Modell entsteht aus einem Modellordnungsreduktionsverfahren, um eine Implementierung in einem eingebetteten System möglich zu machen.

Zum Schluss wird ein Hybrid-Online-Parameteridentifikationsverfahren vorgestellt, welches aus der Zusammenstellung vom Flussverkettung-basierenden dq-Ersatzschaltbild und thermischen Netzwerkmodell besteht. Das Hybridverfahren liefert die mittleren Magnet- und Wicklungstemperaturen, Koeffizienten-Schätzungen der Flussverkettungspolynomen und dem Phasenwiderstand. Das Zusammenspiel zwischen dem mit vorgegebenen Nebenbedingungen Parameteridentifikationsoptimierungsverfahren und das thermische Modell erlaubt die Parameterbestimmung unabhängig vom Arbeitspunkt, da das thermische Netzwerkmodell indirekt die Parameterschätzung bei unzureichendem Phasenstrom oder Rotor-Geschwindigkeit übernimmt und umgekehrt das Parameteridentifikationsverfahren die Temperaturschätzung macht.



# Contents

<b>Contents</b>	<b>vii</b>
<b>List of Figures</b>	<b>xi</b>
<b>List of Tables</b>	<b>xv</b>
<b>List of Symbols</b>	<b>xvii</b>
<b>1 Introduction</b>	<b>1</b>
1.1 Related Work . . . . .	2
1.2 Contributions . . . . .	4
1.2.1 Machine Model . . . . .	4
1.2.2 Machine Model Identification . . . . .	5
1.2.3 Parameter Estimation . . . . .	5
1.2.4 Machine Thermal Model . . . . .	5
1.2.5 Hybrid Online Parameter Identification . . . . .	6
1.3 Outline . . . . .	6
<b>2 Non-Linear Machine Model</b>	<b>9</b>
2.1 Machine Model . . . . .	9
2.2 Flux-Linkage Mathematical Description . . . . .	12
2.2.1 Flux-Linkage Model . . . . .	16
2.2.2 Considering Mutual Terms . . . . .	19
2.2.3 Machine Inductance Expressions . . . . .	21
2.2.4 Motor Torque Constant . . . . .	23
2.2.5 Separation of Nonlinear Effects . . . . .	24
2.3 Considering Magnet-Flux variations . . . . .	25
2.3.1 Flux-linkage Expressions . . . . .	27
2.3.2 Inductance and Torque Constant Dependency on Magnet Flux-linkage . . . . .	29
2.4 Considering Field Currents in Wound Field Synchronous Machines . . . . .	32
<b>3 Flux-Linkage Model Parameter Identification</b>	<b>39</b>
3.1 Optimization Theory . . . . .	39
3.1.1 Optimization Methods . . . . .	39
3.1.1.1 Linear Optimization . . . . .	39
3.1.1.2 Nonlinear Optimization . . . . .	42
3.1.1.3 Kalman Filtering . . . . .	46

## Contents

3.1.1.4	Metaheuristics . . . . .	48
3.1.1.5	Particle Swarm Optimization . . . . .	48
3.1.2	Coefficient's Calculation . . . . .	49
3.2	Coefficient of Determination . . . . .	51
3.3	Offline Identification of PMSMs: FEA Simulation Data . . . . .	51
3.3.1	Flux-Linkages . . . . .	55
3.3.2	Machine Inductances . . . . .	57
3.3.3	Electromagnetic Torque . . . . .	60
3.3.4	Permanent Magnet Flux Variations . . . . .	63
3.3.4.1	Flux-linkages . . . . .	64
3.3.4.2	Machine inductances . . . . .	68
3.3.4.3	Torque constant . . . . .	70
3.4	Offline Identification of WFSMs: FEA Simulation Data . . . . .	72
3.5	Offline Identification: Experimental Data . . . . .	79
3.5.1	Constant Magnet Temperature . . . . .	79
3.5.2	Magnet Temperature Variation . . . . .	91
<b>4</b>	<b>Considering Electromagnetic Losses</b>	<b>97</b>
4.1	Resistive Losses . . . . .	97
4.2	Iron Losses . . . . .	97
4.2.1	Iron Losses Model . . . . .	98
4.2.2	Iron Loss Resistance Identification . . . . .	103
<b>5</b>	<b>Motor Thermal Model</b>	<b>111</b>
5.1	Thermal Modeling . . . . .	111
5.1.1	Lumped Parameter Modeling . . . . .	111
5.2	Modeling Approach . . . . .	114
5.2.1	Model Reduction . . . . .	115
5.2.2	Thermal Model Parameter Identification . . . . .	125
<b>6</b>	<b>Online Parameter Estimation</b>	<b>139</b>
6.1	Hardware Setup . . . . .	139
6.2	Parameter Identification . . . . .	145
6.2.1	Optimization Solver . . . . .	146
6.2.2	Solver Performance . . . . .	147
6.3	Identification Algorithm . . . . .	150
6.3.1	Dynamic Constraints . . . . .	151
6.4	Hybrid Identification Scheme . . . . .	152
6.5	Algorithm Simulation . . . . .	156
6.6	Online Estimation . . . . .	160
6.6.1	Unbalanced Phase Resistance . . . . .	160
6.6.2	Test Profiles . . . . .	162
6.6.3	Unconstrained Identification . . . . .	169

<b>7</b>	<b>Conclusions</b>	<b>173</b>
7.1	Summary . . . . .	173
7.2	Future Work . . . . .	175
	<b>Bibliography</b>	<b>177</b>
<b>A</b>	<b>Appendix</b>	<b>185</b>
A.1	Taylor’s Theorem for Multi-variable Functions . . . . .	185
A.2	Test Machines . . . . .	187
A.3	Hardware Implementation . . . . .	188
A.4	OSQP Algorithm . . . . .	189
A.5	Terminal Voltage Measurement . . . . .	190



# List of Figures

2.1	Flux-Linkage vs. Current . . . . .	10
2.2	DQ reference axes in PMSMs. . . . .	11
2.3	Nonlinear behavior of electrical steel NO30-15. . . . .	12
2.4	Example of nonlinear magnetic equivalent circuit extracted from [1]. . . . .	13
2.5	4-pole pair IPMSM. . . . .	16
2.6	FE Simulation current data points definition . . . . .	17
2.7	Example of the DQ-Flux-linkages . . . . .	17
2.8	IPMSM Flux-Linkage - FE Simulation . . . . .	18
2.9	Magnetic coenergy . . . . .	19
2.10	IPMSM Mutual Inductances - FE Data . . . . .	20
2.11	IPMSM torque constant. . . . .	23
2.12	Flux-linkage at different $\psi_m$ values . . . . .	28
2.13	Wound field synchronous machine . . . . .	32
2.14	WFSM flux-linkages vs. rotor field current . . . . .	34
3.1	Overview of system identification methods. . . . .	40
3.2	Types of convex sets. . . . .	42
3.3	Convex and nonconvex functions. . . . .	43
3.4	Types of minimum. . . . .	44
3.5	FE Simulation data point selection . . . . .	53
3.6	Current phase advance angle. . . . .	55
3.7	IPMSM Flux-Linkages . . . . .	56
3.8	FEA Flux-linkages. . . . .	58
3.9	D-axis absolute inductance. . . . .	58
3.10	Q-axis absolute inductances. . . . .	59
3.11	Differential inductances. . . . .	60
3.12	IPMSM electromagnetic torque . . . . .	61
3.13	IPMSM torque constant . . . . .	62
3.14	Flux-linkage at different $B_r$ . . . . .	63
3.15	Flux-linkages at increasing current for different $\psi_m$ . . . . .	65
3.16	Extrapolated flux-linkages at increasing current for different $\psi_m$ . . . . .	67
3.17	D-axis inductances at different $\psi_m$ . . . . .	69
3.18	Inductances at different $\psi_m$ . . . . .	70
3.19	IPMSM torque constant at different $\psi_m$ . . . . .	71
3.20	Flux-linkages at increasing current for different $i_f$ values. . . . .	74
3.21	Coefficients for different $i_f$ values. . . . .	75

List of Figures

3.22	Wound Field Synchronous Machine (WFSM) flux-linkages at increasing current for different $i_f$ values. . . . .	76
3.23	WFSM magnetizing inductance $L_{mf}$ vs $i_q$ . . . . .	77
3.24	WFSM absolute inductances at different $i_f$ values. . . . .	78
3.25	WFSM torque constant at different $i_f$ values. . . . .	79
3.26	Testrig setup. . . . .	81
3.27	Test current ramps . . . . .	82
3.28	Estimated signals. . . . .	85
3.29	Torque constant. . . . .	86
3.30	Identified flux-linkage surfaces. . . . .	88
3.31	4-pole pair IPMSM Inductances. . . . .	89
3.32	7-pole pair outer rotor PMSM Inductances. . . . .	90
3.33	DQ-axes flux-linkages . . . . .	92
3.34	IPMSM - Inductances at different magnet temperatures . . . . .	94
3.35	DQ-axes flux-linkages at different magnet temperatures. . . . .	94
3.36	Flux-linkages at increasing current for different $\psi_m$ . . . . .	95
4.1	IPMSM open circuit shaft loss . . . . .	99
4.2	Voltage model considering iron losses . . . . .	102
4.3	4-pole pair IPMSM input power measurement. . . . .	107
4.4	IPMSM open circuit shaft loss. . . . .	108
4.5	4-pole pair IPMSM loss maps. . . . .	109
4.6	4-pole pair IPMSM iron loss maps. . . . .	109
5.1	MotorCAD - 4 pole pair IPMSM thermal network . . . . .	114
5.2	Example of a simple LPTN. . . . .	116
5.3	General thermal network for 13 nodes. . . . .	120
5.4	Thermal model reduction. . . . .	121
5.5	Reduced thermal network from parent MotorCAD model. . . . .	122
5.6	Reduced model temperature. . . . .	123
5.7	Reduced temperature deviations of all nodes. . . . .	124
5.8	Thermo couples positions. . . . .	125
5.9	Test rig - thermal couples positions . . . . .	126
5.10	Thermal model identification. . . . .	127
5.11	Measured data profile. . . . .	128
5.12	Thermal network. . . . .	130
5.13	Reduced model temperature. . . . .	132
5.14	Thermal model identification for several rotor speeds. . . . .	133
5.15	Speed dependent thermal resistance. . . . .	134
5.16	Test profile 1. . . . .	135
5.17	Reduced model temperature. . . . .	135
5.18	Steering park cycle profile. . . . .	136
5.19	Reduced model temperature. . . . .	137

6.1	Hardware setup. . . . .	140
6.2	Second order low-pass filter. . . . .	141
6.3	Filter's Bode diagram. . . . .	142
6.4	Filter phase shift of the voltage signals. . . . .	142
6.5	Low-pass filter group delay. . . . .	143
6.6	Compensation factor for the voltage attenuation . . . . .	144
6.7	Voltage model considering iron losses . . . . .	146
6.8	Software setup. . . . .	149
6.9	Identification block diagram. . . . .	151
6.10	Example of dynamic tolerance bands. . . . .	152
6.11	Identification block diagram. . . . .	153
6.12	Identification block diagram. . . . .	154
6.13	Temperature nodes update. . . . .	155
6.14	Steering Cycle. . . . .	157
6.15	Simulated steering park cycle - voltage signals. . . . .	157
6.16	Simulated steering park cycle -torque signals. . . . .	158
6.17	Simulated temperature estimation. . . . .	159
6.18	Online temperature estimation. . . . .	160
6.19	Effects of asymmetric winding resistance. . . . .	162
6.20	Steering park cycle profile. . . . .	163
6.21	Online temperature estimation. . . . .	163
6.22	Identified parameters. . . . .	164
6.23	Online temperature estimation. . . . .	165
6.24	Effects of $L_d$ on magnet temperature estimation. . . . .	166
6.25	Identified parameters. . . . .	166
6.26	Temperature dependency of $l_{qd10}$ . . . . .	167
6.27	Online estimation with and without iron loss model . . . . .	167
6.28	Online estimation with and without iron loss model . . . . .	168
6.29	Online temperature estimation. . . . .	170
6.30	Online temperature estimation. . . . .	170
A.1	Avnet ZeadBoard. . . . .	188
A.2	Testrig setup . . . . .	189
A.3	Filter characterization. . . . .	190



# List of Tables

2.1	IPMSM - <i>Machine data</i> . . . . .	16
2.2	Typical reversible temperature coefficients . . . . .	27
2.3	WFSM - <i>Machine data</i> . . . . .	34
3.1	Coefficients for $n = 3$ and $n = 5$ . . . . .	54
3.2	IPMSM - Coefficient of determination . . . . .	56
3.3	IPMSM - CoD for $n = 5$ . . . . .	66
3.4	<i>Machine to be identified</i> . . . . .	82
3.5	IPMSM Linear Parameters . . . . .	83
3.6	SMPMSM Linear Parameters . . . . .	84
3.7	ORPMSM Linear Parameters . . . . .	84
3.8	identified cross-saturation parameters . . . . .	84
3.9	CoD . . . . .	87
3.10	IPMSM linear signal inductance coefficients . . . . .	93
4.1	IPMSM loss resistances with PWM based excitation . . . . .	107
4.2	IPMSM mechanical loss coefficients . . . . .	108
5.1	Equivalent thermal to electrical elements . . . . .	112
5.2	Power loss sources . . . . .	113
5.3	Thermal network nodes mapping . . . . .	126
5.4	Operating point of profiles according to definition in Fig. 5.11 . . . . .	129
5.5	Operating point of profiles for speed dependent terms. . . . .	133
6.1	Power electronics key figures. . . . .	139
6.2	Loss-pass filter values. . . . .	141
6.3	IPMSM - identified coefficients relative deviation . . . . .	148
6.4	IPMSM - Coefficient of determination . . . . .	148
6.5	OSQP - computational time duration . . . . .	149
6.6	IPMSM - coefficients expected variation with respect to $\psi_m$ . . . . .	156
6.7	RLS algorithms setups . . . . .	169
A.1	4-pole pair IPMSM. . . . .	187
A.2	Avnet ZedBoard system on chip (SoC). . . . .	188
A.3	Test rig setup. . . . .	189
A.4	IPMSM - identified coefficients . . . . .	189
A.5	OSQP settings. . . . .	190



# List of Symbols

$\psi$	flux-linkage.
$\phi$	magnetic flux.
$u_d$	d-axis voltage.
$u_q$	q-axis voltage.
$i_d$	d-axis current.
$i_q$	q-axis current.
$\omega_r$	rotor angular velocity.
$\psi_d$	d-axis flux-linkage.
$\psi_q$	q-axis flux-linkage.
$L_{dd}$	d-axis incremental self-inductance.
$L_{qq}$	q-axis incremental self-inductance.
$L_{dq}$	d-axis incremental mutual-inductance.
$L_{qd}$	q-axis incremental mutual-inductance.
$T_e$	electromagnetic torque.
$p$	number of pole pairs.
$W_c$	magnetic coenergy.
$W_{cdq}$	total dq-axes magnetic coenergy.
$L_d$	absolute d-axis inductance.
$L_q$	absolute q-axis inductance.
$K_t$	torque constant.
$B_r$	permanent magnet remanence.
$H_{ci}$	permanent magnet intrinsic coercivity.
$i_f$	field current.
$N_d$	minimum number of d-axis current FEA data points.
$N_q$	minimum number of q-axis current FEA data points.
$T_{rel}$	reluctance torque.
$\mathcal{P}$	magnetic permeance.
$\mu_r$	relative permeability.
$\theta_m$	rotor mechanical angle position.
$k_c$	Coulomb friction torque.
$k_v$	viscous friction coefficient.
$T_{iron}$	iron loss torque.
$P_m$	mechanical power.
$\omega_m$	mechanical angular velocity.
$f_e$	electrical frequency.
$k_{hy}$	hysteresis loss coefficient.

## List of Symbols

$k_{exc}$	excess loss coefficient.
$k_{eddy}$	eddy current loss coefficient.
$P_{iron}^{OC}$	open circuit iron loss.
$P_{iron}^{SC}$	short circuit iron loss.
$P_{in}$	machine input power.
$P_{resistive}$	winding ohmic loss.
$P_{iron}$	total iron loss.
$P_e$	electromagnetic power.
$R_m$	magnetizing loss resistor.
$R_d$	demagnetizing loss resistor.
$i_{qm}$	magnetizing q-axis current.
$i_{dm}$	magnetizing d-axis current.
$\psi_m$	permanent magnet flux-linkage.
$f_{PWM}$	PWM switching frequency.
$R_s$	winding resistor.

# 1 Introduction

Due to the growing demand for more efficient and fault tolerant systems in the automotive industry the parameter estimation of PMSM in embedded systems is gaining importance. In a specific application like the steering system in passenger cars, the system's robustness is relying more and more on model based schemes. The knowledge of PMSM's parameters offers the possibility to improve the machine's output performance at all operating points; it opens the door to the development of more robust fault diagnostic strategies and at higher level it helps for example to have a detailed motor model for torque assist control in the steering system. The rise of the motor temperature affects directly parameters such as winding resistances and the rotor flux linkage [2, 3]. These changes on the temperature can be originated by different operating points of the machine or by changes in the ambient temperature and at the same time temperature variations may cause significant deviations of the two parameters mentioned before with respect to the room temperature values captured in the lab. If the system requires a high fidelity motor model, winding, and rotor temperatures need to be directly measured, it adds significant cost to the product.

On the other hand magnetic saturation is responsible for variations of the dq-axis inductances [2, 4, 5, 6]. Depending on the application a full identification with respect to the dq-axis currents may be needed. Parameter estimation of PMSM has been reported extensively in the literature. One main issue when trying to estimate a set of motor parameters is the lack of information. This is reflected in the fact the dq-axis model is described by two equations having four unknown variables. The non-linear characteristics of the machine pose then a challenge for a full parameter identification. Approaches with additional machine's excitation [7] or partial parameter identification [8, 9] have been proposed to deal with deficient rank of the available equations and the current dependency of the non-linear effects. Whereas in the former, the acoustic noise generated by injected signals poses a problem for noise sensitive applications like a steering system. However, the superposition of a signal partially solves the estimation of the machine's parameters when the machine is inactive or at no load conditions. Nevertheless this identification is limited to current dependent parameters such as winding resistance or the inductances, the permanent flux-linkage which is tied to the rotor speed through the Back Electromotive Force (bemf) voltage cannot be determined with such methods. Finally, the frequency of the injected signal is typically several times higher than the machine's fundamental frequency in order to avoid any interference with the normal operation of the machine. As a result, the estimated parameters relate to the injected frequency with its corresponding effects leading to a deviation of the values needed for the fundamental frequency of operation. Hence a full parameter identification as pro-

## 1 Introduction

posed in the literature comes with certain trades, either side effects like acoustic noise or parameters involving additional non-linear components such as frequency dependency effects.

Besides temperature estimation based on parameter identification, machine thermal models are employed to estimate the temperature development inside the machine [10]. However, the challenge that arises when using a machine thermal model in an embedded system is temperature initial conditions, as the machine might be colder or warmer than any predefined initial temperature of the thermal model.

### 1.1 Related Work

A variety of machine's model simplifications have been reported in the literature [11, 12, 13] partly due to limitations on the computational capacity of embedded systems, where to capture the nonlinear and cross-coupling effects of the dq-axes flux-linkages are measured for different dq-axes current combinations. The flux-linkage data is saved as a look-up table to be used in the embedded system. Nevertheless, the trade between memory and accuracy arises as the flux-linkage data points in the application are typically obtained through simple linear interpolation methods and a reduced set of elements in the look-up tables might lead to large errors. Specially when derivatives are needed, the discretization error can be critical. Model based approaches such as flux-linkage and current observers, require machine parameters [11] to perform the variables prediction in combination with the flux data saved in look-up tables. The simplest analytical model is the inductance based one and more advanced models include the cross-coupling in the form of constant incremental inductances [14]. Considering the aspects already mentioned, there is no established analytical machine model that includes the non-linear and cross-coupling effects in the literature. However, there are contributions where the dq-axes flux-linkages are described by Taylor series, as proposed in [15, 16] for a WFSM or fourth degree polynomial expressions as presented in [17, 18] for a Interior Permanent Magnet Synchronous Machine (IPMSM). Nevertheless, the polynomials are formulated in the generic form with no simplification of coefficients according to the nature of the flux-linkage surfaces with respect the dq-axes currents. Moreover, the polynomials coefficients were only obtained from finite element analysis (FEA) simulation data and not from experimental data. In a similar fashion, polynomials of different grades have been proposed to represent the dq-axes inductances of synchronous reluctance by the authors in [19, 20, 21]. As the modeling approach focuses on the inductances, individual polynomial expressions for the absolute and incremental inductances are required. Acknowledging the benefits of working the flux-linkages, because of their inclusion of nonlinear effects and the possibility of derive the absolute and incremental inductances from them, it is then crucial the measurement of the flux-linkages, which is widely reported in the literature [4, 22, 23].

Since the advent of microprocessors, real time estimation of machines parameters or temperatures has been a topic of research [10]. The interest in online estimation of electric machines has been pushed by the increasing demand for more efficient and robust systems, specially in the automotive industry. Real time monitoring of the winding and magnet temperatures can enable an optimal utilization of the maximum output power of the machine or it can prevent an over heating of winding wires or the magnets. Similarly, the estimation of the average winding resistance can be used to detect a failure in the windings, such as an open circuit condition.

Parameter estimation of PMSMs has been reported extensively in the literature. One main issue when trying to estimate a set of motor parameters is the limited information available. This is reflected in the fact that the dq-axis model is described by two equations having four unknown variables. Several system identification approaches have been proposed in order to avoid this problem. In [24] an Extended Kalman Filter (EKF) is used to determine three parameters, the phase resistance, the torque constant and the average phase inductance. The algorithm is only active during transients to overcome the rank-deficiency problem, however, the cross-coupling effects are neglected. An optimization algorithm is used in [25] to estimate the dq-axis inductances and the phase resistance with previous knowledge of the permanent flux. Other kind of approach involves the use of a Model Reference Adaptive System (MRAS) [8] to estimate the resistance and the flux of a Surface-Mounted PMSM, where the magnetic saturation is neglected by assuming the inductance constant. In [9] the q-axis inductance is assumed constant, the phase resistance, d-axis inductance and the flux linkage are estimated at specific operation conditions by means of an unknown input observer.

Optimization algorithms like Particle Swarm Optimization (PSO) have been presented in [26, 27, 28] for parameter identification. In the first approach, four parameters are determined at different machine operation points and in the second one the dq-axis inductances are estimated offline by collecting data from different speed, voltages and load conditions; the phase resistance and permanent flux-linkage are determined with conventional methods and assumed constant for the estimation of the inductances. The recursive least squares (RLS) algorithm has been employed extensively in the literature for parameter identification. The proposed scheme by [2], a two level identification of the resistance, permanent magnet flux-linkage and the dq-axes inductances was presented to offer a solution to the underdetermined system of equations. Consequently, some solutions with RLS use fix parameters like the resistance and permanent flux to identify the dq-axis inductances [6].

In order to overcome the rank-deficient problem, a signal can be superimposed to the motor signals. In [29] a sinusoidal signal is injected into the d-axis current providing a full rank solution for the four parameters estimation. The effects of the inverter non-linearity are eliminated by using a power amplifier to drive the motor. The four electrical motor parameters and the Voltage Source Inverter (VSI) non-linear behavior are estimated in [30] by injecting different d-axis current levels in a steady state scheme. Pseudorandom

## 1 Introduction

sequence signals are used in [31] to guarantee persistent excitation in order to identify the dq-axis inductances and the phase resistance. There are also approaches which address specific solutions such a torque control as in [32], where the permanent magnet flux-linkage is estimated with an observer for the special case of  $i_d = 0A$ . However, parameters like the phase resistance need to be known before hand.

Many authors have proposed online parameter estimation schemes for general purposes, most of the methods involve simplifications assuming some parameters as known, and other solutions are aimed to improve the performance of a certain control scheme, like sensorless control, adaptive control or maximum torque per ampere control strategies. Depending on the application it may be acceptable to trade estimation accuracy for simplicity when implementing such algorithms. However, for applications such as Steering Systems, the use of active identification algorithms might end up with negative side effects such as acoustic noise.

## 1.2 Contributions

### 1.2.1 Machine Model

This work proposes a solution for two aspects of the electrical machines modeling based on the work presented by the author in [1]: the first one is the inclusion of saturation and cross-coupling effects, the second one is the analytical model of those effects. A generalized formulation of the dq-axes flux-linkages in terms of polynomials for a given polynomial degree  $n$  is presented. Through the analytical description of the flux-linkages, key parameters like absolute inductances, permanent flux-linkage or incremental inductances are formulated in terms of the dq-axes currents. In particular, the polynomial description of the dq-axes flux-linkages enables a clear the separation of the non-linear effects that are rooted in the interaction between the permanent magnet flux-linkage and the dq-axes currents. The interaction between the q-axis current and the permanent magnet flux-linkage that impacts the torque production can be clearly identified, as well as the cross-coupling terms between the dq-axes flux-linkages and the associated absolute and incremental inductances. The flux-linkage model accuracy not only depends on the chosen polynomial degree, but it also offers a straightforward implementation in an embedded system for model based algorithms which require a machine model. Furthermore, the interaction between winding current and permanent magnet flux-linkage was modeled in order to take into account the effects of the magnet temperature on the overall flux-linkage. Moreover, the analytical modeling approach was extended to WFSMs, where a novel polynomial structure was presented to improve the model's accuracy when dealing with the strong nonlinear behavior that results from the interaction between the rotor field winding flux and the armature flux.

### 1.2.2 Machine Model Identification

In addition to the theoretical treatment, a fast and simple measurement procedure [1] is presented in order to identify the polynomials coefficients experimentally, where a model based approach is used to obtain the dq-axes flux-linkage and winding resistance without previous knowledge of the latter as it is typically proposed in the literature [4, 33]. At a constant speed, current ramps with a duration of 3.6s are proposed to characterize one quadrant of the machine. In a post-processing step, the polynomials coefficients are determined showing a high degree of correspondence with the key machine parameters such as the small signal dq-axes inductances, the open circuit bmf and DC-winding resistance.

### 1.2.3 Parameter Estimation

The polynomial based machine model is then used as the foundation of an online parameter identification scheme for a PMSM, which is based on voltage and current signals of the fundamental frequency. The machine's non-linear effects are then described in the form of polynomials with constant coefficients and in conjunction with a recursive estimation scheme it provides a solution to the rank deficient problem. Regardless of the load conditions, the coefficients that describe the flux-linkage's cross-coupling and saturation effects remain constant. Therefore by recollecting the data of several different operating points a full-rank solution to the estimation problem can be found. Consequently, the temperature dependent parameters such as the winding resistance and the permanent flux-linkage are treated as constant values for short periods of time compared to the machine's thermal time constant. As a result, the parameter variation due to the average winding and rotor magnets temperatures could be tracked. In order to account for the speed dependent iron losses that interact with the flux-linkages, two equivalent loss resistors were employed. The first one represents the magnetizing losses associated to the dq-axes flux-linkages and the second one models the demagnetizing losses associated to the current dependent d-axis flux-linkage terms.

### 1.2.4 Machine Thermal Model

A reduced modeling method was proposed to generate a machine thermal model without the knowledge of the machine's geometry or materials characteristics. The proposed approach was applied to an existing large Lumped-parameter thermal network (LPTN) model and measured data. For a 66 nodes LPTN a maximum temperature deviation of  $0.7^{\circ}\text{C}$  was achieved using a 13-nodes reduced network. Furthermore, using the generic formulation of the reduced model, a 6-nodes network was obtained directly from measured temperature data. It delivered a maximum temperature of  $3.4^{\circ}\text{C}$  at different test profiles.

### 1.2.5 Hybrid Online Parameter Identification

An online parameter identification algorithm was proposed, that is backed up by a machine's thermal model. This hybrid setup seeks to provide a solution to the limitations of each estimation method. Firstly, the proposed hybrid approach delivers parameter estimates at any operating condition of the machine, as the thermal model takes over the estimation of the average winding and magnet temperatures when the machine doesn't have enough excitation in terms of phase currents or rotor speed. The average winding resistance and permanent magnet flux-linkage values are then derived from the corresponding estimated temperatures. Secondly, the parameter estimates, when the machine is operating in regions with proper excitation, are used to update the thermal model's winding and magnet temperatures in case where the identification algorithm started at an initial thermal condition different to the real machine temperatures.

## 1.3 Outline

This work starts addressing the analytical model of PMSMs in Chapter 2, providing general expressions to describe the dq-axes flux-linkage maps of such machines, while using exemplary machines to illustrate and plot the aforementioned non-linear effects. This approach, which was already presented by the author of this project in [1], was also extended to consider permanent magnet remanence variations due to temperature effects or manufacturing tolerances in this work. Moreover, the modeling approach is extended to WFSMs where instead of rotor magnets, field coils generate a variable flux-linkage. Similar to the PMSMs, the non-linear interaction between the dq-axes currents and the rotor field current can be described in polynomial form.

In Chapter 3 the determination of the polynomial's coefficients is discussed from an offline and online perspective. Initially, the FEA models of Chapter 2 are used to demonstrate the validity of the proposed analytical expressions. Furthermore, a measurement procedure is presented to capture the flux-linkage information in terms of polynomial coefficients of the three different PMSMs. In addition, this measurement method was carried out to determine the coefficients of the flux-linkage expressions of an IPMSM for different magnet temperatures.

Chapter 4 deals with the extension of the equivalent dq-axes circuit to consider electromagnetic losses as they interact directly with the flux-linkages. On the other hand, together with the Joule loss, the iron losses form the set of heat sources of the thermal model derived in Chapter 5. A model reduction approach was employed to generate a machine's thermal model. This method was validated in two steps, firstly using a complex LPTN of a PMSM, secondly using measured temperature data of the IPMSM already characterized in Chapter 2. The latter network was then employed to estimate the average winding and magnet temperatures.

Finally, in Chapter 6 a hybrid online parameter identification is presented. The flux-linkage expressions of Chapter 3, the equivalent iron loss model of Chapter 4 and the thermal model of Chapter 5 are combined to form a hybrid estimation scheme. Simulated data and test bench data of the IPMSM in question are used to assess the performance of the proposed method.



## 2 Non-Linear Machine Model

Electrical machines are typically described in terms of inductances, which for simplicity are assumed to be constant. However, at machines with soft magnetic cores, the inductances might exhibit a non-linear behavior. Therefore a model that captures those non-linear characteristics should be considered.

### 2.1 Machine Model

The analysis of three phase machines is well documented in the literature [34, 35]. The bmf, the induced voltage when there is no winding current excitation, is the result of the magnetic flux produced by rotating magnets. This voltage is derived from Faraday's law, the bmf in one winding coil is defined as :

$$bmf = \frac{d\psi}{dt} = \frac{d\psi}{d\theta_r} \cdot \frac{d\theta_r}{dt} = \omega_r \cdot \frac{d\psi}{d\theta_r} \quad (2.1)$$

where  $\psi$  in (2.1) is the flux-linkage in the coil, which is the product of the  $N$  coil turns linking the magnetic flux  $\phi$  as shown in (2.2).  $\theta_r$  the electrical rotor position and  $\omega_r$  the electrical angular velocity.

$$\psi = N \cdot \phi \quad (2.2)$$

A magnetic flux is also created by a current carrying a conductor, such as current flowing in a wound coil [35]. Being that the case, the flux-linkage per Ampere in the coil is defined in terms of the inductance  $L$  as:

$$\psi = L \cdot i \quad (2.3)$$

the relationship (2.3) can then be used to obtain the voltage produced according to Faraday's law:

$$V = \frac{d\psi}{dt} = L \cdot \frac{di}{dt} + i \cdot \frac{dL}{dt} \quad (2.4)$$

Nevertheless  $L$  in (2.3) can become nonlinear due to saturation effects in the machine's core material. This nonlinear relationship between flux-linkage and current leads to different definitions of inductance such as the absolute inductance  $L_{abs}$  and the incremental inductance  $L_{inc}$  as expressed in (2.5).

$$L_{abs} = \frac{\psi}{i} \quad L_{inc} = \frac{d\psi}{di} \quad (2.5)$$

Fig.2.1 exemplifies a nonlinear flux-linkage curve, the slope of the red line represents an ideal constant inductance, whereas the slope of the yellow line makes emphasis on the

## 2 Non-Linear Machine Model

incremental inductance at the intersection with the flux-linkage represented by the blue curve.

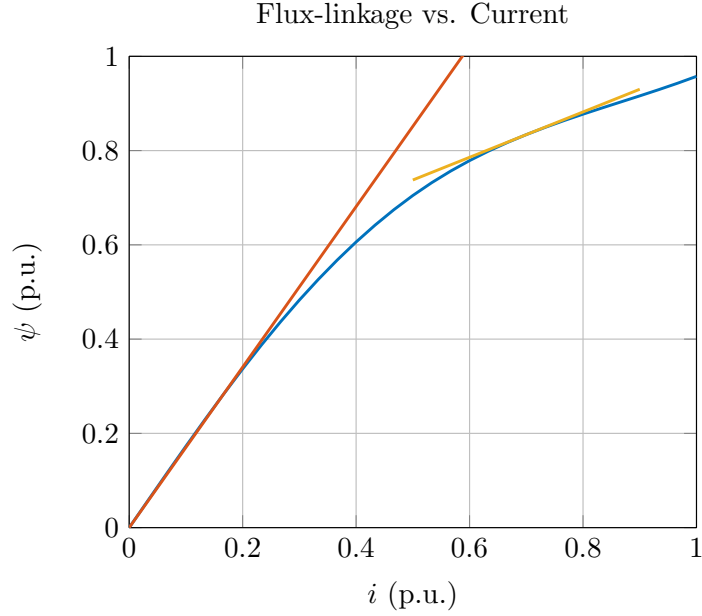


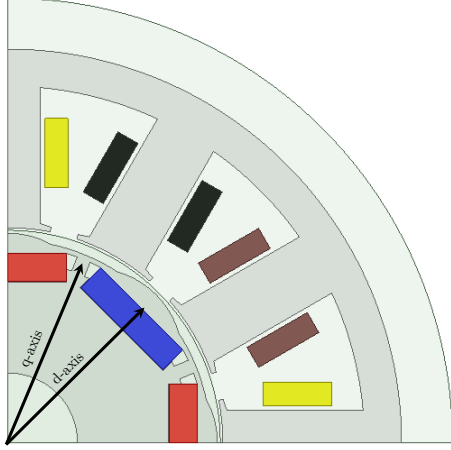
**Figure 2.1:** Flux-Linkage vs. Current

The flux-linkage in each machine phase winding is the sum of flux-linkage contributions from both magnets and windings. Consequently, the phase voltage is expressed in terms of the bemf as in (2.1) and the inductance according to (2.4). The voltage equations of a three phase PMSM's can be written as:

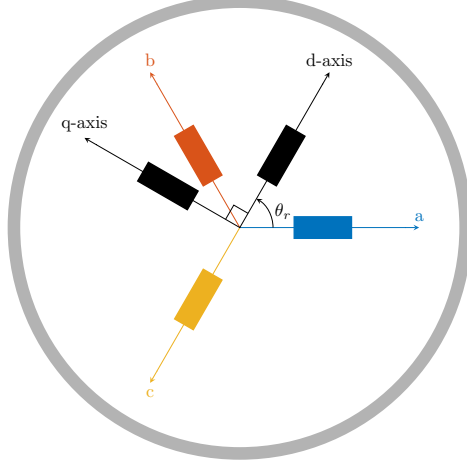
$$\begin{aligned}
 V_{ph_a} &= R_s \cdot i_{ph_a} + L \cdot \frac{di_a}{dt} + i_a \cdot \frac{dL}{dt} + bemf_a \\
 V_{ph_b} &= R_s \cdot i_{ph_b} + L \cdot \frac{di_b}{dt} + i_b \cdot \frac{dL}{dt} + bemf_b \\
 V_{ph_c} &= R_s \cdot i_{ph_c} + L \cdot \frac{di_c}{dt} + i_c \cdot \frac{dL}{dt} + bemf_c
 \end{aligned} \tag{2.6}$$

As a rotating system and assuming sinusoidal currents, the quantities in (2.6) change with the rotor position over time. In order to facilitate the analysis of such machines, a balanced three phase machine can be transformed into a two axes equivalent system removing the rotor position dependency as shown in Fig. 2.2b. The new axes, the dq-axes represent the magnetic path from the rotor perspective as illustrated in Fig. 2.2a. The dq0 transformation [34] is performed with through the matrix in (2.7).

$$\begin{bmatrix} S_d \\ S_q \\ S_0 \end{bmatrix} = \frac{2}{3} \begin{bmatrix} \cos(\theta_r) & \cos(\theta_r - 120^\circ) & \cos(\theta_r + 120^\circ) \\ -\sin(\theta_r) & -\sin(\theta_r - 120^\circ) & -\sin(\theta_r + 120^\circ) \\ \frac{1}{2} & \frac{1}{2} & \frac{1}{2} \end{bmatrix} \begin{bmatrix} S_a \\ S_b \\ S_c \end{bmatrix} \quad (2.7)$$



(a) PMSM cross-section and DQ rotor reference axes.



(b) 3-phase PMSM reference axes.

**Figure 2.2:** DQ reference axes in PMSMs.

In a balanced 3-phase winding system the zero sequence  $S_0$  is zero. The remaining expressions  $S_d$  and  $S_q$  are the equivalent dq-axes quantities. Therefore the voltage equations in (2.6) can be transformed in the following form:

$$\begin{bmatrix} u_d \\ u_q \end{bmatrix} = \frac{2}{3} \begin{bmatrix} \cos(\theta_r) & \cos(\theta_r - 120^\circ) & \cos(\theta_r + 120^\circ) \\ -\sin(\theta_r) & -\sin(\theta_r - 120^\circ) & -\sin(\theta_r + 120^\circ) \end{bmatrix} \begin{bmatrix} V_{ph_a} \\ V_{ph_b} \\ V_{ph_c} \end{bmatrix} \quad (2.8)$$

where  $u_d$  and  $u_q$  represent to the dq-axes voltages and consequently applying the same transformation to the phase currents produces the dq-axes currents  $i_d$  and  $i_q$ .

Finally, replacing (2.6) into (2.8), assuming a sinusoidal current excitation, leads to the following dq-axes voltage expressions in terms of rotor angular velocity  $\omega_r$  and the flux-linkages  $\psi_d$  and  $\psi_q$ :

$$\begin{bmatrix} u_d \\ u_q \end{bmatrix} = R_s \begin{bmatrix} i_d \\ i_q \end{bmatrix} + \omega_r \begin{bmatrix} -\psi_q(i_d, i_q) \\ \psi_d(i_d, i_q) \end{bmatrix} + \begin{bmatrix} \dot{\psi}_d(i_d, i_q) \\ \dot{\psi}_q(i_d, i_q) \end{bmatrix} \quad (2.9)$$

where the flux-linkage derivatives presented in dot notation can be further developed in the following form:

$$\dot{\psi}(i) = \frac{d\psi}{dt} = \frac{\partial \psi}{\partial i} \cdot \frac{di}{dt} \quad (2.10)$$

## 2 Non-Linear Machine Model

Consequently, applying (2.10) to (2.9) produces the relationships in (2.11) in terms of the incremental dq-axes inductances,  $L_{dd}$ ,  $L_{qq}$ ,  $L_{dq}$  and  $L_{qd}$ :

$$\begin{bmatrix} \dot{\psi}_d(i_d, i_q) \\ \dot{\psi}_q(i_d, i_q) \end{bmatrix} = \begin{bmatrix} L_{dd}(i_d, i_q) & L_{dq}(i_d, i_q) \\ L_{qd}(i_d, i_q) & L_{qq}(i_d, i_q) \end{bmatrix} \begin{bmatrix} \dot{i}_d \\ \dot{i}_q \end{bmatrix} \quad (2.11)$$

Similarly, the d-axis flux-linkage in (2.9) can be further developed, as the bemf voltages are aligned with rotor position. Therefore, assuming sinusoidal bemf wave forms, leads only to a d-axis flux-linkage contribution in the following form:

$$\psi_d(i_d, i_q) = \omega_r \cdot \psi_m + \psi_{d0}(i_d, i_q) \quad (2.12)$$

where  $\psi_m$  is the permanent magnet flux-linkage and the subscript 0 refers to the d-axis flux-linkage contribution of the currents only. Besides the voltage equations, the electromagnetic torque  $T_e$  can also be expressed in term of the dq quantities [14] as:

$$T_e(i_d, i_q) = \frac{3}{2}p(\psi_d(i_d, i_q) \cdot i_q - \psi_q(i_d, i_q) \cdot i_d) \quad (2.13)$$

where  $p$  is the number of pole pairs and the constant  $\frac{3}{2}$  relates to the number of machine phases.

## 2.2 Flux-Linkage Mathematical Description

The nonlinear behavior of the flux-linkage in a PMSM can be traced back to the characteristics of the electrical steel used in such machines. The nonlinear magnetization curve, Fig. 2.3a, which is reflected in the relative permeability in Fig. 2.3b leads to nonlinear magnetic circuit that describes the machine.

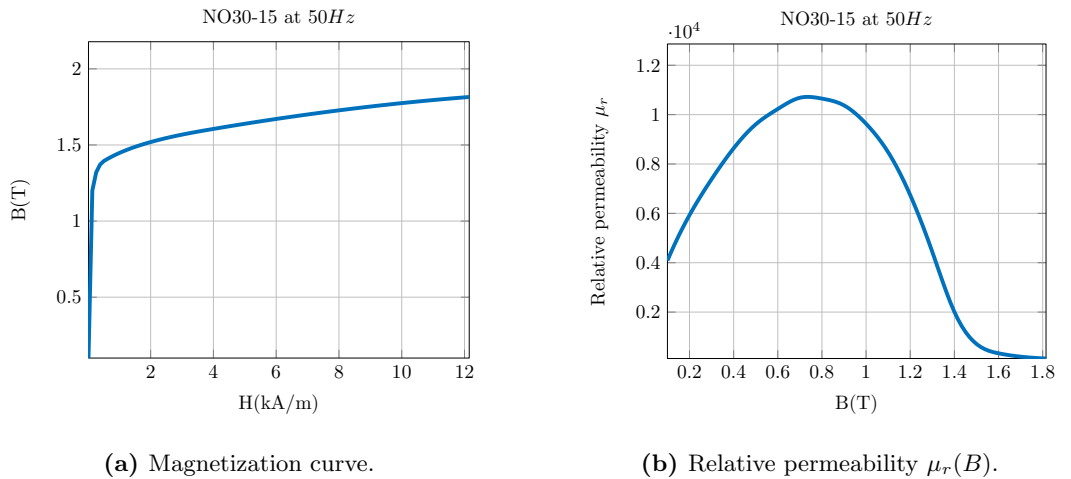


**Figure 2.3:** Nonlinear behavior of electrical steel NO30-15.

## 2.2 Flux-Linkage Mathematical Description

These nonlinear magnetic circuit can be represented according to [36, 1], as shown in Fig. 2.4. Where the iron reluctance  $R$  depends on its own magnetic flux and the magnetic properties of the machine's core material:

$$R(\phi, A) = \frac{l}{A\mu_0\mu_r(B)}, \quad \text{where } B = \frac{\phi}{A} \quad (2.14)$$

Where  $A$  is the machine's section area of interest,  $l$  is its length,  $\phi$  is the magnetic flux crossing the area in question,  $\mu_0$  is the magnetic permeability of free space and  $\mu_r$  is the relative permeability of the core material. As the most common magnetic materials used in electric machines are electrical steels with characteristics like in Fig. 2.3, the steel parts of the machine including stator and rotor exhibit a nonlinear magnetic behavior.

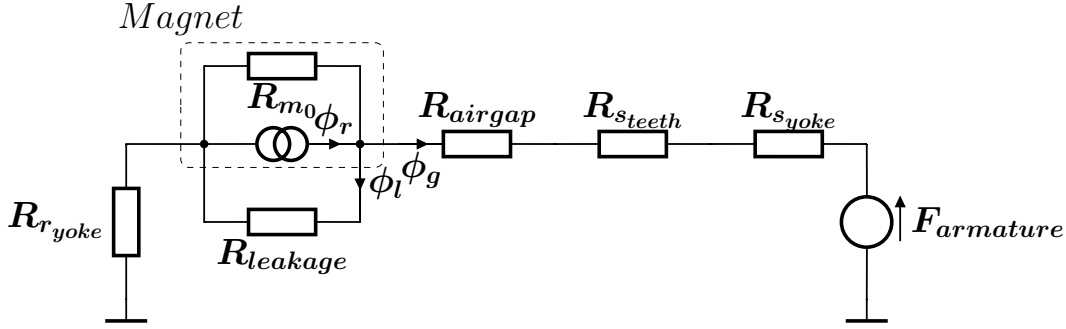


**Figure 2.4:** Example of nonlinear magnetic equivalent circuit extracted from [1].

The equivalent circuit depicted in Fig. 2.4 help to visualize the key actors that describe the machine, the armature Magneto Motive Force (m.m.f),  $F_{armature}$ , which depends of the winding current, the permanent magnet flux and the different reluctances. This leads to air-gap flux expressions depending on the already mentioned elements. Furthermore, the dq-axes magnetic flux  $\phi_{gd}$  and  $\phi_{gq}$  can be expressed with respect the magnet remanent flux  $\phi_r$  and dq-axes currents  $i_d$  and  $i_q$ , in the following form:

$$\phi_{gd} = \phi_r \alpha(\phi_r, i_d, i_q) + i_d \beta(\phi_r, i_d, i_q) + i_q \gamma(\phi_r, i_d, i_q) \quad (2.15)$$

$$\phi_{gq} = \phi_r A(\phi_r, i_d, i_q) + i_d B(\phi_r, i_d, i_q) + i_q \Gamma(\phi_r, i_d, i_q) \quad (2.16)$$

the functions  $A$ ,  $B$ ,  $\Gamma$ ,  $\alpha$ ,  $\beta$  and  $\gamma$  represent the nonlinear behavior due to the interaction between flux and iron reluctances. Assuming constant magnet temperature,  $\phi_r$  can be assumed to be constant as well. Therefore, the remaining variables are the dq-axes currents. Following the same rationale presented in [1], by applying Taylor's theorem for multi-variable functions [37], the flux expressions (2.15) and (2.16) can be then represented by a Taylor polynomial  $\mathcal{T}$  with degree  $n$  and a reminder function  $E_n^1$ , as:

$$\begin{aligned} \phi_{gd}(i_d, i_q) &= \mathcal{T}_{\phi_{gd}}(i_d, i_q) + E_{d_n}^1(i_d, i_q) \\ \phi_{gq}(i_d, i_q) &= \mathcal{T}_{\phi_{gq}}(i_d, i_q) + E_{q_n}^1(i_d, i_q) \end{aligned} \quad (2.17)$$

<sup>1</sup>see Appendix A.1 further references.

## 2 Non-Linear Machine Model

where the Taylor polynomials  $\mathcal{T}_{\phi_{g_d}}$  and  $\mathcal{T}_{\phi_{g_q}}$  are expressed in terms of the partial derivatives of  $\phi_{g_d}$  and  $\phi_{g_q}$  evaluated at  $\mathbf{i} = (i_{d_0}, i_{q_0})$ . Defining  $\Delta i_d = i_d - i_{d_0}$  and  $\Delta i_q = i_q - i_{q_0}$ , the Taylor polynomial takes the form:

$$\begin{aligned} \mathcal{T}_{g_d}(i_d, i_q) &= \phi_{g_d}(\mathbf{i}) + \Delta i_d \frac{\partial \phi_{g_d}}{\partial i_d}(\mathbf{i}) + \Delta i_q \frac{\partial \phi_{g_d}}{\partial i_q}(\mathbf{i}) \\ &+ \frac{1}{2!} \left[ (\Delta i_d)^2 \frac{\partial^2 \phi_{g_d}}{\partial i_d^2}(\mathbf{i}) + 2\Delta i_d \Delta i_q \frac{\partial^2 \phi_{g_d}}{\partial i_d \partial i_q}(\mathbf{i}) + (\Delta i_q)^2 \frac{\partial^2 \phi_{g_d}}{\partial i_q^2}(\mathbf{i}) \right] + \dots \end{aligned} \quad (2.18)$$

$$\begin{aligned} \mathcal{T}_{g_q}(i_d, i_q) &= \phi_{g_q}(\mathbf{i}) + \Delta i_d \frac{\partial \phi_{g_q}}{\partial i_d}(\mathbf{i}) + \Delta i_q \frac{\partial \phi_{g_q}}{\partial i_q}(\mathbf{i}) \\ &+ \frac{1}{2!} \left[ (\Delta i_d)^2 \frac{\partial^2 \phi_{g_q}}{\partial i_d^2}(\mathbf{i}) + 2\Delta i_d \Delta i_q \frac{\partial^2 \phi_{g_q}}{\partial i_d \partial i_q}(\mathbf{i}) + (\Delta i_q)^2 \frac{\partial^2 \phi_{g_q}}{\partial i_q^2}(\mathbf{i}) \right] + \dots \end{aligned} \quad (2.19)$$

The polynomials in (2.18) and (2.19) define the general structure of the polynomial itself, however due to the laborious task of determining the partial derivatives, a simpler method is chosen to find the approximation polynomials. The least-square approximation method is preferred as it deals directly with the minimization of the approximation error for a given interval, where the polynomial with minimum sum of least-squares is sought:

$$\text{minimize} \quad \sum_{k=0}^m (\phi_{g_d}(i_{d_k}, i_{q_k}) - \mathcal{T}_{g_d}(i_{d_k}, i_{q_k}))^2 \quad (2.20)$$

$$\text{minimize} \quad \sum_{k=0}^m (\phi_{g_q}(i_{d_k}, i_{q_k}) - \mathcal{T}_{g_q}(i_{d_k}, i_{q_k}))^2 \quad (2.21)$$

(2.20) and (2.21) depict the minimization of a set of  $m$  discrete points which could be for example the FEA simulation results of a given machine.

On the other hand, the polynomial structure can be simplified by replacing the derivatives and constants by coefficients and the repetition of variables combinations is avoided<sup>2</sup>. A generalization based on (2.18) and (2.19) is used to formulate the approximation polynomials with degree  $n$ :

$$\phi_{g_d}(i_d, i_q) \approx \mathcal{T}_{g_d}(i_d, i_q) = \sum_{i=0}^n \sum_{j=0}^i c_{d(i-j)(j)} i_d^{(i-j)} i_q^{(j)} \quad (2.22)$$

$$\phi_{g_q}(i_d, i_q) \approx \mathcal{T}_{g_q}(i_d, i_q) = \sum_{i=0}^n \sum_{j=0}^i c_{q(i-j)(j)} i_d^{(i-j)} i_q^{(j)} \quad (2.23)$$

<sup>2</sup>see A.12 in appendix A.1 for further information.

## 2.2 Flux-Linkage Mathematical Description

With the minimization of the approximation error, expressions (2.22) and (2.23) are then adopted to describe the magnetic fluxes for a given polynomial degree  $n$ . However as the target machine model is a flux linkage one, it is prudent at this point to switch from magnetic flux expressions to flux linkage expressions [38], for a given number of turns  $N$ :

$$\psi_d(i_d, i_q) = N\phi_{gd}(i_d, i_q) \quad (2.24)$$

$$\psi_q(i_d, i_q) = N\phi_{gq}(i_d, i_q) \quad (2.25)$$

The dq-flux linkages can be expressed in polynomial form by replacing (2.22) and (2.23) in (2.24) and (2.25). Furthermore new coefficients labels are introduced to emphasize that current-flux-linkage relationship relates to the inductance as discussed in section 2.1. The resulting expressions for a given polynomial degree  $n$  are then written in the following manner:

$$\psi_d(i_d, i_q) = \sum_{k=0}^{\infty} \sum_{i=0}^k l_{dq(k-i)(i)} i_d^{(k-i)} i_q^{(i)} \quad (2.26)$$

$$\psi_q(i_d, i_q) = \sum_{k=0}^{\infty} \sum_{i=0}^k l_{qd(k-i)(i)} i_q^{(k-i)} i_d^{(i)} \quad (2.27)$$

where  $\psi_d$  and  $\psi_q$  are the d- and q-axis flux-linkages respectively. The most relevant aspect of the expressions (2.26) and (2.27) is the fact that it is a function only of the currents along with constant coefficients. This formulation comes handy when these type of expressions are used to identify the flux-linkages of a machine, because the coefficients or constant values can be obtained for a given number of operating points and under certain circumstances they are time invariant. This opens the door for new approaches for online parameter identification, where routines at low execution rates can be used to perform the parameter identification, instead of demanding algorithms that need to be executed really fast in order to capture the nonlinear characteristics for each machine operating point.

### 2.2.1 Flux-Linkage Model

In general terms, expressions in (2.26) and (2.27) can describe the dq-axes flux-linkages, however, there are some symmetry properties with respect the dq-axes currents that can facilitate a simplification of the polynomials already introduced. The machine depicted in Fig. 2.5 represents a 4-pole pair IPMSM with key parameters listed in table 2.1. The 2D FEA simulation results of this machine will be used to illustrate the properties in question.

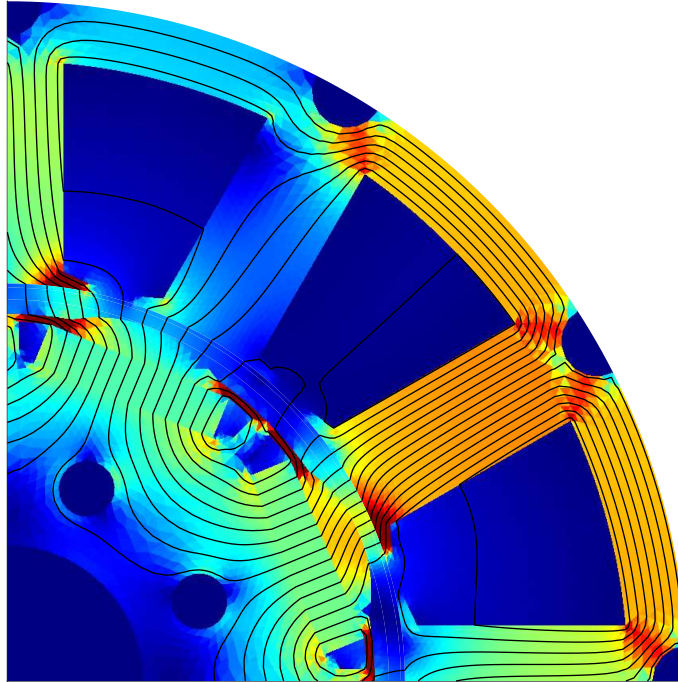


**Figure 2.5:** 4-pole pair IPMSM.

**Table 2.1:** IPMSM - Machine data

<i>Nominal Torque</i>	<i>4.6 Nm</i>
<i>Peak output power</i>	<i>600 W</i>
<i>Number of pole pairs</i>	<i>4</i>
<i>Nominal voltage</i>	<i>12 V</i>

The d- and q-axis flux-linkages were obtained for several combinations of  $i_d$  and  $i_q$  as illustrated in Fig. 2.6. This approach intends to cover the machine's four quadrants of

## 2.2 Flux-Linkage Mathematical Description

operation in order to analyze the different symmetries found with respect the current axes.

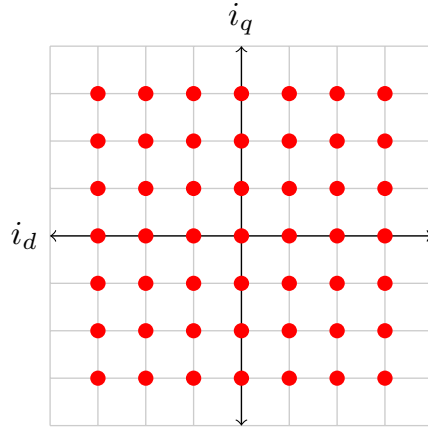


**Figure 2.6:** FE Simulation current data points definition

Each operating point, that corresponds to a given d- and q-axis current is simulated for one electrical cycle. The flux-linkage of three machine phases are transformed into d- and q-axis flux-linkages using the Park transformation (2.7), as shown in Fig. 2.7. The flux-linkage obtained contains several frequency components, as for example the 6th electrical harmonic component in this machine. The d- and q-axis flux-linkages used for further analysis correspond to the average value for one electrical cycle, which means, that only the information of the fundamental frequency is considered.

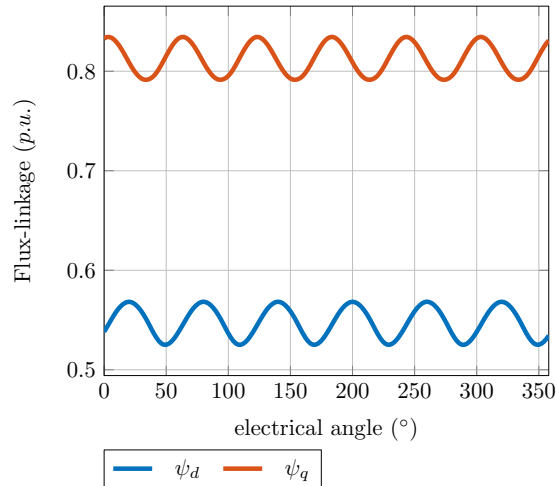


**Figure 2.7:** Example of the DQ-Flux-linkages

## 2 Non-Linear Machine Model

As shown in Fig. 2.8b, the q-axis flux-linkage surface is symmetric along the q-axis current, which means that  $\psi_q$  is an odd function with respect  $i_q$ . The amount of coefficients in the polynomial (2.27) can be reduced by setting the coefficients of terms with even powers of  $i_q$  to zero. Similarly,  $\psi_d$  exhibits a symmetric behavior with respect  $i_q$  as illustrated in Fig. 2.8a. Therefore, the coefficients of terms with odd powers of  $i_q$  in (2.26) can be set to zero.

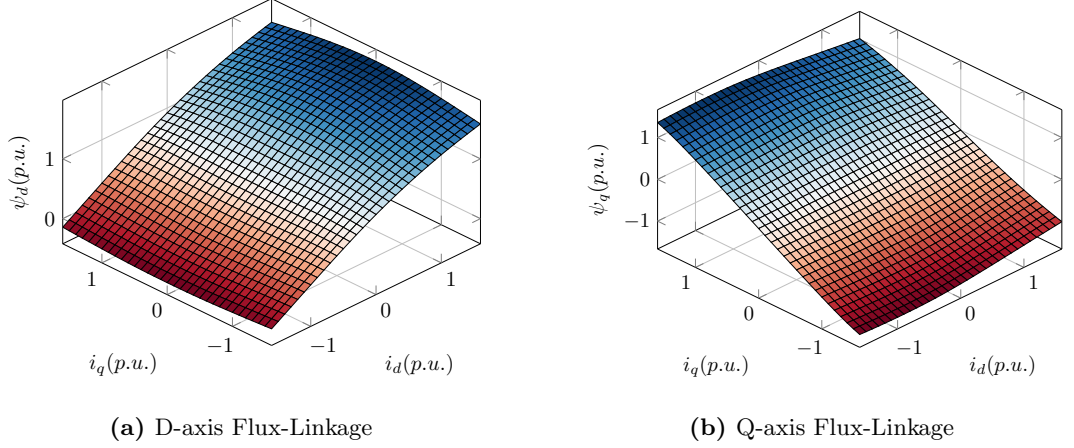


**Figure 2.8:** IPMSM Flux-Linkage - FE Simulation

Given the aforementioned simplifications in (2.26) and (2.27), the d-axis flux-linkage is rewritten in a simplified form for a polynomial degree  $n$  as [1]:

$$\psi_d(i_d, i_q) = \sum_{k=0}^P \sum_{i=0}^{n-2k} l_{dq(i)(2k)} i_d^{(i)} i_q^{(2k)} \quad (2.28)$$

with,  $P = \frac{n - \text{mod}(n, 2)}{2} \mid n \in \mathbb{N}^+$

where the sub-indexes in the notation  $l_{dq(i)(j)}$  indicates the power of  $i_d$  and  $i_q$  respectively. For the polynomial degree  $n = 3$ , the resulting d-axis flux-linkage expression can be written in the following form:

$$\psi_d(i_d, i_q) = l_{dq00} + l_{dq10} i_d + l_{dq02} i_q^2 + l_{dq20} i_d^2 + l_{dq12} i_d i_q^2 + l_{dq30} i_d^3 \quad (2.29)$$

where the constant term  $l_{dq00}$  corresponds to the permanent magnet flux-linkage  $\psi_m$ . Following the mentioned notation,  $l_{dq10}$  depicts the linear d-axis inductance and the remaining coefficients describe the cross-coupling and saturation effects.

## 2.2 Flux-Linkage Mathematical Description

The simplification of (2.28) leads to the following q-axis flux-linkage expression for a polynomial degree  $n$ :

$$\psi_q(i_d, i_q) = \sum_{k=0}^P \sum_{i=0}^{n-(2k+1)} l_{qd(2k+1)(i)} i_q^{(2k+1)} i_d^i \quad (2.30)$$

with,  $P = \frac{(n-1) - \text{mod}((n-1), 2)}{2} \mid n \in \mathbb{N}^+$

Where in this case, the sub-indexes in the notation  $l_{qd(i)j}$  represent the power of  $i_q$  and  $i_d$ , respectively. The resulting  $\psi_q(i_d, i_q)$  polynomial for  $n = 3$  takes the following form:

$$\psi_q(i_d, i_q) = l_{qd10} i_q + l_{qd11} i_q i_d + l_{qd30} i_q^3 + l_{qd12} i_q i_d^2 \quad (2.31)$$

where the coefficient  $l_{qd10}$  corresponds to the linear q-axis inductance and the other coefficients depict the cross-saturation and saturation effects.

### 2.2.2 Considering Mutual Terms

The dq-axes flux-linkage expressions (2.28) and (2.30) describe the nonlinear and cross-coupling effects from each axis, nevertheless the analysis of the magnetic coenergy enables further simplifications of the flux-linkages polynomials. The magnetic coenergy  $W_c$  is defined as [39]:

$$W_c = \int \psi di \quad (2.32)$$

Mathematically, this is the area below the curve  $\psi$  vs.  $i$  as depicted in Fig. 2.9:

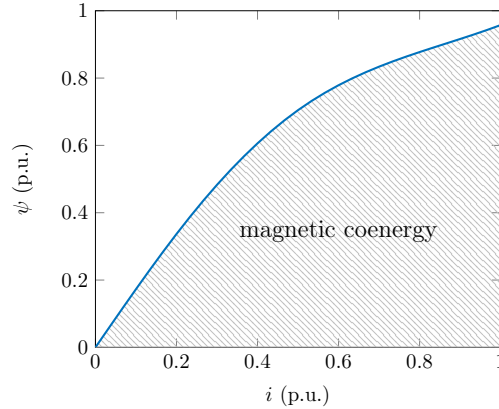


**Figure 2.9:** Magnetic coenergy

Applying (2.32) to the dq-axes flux-linkages leads to the total coenergy  $W_{cdq}$ :

$$W_{cdq} = \int \psi_d(i_d, i_q) di_d + \int \psi_q(i_d, i_q) di_q \quad (2.33)$$

## 2 Non-Linear Machine Model

The dq-axes flux-linkages can be then formulated in terms of the coenergy by calculating the partial derivative with respect to  $i_d$  and holding  $i_q$  and vice versa [34, 40]:

$$\begin{aligned}\frac{\partial W_{c_{dq}}}{\partial i_d} &= \psi_d(i_d, i_q) \\ \frac{\partial W_{c_{dq}}}{\partial i_q} &= \psi_q(i_d, i_q)\end{aligned}\quad (2.34)$$

The cross partial derivatives of the dq-axes flux-linkages in terms of the coenergy (2.34) lead to:

$$\begin{aligned}\frac{\partial \psi_d(i_d, i_q)}{\partial i_q} &= \frac{\partial^2 W_{c_{dq}}}{\partial i_q \partial i_d} \\ \frac{\partial \psi_q(i_d, i_q)}{\partial i_d} &= \frac{\partial^2 W_{c_{dq}}}{\partial i_d \partial i_q}\end{aligned}\quad (2.35)$$

Finally, with  $\frac{\partial^2 W_{c_{dq}}}{\partial i_q \partial i_d} = \frac{\partial^2 W_{c_{dq}}}{\partial i_d \partial i_q}$ , the following equality holds:

$$\frac{\partial \psi_d(i_d, i_q)}{\partial i_q} = \frac{\partial \psi_q(i_d, i_q)}{\partial i_d}\quad (2.36)$$

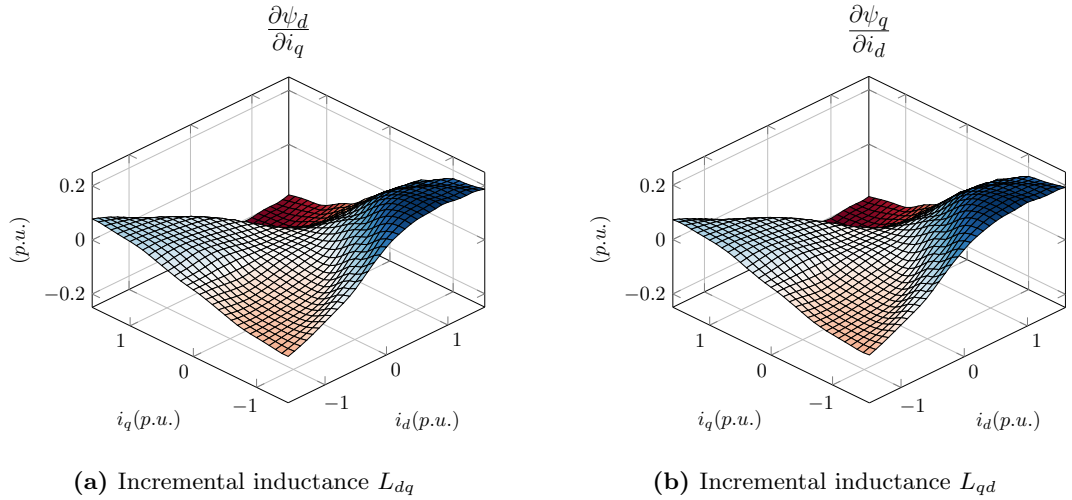


**Figure 2.10:** IPMSM Mutual Inductances - FE Data

The equality in (2.36) can be easily seen when the partial derivatives are applied to the dq-flux linkages to obtain the mutual inductances. Figure 2.10 depicts the mutual inductances  $L_{dq}(i_d, i_q)$  and  $L_{qd}(i_d, i_q)$  of the IPMSM using the flux-linkage information

obtained from the 2D-FE simulation.

One key aspect of describing the flux-linkage mathematically as a polynomial, is the fact that its derivatives with respect to the dq-currents can be easily calculated. The partial derivatives in (2.36) result into the following expressions:

$$\begin{aligned}\frac{\partial \psi_d}{\partial i_q} &= \sum_{k=1}^P \sum_{i=0}^{n-2k} 2k \cdot l_{dq(i)(2k)} \cdot i_d^{(i)} \cdot i_q^{(2k-1)} \\ \frac{\partial \psi_q}{\partial i_d} &= \sum_{k=0}^P \sum_{i=1}^{n-(2k+1)} i \cdot l_{qd(2k+1)(i)} \cdot i_q^{(2k+1)} \cdot i_d^{(i-1)}\end{aligned}\quad (2.37)$$

As (2.36) holds, then the number of coefficients needed to describe the flux-linkages for a given polynomial order can be reduced. By equating (2.37), expressions (2.28) and (2.30) can be rewritten as:

$$\begin{aligned}\psi_d(i_d, i_q) &= \sum_{i=0}^n l_{dq(i)(0)} i_d^{(i)} + \sum_{k=1}^P \sum_{i=0}^{n-2k} \frac{c_{dq(i)(2k-1)}}{2k} i_d^{(i)} i_q^{(2k)} \\ \text{with, } P &= \frac{n - \text{mod}(n, 2)}{2} \mid n \in \mathbb{N}^+ \quad \text{and} \quad \psi_m = l_{dq00}\end{aligned}\quad (2.38)$$

$$\begin{aligned}\psi_q(i_d, i_q) &= \sum_{k=0}^P l_{qd(2k+1)(0)} i_q^{(2k+1)} + \sum_{k=0}^P \sum_{i=1}^{n-(2k+1)} \frac{c_{dq(i-1)(2k+1)}}{i} i_q^{(2k+1)} i_d^{(i)} \\ \text{with, } P &= \frac{(n-1) - \text{mod}((n-1), 2)}{2} \mid n \in \mathbb{N}^+\end{aligned}\quad (2.39)$$

where  $n$  is the given polynomial degree. The symbols  $c_{dq(i)j}$  are coefficients with subindexes indicating the power of  $i_d$  and  $i_q$ , respectively. The mutual terms  $c_{dq(i)j}$  that appear in (2.38) and (2.39) describe the coupling between the d- and q-axes.

### 2.2.3 Machine Inductance Expressions

Recalling the definition of the inductances in (2.5), the absolute inductance is defined as the flux-linkage to current ratio. In the case of the  $\psi_d$  only the terms that depend on  $i_d$  contribute to the d-axis inductance  $L_d$ . Therefore the term  $\psi_d(0, i_q)$  is subtracted from  $\psi_d$  to obtain the flux-linkage related to  $L_d$  in the following manner:

$$L_d(i_d, i_q) = \frac{\psi_d(i_d, i_q) - \psi_d(0, i_q)}{i_d}\quad (2.40)$$

The d-axis absolute inductance according to (2.40) can be then expressed in a polynomial form by replacing (2.38) in (2.40) as:

$$\begin{aligned}L_d(i_d, i_q) &= \sum_{i=1}^n l_{dq(i)(0)} i_d^{(i-1)} + \sum_{k=1}^P \sum_{i=1}^{n-2k} \frac{c_{dq(i)(2k-1)}}{2k} i_d^{(i-1)} i_q^{(2k)} \\ \text{with, } P &= \frac{n - \text{mod}(n, 2)}{2} \mid n \in \mathbb{N}^+\end{aligned}\quad (2.41)$$

## 2 Non-Linear Machine Model

The same procedure can be carried out for the absolute q-axis inductance  $L_q$  as shown in (2.53).

$$L_q(i_d, i_q) = \frac{\psi_q(i_d, i_q)}{i_q} \quad (2.42)$$

$$L_q(i_d, i_q) = \sum_{k=0}^P l_{qd(2k+1)(0)} i_q^{(2k)} + \sum_{k=0}^P \sum_{i=1}^{n-(2k+1)} \frac{C_{dq(i-1)(2k+1)}}{i} i_q^{(2k)} i_d^{(i)} \quad (2.43)$$

with,  $P = \frac{(n-1) - \text{mod}((n-1), 2)}{2} \mid n \in \mathbb{N}^+$

Similarly to the absolute inductances, the incremental inductances can be easily formulated with help of the flux-linkages. In this specific case, the fact that the flux-linkages are described using analytic functions comes quite handy, as the derivatives of polynomials are a straightforward calculation. Recalling again the definition of the incremental inductances as the rate of change of flux-linkage with respect the current, they are obtained by calculating the partial derivatives of the flux-linkage with respect the dq-axes currents. This will result in the incremental self- and mutual-inductances, which are then calculated in the following manner:

$$L_{dd}(i_d, i_q) = \frac{\partial \psi_d(i_d, i_q)}{\partial i_d} \quad \text{and} \quad L_{qq}(i_d, i_q) = \frac{\partial \psi_q(i_d, i_q)}{\partial i_q} \quad (2.44)$$

$$L_{dd}(i_d, i_q) = \sum_{i=1}^n i l_{dq(i)(0)} i_d^{(i-1)} + \sum_{k=1}^P \sum_{i=1}^{n-2k} \frac{i C_{dq(i)(2k-1)}}{2k} i_d^{(i-1)} i_q^{(2k)} \quad (2.45)$$

with,  $P = \frac{n - \text{mod}(n, 2)}{2} \mid n \in \mathbb{N}^+$

$$L_{qq}(i_d, i_q) = \sum_{k=0}^P (2k+1) l_{qd(2k+1)(0)} i_q^{(2k)} + \sum_{k=0}^P \sum_{i=1}^{n-(2k+1)} \frac{(2k+1) C_{dq(i-1)(2k+1)}}{i} i_q^{(2k)} i_d^{(i)} \quad (2.46)$$

with,  $P = \frac{(n-1) - \text{mod}((n-1), 2)}{2} \mid n \in \mathbb{N}^+$

The mutual incremental inductances were already mentioned in section 2.2.2, where the energy conservation law was used to simplify further the flux-linkage expressions. The mutual inductances  $L_{dq}$  and  $L_{qd}$  are calculated knowing before hand from (2.36) that they are equal.

$$L_{dq}(i_d, i_q) = \frac{\partial \psi_d(i_d, i_q)}{\partial i_q} = \frac{\partial \psi_q(i_d, i_q)}{\partial i_d} = L_{qd}(i_d, i_q) \quad (2.47)$$

$$L_{dq}(i_d, i_q) = L_{qd}(i_d, i_q) = \sum_{k=1}^P \sum_{i=0}^{n-2k} c_{dq(i)(2k-1)} i_d^{(i)} i_q^{(2k-1)} \quad (2.48)$$

with,  $P = \frac{n - \text{mod}(n, 2)}{2} \mid n \in \mathbb{N}^+$

The advantage of having an analytical description of the flux-linkages is the fact that the inductances, either the absolute or the differential ones can be calculated directly with the help of the coefficients. There is no need for any data manipulation, like interpolation and in the case of the differential inductances the calculation is straightforward as there is no need for any discrete derivative of the data, it is just performed analytically.

### 2.2.4 Motor Torque Constant

As presented in [35] and [14], the concept of  $K_t$  originates from the idea of a motor with no magnetic nonlinearities, where the permanent flux-linkage  $\psi_m$  and  $K_t$  are linearly proportional. Specially the case where the d-axis current is zero leads to the interaction between permanent flux-linkage and q-axis current, which is represented by  $\psi_d(0, i_q)$ . Where  $i_q$  contributes to the saturation of the resultant d-axis flux-linkage. This effect is evident when looking at the relationship between electromagnetic torque  $T_e$  and phase current, which is known as motor torque constant  $K_t$ , with units  $Nm/A$ , is defined as:

$$K_t = \frac{T_e}{i_q} \quad (2.49)$$

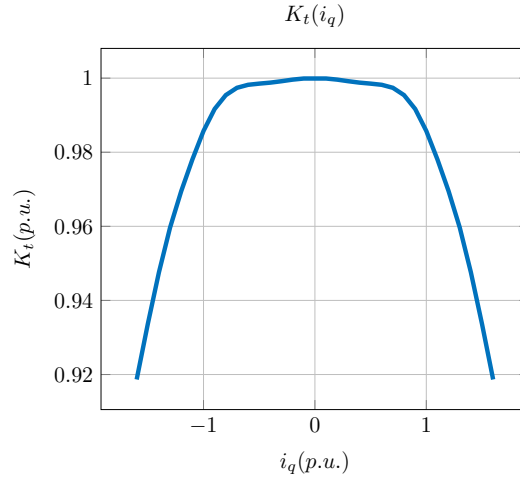


**Figure 2.11:** IPMSM torque constant.

At the presence of reluctance torque, e.g. at IPMSMs, the current used to calculate  $K_t$  is  $i_q$ . Fig. 2.11 depicts the motor torque constant derived from FEA data of Fig. 2.8. It can be appreciated in Fig. 2.11 the reduction of  $K_t$  of about 8% at increasing  $i_q$ . The torque is a function of stator current and flux-linkage, as in (2.13), the d-axis current is set to zero and the d-axis flux-linkage is replaced by (2.38), the torque expression takes the following form:

$$T_e(0, i_q) = \frac{3}{2} p \cdot \psi_d(0, i_q) \cdot i_q \quad (2.50)$$

## 2 Non-Linear Machine Model

Where  $\psi_d(0, i_q)$  is the permanent magnet flux-linkage and the terms with coefficients of the type  $c_{dq(0)}$  represent the cross-saturation in  $\psi_d$  due to  $i_q$ . This means that even at the absence of  $i_d$ ,  $i_q$  affects  $\psi_d$ . Replacing  $T_e$  by (2.50) and  $I$  by  $i_q$  in (2.49), it yields

$$K_t(i_q) = \frac{3}{2}p \left( \psi_m + \sum_{k=1}^R \frac{c_{dq(0)(2k-1)} i_q^{(2k)}}{2k} \right) \quad (2.51)$$

with,  $R = \frac{n - \text{mod}(n, 2)}{2} \mid n \in \mathbb{N}^+$

If the machine is linear, all the coefficients multiplied by  $i_q$  in (2.51) would be zero, making  $K_t$  linearly proportional to  $\psi_m$ . In the case of a nonlinear machine, the terms with coefficients  $c_{dq(0)}$  describe the cross-saturation due to  $i_q$ . They even could be used as design indicator to assess the saturation of  $K_t$  at maximum current magnitude.

### 2.2.5 Separation of Nonlinear Effects

Determining PMSM's parameters in unsaturated and saturated conditions has been a research topic for many years. There have been many reported approaches to capture the saturation and cross-coupling effects. Especially in the domain of Finite Elements Analysis, a method excels for its popularity, which is the *frozen permeabilities method* [41]. The main premise of this approach is to run a FE simulation and store the magnetic permeabilities and use these values for two further FE simulations where the influence of the permanent magnets and the winding currents is simulated separately. To obtain the different machine parameters such as absolute inductance, permanent magnet flux-linkage and incremental inductance, the authors in [41] consider various simplified machine models. With respect to the validity of the resulting parameters presented in [41], it is acknowledged that the incremental inductances can be clearly determined. They are defined as the flux-linkage rate of change with respect to the dq-axes currents, so they can be evaluated if the flux-linkage and current information is available. The challenging part appears when dealing with absolute inductance and permanent magnet flux-linkage. The *frozen permeabilities method* is used as a way to separate those parameters. It is proposed in [41] to carry out three FE simulations in order to have enough data to separate the parameters already mentioned, but it seems quite difficult to verify the validity of this approach experimentally as it was reported in [42].

As this work proposes to model the nonlinear effects of PMSMs analytically, a straight forward result is the implicit separation of contribution of the permanent magnets and the winding currents. The absolute inductances can be clearly identified in the flux-linkage expressions (2.38) and (2.39). The interaction between current and the permanent magnet flux-linkage that can be appreciated on the electromagnetic torque at increasing  $i_q$  and at the absent of  $i_d$  can be seen as well. In order to illustrate the separation of these parameters and effects, a polynomial degree  $n = 3$  is chosen for simplicity:

### 2.3 Considering Magnet-Flux variations

$$\psi_d(i_d, i_q) = \underbrace{\psi_m + \frac{c_{dq01}i_q^2}{2}}_{\psi_{m_{sat}}(i_q)} + \underbrace{l_{dq10}i_d + l_{dq20}i_d^2 + l_{dq30}i_d^3 + \frac{c_{dq11}i_d i_q^2}{2}}_{L_d(i_d, i_q)i_d} \quad (2.52)$$

$$\psi_q(i_d, i_q) = \underbrace{l_{qd10}i_q + l_{qd30}i_q^3 + c_{dq01}i_d i_q + \frac{c_{dq11}i_d^2 i_q}{2}}_{L_q(i_d, i_q)i_q} \quad (2.53)$$

Basically, what the groups of terms in (2.52) are indicating is the contribution of the permanent magnet flux-linkage and of  $i_d$  with the corresponding cross-saturation due to  $i_q$ . Keeping that in mind,  $\psi_d$  can then be rewritten in the following form :

$$\begin{aligned} \psi_d(i_d, i_q) &= \underbrace{\psi_m + \sum_{k=1}^P \frac{c_{dq(0)(2k-1)}}{2k} i_q^{(2k)}}_{\psi_{m_{sat}}(i_q)} \\ &+ \underbrace{\sum_{i=1}^n l_{dq(i)(0)} i_d^{(i)} + \sum_{k=1}^P \sum_{i=1}^{n-2k} \frac{c_{dq(i)(2k-1)}}{2k} i_d^{(i)} i_q^{(2k)}}_{\psi_{d_0}(i_d, i_q)} \end{aligned} \quad (2.54)$$

with,  $P = \frac{n - \text{mod}(n, 2)}{2} \mid n \in \mathbb{N}^+$

the two flux-linkages terms presented in (2.54) clearly show the contribution of the permanent magnet flux-linkage and its dependency with respect  $i_q$  and the flux-linkage generated by  $i_d$  as well. With the proposed approach, the polynomial degree  $n$  is determined by the number of operating points obtained in the FE simulation. This opens the possibility to minimize or optimize the number of simulations required to describe the machine. Which in the case of a FE simulation could mean a significant reduction of computation time.

### 2.3 Considering Magnet-Flux variations

The main motivation to consider the effects of the permanent magnets on the overall flux-linkage comes from the necessity to assess the impact of magnet flux-linkage variations on the dq-axes inductances. This need is due to the main target of creating an algorithm for online parameter and temperature estimation, where the magnet temperature is derived from the estimation of the permanent flux-linkage. On the other hand, for simulation purposes, the inclusion of magnet temperature effects enables the creation of a high fidelity machine model that can be coupled to a machine thermal model. The latter will facilitate the previous analysis required for the development of the online estimation algorithm. As a final remark, a model or expression of the inductance

## 2 Non-Linear Machine Model

dependency on the permanent magnet flux-linkage can help to estimate the expected maximum and minimum limits the inductances for the online estimation.

It is important to note, that this work moves around permanent magnet synchronous machines, where the rotor of the machine contains permanent magnets, contributing to a bias magnetic flux which tend to be constant and can vary in the context of temperature or manufacturing tolerances if normal operation is assumed. The potential of extending the flux-linkage expressions to consider variable  $\psi_m$  allows the model to be extended to wound field synchronous machines, where the flux-linkage due to the rotor's current excitation can be replaced by  $\psi_m$ .

The past sections introduced a simplified model that describes the flux-linkage including saturation and cross-coupling effects that depends only on the dq-axes currents. The polynomial degree determines the accuracy of the representation of the flux-linkages, but it can even represent the classical linear inductance based model when choosing a first degree polynomial. So far the permanent magnet flux-linkage  $\psi_m$  has been assumed to remain constant. But in reality it depends on the rotor magnet characteristics, such as material properties or even manufacturing process tolerances. Temperature can affect the magnet materials [36, 43], high temperatures exposure, for long periods of time particularly coupled with high currents can lead to irreversible losses.

The most extreme scenario is when the so called Curie temperature is reached, as the saturation magnetization of the material becomes zero [36, 44]. The reversible temperature effects can be understood as the loss of remanence when the magnet temperature increases. This loss is represented by two coefficients [44], the remanence  $B_r$  temperature coefficient  $\alpha$  and the intrinsic coercivity  $H_{ci}$  temperature coefficient  $\beta$ . Which means that the temperature dependency is assumed to be linear in the form:

$$B_r(T) = B_{rT_0} [1 + \alpha(T - T_0)] \quad (2.55)$$

$$H_{ci}(T) = H_{ciT_0} [1 + \beta(T - T_0)] \quad (2.56)$$

The reversible temperature coefficients are normally specified for a determined range, starting at room temperature. The coefficient is then fitted assuming a linear relationship with the temperature. Extending this range could lead to a different value of the temperature coefficient, as for wider temperature ranges the remanence and the intrinsic coercivity have a nonlinear behavior with respect the temperature [44, 45]. Table 2.2 summarizes the remanence temperature coefficients of some magnet materials [46].

**Table 2.2:** Typical reversible temperature coefficients

Material	Grade	Max. Temp. (°C)	$\alpha$ (%/°C)	$\beta$ (%/°C)
<i>Alnico</i> , cast	5	100	-0.02	-0.01
<i>Alnico</i> , cast	8	100	-0.02	-0.01
<i>SmCo</i> <sub>5</sub>	20 MGOe	120	-0.04	-0.4
<i>Sm</i> <sub>2</sub> <i>Co</i> <sub>17</sub>	27 MGOe	120	-0.035	-0.2
<i>NdFeB</i> , bonded	MQP-B	100	-0.11	-0.4
<i>NdFeB</i> , sintered	L-38UHT	180	-0.10	-0.5
Ferrite, sintered	C-5,-8	120	-0.20	0.27

Recalling the relationship between flux-density and magnetic flux as per (2.14) and the equivalent magnetic circuit of a pole in a permanent magnet synchronous machine of Fig. 2.4, the following expression is considered:

$$\phi_r = B_r A \quad (2.57)$$

where  $B_r$  is the remanence of the pole magnet,  $A$  is the corresponding area of the magnet and  $\phi_r$  is the magnetic flux in that area. The temperature dependency of  $B_r$  as in (2.55) will lead to variations in the biasing of the machine's magnetic circuit over the working temperature range of the machine. In addition to the temperature effects on  $B_r$ , the magnet manufacturing tolerances play another role in the final value of the magnet remanence. For example, variations of dimensions and magnetization lead to a certain distribution part to part of the  $B_r$  value in the magnets. Therefore the expected variations of the permanent magnet flux-linkage will be a combination of part-to-part tolerances and temperature effects.

### 2.3.1 Flux-linkage Expressions

The flux-linkage expansions (2.26) and (2.27) that are valid for a given  $\psi_{m_0}$  can then be reformulated to include the influence of the permanent magnet flux-linkage  $\psi_m$ . The expansions can be rewritten in the following form for a given polynomial degree  $n$ :

$$\psi_d(i_d, i_q, \psi_m) = \sum_{j=0}^n \sum_{i=0}^j \sum_{k=0}^{n-j} l_{dq(j-i)(i)(k)} i_d^{(j-i)} i_q^{(i)} \psi_m^{(k)} \quad (2.58)$$

$$\psi_q(i_d, i_q, \psi_m) = \sum_{j=0}^n \sum_{i=0}^j \sum_{k=0}^{n-j} l_{qd(j-i)(i)(k)} i_q^{(j-i)} i_d^{(i)} \psi_m^{(k)} \quad (2.59)$$

## 2 Non-Linear Machine Model

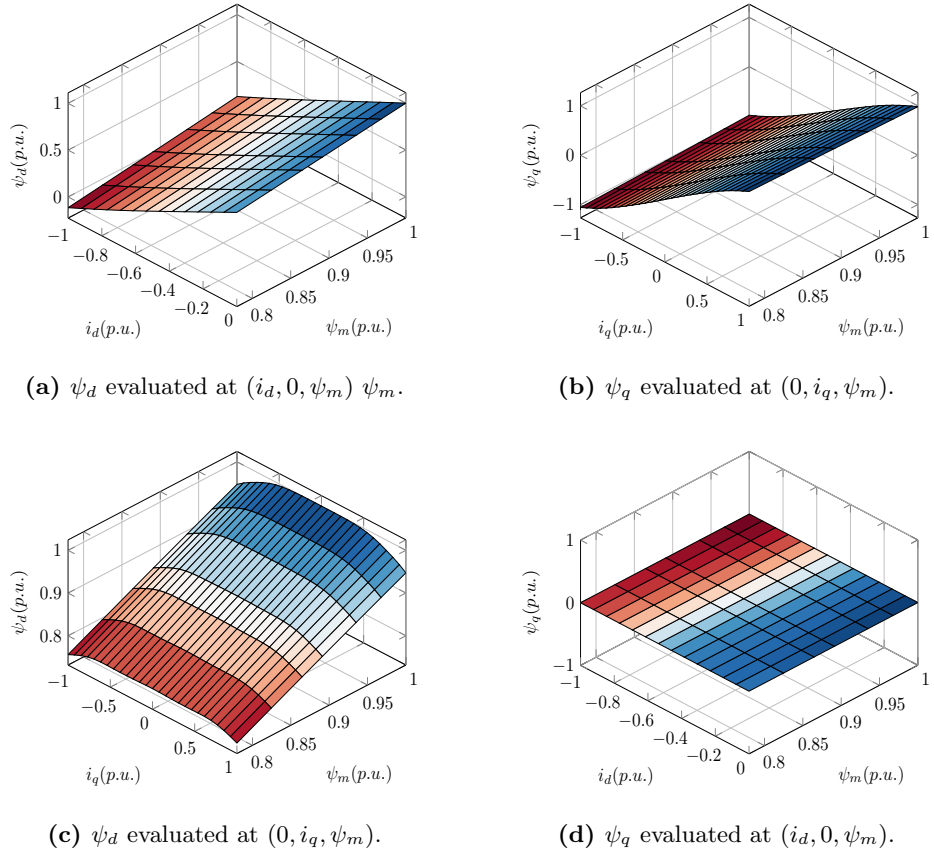


**Figure 2.12:** Flux-linkage at different  $\psi_m$  values

As in the previous section, these expansions can be simplified if the form of the flux-linkages with respect to  $\psi_m$  is considered. The most evident relationships can be observed in Fig. 2.12c and 2.12d, where the DQ-axes flux-linkages were obtained, through a 2D-FE simulation of the same machine of section 2.2.1 for seven different  $\psi_m$  values ranging from  $1p.u.$  to  $0.78p.u.$ , covering a reasonable variation range which can be the result of magnet temperature and manufacturing tolerances.

$$\begin{aligned}\psi_d(0, i_q, \psi_m) &= \psi_d(0, -i_q, \psi_m) \\ \psi_q(i_d, 0, \psi_m) &= 0\end{aligned}\tag{2.60}$$

The expressions in (2.60) imply that the variables  $i_d$  and  $\psi_m$  contribute to  $\psi_q$  only at the presence of  $i_q$  and  $\psi_d$  is affected directly by  $i_q$  regardless of  $i_d$ . In addition to (2.60), at the absence of  $\psi_m$ ,  $\psi_d$  with respect to  $i_d$  would follow the same law as  $\psi_q$  with respect  $i_q$ , as the winding currents will solely be responsible for the magnetic flux in the machine. The latter leads to the equality  $\psi_d(i_d, i_q, 0) = -\psi_d(-i_d, i_q, 0)$ . All these observations enable the simplification or the exclusion of coefficients with determined powers, leading to the following expressions:

$$\begin{aligned}
 \psi_d(i_d, i_q, \psi_m) &= \sum_{i=0}^{P_1} \sum_{j=0}^{R_1} \sum_{k=0}^{S_1} l_{dq(2i+1)(2j)(2k)} i_d^{(2i+1)} i_q^{(2j)} \psi_m^{(2k)} \\
 &\quad + \sum_{i=0}^{P_2} \sum_{j=0}^{R_2} \sum_{k=1}^{S_2} l_{dq(2i)(2j)(k)} i_d^{(2i)} i_q^{(2j)} \psi_m^{(k)} \\
 \text{with, } P_1 &= \frac{n-1-\text{mod}(n-1, 2)}{2} \mid n \in \mathbb{N}^+ \\
 R_1 &= \frac{n-(2i+1)-\text{mod}(n-(2i+1), 2)}{2} \\
 S_1 &= \frac{n-(2i+1)-2j-\text{mod}(n-(2i+1)-2j, 2)}{2} \\
 P_2 &= \frac{n-\text{mod}(n, 2)}{2} \\
 R_2 &= \frac{n-2i-\text{mod}(n-2i, 2)}{2} \\
 S_2 &= n-2i-2j
 \end{aligned} \tag{2.61}$$

$$\begin{aligned}
 \psi_q(i_d, i_q, \psi_m) &= \sum_{i=0}^n \sum_{j=0}^R \sum_{k=0}^S l_{qd(2j+1)(i)(2k+S)} i_q^{(2j+1)} i_d^{(i)} \psi_m^{(k)} \\
 \text{with, } R &= \frac{n-i-1-\text{mod}(n-i-1, 2)}{2} \mid n \in \mathbb{N}^+ \\
 S &= n-i-(2j+1)
 \end{aligned} \tag{2.62}$$

These two expressions (2.61) and (2.62) enable again the separation of the three parameters considered so far; dq-axes inductances and torque constant. This analytical way of describing the flux-linkages is a tool for a clean representation of the nonlinear effects that produces the interaction of the magnets and the winding currents. Not only the saturation effects caused by large currents can be captured and isolated but the effects of the bias flux coming from the magnets. The next subsection will look into the already mentioned parameters and its dependency on  $\psi_m$ .

### 2.3.2 Inductance and Torque Constant Dependency on Magnet Flux-linkage

With the consideration of  $\psi_m$  as a third variable, in the flux-linkage expressions, the absolute d-axis inductance (2.40) is then extended in the following form:

$$L_d(i_d, i_q, \psi_m) = \frac{\psi_d(i_d, i_q, \psi_m) - \psi_d(0, i_q, \psi_m)}{i_d} \tag{2.63}$$

Ultimately (2.63) depicts the effect that  $i_d$  has on  $\psi_d$  by subtracting the terms where  $i_d$  is not involved. The absolute inductance expression is then obtained by replacing (2.61) in (2.63) producing:

## 2 Non-Linear Machine Model

$$\begin{aligned}
L_d(i_d, i_q, \psi_m) &= \sum_{i=0}^{P_1} \sum_{j=0}^{R_1} \sum_{k=0}^{S_1} l_{dq(2i+1)(2j)(2k)} i_d^{(2i)} i_q^{(2j)} \psi_m^{(2k)} \\
&\quad + \sum_{i=1}^{P_2} \sum_{j=0}^{R_2} \sum_{k=1}^{S_2} l_{dq(2i)(2j)(k)} i_d^{(2i-1)} i_q^{(2j)} \psi_m^{(k)} \\
\text{with, } P_1 &= \frac{n-1 - \text{mod}(n-1, 2)}{2} \mid n \in \mathbb{N}^+ \\
R_1 &= \frac{n - (2i+1) - \text{mod}(n - (2i+1), 2)}{2} \\
S_1 &= \frac{n - (2i+1) - 2j - \text{mod}(n - (2i+1) - 2j, 2)}{2} \\
P_2 &= \frac{n - \text{mod}(n, 2)}{2} \\
R_2 &= \frac{n - 2i - \text{mod}(n - 2i, 2)}{2} \\
S_2 &= n - 2i - 2j
\end{aligned} \tag{2.64}$$

In a similar manner, the general formulation of the absolute q-axis inductance is rewritten to account for  $\psi_m$  in the following way:

$$L_q(i_d, i_q, \psi_m) = \frac{\psi_q(i_d, i_q, \psi_m)}{i_q} \tag{2.65}$$

The final formulation of  $L_q$  depending on the currents and  $\psi_m$  can be found by replacing (2.62) into (2.65):

$$\begin{aligned}
L_q(i_d, i_q, \psi_m) &= \sum_{i=0}^n \sum_{j=0}^R \sum_{k=0}^S l_{qd(2j+1)(i)(2k+S)} i_q^{(2j)} i_d^{(i)} \psi_m^{(k)} \\
\text{with, } R &= \frac{n - i - 1 - \text{mod}(n - i - 1, 2)}{2} \mid n \in \mathbb{N}^+ \\
S &= n - i - (2j + 1)
\end{aligned} \tag{2.66}$$

The same treatment is applied to the torque constant, where interaction between  $i_q$  and  $\psi_m$  is also expressed in terms of flux-linkage. The electromagnetic torque as per (2.13) is rewritten as :

$$T_e(i_d, i_q, \psi_m) = \frac{3}{2} p (\psi_d(i_d, i_q, \psi_m) i_q - \psi_q(i_d, i_q, \psi_m) i_d) \tag{2.67}$$

Given the definition of the torque constant (2.49), only the contribution of  $i_q$  is taken into account, letting  $i_d = 0$  in (2.67) and replacing into (2.49) it yields:

$$K_t(i_q, \psi_m) = \frac{T_e(0, i_q, \psi_m)}{i_q} = \frac{3}{2} p \cdot \psi_d(0, i_q, \psi_m) \tag{2.68}$$

Finally, (2.61) is replaced into (2.68) leading to the following compact expression as all the terms containing  $i_d$  equal zero:

$$K_t(i_q, \psi_m) = \frac{3}{2}p \left( \sum_{j=0}^R \sum_{k=1}^{n-2j} l_{dq(0)(2j)(k)} i_q^{(2j)} \psi_m^{(k)} \right) \quad (2.69)$$

with,  $R = \frac{n - \text{mod}(n, 2)}{2} \mid n \in \mathbb{N}^+$

Thanks to the polynomial representation of the flux-linkages, it is possible to clearly identify the influence of  $\psi_m$  in the parameters of interest. It is then possible to formulate the dq-axes flux-linkage expressions in a way that the absolute inductances and permanent magnet flux-linkage terms are clearly grouped. This is done by making use of the new expressions for  $L_d$ ,  $L_q$  and  $K_t$  presented in (2.64), (2.66) and (2.69) respectively, in the following form for  $n = 3$  :

$$\begin{aligned} \psi_d(i_d, i_q, \psi_m) &= \underbrace{l_{dq001} \psi_m + l_{dq021} i_q^2 \psi_m}_{\psi_d(0, i_q, \psi_m)} \\ &+ \underbrace{(l_{dq100} + l_{dq102} \psi_m^2 + l_{dq201} i_d \psi_m + l_{dq300} i_d^2 + l_{dq120} i_q^2) i_d}_{L_d(i_d, i_q, \psi_m) i_d} \end{aligned} \quad (2.70)$$

The first term in (2.70) describes the permanent magnet flux and its q-axis current dependency similar to the term in (2.52), with the additional information that the saturation term is accompanied by  $\psi_m$ . This indicates that the saturation effect observed in  $K_t$  depends directly on  $\psi_m$  itself. The immediate consequence of this dependency is that the degree of saturation is also magnet temperature dependent. In the second term of (2.70) it is evident the contribution of  $i_d$  and  $\psi_m$  to the linear inductance term, so far represented by the coefficient  $l_{dq10}$ . The term  $l_{dq102} i_d \psi_m^2$  indicates the dependency of  $L_d$  with respect to permanent magnet flux-linkage or the magnet temperature. The coefficient  $l_{dq10}$  is actually represented by the coefficients with subscript  $10X$  :

$$l_{dq10} = l_{dq100} + l_{dq102} \psi_m^2 \quad (2.71)$$

expression (2.71) exposes then the linear inductance without the effect of the magnets in the form of  $l_{dq100}$ . Additionally,  $l_{dq102}$  represents the biasing effect of the magnetic flux produced by the magnets in the magnetic circuit, which leads to a different linear inductance. Although it is common to assume the inductances are temperature independent, the role of  $\psi_m$  in the resultant coefficient (2.71) becomes evident. However variations of  $\psi_m$  would impact in this example the second term which at the same time is just a fraction of  $l_{dq10}$  leading to small variations<sup>3</sup>.

<sup>3</sup>The effects of  $\psi_m$  on the inductances will be discussed graphically in section 3.3.4.2

## 2 Non-Linear Machine Model

Analogue to the  $\psi_d$ ,  $\psi_q$  can be written in terms of the absolute inductance as:

$$\psi_q(i_d, i_q, \psi_m) = \underbrace{(l_{qd100} + l_{qd102}\psi_m^2 + l_{qd300}i_q^2 + l_{qd110}i_d + l_{qd111}i_d\psi_m + l_{qd120}i_d^2)}_{L_q(i_d, i_q, \psi_m)} i_q \quad (2.72)$$

Similarly the term  $l_{qd102}i_q\psi_m^2$  in (2.72) shows the same dependency on the linear  $L_q$  also named in the previous sections as  $l_{qd10}$ .

### 2.4 Considering Field Currents in Wound Field Synchronous Machines

This section aims to look into the flux-linkage description of a wound field synchronous machine. Which is a machine topology analogue to the PMSM, as instead of using permanent magnets, the magnetic circuit in the machine is biased with a DC-field generated by a rotor coil, as shown in Fig. (2.13).

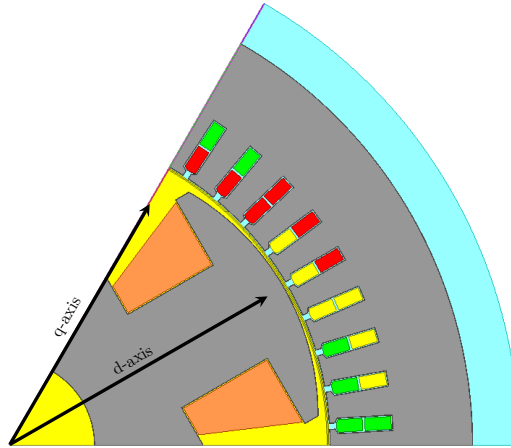


**Figure 2.13:** Wound field synchronous machine

The FE drawing displayed in Fig. (2.13) corresponds to one pole of a 3-pole pair WFSM. The constant flux coming from the rotor is aligned to the d-axis, in the same way as the permanent magnet flux does in a PMSM. For this type of machine the additional third variable, namely the field current  $i_f$ , plays an important role in the determination, for example, of the optimal torque or efficiency maps at determined operating points. With respect PMSMs, the FE simulation analysis is often restricted to a few permanent magnet flux-linkage values corresponding to different magnet temperatures. So the required simulation data depends mainly on the variation of  $i_d$  and  $i_q$ . On the other hand, for WFSMs, the field current amount  $i_f$  should be considered for a

## 2.4 Considering Field Currents in Wound Field Synchronous Machines

certain range increasing the simulation effort. This is then an important driver for the use of an analytical description of the flux-linkages in a WFSM. The phase voltages of the WFSM can be described in terms of flux-linkage [38] as:

$$\mathbf{V}_{abc} = \mathbf{R} \cdot \mathbf{I}_{abc} + \dot{\Psi}_{abc} \quad (2.73)$$

The flux-linkage time derivative  $\dot{\Psi}_{abc}$  in (2.73) represents the contributions of stator and rotor m.m.f. Similarly as with PMSM, the resulting air-gap flux is the interaction of both fluxes, in this case we have the flux generated by the field current instead of the one produced by the permanent magnet. The dq-frame equation takes then the following form:

$$\begin{bmatrix} u_d \\ u_q \end{bmatrix} = R_s \begin{bmatrix} i_d \\ i_q \end{bmatrix} + \omega_r \begin{bmatrix} -\psi_q(i_d, i_q, i_f) \\ \psi_d(i_d, i_q, i_f) \end{bmatrix} + \begin{bmatrix} \dot{\psi}_d(i_d, i_q, i_f) \\ \dot{\psi}_q(i_d, i_q, i_f) \end{bmatrix} \quad (2.74)$$

where  $i_f$  represents the rotor field current. Due to the similarities mentioned before, for a given  $i_f$ , the dq-axes flux-linkages show the same properties as with a PMSM:

$$\begin{aligned} \psi_d(i_d, i_q, i_f) &= \psi_d(i_d, -i_q, i_f) \\ \psi_q(i_d, i_q, i_f) &= -\psi_q(i_d, -i_q, i_f) \end{aligned} \quad (2.75)$$

By considering (2.75) it leads to a similar set of expression as in (2.61) and (2.62) :

$$\begin{aligned} \psi_d(i_d, i_q, i_f) &= \sum_{i=0}^{P_1} \sum_{j=0}^{R_1} \sum_{k=0}^{S_1} l_{dq(2i+1)(2j)(2k)} i_d^{(2i+1)} i_q^{(2j)} i_f^{(2k)} \\ &\quad + \sum_{i=0}^{P_2} \sum_{j=0}^{R_2} \sum_{k=1}^{S_2} l_{dq(2i)(2j)(k)} i_d^{(2i)} i_q^{(2j)} i_f^{(k)} \end{aligned}$$

with,  $P_1 = \frac{n-1-\text{mod}(n-1,2)}{2} \mid n \in \mathbb{N}^+$

$$R_1 = \frac{n-(2i+1)-\text{mod}(n-(2i+1),2)}{2} \quad (2.76)$$

$$S_1 = \frac{n-(2i+1)-2j-\text{mod}(n-(2i+1)-2j,2)}{2}$$

$$P_2 = \frac{n-\text{mod}(n,2)}{2}$$

$$R_2 = \frac{n-2i-\text{mod}(n-2i,2)}{2}$$

$$S_2 = n-2i-2j$$

$$\begin{aligned} \psi_q(i_d, i_q, i_f) &= \sum_{i=0}^n \sum_{j=0}^R \sum_{k=0}^S l_{qd(2j+1)(i)(2k+S)} i_q^{(2j+1)} i_d^{(i)} i_f^{(k)} \end{aligned}$$

with,  $R = \frac{n-i-1-\text{mod}(n-i-1,2)}{2} \mid n \in \mathbb{N}^+$

$$S = n-i-(2j+1) \quad (2.77)$$

## 2 Non-Linear Machine Model

At this point it is important to consider, the case of a highly saturated machine or with strong non-linear flux-linkage characteristics. The flux-linkages with respect  $i_f$  of a traction machine with characteristic 2.3 are shown in Fig. 2.14, where the maximum phase current is the same for each surface that corresponds to a  $i_f$  value. It can be appreciated how the area covered by the dq flux-linkages decreases by increasing field current, meaning that the magnetic material, in this case only the stator and rotor steel, is being saturated. Apart from that, the relationship of d- and q-axis fluxes along each surface indicates a accentuated curvature or non-linear trajectory. These two characteristics make this machine a good exponent to validate the expressions in (2.76) and (2.77), as it recognized that a polynomial approach may encounter certain difficulties to describe accurately these type of machines.

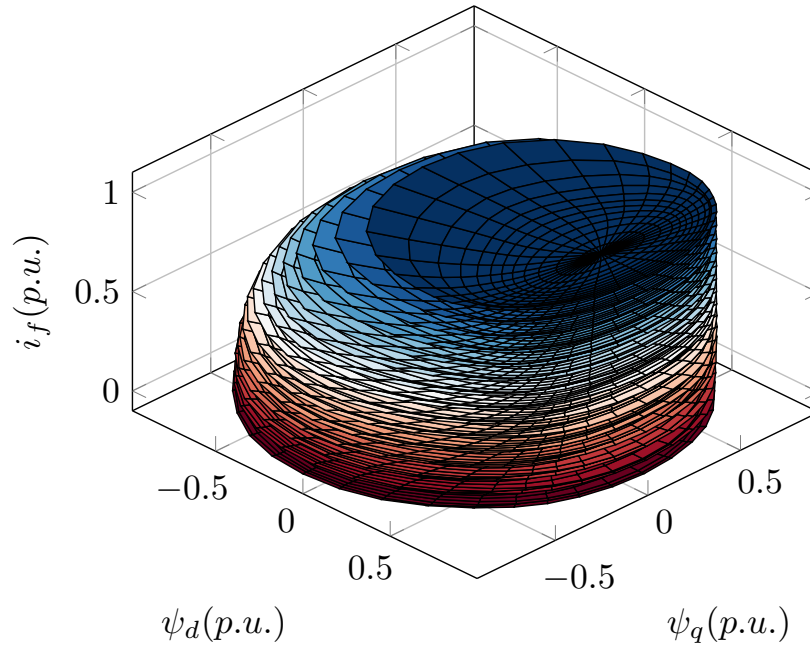


**Figure 2.14:** WFSM flux-linkages vs. rotor field current

**Table 2.3:** WFSM - Machine data

<i>Output power</i>	150kW
<i>Number of pole pairs</i>	3
<i>Nominal voltage</i>	400V

An alternative approach is proposed to enhance the capabilities of the polynomial formulation. The starting point relies on the notion that the expressions (2.38) and (2.39) evaluated a given field current value  $i_{f_n}$  can capture accurately the non-linear

## 2.4 Considering Field Currents in Wound Field Synchronous Machines

effects of the dq-axes flux-linkages.

$$\psi_d(i_d, i_q) \Big|_{i_{fh}} \quad \text{and} \quad \psi_q(i_d, i_q) \Big|_{i_{fh}} \quad (2.78)$$

the structure of flux-linkage expressions used for the PMSM (2.38) and (2.39) are used as the characteristics of the dq-axes flux-linkages observed at the PMSM still hold. The magnetic circuit is the same with the difference that the biasing magnetic flux is generated by a rotor coil instead of a magnet. Therefore the flux-linkages for a given  $i_{fh}$  are formulated in a similar fashion as:

$$\psi_d(i_d, i_q) \Big|_{i_{fh}} = \sum_{i=0}^n l_{dq(i)(0)} i_d^{(i)} + \sum_{k=1}^P \sum_{i=0}^{n-2k} \frac{c_{dq(i)(2k-1)}}{2k} i_d^{(i)} i_q^{(2k)} \quad (2.79)$$

with,  $P = \frac{n - \text{mod}(n, 2)}{2} \mid n \in \mathbb{N}^+$

$$\psi_q(i_d, i_q) \Big|_{i_{fh}} = \sum_{k=0}^P l_{qd(2k+1)(0)} i_q^{(2k+1)} + \sum_{k=0}^P \sum_{i=1}^{n-(2k+1)} \frac{c_{dq(i-1)(2k+1)}}{i} i_q^{(2k+1)} i_d^{(i)} \quad (2.80)$$

with,  $P = \frac{(n-1) - \text{mod}((n-1), 2)}{2} \mid n \in \mathbb{N}^+$

the coefficients in (2.79) and (2.79) are valid only for each field current value. To fully describe the machine for a given range of  $i_f$  values, these coefficients are used to determine their dependency on  $i_f$  through the following expressions:

$$l_{dq(i)(k)}(i_f) = \sum_{m=0}^{n_f} l_{dq(i)(k)(m)} \cdot i_f^m \quad (2.81)$$

$$l_{qd(i)(k)}(i_f) = \sum_{m=0}^{n_f} l_{qd(i)(k)(m)} \cdot i_f^m$$

where subscripts  $i$  and  $k$  correspond to the power of  $i_d$  and  $i_q$  respectively and  $n_f$  the polynomial order used to describe the coefficients with respect to the field current. Finally, (2.81) is replaced in (2.79) and (2.80) to get to the final expressions of the flux-linkages:

$$\psi_d(i_d, i_q, i_f) = \sum_{i=0}^n \sum_{m=1}^{n_f} l_{dq(i)(0)(m)} i_d^{(i)} i_f^{(m)} + \sum_{k=1}^P \sum_{i=0}^{n-2k} \sum_{m=0}^{n_f} \frac{c_{dq(i)(2k-1)(m)}}{2k} i_d^{(i)} i_q^{(2k)} i_f^{(m)}$$

with,  $P = \frac{n - \text{mod}(n, 2)}{2} \mid n \in \mathbb{N}^+$

(2.82)

## 2 Non-Linear Machine Model

$$\begin{aligned}
\psi_q(i_d, i_q, i_f) &= \sum_{k=0}^P \sum_{m=0}^{n_f} l_{dq(2k+1)(0)(m)} i_q^{(2k+1)} i_f^{(m)} \\
&+ \sum_{k=0}^P \sum_{i=1}^{n-(2k+1)} \sum_{m=0}^{n_f} \frac{c_{dq(i-1)(2k+1)(m)}}{i} i_q^{(2k+1)} i_d^{(i)} i_f^{(m)} \quad (2.83) \\
\text{with, } P &= \frac{(n-1) - \text{mod}((n-1), 2)}{2} \mid n \in \mathbb{N}^+
\end{aligned}$$

where  $n$  is the polynomial degree of the dq-axes current dependency and  $n_f$  of the coefficients depending on the field current. The d-axis flux-linkage  $\psi_d$  governed by the contributions of  $i_d$  and  $i_f$ , this can be appreciated when rewriting the (2.82) as:

$$\begin{aligned}
\psi_d(i_d, i_q, i_f) &= \underbrace{\sum_{m=1}^{n_f} l_{dq(0)(0)(m)} i_f^{(m)} + \sum_{k=1}^P \sum_{m=0}^{n_f} \frac{c_{dq(0)(2k-1)(m)}}{2k} i_q^{(2k)} i_f^{(m)}}_{\psi_f(i_q, i_f)} \\
&+ \underbrace{\sum_{i=1}^n \sum_{m=1}^{n_f} l_{dq(i)(0)(m)} i_d^{(i)} i_f^{(m)} + \sum_{k=1}^P \sum_{i=1}^{n-2k} \sum_{m=0}^{n_f} \frac{c_{dq(i)(2k-1)(m)}}{2k} i_d^{(i)} i_q^{(2k)} i_f^{(m)}}_{\psi_{d_0}(i_d, i_q, i_f)} \quad (2.84) \\
\text{with, } P &= \frac{n - \text{mod}(n, 2)}{2} \mid n \in \mathbb{N}^+
\end{aligned}$$

In (2.84) the d-axis flux-linkage was divided into flux contributions.  $\psi_f(i_d, i_q, i_f)$ , which covers the terms with field current contribution and the cross-saturation due to  $i_q$ . This expression is analogue to the one in (2.54), where the permanent flux-linkage terms with the cross-saturation due to  $i_q$  are grouped to form  $\psi_{m_{sat}}$ .

Continuing with the same treatment as with PMSM, the terms in (2.82) and (2.83) can be rearranged to separate the contributions of the dq-axes currents and the field current. The contribution of the latter is labeled as magnetizing inductance  $L_{mf}$ , in the following polynomial example for  $n = 3$  :

$$\begin{aligned}
\psi_d(i_d, i_q, i_f) &= \underbrace{l_{dq00}(i_f) + \frac{c_{dq01}(i_f) i_q^2}{2}}_{\psi_f(i_q, i_f) = L_{mf}(i_q, i_f) \cdot i_f} + \underbrace{l_{dq10}(i_f) i_d + l_{dq20}(i_f) i_d^2 + l_{dq30}(i_f) i_d^3 + \frac{c_{dq11}(i_f) i_d i_q^2}{2}}_{L_d(i_d, i_q, i_f) \cdot i_d} \quad (2.85)
\end{aligned}$$

$$\begin{aligned}
\psi_q(i_d, i_q, i_f) &= \underbrace{l_{qd10}(i_f) i_q + l_{qd30}(i_f) i_q^3 + c_{dq01}(i_f) i_d i_q + \frac{c_{dq11}(i_f) i_d^2 i_q}{2}}_{L_q(i_d, i_q, i_f) \cdot i_q} \quad (2.86)
\end{aligned}$$

## 2.4 Considering Field Currents in Wound Field Synchronous Machines

in (2.85) the cross-saturation due to  $i_q$  is grouped into the magnetizing inductance  $L_{mf}$ , as it accounts for magnetic saturation on the torque producing term. Finally the three inductances can be written in analytical form as:

$$L_{mf}(i_q, i_f) = \sum_{i=0}^n \sum_{m=1}^{n_f} l_{dq(i)(0)(m)} i_d^{(i)} i_f^{(m-1)} + \sum_{k=1}^P \sum_{m=0}^{n_f} \frac{c_{dq(i)(2k-1)(m)}}{2k} i_q^{(2k)} i_f^{(m-1)} \quad (2.87)$$

$$L_d(i_d, i_q, i_f) = \sum_{k=1}^P \sum_{i=1}^{n-2k} \sum_{m=0}^{n_f} \frac{c_{dq(i)(2k-1)(m)}}{2k} i_d^{(i-1)} i_q^{(2k)} i_f^{(m)} \quad (2.88)$$

$$\text{with, } P = \frac{n - \text{mod}(n, 2)}{2} \mid n \in \mathbb{N}^+$$

$$L_q(i_d, i_q, i_f) = \sum_{k=0}^P \sum_{m=0}^{n_f} l_{qd(2k+1)(0)(m)} i_q^{(2k)} i_f^{(m)} + \sum_{k=0}^P \sum_{i=1}^{n-(2k+1)} \sum_{m=0}^{n_f} \frac{c_{dq(i-1)(2k+1)(m)}}{i} i_q^{(2k)} i_d^{(i)} i_f^{(m)} \quad (2.89)$$

$$\text{with, } P = \frac{(n-1) - \text{mod}((n-1), 2)}{2} \mid n \in \mathbb{N}^+$$

From the general formulation of the electromagnetic torque (2.13) in terms of flux-linkage, the following expression for the WFSM is obtained:

$$T_e(i_d, i_q, i_f) = \frac{3}{2} p \left[ \psi_d(i_d, i_q, i_f) \cdot i_q - \psi_q(i_d, i_q, i_f) \cdot i_d \right] \quad (2.90)$$

the torque expression (2.90) can be further developed using the separation of flux-linkage contributions of (2.84):

$$T_e(i_d, i_q, i_f) = \frac{3}{2} p \left[ \left( \psi_f(i_q, i_f) + \psi_{d0}(i_d, i_q, i_f) \right) \cdot i_q - \psi_q(i_d, i_q, i_f) \cdot i_d \right] \quad (2.91)$$

finally, in order to make a clear distinction of the various contributions, (2.91) is rewritten in terms of inductances according to (2.87), (2.88) and (2.89), as:

$$T_e(i_d, i_q, i_f) = \frac{3}{2} p \left[ L_{mf}(i_q, i_f) \cdot i_f \cdot i_q + \left( L_d(i_d, i_q, i_f) - L_q(i_d, i_q, i_f) \right) \cdot i_d \cdot i_q \right] \quad (2.92)$$

where it is then clear that at the absence of  $i_d$ , the field current is the main driver for torque generation through the inductance  $L_{mf}$  or in more generic terms through the flux-linkage  $\psi_f$ . This is then the basis for a formulation of the torque constant  $K_t$  for a WFSM under the definition:

$$K_t(i_q, i_f) = \frac{T_e(0, i_q, i_f)}{i_q} \quad (2.93)$$

## 2 Non-Linear Machine Model

expression (2.93) leads to the following relationships with respect to the field current flux-linkage contribution:

$$K_t(i_q, i_f) = \frac{3}{2}p \left( L_{mf}(i_q, i_f) \cdot i_f \right) = \frac{3}{2}p \left( \psi_f(i_q, i_f) \right) \quad (2.94)$$

$$K_t(i_q, i_f) = \frac{3}{2}p \left( \sum_{m=1}^{n_f} l_{dq(0)(0)(m)} i_f^{(m)} + \sum_{k=1}^P \sum_{m=0}^{n_f} \frac{c_{dq(0)(2k-1)(m)}}{2k} i_q^{(2k)} i_f^{(m)} \right) \quad (2.95)$$

with,  $P = \frac{n - \text{mod}(n, 2)}{2} \mid n \in \mathbb{N}^+$

where  $K_t$  shows a cross-saturation with respect to  $i_q$  in the same manner as with PMSMs in (2.69).

This section showed the derivation of analytical expressions that described the flux-linkages of a WFSM where the additional degree of complexity due to the field current was addressed. A method was presented to cope with the additional simulation burden of covering an extended region of operation of the machine due to the fact that  $i_f$  can take any value up to a maximum value. Analytical formulation for figures of merit such as the inductances and the torque constant were shown as well. Finally, the analytical expressions shown so far will be validated against FE simulations data and measured data in the following chapter.

A solution for two aspects of the electrical machines modeling was proposed in this chapter. The first one is the inclusion of saturation and cross-coupling effects, the second one is the analytical model of those effects. A generalized formulation of the dq-axes flux-linkages in terms of polynomials for a given polynomial degree  $n$  was presented. Through the analytical description of the flux-linkages, key parameters like absolute inductances, permanent flux-linkage or incremental inductances were formulated in terms of the dq-axes currents. In particular, the polynomial description of the dq-axes flux-linkages enabled a clear the separation of non-linear effects that are rooted in the interaction between the permanent magnet flux-linkage and the dq-axes currents. The interaction between the q-axis current and the permanent magnet flux-linkage that impacts the torque production could be clearly identified, as well as the cross-coupling terms between the dq-axes flux-linkages and the associated absolute and incremental inductances. The flux-linkage model accuracy depends only on the chosen polynomial degree and offers a straightforward implementation in an embedded system or model based algorithm which requires a machine model. Furthermore, the interaction between winding current and permanent magnet flux-linkage was modeled in order to take into account the effects of the magnet temperature on the overall flux-linkage. Moreover, the analytical modeling approach was extended to WFSMs, where a novel polynomial structure was presented to improve the model's accuracy when dealing the strong nonlinear behavior that results from the interaction between the rotor field winding flux and the armature flux.

## 3 Flux-Linkage Model Parameter Identification

### 3.1 Optimization Theory

After having laid the grounds to describe the nonlinear behavior of the machine in an analytical form, the next step is the identification of the model parameters. More specifically the determination of the coefficients of (2.38) and (2.39). Firstly a method to obtain the coefficients from FEA simulation results is needed, as this is the basis for the generation of high fidelity models for analysis and simulation purposes. Secondly a proper approach needs to be developed to capture these coefficients from experimental data and thirdly a method or strategy needs to be elaborated to enable a proper online estimation of the coefficients in question. These three steps lead to the need of a proper identification method to get hold of the model parameters. By identification method is meant an optimization algorithm that can be applied in the three scenarios already mentioned. The decisive criteria for the selection of the identification method is the number of unknown parameters and the characteristics of the system that is described by these parameters. It is the line between nonlinear and linear that may lead to the use of a determined approach. Additionally there is a fundamental difference between offline and online identification procedures, as the offline processing of the data offers wide range of possibilities, because with a standard PC many methods can be used to extract the desired results. On the other hand the online identification is constrained by the embedded system capabilities where it is supposed to run.

#### 3.1.1 Optimization Methods

There is a variety of optimizations methods in the literature, where broadly speaking three interesting categories can be recognized. Each category tries to address a specific type of problem. Some methods are meant to be used offline as they required a finite amount of data to solve the problem in question, other approaches have recursive structures where for each data point the knowledge of the previous data a solution is provided. In addition to this, some approaches have a mathematical foundation and others are based on heuristic techniques.

##### 3.1.1.1 Linear Optimization

In this section, optimization methods that consider the linear systems are explored. This type of the methods are often used in real applications where there are data points or samples affected by external sources, for example white noise, when the error between

### 3 Flux-Linkage Model Parameter Identification

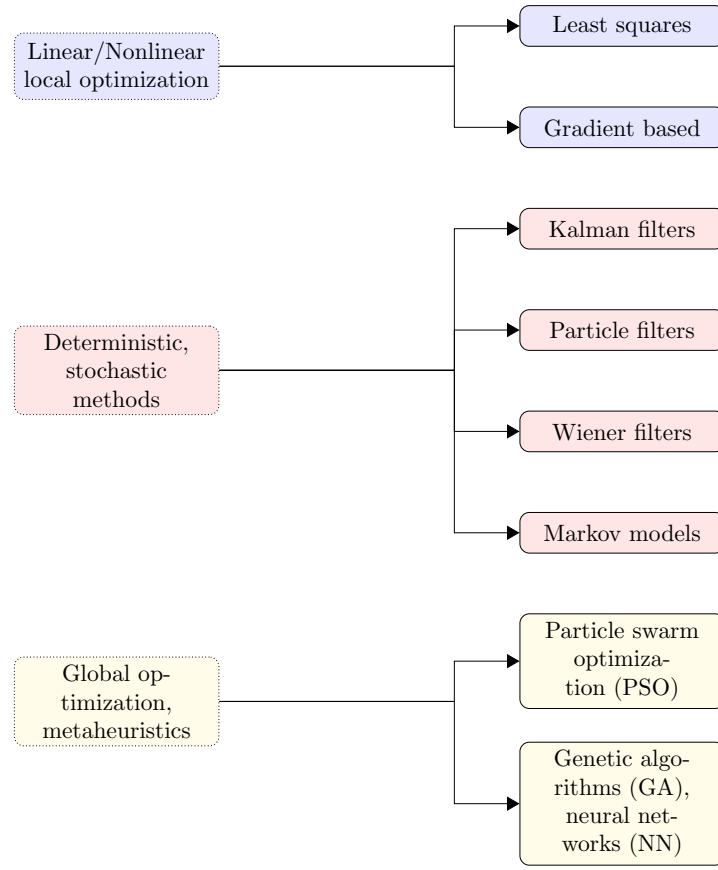


**Figure 3.1:** Overview of system identification methods.

process and the system output is linear. This type of methods seek to optimize a loss function defined as the error sum of squares of a system with output linearly dependent on system parameters (3.1). This kind of system fits with the formulation of the flux-linkage expressions (2.38) and (2.39).

$$y(x) = \sum_{i=1}^n \theta_i x_i \quad (3.1)$$

The most common method of this type is the *least squares* method presented by Gauss [47], where the main idea is to find the output  $\hat{y}$  that best approximates to the ideal system output  $y$  by having as a criteria the minimum sum of squared error. The optimization problem can be then defined in matrix notation as the minimization of  $F(x)$ .

$$\begin{aligned} \min \quad & F(X) = \frac{1}{2} e^T e \\ \text{with} \quad & e = y - \hat{y} \quad \text{and} \quad \hat{y} = \theta X \end{aligned} \quad (3.2)$$

Where the parameters vector is represented by  $X$  and the regressors matrix by  $\theta$ . This formulation of the  $F(X)$  is a quadratic function as shown in (3.3), with Hessian  $H$  and first derivative  $h$ .

$$F(X) = \frac{1}{2}X^T H X + h^T X + h_0 \quad (3.3)$$

Taking into account that the minimum of the loss function  $F(X)$  is reached when its gradient with respect to the parameter vector  $X$  is zero, a solution for the optimal estimates  $\hat{X}$  can be formulated as in (3.4) using the orthogonal equation.

$$\begin{aligned} \frac{\partial F(X)}{\partial X} &= -\theta^T (y - \theta X) = 0 \\ \hat{X} &= (\theta^T \theta)^{-1} \theta^T y \end{aligned} \quad (3.4)$$

Ideally the residuals  $e = y - \theta X$  should be zero but in reality at the presence of noise in the data points they are nonzero values. Actually the residuals can indicate the quality of the estimated parameters itself. At this point it is important to point out the numerical difficulties that may represent the inversion of the Hessian  $H = \theta^T \theta$ , for this reason, there are several mathematical approaches that seek to offer an alternative for an adequate matrix inversion. On the other hand even that minimization cannot deliver proper results due to the nature of the noise in the system, for that there are modifications or extensions to the classical least square method. The variations can range from giving different weights to the squared error values as in the *weighted least squares* method or the inclusion of equality constrains to the problem formulation.

One of the most known modification of the LS method is the *recursive least squares (RLS)* method, which is a formulation of the least square problem intended to be used online, in real time applications. As the LS method processes a whole set of data, it is more fitted to be used offline. The computational cost would be big for an online usage, for this reason a recursive calculation for each new data available is more convenient for such cases. The RLS algorithm [47, 48], is then defined by (3.5), where  $\hat{\theta}(k)$  is the current estimate,  $x(k)$  the regressors vector,  $y(k)$  the target output and  $P(k)^{-1}$  is the approximated Hessian  $X^T(k)X(k)$ .

$$\begin{aligned} \hat{\theta}(k) &= \hat{\theta}(k-1) + P(k)x(k) \left[ y(k) - x^T(k)\hat{\theta}(k-1) \right] \\ \text{where } P^{-1}(k) &= P^{-1}(k-1) + x(k)x^T(k) \end{aligned} \quad (3.5)$$

The update equation (3.5) requires the matrix inversion  $P(k) = (X^T(k)X(k))^{-1}$  which sets the computational complexity to  $\mathcal{O}(n^3)$ . Therefore the RLS algorithm is reformulated (see e.g. [48]) to the set of equations in (3.6), where for one output  $y$  the matrix inversion is avoided reducing the algorithm complexity to  $\mathcal{O}(n^2)$ . This new formulation introduces the forgetting factor  $0 \leq \lambda \leq 1$  which intends to weigh past samples in an exponential manner, in order to influence the convergence speed of the algorithm. If the forgetting factor takes the value 1, all the data values, past and present are equally weighted. Conversely if  $\lambda$  tends to zero, the latest data samples get more weight.

### 3 Flux-Linkage Model Parameter Identification

Due to the low computational complexity of the algorithm depicted in (3.6), it is commonly used in online parameter estimation of electrical machines. The RLS algorithm with  $\lambda = 1$  is adequate for the estimation of time-invariant parameters, with proper tune of the forgetting factor, tracking the variations of parameters over time is then feasible. These characteristics make the *recursive least squares (RLS)* method attractive for the online estimation of the coefficients in (2.38) and (2.39).

$$\begin{aligned}\hat{\theta}(k) &= \hat{\theta}(k-1) + \gamma(k) \left[ y(k) - x^T(k)\hat{\theta}(k-1) \right] \\ \gamma(k) &= \frac{1}{x^T(k)P(k-1)x(k) + \lambda} P(k-1)x(k) \\ P(k) &= \frac{1}{\lambda} (I - \gamma(k)x^T(k))P(k-1)\end{aligned}\quad (3.6)$$

#### 3.1.1.2 Nonlinear Optimization

This section will explore the different algorithms in the area of nonlinear local optimization. As the main objective is to obtain the coefficients of the nonlinear expressions in (2.38) and (2.39). The main objective of the algorithms in this category is to find the best solution of a problem that is mathematically defined. In general terms the optimization problem is formulated in terms of an objective function that is minimized when the optimal solution  $x$  is found. In the specific case of this work, a mathematical formulation of an objective function is possible as (2.38) and (2.39) are analytical functions.

$$\begin{aligned}\min \quad & f(x) \\ \text{with } & x \in R^n\end{aligned}\quad (3.7)$$

The objective function in (3.7) can take various forms, it can be convex or non-convex. Convex functions and convex sets are addressed by the optimization methods as it exhibits at least one minimum. A convex set is defined in geometry as the set  $S$  of points, in which any pair of points  $x_1$  and  $x_2$  can be connected by a line segment completely contained in  $S$  as in Fig. 3.2, otherwise it is defined as a nonconvex set.

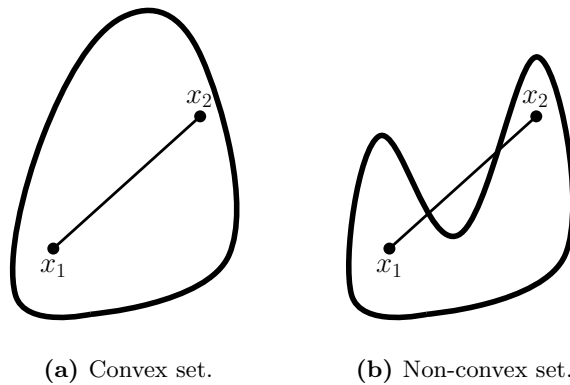


**Figure 3.2:** Types of convex sets.

In the case of a function, as depicted in Fig 3.3, if there are function values equal or less than a chord or line segment between two points of the function, then it is said that the function is convex, in the opposite case it is a concave function .

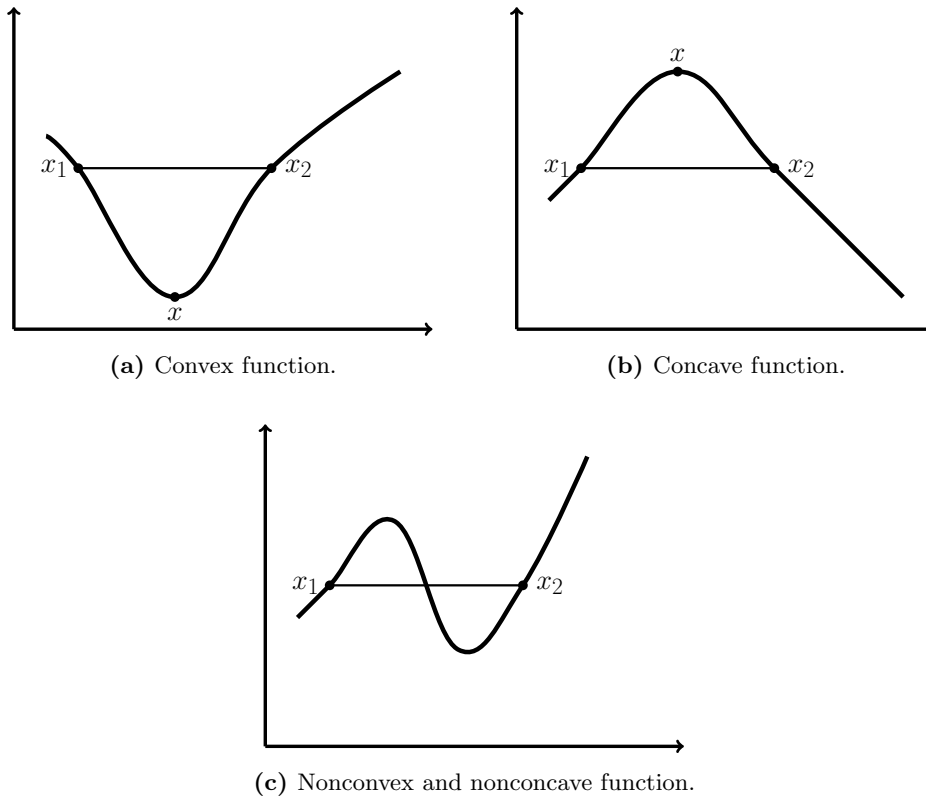


**Figure 3.3:** Convex and nonconvex functions.

The focus in optimization theory lays on convex functions or sets as the objective of the optimization procedures is to find the set of points at the minimum. Finding the minima or the smallest value of the objective function could be a difficult task, as a function can have more than one minimal value. Here is where the concept of the global minimum and local minimum needs to be introduced as defined in Fig. 3.4. It is important to acknowledge the type of function as many optimization algorithms perform a local search of a minimum and conversely global optimization algorithms solve several local problems.

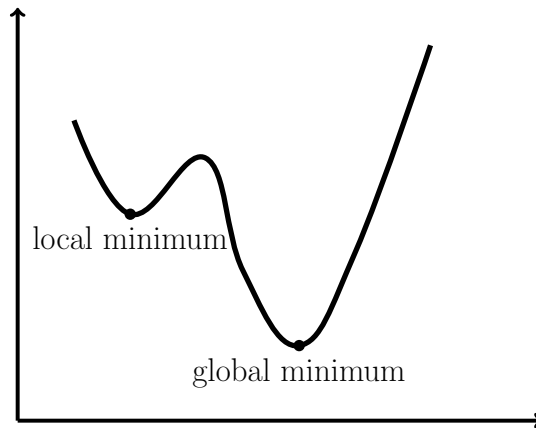


**Figure 3.4:** Types of minimum.

In the case that the objective function is convex or at least a convex region, the optimization process can be carried out based in the objective function and its properties. The *line search* method, an optimization algorithm set for an unconstrained problem, is an iterative approach that seeks to find the minimum of a given objective function  $f(x)$ . An optimal direction vector  $d_k$  with a step size  $\alpha_k$  is found at each iteration [49]. The key point of this method is to find the most suitable step size. This method performs a one-dimensional search, this means it handles a univariable objective function, nevertheless multivariable optimization can be based on this approach.

Most precise procedures involve the use of the gradient information of the objective function on (3.7) to find the optimal solution. The *Steepest descent* method, on the so-called Newton's Methods, is a simple minimization procedure, it uses the negative gradient of  $f(x)$  as its descent direction. This method performs well for finding local minima but when approaching a stationary point it starts to get slow showing a zigzagging trajectory towards the minimum. With regards of use of the objective function information, the *Newton's* method goes further, as it uses second-order Taylor expansion or quadratic approximation of  $f(x)$  around the iteration point  $x_k$ . To formulate the quadratic approximation of  $f(x)$  not only the first derivative  $\nabla f(x)$  but the second derivative  $\nabla^2 f(x)$  is required.

$$f(x_k + s) \approx f(x_k) + \nabla f(x_k)^T s + \frac{1}{2} s^T \nabla^2 f(x_k) s \quad (3.8)$$

If the objective function is quadratic function and the Hessian  $\nabla^2 f(x)$  is positive definite, the method can reach the minimum point with one iteration. This makes the Newton's method quite powerful but some drawbacks such as the expensive computational cost, due to the effort to obtain the Hessian matrices and the difficulty when the Hessian is not available. Alternative approaches emerged to offer a work around to those issues. The *Quasi-Newton's* methods are a group of methods which work with Hessian approximations maintaining a fast convergence speed making them quite powerful. Some of the

most known methods to approximate the Hessian are the Symmetric Rank-One update, the DFP update and the most popular BFGS update. In order to reduce the computational cost approaches like the *Gauss-Newton* or *Levenberg-Marquardt* methods neglect the second order information of the quadratic approximation (3.8). This effectively reduces the performance for large residual problems [49, 47].

So far nonlinear unconstrained optimization methods were considered, now the optimization problem can be defined as a nonlinear constrained optimization as in (3.9). The idea of reducing the solution search space is quite compelling as in many situations there is certain previous knowledge of the objective function. In the specific case of (2.38) and (2.39) it is known before hand that coefficients like  $\psi_m$ ,  $l_{dq10}$  and  $l_{qd10}$  are positive as they relate directly to the permanent magnet flux-linkage, the linear d-axis inductance and the linear q-inductance respectively. Incorporating constraints in the optimization procedure means additional complexity to the method, nevertheless in general terms the convergence of the algorithm improves.

$$\begin{aligned}
 & \min f(x) \\
 & \text{with } x \in R^n \\
 & c_i = 0, i \in E \\
 & c_i \geq 0, i \in I
 \end{aligned} \tag{3.9}$$

If the constraints in (3.9), equality and inequality constraints, are linear functions, then it is said that the optimization problem is linearly constrained. Which is the case of the specific optimization problem that needs to be formulated to find the coefficients of (2.38) and (2.39), where the constraints consist of inequalities of some the coefficients in question.

A method created to handle this type of problems is the *quadratic programming (QP)* method. It is defined as a linearly constrained nonlinear optimization problem, where the objective function is quadratic.

$$\begin{aligned}
 \text{Minimize } & Q(x) = \frac{1}{2}x^T Gx + g^T x \\
 & a_i^T x = b_i, i \in E \\
 & a_i^T x \geq b_i, i \in I
 \end{aligned} \tag{3.10}$$

Where  $x$  is the set of unknown coefficients,  $G$  is the Hessian of the objective function  $f(x)$  and  $g = \nabla f(x) - Gx$ . The vectors  $a_i$  and  $b_i$  define the constraints of the problem. Similarly to (3.9) in the QP formulation there are equality and inequality constraints but the definition of the objective function is similar to (3.8) as it deals with quadratic functions and the second-order Taylor expansion describes them, but as expected, the minimum of the objective function can be determined with the two terms of the expansion carrying the variables or unknowns, extensive analysis of the variations of the QP algorithms can be found in [49, 50].

### 3.1.1.3 Kalman Filtering

Originally intended to estimate the states of a time-variant discrete system, the Kalman filter can be formulated to estimate the parameters of the system as well. It is an algorithm that predicts and corrects the corresponding states based on the least squares optimality. The Kalman filter is derived around linear dynamic systems [48, 51], it is assumed that the system's future states can be represented by (3.11). Where  $A(k)$  is the transition matrix from the  $k$  state to the  $k+1$  state,  $B(k)$  control-input matrix,  $v(k)$  the system noise. On the other hand the measurement of the variable  $x(k)$  is modeled as (3.12), where  $y(k)$  is the current measurement,  $C(k)$  is the noiseless connection between state and observation and  $n(k)$  is the corresponding measurement noise.

$$x(k+1) = A(k)x(k) + B(k)u(k) + v(k) \quad (3.11)$$

$$y(k) = C(k)x(k) + n(k) \quad (3.12)$$

Additionally it is assumed that the system noise and the measurement are uncorrelated zero mean Gaussian white noise processes. Furthermore their covariance  $Q$  and  $R$  is assumed to be known as well.

$$Q = E [v(k)v^T(k)] \quad (3.13)$$

$$R = E [n(k)n^T(k)] \quad (3.14)$$

Following into the derivation of the Kalman filter, the minimization of the mean squared error (3.15) yields to the optimal filter as described in [48, 51], where  $P(k)$  is the covariance matrix of the error  $e(k) = x(k) - \hat{x}(k)$ .

$$E [e(k)e^T(k)] = P(k) \quad (3.15)$$

The resulting recursive filter takes the form of (3.16), where  $K(k)$  is the Kalman gain. It is important to remark at this point that the formulation of the filter in (3.16) implies a high computational cost produced by the calculation of the covariance matrix  $P(k)$  and the Kalman gain  $K(k)$ , as for example, a matrix inversion is needed.

$$\begin{aligned} K(k) &= P'(k)C(k)^T (C(k)P'(k)C(k)^T + R(k))^{-1} \\ \hat{x}(k) &= \hat{x}'(k) + K(k) (y(k) - C(k)\hat{x}'(k)) \\ P(k) &= (I - K(k)C(k)) P'(k) \\ \hat{x}'(k+1) &= A(k)\hat{x}(k) + B(k)u(k) \\ P'(k+1) &= A(k)P(k)A^T(k) + Q(k) \end{aligned} \quad (3.16)$$

At this point it is important to point out that the formulation of the Kalman filter is quite similar to the RLS algorithm in (3.6). Both algorithms seek to minimize the least squared error but with different assumptions, as the Kalman filter focuses on the process noise. For a system of the form (3.17) and (3.18), the resultant update equations get simplified to a point where it is similar to the RLS algorithm formulation.

$$x(k+1) = x(k) + v(k) \quad (3.17)$$

$$y(k) = C(k)x(k) + n(k) \quad (3.18)$$

The Kalman filter update equations get simplified to (3.19) where it is evident that the Kalman Gain  $K(k)$  is similar to the adaptation matrix  $\gamma(k)$  of the RLS algorithm. The difference relies on the forgetting factor  $\lambda$  and the covariance matrix  $R(k)$ . In addition to this, the system covariance matrix  $Q(k)$  plays a role in the update of the matrix  $P(k)$  in the Kalman filter and in the RLS update equation this matrix is not considered or its value would be zero. Having said that, for a forgetting factor  $\lambda = 1$ , where no variations over time is expected, it would be equivalent to the assumption that covariance  $Q(k)$  of the system is zero.

On the other hand in the Kalman gain the difference would be that each variable is weighted differently due to the knowledge of  $R(k)$  but for the RLS, each variable is weighted equally by the forgetting factor  $\lambda$ . This similarities make the Kalman filter attractive in the sense that if the covariance matrix  $R(k)$  is known before hand the Kalman filter would be the proper alternative.

$$\begin{aligned}\hat{x}(k) &= \hat{x}(k-1) + K(k)(y(k) - C(k)\hat{x}(k-1)) \\ K(k) &= P'(k)C(k)^T (C(k)P'(k)C(k)^T + R(k))^{-1} \\ P(k) &= (I - K(k)C(k))P(k-1) + Q(k)\end{aligned}\quad (3.19)$$

The set of equations in (3.16) were derived for a linear dynamic system but in many applications a solution for a nonlinear system of the form is required. Therefore a new update sequence is derived, the Extended Kalman Filter (EKF), for nonlinear systems in the form of (3.20) and (3.21).

$$x(k+1) = f_k(x(k) + u(k)) + v(k) \quad (3.20)$$

$$y(k) = g_k(x(k)) + n(k) \quad (3.21)$$

Where  $f_k$  and  $g_k$  are time varying functions. The future update is obtained from the nonlinear model. Additionally, the covariance matrix  $P(k)$  update is derived from Taylor's first order expansion of (3.20) and (3.21). By doing this approximation the filter isn't optimal anymore, as the linearization around operating points might lead to incorrect results. On the other hand, the nonlinear transformations will change the distribution of the random variables, so far expected to be Gaussian. Nevertheless the EKF is used successfully in many applications such as in Navigation systems or in parameter estimation.

$$\begin{aligned}K(k) &= P'(k)G(k)^T (G(k)P'(k)G(k)^T + R(k))^{-1} \\ \hat{x}(k) &= \hat{x}'(k) + K(k)(y(k) - g_k(\hat{x}'(k))) \\ P(k) &= (I - K(k)G(k))P'(k) \\ \hat{x}'(k+1) &= f_k(\hat{x}'(k), u(k)) \\ P'(k+1) &= F(k)P(k)F^T(k) + Q(k)\end{aligned}\quad (3.22)$$

with,  $F(k) = \left. \frac{\partial f_k(x, u)}{\partial x} \right|_{x=\hat{x}'(k), u=u(k)}$  and  $G(k) = \left. \frac{\partial g_k(x)}{\partial x} \right|_{x=\hat{x}'(k)}$

### 3.1.1.4 Metaheuristics

Metaheuristics are optimization methods which are not based directly on mathematical assumptions but on the observation of the behavior in the nature itself. In this category, methods like artificial neural networks or genetic algorithms can be found. As their names hint it, those algorithms are based on the human neural networks behavior and genetics. Their relevance for this work isn't big for instance because their applicability on an embedded system, the need for training data sets and convergence time. In this category many methods are called global optimizers, as they are appropriate for large amount of variables. Which means that in the case of a large search area, there might be several minima, or in other words the objective function is non-convex (see Fig.3.4). In those scenarios a global optimization method is the proper solution compared to the gradient based algorithms of section 3.1.1.2, which are primarily local optimizers. They would find the global minimum just in the cases where the objective functions are convex.

The scenario with a non-convex function leads to the logical conclusion to consider the use of an global optimization method. On the other hand Metaheuristics approaches are helpful when there isn't an mathematical description of the system in consideration, the so called black-box systems, in those cases the methods described in sections 3.1.1.1 to 3.1.1.3 are of no use. In [52] an hybrid optimization strategy is used to identify the parameters of a PMSM's thermal model. Where a global optimizer (Particle Swarm Optimization) would make the initial search for the global optimum and a local optimizer (Sequential Quadratic Programming) would find the more exact solution.

### 3.1.1.5 Particle Swarm Optimization

Due to the level of complexity of the optimization problem, it is reasonable to try approaches with low level of implementation difficulty. The main objective is to develop an algorithm that can be fitted in a embedded system, so the calculation effort should be limited as much as possible. Kennedy and Eberhart [53] presented an optimization method for nonlinear problems based on observations of the nature, in special the social behavior of animals that interact as an entity like fish schooling or bird flocking. What they proposed is at some extend similar to other approaches that try to imitate some behavior observed in the nature like neural networks or genetic algorithms. The concept behind consist of a swarm composed of n particles which are aware of their current position and exchange their position with each other. The position is a m-dimensional vector containing the parameters to be estimated. Each particle knows its best position and has access to the best position of the swarm. The PSO-algorithm is defined by a set of equations that describe the flocking behavior of birds:

$$\vec{v}_m^{k+1} = w_m \vec{v}_m^k + c_1 rand_1 \left( \vec{pbest}_m - \vec{x}_m^k \right) + c_2 rand_2 \left( \vec{gbest} - \vec{x}_m^k \right) \quad (3.23)$$

where:

- $\vec{x}_m^k$  corresponds to the position the  $m^{th}$  particle in other words it is the vector of the estimated parameters of the  $m^{th}$  particle.

- $\vec{v}_m$  corresponds to velocity vector of the  $m^{th}$  particle.
- $w_m$  is called the inertia weight factor of the  $m^{th}$  particle.
- $c_1$  and  $c_2$  are two positive constants.
- $\vec{pbest}_m$  is the best position achieved by the  $m^{th}$  particle.
- $\vec{gbest}$  is the best position recorded of the whole swarm.

As presented in [52], PSO can be used to calibrate a thermal model, where the PSO performs a global search and then a gradient based optimizer finds the final optimal solution of the model parameters. Furthermore, the authors of [28, 26] propose a scheme where parameters of a PMSM are estimated online in an embedded system using PSO. However, the estimation accuracy presented in [28] leaves room to certain considerations. The bigger the swarm the better the accuracy of the estimates, or even increased number of iterations with a small velocity factor might be necessary to improve the estimation quality. As a global search algorithm PSO is attractive due to its simple structure, however the local optimization methods discussed in the previous sections are capable of delivering more accurate solutions.

### 3.1.2 Coefficient's Calculation

The machine's parameter identification is divided in two categories; the parameter identification from FE data and from measured data. The former is the determination of a set of polynomial's coefficients to minimize the approximation error between a function based on FEA simulation results and a given flux-linkage polynomial of degree  $n$ . Furthermore, as discussed in section 2.2, the least-square approximation method [37] is a suitable approach to minimize the approximation error for a given interval of dq-axes currents. Consequently, the coefficients of the flux-linkage expressions (2.38) and (2.39) are determined through the minimization of the least-squares. For this purpose any of the methods discussed through the section 3.1.1 are applicable.

As seen through the section 3.1.1, the characteristics of the objective function are decisive for the selection of the optimization method. In the case of the flux-linkage expressions, the objective function is defined as:

$$f(x) = \sum_{k=1}^N (\psi_k - \hat{\psi}_k)^2 \quad (3.24)$$

where  $N$  is the number of data points and  $x$  the set of coefficients of the approximation polynomial  $\hat{\psi}$ . When  $N$  is selected to form a system of equations that at least equals the number of variables in  $x$ , there is a unique solution  $x$  of the minimization problem [54]. Therefore the objective function (3.24) becomes convex with one minima, which is an important property that enables the consideration of local optimization methods.

### 3 Flux-Linkage Model Parameter Identification

On the other hand, when dealing with measured data, two aspects need to be considered. The first one is the data noise that comes from the measurement devices and the second one is if whether the minimization is performed offline in a personal computer or online in an embedded system with limited computational resources. Under the consideration of these two aspects, a traditional least-squares minimization cannot be adopted. Therefore recursive or even simple algorithms are needed in order to be able to implement the least-squares minimization in an embedded system properly. One important factor to consider is the characteristics of the system to be identified. At simulation level, the magnetic information such as flux-linkage can be easily extracted from a FEA model, however when trying to obtain the flux-linkage experimentally, it is normally done with an indirect measurement. Under normal conditions the flux-linkage cannot be obtained directly, additional hardware needs to be placed into the machine, like a search coil, to measure directly the flux-linkage. This is expensive and time consuming, thus it cannot be done for a large amount of samples. So the alternative is to derive the flux-linkages from indirect measurements such as the phase voltages (2.9) and the electromagnetic torque (2.13) of the machine. Consequently the objective function when working with measured data is formulated in terms of voltages and electromagnetic torque. However it is still based on the flux-linkage expressions (2.38) and (2.39).

Numerically compact algorithms like PSO are very compelling for embedded applications, nevertheless simplicity comes with the cost of accuracy. Typically global search methods are complemented with gradient based local optimizers [52] to improve the solution's accuracy. As the objective function (3.24) can be described analytically in terms of polynomials, gradient based approaches, like the ones presented in sections 3.1.1.1 and 3.1.1.2 can be taken into account. In this group, Quadratic Programming (QP) is a proper alternative for optimization problems where the objective function has a quadratic form and the derivatives of the function are available. In addition to this, the possibility to apply constraints to the problem makes the method attractive when considering measured data. Conversely, at the minimization of least-squared errors of noisy data, the Kalman filters introduced in section 3.1.1.3 seems to be the better option. Similarly, the RLS algorithm is widely used in online applications, due to its compact numerical formulation that has a low computational cost. However, gradient based approaches have similar characteristics, as they use the derivatives of the objective function to find the optimal solution. They differ, in the degree of information taken from the derivatives, as some approaches use the first derivative, others the second one and other approaches approximate the latter for computational reasons.

Another aspect to consider is the fact that there is additional information contained in the electrical and magnetic nature of the machine, that can be used during the optimization procedure. The permanent magnet flux-linkage  $\psi_m$ , the winding resistance contained in the voltage equations, the dq-axes linear inductances all take positive values, which means that the search area for a solution during the optimization could be constrained. This is specially interesting for the online identification as a robustness

feature to bound parameters and guarantee a parameter prediction in valid ranges.

To summarize, the calculation of the polynomial's coefficients in the case of FEA simulation data can be carried out with a standard least-squares minimization methods. On the other hand when dealing with measured data approaches like RLS or QP are attractive, the former due to its low computational cost and the latter because of the constraints. Whereas an unconstrained QP optimization of (3.24) can be seen as a simple least-squares minimization.

## 3.2 Coefficient of Determination

To obtain certain degree of confidence on the flux-linkage meta-models presented throughout chapter 2, a measure of model fitness was adopted. The Coefficient of Determination (CoD),  $R^2$ , also known as multiple correlation coefficient [55] offers well documented measure of goodness of fit for regression models of the form:

$$y = \beta_0 + \sum_{j=1}^k \beta_j x_j + \varepsilon \quad (3.25)$$

where  $\beta$  represent the set of model parameters,  $x_j$  the model variables and  $\varepsilon$  a residual variable [56]. The general form in (3.25) describes actually the same polynomial structure of the flux-linkage expressions already mentioned, making the CoD a suitable tool to asses the polynomial degree chosen for a given machine design. The CoD is then defined as:

$$CoD = R^2 = 1 - \frac{\sum (y - \hat{y})^2}{\sum (y - \bar{y})^2} \quad (3.26)$$

In (3.26),  $\bar{y}$  is the arithmetic mean of the observed data set  $y$  and  $\hat{y}$  denotes the set of fitted values. Therefore, the expression  $\sum (y - \bar{y})^2$  is a sum of squares proportional to the variance of the data set  $y$ . Moreover  $\sum (y - \hat{y})^2$  corresponds to the sum of squares of residuals of the fitted function  $\hat{y}$ . Finally the CoD is a measure, that per definition will deliver a value  $R^2 = 1$  for model that describes perfectly the reference data set and  $R^2$  closer to 0 for models with worse predictions.

## 3.3 Offline Identification of PMSMs: FEA Simulation Data

This section presents the identification of the coefficients of expressions (2.38) and (2.39) for a given polynomial degree  $n$ . For that purpose the least-square approximation method is selected as discussed in section 2.2. To avoid numerical issues and to be able to use similar optimization setups, the currents and the fluxes are normalized. In general, the minimization of sum of the least squares can be carried out with a standard least-squares method. However, the use of constraints to solve an optimization problem when dealing with measured data brings certain control over the solutions, as valid parameter range can be defined before hand to guarantee a stable solution. For

### 3 Flux-Linkage Model Parameter Identification

the sake of continuity, the optimization method used with FEA simulation results and measured data will be the same. Whereas the task to solve remains the same, which is the minimization of the error between the given target flux data and the approximation polynomial. The optimization problem is then formulated as a constrained problem, a quadratic programming (QP) problem, where permanent magnet flux-linkage and linear inductances are positive. As the expressions (2.38) and (2.39) share the cross coupling coefficients of the type  $c_{dq(0)}$ , the parameter identification is performed jointly using one objective function:

$$f_n(x) = \sum_{k=1}^N \left[ (\psi_d(i_{d_k}, i_{q_k}) - \widehat{\psi}_d(i_{d_k}, i_{q_k}))^2 + (\psi_q(i_{d_k}, i_{q_k}) - \widehat{\psi}_q(i_{d_k}, i_{q_k}))^2 \right] \quad (3.27)$$

with,  $\widehat{\psi}_d = \nabla \psi_d x^T$ ;    and     $\widehat{\psi}_q = \nabla \psi_q x^T$

Where  $x$  is the set of unknown coefficients,  $N$  is the number of the simulation data points and  $n$  is the polynomial degree. The letters with a hat notation represent estimated values and the letters with no hat notation are the values of the FE simulation data. The constrained optimization problem can be then formulated in the following form:

$$\begin{aligned} \text{Minimize} \quad & Q(x) = \frac{1}{2} x^T G x + g^T x \\ \text{with,} \quad & \psi_m > 0, \quad l_{dq10} > 0 \quad \text{and} \quad l_{qd10} > 0 \\ \text{where,} \quad & G = \nabla \psi_d \nabla \psi_d^T + \nabla \psi_q \nabla \psi_q^T \\ & g = -2\psi_d \nabla \psi_d - 2\psi_q \nabla \psi_q \end{aligned} \quad (3.28)$$

Where  $G$  is the Hessian of the objective function  $f(x)$  and  $g = \nabla f(x) - Gx$ . The symbol  $x$  represents the set of coefficients to be identified and  $N$  the number of data points used for the optimization<sup>1</sup>. The FEA simulation results of the machine depicted in Fig. 2.5 were used to illustrate the validity of the proposed flux-linkage expressions, as a starting point the polynomial degrees  $n = 3$  and  $n = 5$  will be explored. Depending on the chosen polynomial degree, the FEA simulation data points can be selected according to the number of coefficients to be determined. The minimum amount data points  $N_d$  for  $i_d$  is given by the rule:

$$N_d = n + 1 + \text{mod}(n - 1, 2) \quad (3.29)$$

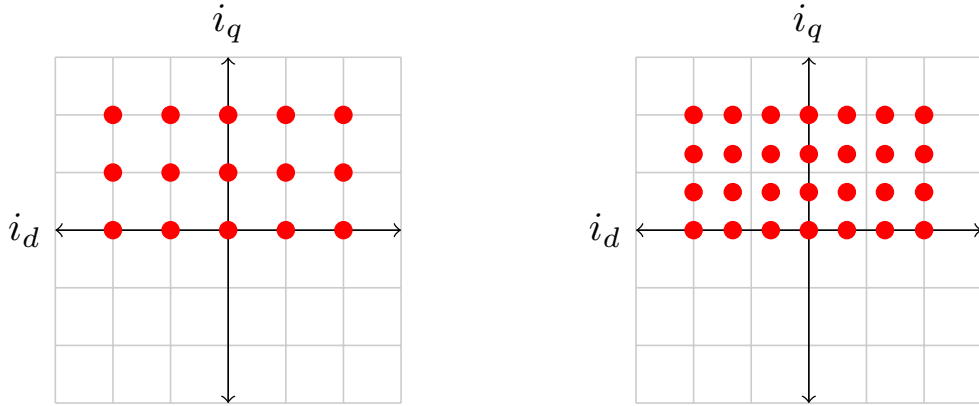
where (3.29) takes into account the coefficients associated to  $i_d$  in the d-axis flux-linkage expression (2.38) and in the case of an odd polynomial degree it adds an additional point to create a symmetric data points grid along the d-axis current. In a similar fashion, the rule for the minimum q-axis current data points  $N_q$  is given by the coefficients associated to  $i_q$  in the q-axis flux-linkage expression (2.39) and an additional data point along the q-axis current is added to include  $i_q = 0A$ , as it is required by the coefficients associated to  $i_d$  in the d-axis flux-linkage expressions that are not coupled with  $i_q$ .

$$N_q = \frac{n - 1 - \text{mod}(n - 1, 2)}{2} + 2 \quad (3.30)$$

---

<sup>1</sup>The function *quadprog* of the commercial software MATLAB was used to solve the quadratic programming problem.

The proposed minimum FEA data points grids for  $n = 3$  and  $n = 5$  are displayed in Fig. 3.5 in an exemplary manner.



(a) Proposed FEA data points grid for  $n = 3$       (b) Proposed FEA data points grid for  $n = 5$

**Figure 3.5:** FE Simulation data point selection

As the symmetry shown by the flux-linkages with respect to  $i_q$  the flux-linkage was already considered in the flux-linkage polynomials, the data points grid only need to cover positive values of  $i_q$  or the first two quadrants of the  $i_{dq}$  plane. With simulation data points depending on the chosen polynomial degree, the amount of simulations required to generate a flux-linkage model of the machine can be optimized and potentially the overall simulation time can be reduced.

Proceeding according to the rules for simulation data points (3.29) and (3.30), the FEA simulation data for the coefficient identification was obtained. However it can be observed in Fig. 3.5 that the data grid points for  $n = 3$  are a subset of non-equidistant data points of the data set for  $n = 5$ . Therefore the data grid points for  $n = 5$  were used to obtain the simulation data. Finally, the quadratic programming solver returned the values in table 3.1.

### 3 Flux-Linkage Model Parameter Identification

**Table 3.1:** Coefficients for  $n = 3$  and  $n = 5$

Coefficients ( $x$ )	n=3	n=5	
$l_{dq00}$	7.89	7.89	$mWb$
$l_{dq10}$	51.84	52.95	$\mu H$
$l_{dq20}$	-53.32	-52.75	$nH/A$
$l_{dq30}$	-0.32	-0.85	$nH/A^2$
$l_{dq40}$	–	-5.54	$pH/A^3$
$l_{dq50}$	–	-15.55	$fH/A^4$
$c_{dq01}$	-41.73	-13.62	$nH/A$
$c_{dq11}$	-1.06	-1.53	$nH/A^2$
$c_{dq21}$	–	-11.54	$pH/A^3$
$c_{dq31}$	–	-33.44	$fH/A^4$
$c_{dq03}$	–	-4.40	$pH/A^3$
$c_{dq13}$	–	-18.39	$fH/A^4$
$l_{qd10}$	67.84	68.34	$\mu H$
$l_{qd30}$	-0.32	-0.41	$nH/A^2$
$l_{qd50}$	–	-7.27	$fH/A^4$

The polynomial coefficients give a hint of the ratio flux-linkage/current. The most relevant coefficients in this case  $l_{dq10}$  and  $l_{qd10}$  are related directly to the linear, unsaturated, inductances. In this specific example the machine, an IPMSM, which is expected to have reluctance, evidenced by the significant difference between dq-axes inductances. Looking at the values of table 3.1 for  $n = 5$ , the linear q-axis inductance  $L_q = l_{qd10} = 68.34\mu H$  is larger than the linear d-axis inductance  $L_d = l_{dq10} = 52.95\mu H$ , which is the expected indication of reluctance in the IPMSM. Nevertheless it is important to remember that those coefficients represent the unsaturated inductances or small signal inductances, were the currents a so small that the following ratios are true:

$$\begin{aligned} \frac{\psi_d - \psi_m}{i_d} &\approx l_{dq10} = 52.95\mu H \\ \frac{\psi_q}{i_q} &\approx l_{qd10} = 68.34\mu H \end{aligned} \tag{3.31}$$

### 3.3.1 Flux-Linkages

A visualization with respect to the current phase advance angle  $\gamma$  is chosen, in order to show how the different polynomial degrees represent the flux-linkages. This phase advance angle, as depicted in Fig. 3.6, is defined in (3.32) and it will be addressed as *phase advance* for future references.

$$\gamma = \arctan\left(\frac{-i_d}{i_q}\right) \quad (3.32)$$

where minus sign of  $i_d$  indicates that  $\gamma$  is defined to be positive in the second quadrant the currents plane, as it is the quadrant of interest when driving the machine in the field weakening region<sup>2</sup>.

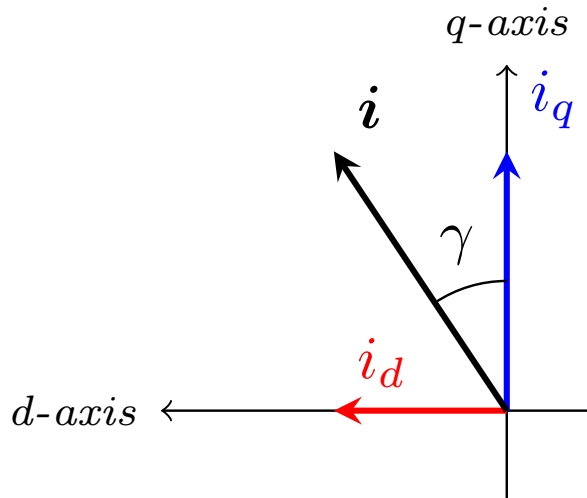


**Figure 3.6:** Current phase advance angle.

<sup>2</sup>Recalling the definition of  $\psi_d = \psi_m + L_d i_d$ , the permanent magnet flux-linkage  $\psi_m$  can be weakened only if  $i_d$  takes negative values, hence the adoption of a positive  $\gamma$  is more practical.

### 3 Flux-Linkage Model Parameter Identification

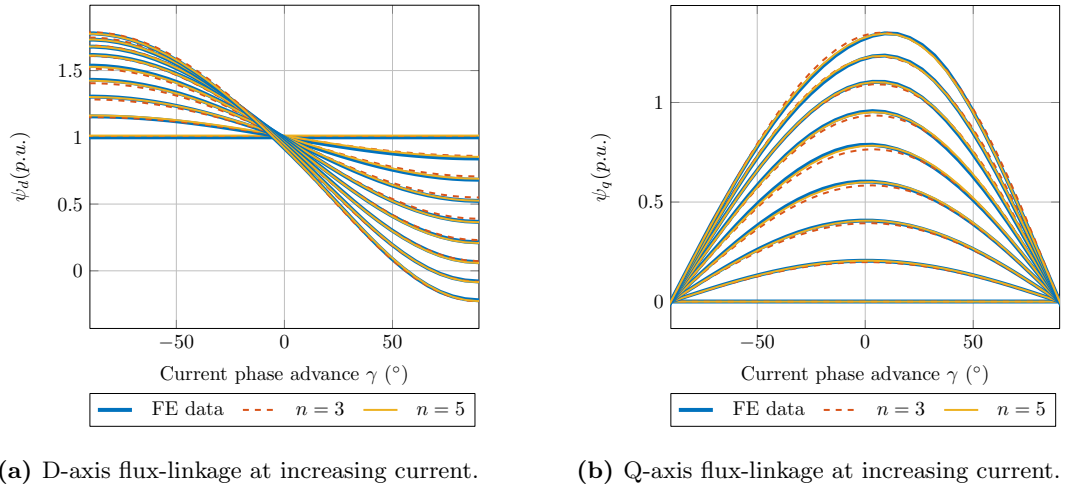


**Figure 3.7:** IPMSM Flux-Linkages

The flux-linkages were plotted in Fig. 3.7 to visualize the accuracy of the expressions with degree  $n = 3$  and  $n = 5$ , where solid lines represent the FE data, dotted and dashed lines correspond to the identified models. In this specific case where the saturation effects are pronounced a high polynomial degree  $n = 5$  seems to capture seemingly well this effect. Conversely, if the machine is analyzed in a reduced current region, a lower polynomial degree e.g.  $n = 3$  would be sufficient to describe the nonlinear effects. The goodness of fit for the corresponding polynomial degrees can be evaluated with the metric, CoD, introduced in (3.26). Table 3.2 summarizes the CoD for different polynomial degrees starting with the linear model  $n = 1$ , where the closeness of  $n = 5$  observed in Fig. 3.7 can be quantified with the largest CoD which is not a surprise. However the difference in magnitude between the CoD for  $n = 3$  and  $n = 5$  confirms the degree of fitness of the latter.

**Table 3.2:** IPMSM - Coefficient of determination

	CoD
$n = 1$	0.9987
$n = 3$	0.99986
$n = 5$	0.9999945

One strong advantage of representing the flux-linkages in terms of a polynomial is that it enables an analytical representation of the various characteristics of the machine, such as the absolute and differential dq-axes inductances, the electromagnetic torque and the motor torque constant  $K_t$ . This is the separation of these characteristics of the machine in individual expressions which enables an easy and accurate analysis of them.

### 3.3.2 Machine Inductances

In the same way as with flux-linkages, the inductances can be compared against FEA results. The polynomial degree is the key factor for the accuracy of the inductances. Conventional approaches use the flux-linkage information at certain operating points to obtain directly the inductances [57, 23], but the number of points is limited due to the effort needed to obtain them. In [57] the authors propose to enhance the inductance results by interpolating between data points.

In addition to this, the calculation of the differential inductances require the partial derivative with respect to the current, which means further mathematical manipulation, discretization errors and sensitivity to noise in the data. As the proposed approach is based already on analytical functions, its derivative is easy to formulate in terms of the polynomials coefficients and as a result it averages any noise in the input data. The approach proposed by this work implicitly interpolates the single data points of the flux-linkage data as an analytical function describes the given data points. The latter is specially relevant when working with measured data.

The inductances can be evaluated for all data points of the FEA simulation according to the definitions in section 2.2.3. For example the absolute inductances for  $n = 3$  are expressed as:

$$L_d(i_d, i_q) \Big|_{n=3} = l_{dq10} + l_{dq20}i_d + l_{dq30}i_d^2 + \frac{c_{dq11}i_q^2}{2} \quad (3.33)$$

$$L_q(i_d, i_q) \Big|_{n=3} = l_{qd10} + l_{qd30}i_q^2 + c_{dq01}i_d + \frac{c_{dq11}i_d^2}{2} \quad (3.34)$$

Ultimately, when talking about absolute inductances, what is being considered is the ratio between flux-linkage and current. A few characteristics of this ratio for all current values can be observed by looking at the dq-axes flux-linkages. It can be seen in Fig. 3.8a that  $\psi_d$  is biased by  $\psi_m$ , leading to saturation in the magnetic circuit producing at the same time an asymmetric d-axis current dependency. In Fig. 3.8a, the saturation degree decreases when  $i_d$  gets negative, straight part of  $\psi_d$ , and increases when  $i_d$  turns positive, curved part of  $\psi_d$ . When  $i_d$  is positive, the magnetic flux due to the  $i_d$  flows in the same direction as the permanent magnet one, saturating even more magnetic core of the machine, reducing the net permeability of the core and thus decreasing the resulting flux-linkage as well. On the other hand, the flux-linkage,  $\psi_q$ , is symmetric with respect to  $i_q$ , as can be seen in Fig. 3.8b, with no flux-linkage bias, the magnetic circuit behaves in a symmetrical way with respect the q-axis current.

### 3 Flux-Linkage Model Parameter Identification

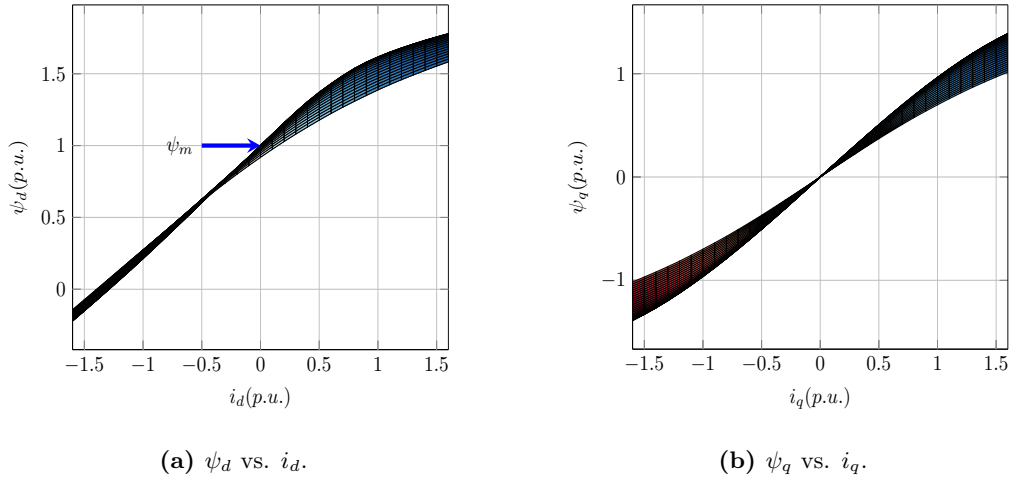


**Figure 3.8:** FEA Flux-linkages.

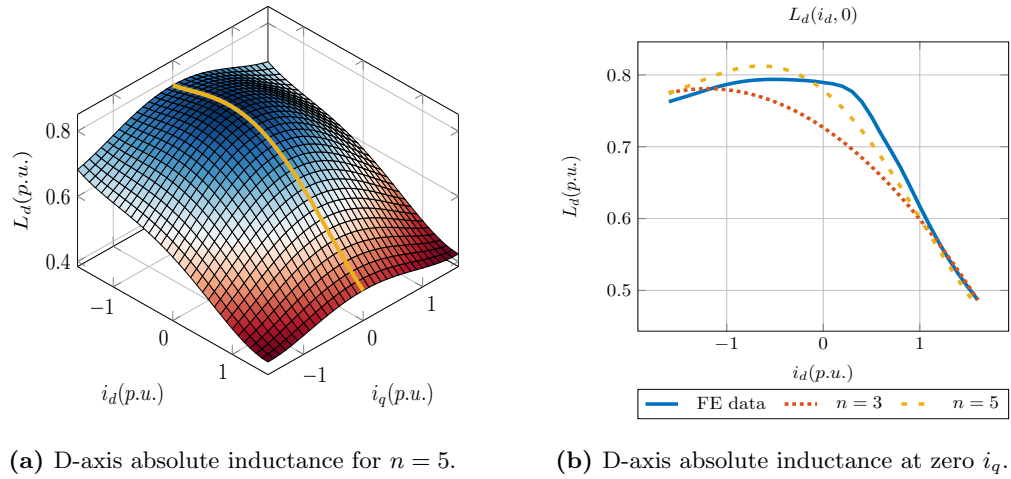


**Figure 3.9:** D-axis absolute inductance.

These two properties have a direct impact on the absolute inductances  $L_d$  and  $L_q$ . As a result  $L_d$  exhibits asymmetry with respect to  $i_d$  as in Fig.3.9b. More importantly, the consequence of this asymmetry was the impossibility to simplify the coefficients<sup>3</sup> of the polynomial with respect to  $i_d$ . Consequently, when trying to describe two quadrants, the polynomial accuracy achieved for  $\psi_d$  can differ from the one obtained for  $\psi_q$ , as can be observed in Fig. 3.10b. However, if the approximation of  $\psi_d$  is limited to one quadrant,

<sup>3</sup>The asymmetry and symmetry of the dq-flux-linkages with respect to the currents were considered in section 2.2.1 to simplify the number of coefficients of the flux-linkage expressions. The asymmetric behavior of  $\psi_d$  with respect to  $i_d$  led to no simplification.

### 3.3 Offline Identification of PMSMs: FEA Simulation Data

i.e. the second one, the accuracy of the polynomial with the same degree increases. This is shown in the following section, nevertheless the reason for the improvement of the approximation relies on the fact that more coefficients with their corresponding current terms are available to describe nonlinear behavior in the reduced area of interest.

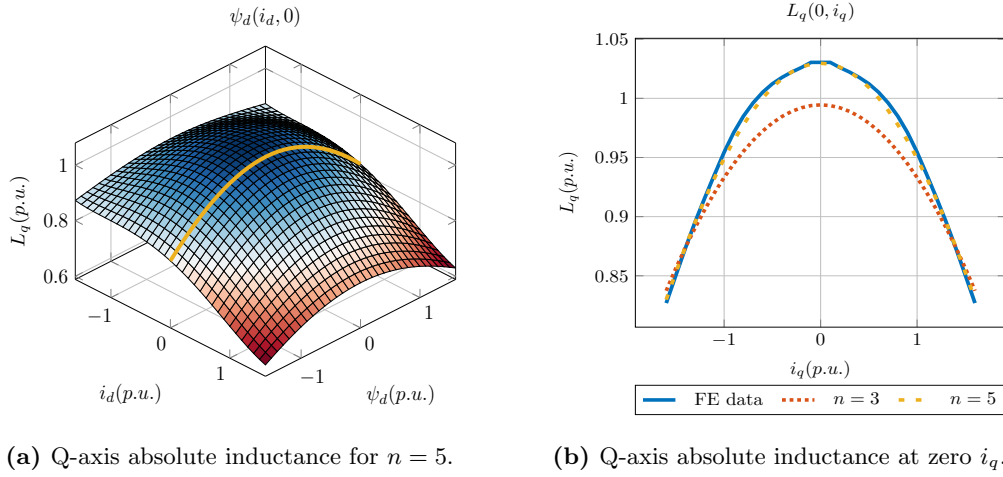


**Figure 3.10:** Q-axis absolute inductances.

In a similar manner, the differential inductances can be calculated according to (2.45), (2.46) and (2.48) for the given polynomial degrees, for  $n = 3$  the incremental inductances would be:

$$L_{dd}(i_d, i_q) \Big|_{n=3} = l_{dq10} + 2l_{dq20}i_d + 3l_{dq30}i_d^2 + \frac{c_{dq11}i_q^2}{2} \quad (3.35)$$

$$L_{qq}(i_d, i_q) \Big|_{n=3} = l_{qd10} + 3l_{qd30}i_q^2 + c_{dq01}i_d + \frac{c_{dq11}i_d^2}{2} \quad (3.36)$$

$$L_{dq}(i_d, i_q) = L_{qd}(i_d, i_q) \Big|_{n=3} = c_{dq01}i_q + c_{dq11}i_d i_q \quad (3.37)$$

### 3 Flux-Linkage Model Parameter Identification

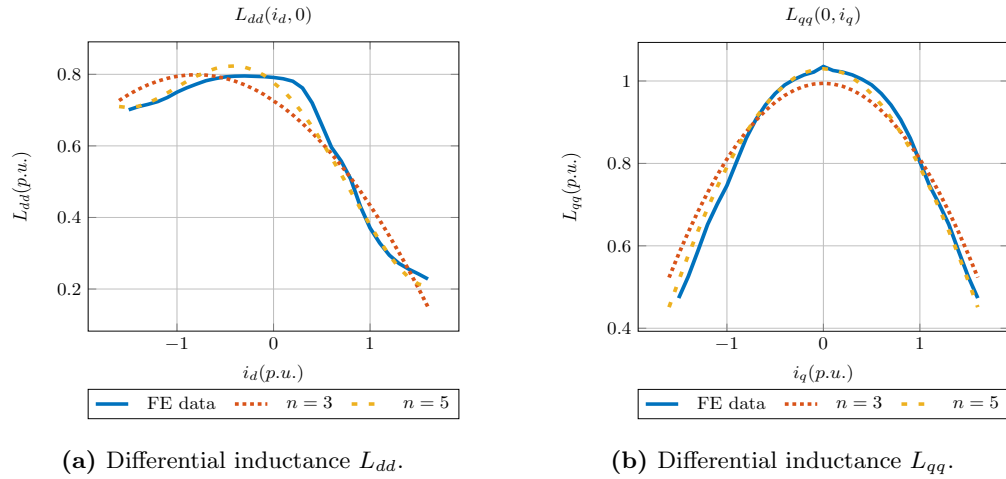


**Figure 3.11:** Differential inductances.

The differential inductances exhibit the same characteristics as the absolute ones, therefore, the coefficients analysis is the same as well. Even though the main objective of the expressions (2.38) and (2.39) is not to obtain the machine inductances, it is a by-product that help to analyze a machine design or it could be used to formulate a phase variable model of the machine in terms of its inductances.

#### 3.3.3 Electromagnetic Torque

One of the metrics to evaluate the accuracy of the flux-linkage expressions (2.38) and (2.39), is the ability to describe the nonlinear behavior of the electromagnetic torque.  $T_e$  as defined in (2.13), indicates that all coefficients contribute to describe the development of torque with respect to the currents  $i_d$  and  $i_q$ .

As already mentioned in chapter 2.1, when the machine has saliency, a difference between d-axis and q-axis inductances, an additional torque contribution arises, called reluctance torque. The reluctance torque only appears when the d-axis current is non-zero, otherwise only the torque contribution coming from the q-axis current is to be seen. The polynomial form of expressions (2.38) and (2.39) enables the separation of this two type of torque. Recalling the definition of electromagnetic torque:

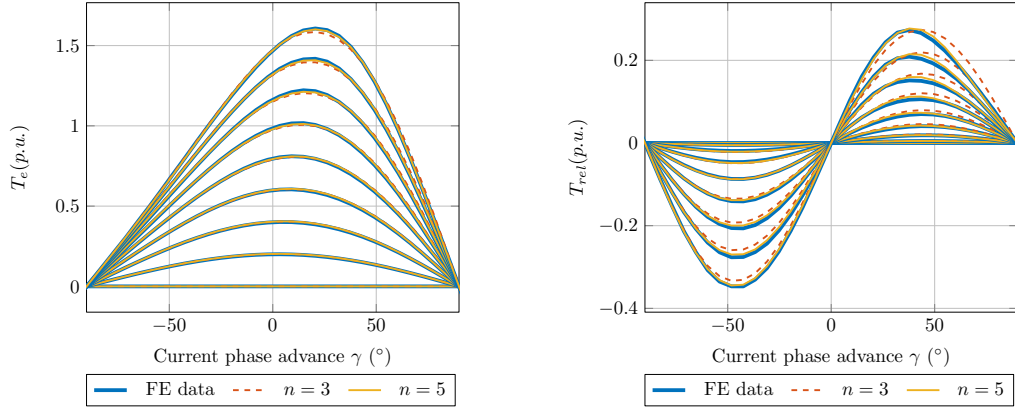
$$T_e(i_d, i_q) = \frac{3}{2}p \cdot (\psi_m \cdot i_q - (L_d - L_q) \cdot i_d \cdot i_q) \quad (3.38)$$

where the reluctance torque is the term that involves the inductances. Once the magnetic circuit starts to saturate, (3.38) needs to include the nonlinear effects. By rewriting (3.38) in terms of flux-linkages, according to (2.13), the expressions (2.38) and (2.39) can be used to separate the nonlinear effects in order to capture the magnet torque and the reluctance torque contributions correctly. For simplicity,  $n = 3$  is chosen once again

to demonstrate the nonlinear effects separation:

$$T_e(i_d, i_q) \Big|_{n=3} = \frac{3}{2}p \left[ \underbrace{\left( \psi_m + \frac{c_{dq01} i_q^2}{2} \right) i_q}_{\text{Main torque}} - \underbrace{\left( l_{dq10} - l_{qd10} + (l_{dq20} - c_{dq01}) i_d + l_{dq30} i_d^2 - l_{qd30} i_q^2 + \frac{c_{dq11} (i_q^2 - i_d^2)}{2} \right) i_d i_q}_{T_{rel}} \right] \quad (3.39)$$

where the first group of terms along  $i_q$  represent the main torque with its corresponding saturation terms that solely come from the q-axis current. These were already addressed in section 2.2.4, where the motor torque constant  $K_t$  were formulated to included the saturation effects. On the other hand, the second group of terms describe the reluctance torque  $T_{rel}$ , including the classical inductance terms  $l_{dq10} - l_{qd10}$  but also the additional coefficients that represent all the nonlinear effects.



(a) Electromagnetic torque at increasing current.

(b) Reluctance torque at increasing current.

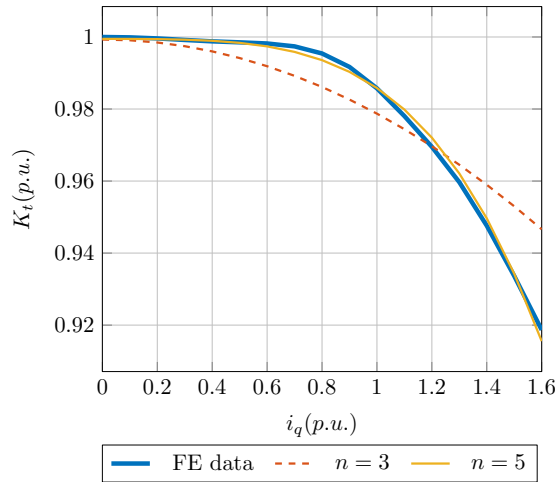
**Figure 3.12:** IPMSM electromagnetic torque

The motor torque constant  $K_t$ , which depicts the torque current ratio at  $\gamma = 0^\circ$ , can be expressed, with the help of (2.51), for  $n = 5$  as:

$$K_t \Big|_{n=5} = \frac{3}{2}p \left( \psi_m + \frac{c_{dq01} i_q^2}{2} + \frac{c_{dq03} i_q^4}{4} \right) \quad (3.40)$$

where the saturation effects due to  $i_q$  need to be captured with the proper polynomial degree according to the saturation in the torque curve. This aspect is evident for the machine chosen (IPMSM), in Fig. 3.13a the saturation of nearly 8% can be properly described with  $n = 5$ :

### 3 Flux-Linkage Model Parameter Identification



(a) Torque constant.

**Figure 3.13:** IPMSM torque constant

Similarly, the nonlinear effects of reluctance torque can be represented with the help of flux-linkage expressions (2.38) and (2.39). The net electromagnetic torque depicted in Fig. 3.12a shows how the pronounced saturation effects at increasing currents requires a higher polynomial degree and how a linear model would reduce drastically the fidelity of the model. This evident observation is the basis for a formulation of the online identification problem. As in the literature many approaches have been proposed but typically linear machine models are adopted. Making the approach valid for operating regions where low magnetic saturation is at play.

### 3.3.4 Permanent Magnet Flux Variations

In section 2.3 an expansion of the flux-linkage expressions with respect to the permanent flux-linkage  $\psi_m$  was introduced. The new functions (2.61) and (2.62) can then depict the influence of the permanent flux-linkage on the inductances for example. Similarly, the magnet temperature effects on the flux-linkages can be captured as well. These two aspects can help to estimate inductance tolerances and to create a high fidelity flux-linkage model that can be coupled to a machine thermal model.

A FE simulation was carried out for different magnet remanence  $B_r$  values. The variation range for  $B_r$  was selected for a NdFeB magnet with temperature coefficient  $-0.11\%/^{\circ}C$  maximum temperature of  $180^{\circ}C$  (see table 2.2). From nominal value at room temperature  $21^{\circ}C$  up to the maximum temperature and a  $B_r$  tolerance of 15%, the resulting variation would correspond to the range 80% – 100% of nominal  $B_r$ . Seven different values,  $[0.8 \ 0.84 \ 0.876 \ 0.9 \ 0.93 \ 0.97 \ 1]$  of  $B_r$  (*p.u.*), are then chosen to run the parameter identification of the extended flux-linkage expressions.

One objective of this section is to visualize the influence of remanence variations on the inductances, for that, a polynomial degree  $n$  needs to be selected in order to run the optimization procedure for the given remanence values. As for the FE simulation setup, is identical to the one used in section 2.2.1, where a set of different d-q axes currents is chosen to capture the flux-linkages in four quadrants (see Fig. 2.6). The resulting flux-linkages can be appreciated in Fig. 3.14.

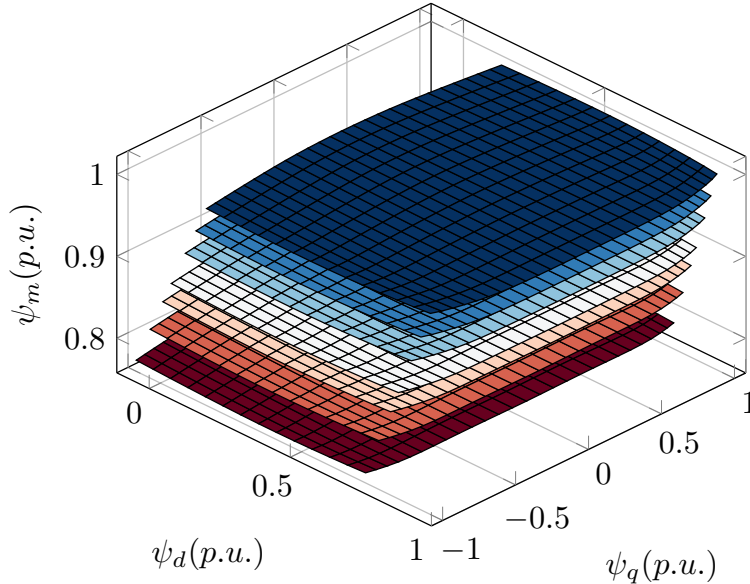


**Figure 3.14:** Flux-linkage at different  $B_r$

### 3 Flux-Linkage Model Parameter Identification

Following the same steps as in the first part of this section, the flux-linkage data showed Fig. 3.14 is used to obtain the coefficients of expressions (2.61) and (2.62). The objective function in (3.27) needs to be modified to include the new variable  $\psi_m$ .

$$\begin{aligned}
 f_n(x) = & \\
 & \sum_{k=1}^N \left[ (\psi_d(i_{d_k}, i_{q_k}, \psi_{m_k}) - \widehat{\psi}_d(i_{d_k}, i_{q_k}, \psi_{m_k}))^2 + (\psi_q(i_{d_k}, i_{q_k}, \psi_{m_k}) - \widehat{\psi}_q(i_{d_k}, i_{q_k}, \psi_{m_k}))^2 \right] \\
 & \text{with,} \quad \widehat{\psi}_d = \nabla \psi_d x^T; \quad \text{and} \quad \widehat{\psi}_q = \nabla \psi_q x^T
 \end{aligned} \tag{3.41}$$

Where  $x$  is the set of unknown coefficients,  $N$  is the number of the simulation data points and  $n$  is the polynomial degree. The letters with a hat notation represent estimated values and the letters with no hat notation are the values of the FE simulation data. The constrained optimization problem can be then formulated in the following form:

$$\begin{aligned}
 \text{Minimize} \quad Q(x) = & \frac{1}{2} x^T G x + g^T x \\
 \text{with,} \quad & l_{dq100} > 0 \quad \text{and} \quad l_{qd100} > 0 \\
 \text{where,} \quad G = & \nabla \psi_d \nabla \psi_d^T + \nabla \psi_q \nabla \psi_q^T \\
 & g = -2\psi_d \nabla \psi_d - 2\psi_q \nabla \psi_q
 \end{aligned} \tag{3.42}$$

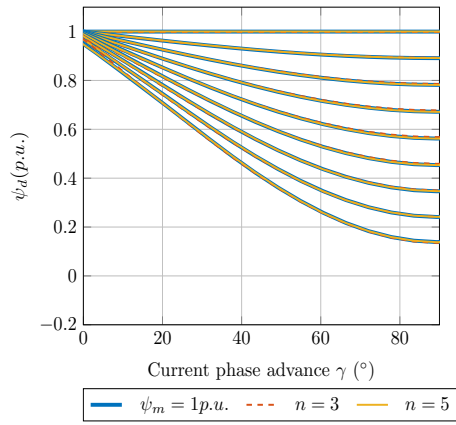
The problem formulation in (3.42) differs with (3.28) only in the constraint that concerns  $\psi_m$  as it is in this case the new additional variable. For the optimization process, the flux-linkages of three runs with different  $B_r$  values are selected. The objective is to emulate a real scenario, where the magnet temperature varies from room conditions up to a maximum value of around  $85^\circ C$  for a given temperature coefficient of  $-0.11\%/^\circ C$ .

#### 3.3.4.1 Flux-linkages

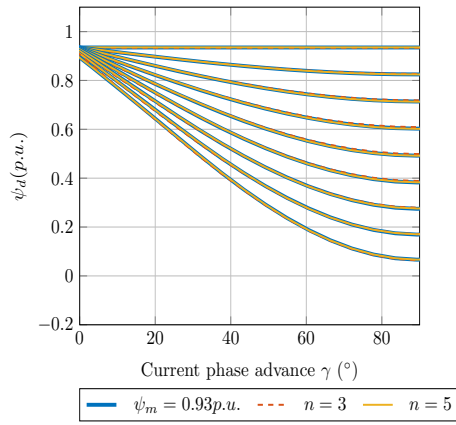
In reality it might be challenging to bring the magnet temperature of the machine over  $160^\circ C$  or the limit  $180^\circ C$  (as per table 2.2) and at the same time drive the machine at maximum load. It is more convenient to establish a model that can be extrapolated to that critical temperatures or  $B_r$  values. With the latter in mind, the set of simulation data is then reduced to:  $[0.93 \quad 0.97 \quad 1]$  of  $B_r$  (*p.u.*) and the remaining four set of data will be used to asses the extrapolation accuracy of the model.

The resulting flux-linkage curves obtained for  $n = 3$  and  $n = 5$  are shown in Fig. 3.15, where  $n = 5$  delivers an accurate description of the flux-linkages despite the additional degree of freedom coming from  $\psi_m$ . The results in Fig. 3.15 are consistent with the ones depicted in section 3.3.1 in terms of the accuracy obtained for a constant value of  $\psi_m$  and polynomial degree. For this specific machine  $n = 5$  is the common value that would describe fairly accurately the associated saturation and non-linear effects.

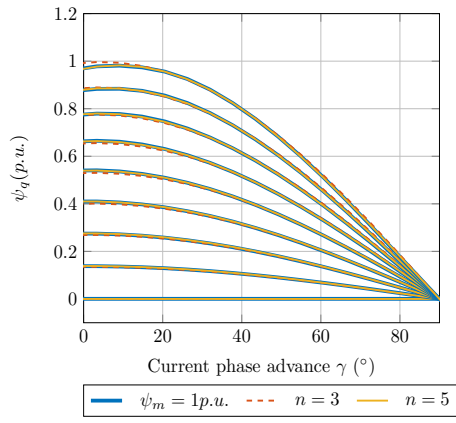
### 3.3 Offline Identification of PMSMs: FEA Simulation Data



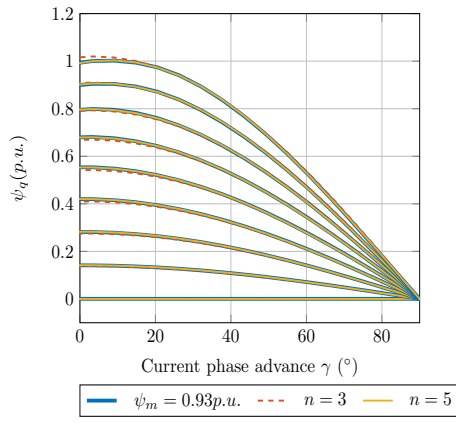
(a) D-axis flux-linkage at  $\psi_m = 1 p.u..$



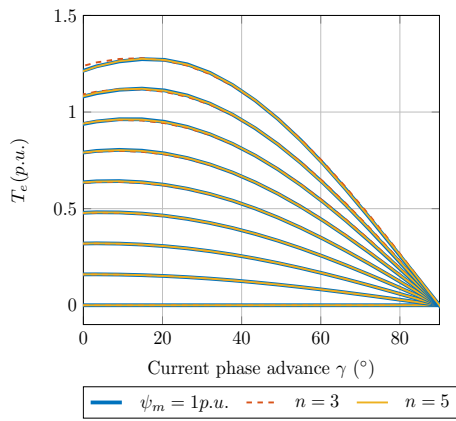
(b) D-axis flux-linkage at  $\psi_m = 0.93 p.u..$



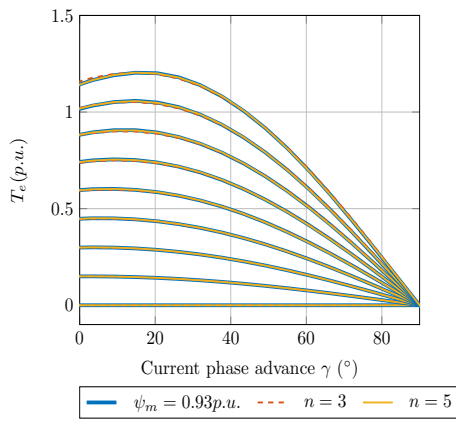
(c) Q-axis flux-linkage at  $\psi_m = 1 p.u..$



(d) Q-axis flux-linkage at  $\psi_m = 0.93 p.u..$



(e) Electromagnetic torque at  $\psi_m = 1 p.u..$



(f) Electromagnetic torque at  $\psi_m = 0.93 p.u..$

**Figure 3.15:** Flux-linkages at increasing current for different  $\psi_m$ .

### 3 Flux-Linkage Model Parameter Identification

On the other hand, Fig. 3.16 shows the extrapolated flux-linkages for the extreme values at  $\psi_m = 0.82p.u.$  and  $\psi_m = 0.78p.u.$ , where the flux-linkage model can extrapolate quite good the target curves. This extrapolation accuracy can be explained by a small change in the flux biasing the lamination in the machine, (20%) of  $B_r$ , which evidently leads to a variation in the nonlinear characteristics of the materials that can be described with a low polynomial order. As an example, for  $n = 5$ , the coefficients  $l_{dq02}$  and  $l_{dq10}$ , which relate to the  $K_t$  saturation and the linear d-axis inductance respectively, become a function of  $\psi_m$  as shown in (3.43). In this example, the mentioned coefficients are analytically described by polynomials of third and fourth degrees, which can track the nonlinear behavior caused by a change in the given range of  $B_r$ .

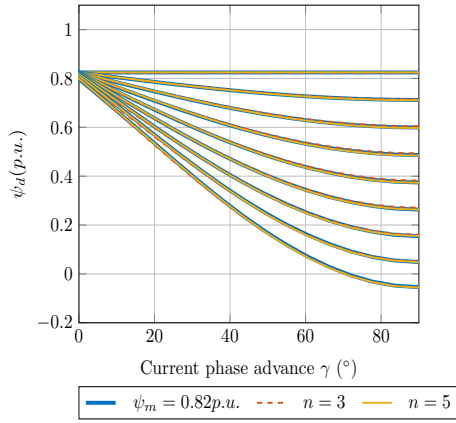
$$\begin{aligned} \psi_d(i_d, i_q, \psi_m) = & l_{dq001} \psi_m + \underbrace{(l_{dq021} \psi_m + l_{dq022} \psi_m^2 + l_{dq023} \psi_m^3)}_{l_{dq02}(\psi_m)} i_q^2 \\ & + \underbrace{(l_{dq100} + l_{dq102} \psi_m^2 + l_{dq104} \psi_m^4)}_{l_{dq10}(\psi_m)} i_d + \dots \end{aligned} \quad (3.43)$$

Despite the subset of the simulation data used for the determination of the coefficients of the flux-linkage expressions, the predicted flux-linkage curves in Fig. 3.16 were close to the actual data. This is then again backed up by the CoD in table 3.3 where the coefficients exhibit digits with values of 9 in the place between thousandths and hundred thousandths. The CoD of the first three positions in table 3.3 reflect the fact that they were used for the coefficient determination and that is why those three CoD evidence a better goodness of fit.

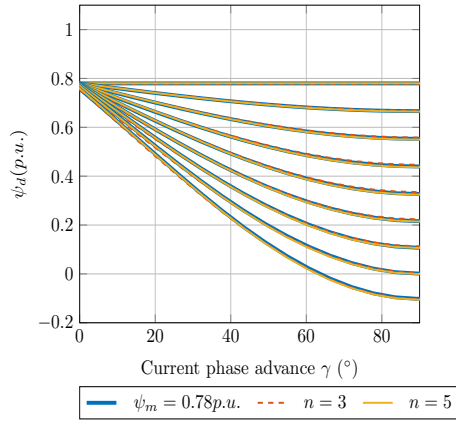
**Table 3.3:** IPMSM - CoD for  $n = 5$

$\psi_m$	CoD
1	0.9999957
0.97	0.9999958
0.93	0.9999951
0.89	0.99999
0.86	0.9999811
0.82	0.9999506
0.78	0.9998724

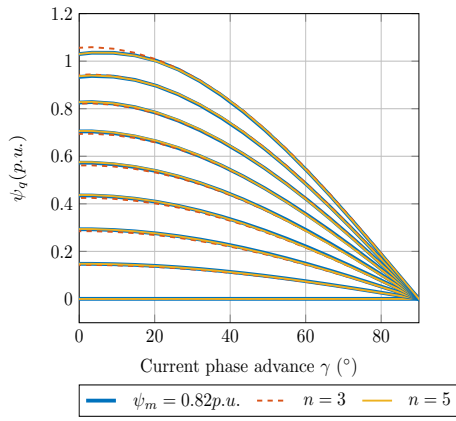
### 3.3 Offline Identification of PMSMs: FEA Simulation Data



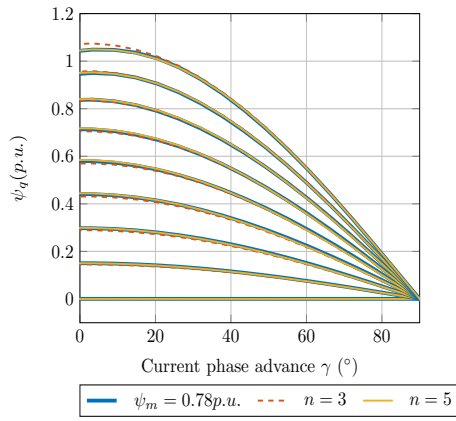
(a) D-axis flux-linkage at  $\psi_m = 0.82p.u.$



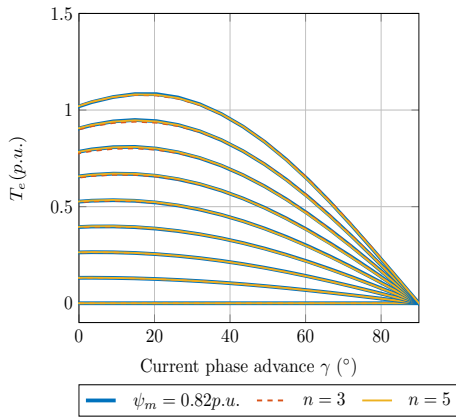
(b) D-axis flux-linkage at  $\psi_m = 0.78p.u.$



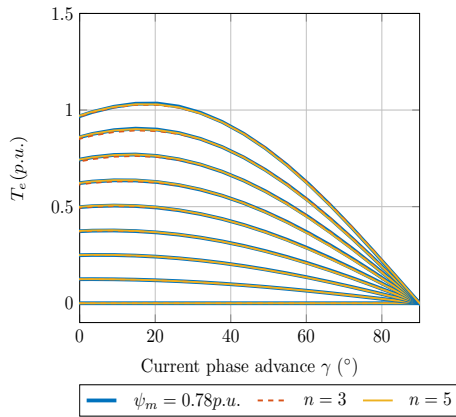
(c) Q-axis flux-linkage at  $\psi_m = 0.82p.u.$



(d) Q-axis flux-linkage at  $\psi_m = 0.78p.u.$



(e) Electromagnetic torque at  $\psi_m = 0.82p.u.$



(f) Electromagnetic torque at  $\psi_m = 0.78p.u.$

**Figure 3.16:** Extrapolated flux-linkages at increasing current for different  $\psi_m$ .

### 3.3.4.2 Machine inductances

Following the previous assessment steps, the accuracy of the inductances with respect to  $\psi_m$  will be evaluated in this section. As hinted in (3.43), each coefficient presented in (2.28) and (2.30) is then represented by a polynomial as a function of  $\psi_m$ . At the same time, this could be seen as indirect temperature dependency of the inductances. Recalling the definition of self-inductance according to [35] :

$$L = \frac{\psi}{i} = \frac{N \cdot \phi}{i} = \frac{N \cdot F \cdot \mathcal{P}}{i} = N^2 \cdot \mathcal{P} \quad (3.44)$$

where  $N$  is the number of coil turns,  $i$  is the coil current,  $\psi$  is the flux-linkage  $N \cdot \phi$ . The magnetic flux  $\phi$  is equal to  $F \cdot \mathcal{P}$ , where  $F$  is the m.m.f, defined as  $N \cdot i$  and  $\mathcal{P}$  is the magnetic circuit permeance. Of all these variables, the permeance  $\mathcal{P}$  is the one linked to the relative permeability  $\mu_r$ , which at the same time depends on  $\phi$ , as it is the inverse value of the magnetic reluctance already mentioned in (2.14). These relationships make  $\mathcal{P}$  current and magnetic flux dependent in a nonlinear manner, given the characteristics of  $\mu_r$  with respect  $\phi$  as depicted in Fig. 2.3b. This flux dependency, which in part comes from the contribution of the permanent magnet flux as shown in 2.4, is then captured in (2.64) and (2.66), where the dq-axes inductances are formulated in terms of the currents and  $\psi_m$ . Expressions (3.45) and (3.46) serve as an example to visualize the polynomials containing  $\psi_m$ :

$$L_d(i_d, i_q, \psi_m) \Big|_{n=3} = \underbrace{l_{dq100} + l_{dq102}\psi_m^2}_{l_{dq10}} + l_{dq201}i_d\psi_m + l_{dq300}i_d^2 + l_{dq120}i_q^2 \quad (3.45)$$

$$L_q(i_d, i_q, \psi_m) \Big|_{n=3} = \underbrace{l_{qd100} + l_{qd102}\psi_m^2}_{l_{qd10}} + l_{qd300}i_q^2 + l_{qd110}i_d + l_{qd111}i_d\psi_m + l_{qd120}i_d^2 \quad (3.46)$$

The terms under braces in (3.45) and (3.46) represent the coefficients related to the linear inductances introduced in section 3.3,  $l_{dq10}$  and  $l_{qd10}$ . The inclusion of  $\psi_m$  in the formulation of these inductances is the direct indication of inductances with and without magnets. The coefficients accompanied by  $\psi_m$  describe the saturation effect that the bias flux of permanent magnets have on the magnetic circuit. An unsaturated machine core, without magnets, delivers larger dq-axes inductances compared to the ones at the presence of rotor magnet. As the magnet flux moves the operating point of the magnetic materials, more specifically, its relative permeability, the resulting flux-linkage increases at a lower rate with respect to the current leading to a decrease of the

### 3.3 Offline Identification of PMSMs: FEA Simulation Data

inductances. This effect is reflected in (3.45) with the equivalent coefficient  $l_{dq10}$ :

$$l_{dq10} = l_{dq100} + l_{dq102}\psi_m^2 \quad (3.47)$$

where in (3.47) a negative value of  $l_{dq102}$  leads to a decrease of  $l_{dq10}$  with respect to  $\psi_m$  as shown in Fig. 3.17.

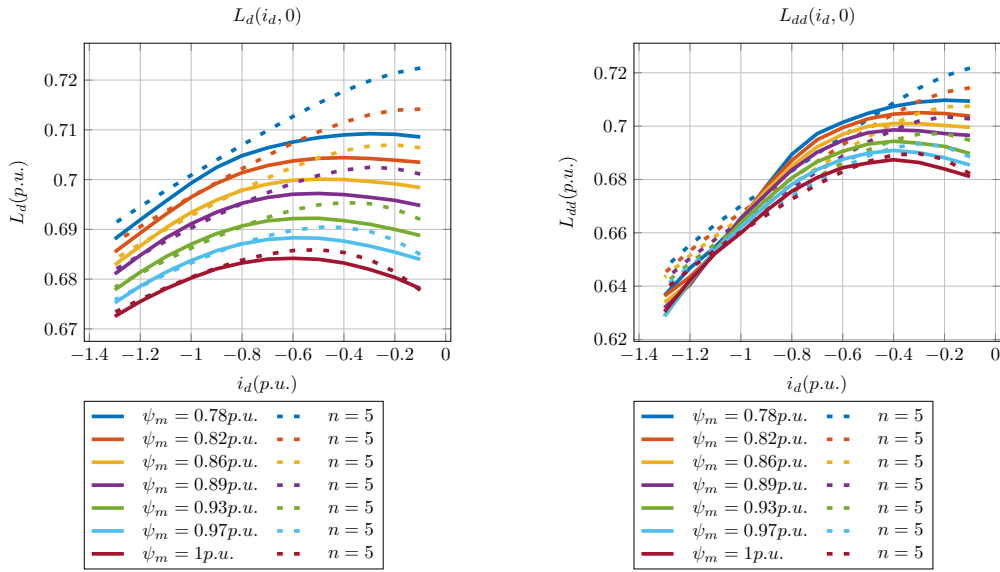


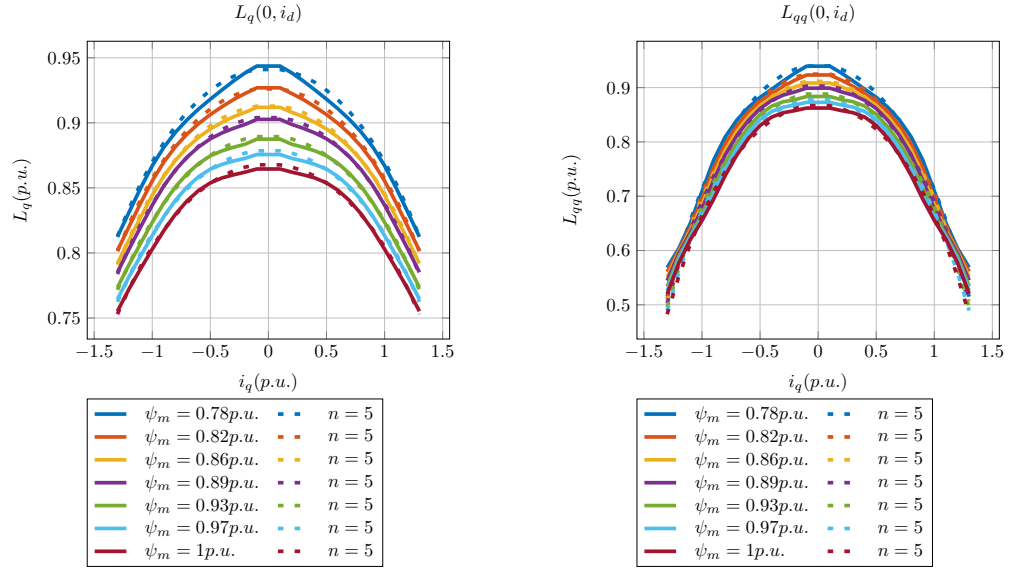
**Figure 3.17:** D-axis inductances at different  $\psi_m$ .

Similarly, in (3.48) the equivalent coefficient  $l_{qd10}$  displays also a dependency on  $\psi_m$ .

$$l_{qd10} = l_{qd100} + l_{qd102}\psi_m^2 \quad (3.48)$$

the coefficient along  $\psi_m^2$  indicates the contribution of the permanent magnet flux-linkage to the small signal q-axis inductance, which is reflected in an increasing inductance at decreasing  $\psi_m$  as displayed in Fig. 3.18.

### 3 Flux-Linkage Model Parameter Identification



(a) Q-axis absolute inductance at zero  $i_q$ . (b) Q-axis differential inductance at zero  $i_q$ .

**Figure 3.18:** Inductances at different  $\psi_m$ .

The three bottom curves,  $\psi_m = [0.93 \ 0.97 \ 1] p.u.$  in Fig. 3.17 and 3.18 correspond to the data sets used for the identification of the coefficients. Conversely, the remaining top curves, correspond to the data set used to obtain extrapolated inductances.

The inductance obtained from extended flux-linkage expressions can fairly follow the expect FEA inductances, where it is important to notice that the inductance variations with respect to  $\psi_m$  are quite small and they can still be tracked by the polynomials. This is an indication of the change of the coefficients when considering its online identification under magnet temperature variations. Specially the absolute inductances, Fig. 3.17a and 3.18a, will have an important impact on the online identification. This will be addressed in chapter 6, where the information of the extended flux-linkage expressions can be used to improve the performance of the estimation.

#### 3.3.4.3 Torque constant

In 3.3.3 it was shown that the saturation of the torque constant  $K_t$  is exclusively due to  $i_q$  when  $\psi_m$  remains constant. On the other hand, when variations of the permanent magnet flux-linkage are considered,  $\psi_m$  plays a role in the saturation terms as hinted in (2.69). In order to visualize the torque constant dependency on  $\psi_m$ ,  $K_t$  is formulated with help of (2.69) for  $n = 5$  :

$$K_t(i_q, \psi_m) \Big|_{n=5} = \frac{3}{2}p \left( \psi_m + l_{dq021} i_q^2 \psi_m + l_{dq022} i_q^2 \psi_m^2 + l_{dq023} i_q^2 \psi_m^3 + l_{dq041} i_q^4 \psi_m \right) \quad (3.49)$$

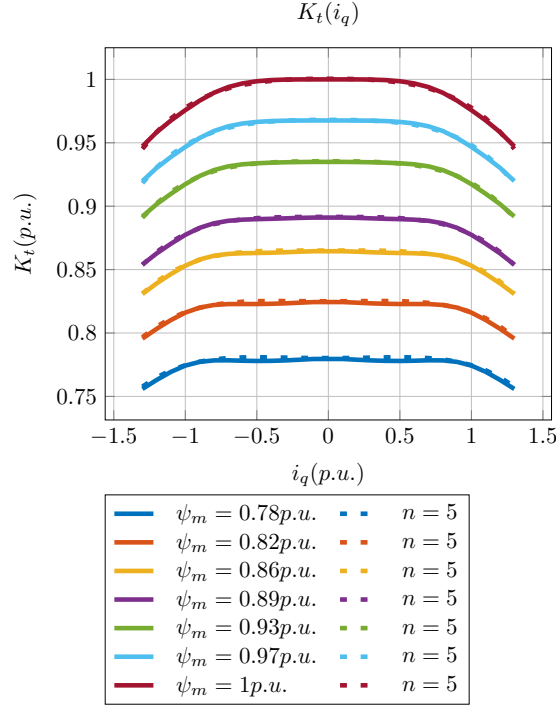


**Figure 3.19:** IPMSM torque constant at different  $\psi_m$ .

The accuracy obtained with  $n = 5$ , confirmed in Fig. 3.19, illustrates that the saturation caused originally by  $i_q$  is also related to  $\psi_m$ . Meaning that the saturation degree seen in the main torque component can be interpreted as magnet temperature dependent and is driven by  $i_q$ .

By normalizing (3.49) with respect to  $\frac{3}{2}p\psi_m$  it is more evident how the saturation is directly related to  $\psi_m$ :

$$K_{t_{norm}} \Big|_{n=5} = 1 + l_{dq021} i_q^2 + l_{dq041} i_q^4 + \underbrace{l_{dq022} i_q^2 \psi_m + l_{dq023} i_q^2 \psi_m^2}_{\text{saturation terms}} \quad (3.50)$$

Even though the main contribution to the saturation comes from  $i_q$  the last two terms in (3.50) show the dependency with respect to  $\psi_m$ . This is the indication that the biasing magnetic flux produced by the magnets might saturate the magnetic circuit in the case that  $l_{dq022}$  and  $l_{dq023}$  become negative in the example (3.50).

### 3.4 Offline Identification of WFSMs: FEA Simulation Data

This section addresses the parameter identification of the flux-linkage expressions presented in 2.4. The machine with characteristics shown in table 2.3 was simulated using the 2D-FE software Ansys-Maxwell. Eleven values of the field current  $i_f$ , ranging from zero to a maximum value were defined to run the simulation for different phase current magnitude and phase advance  $\gamma$  values. The identification approach used was the same as in the previous sections, the coefficients are determined through the formulation of an optimization problem that minimize an objective function. In this case, two approaches are going to be presented. The first approach concerns the flux-linkage expressions (2.76) and (2.77), which are used to define the following objective function:

$$f_1(x_1) = \sum_{k=1}^N \left[ (\psi_d(i_{d_k}, i_{q_k}, i_{f_k}) - \hat{\psi}_d(i_{d_k}, i_{q_k}, i_{f_k}))^2 + (\psi_q(i_{d_k}, i_{q_k}, i_{f_k}) - \hat{\psi}_q(i_{d_k}, i_{q_k}, i_{f_k}))^2 \right] \\ \text{with,} \quad \hat{\psi}_d = \nabla \psi_d x_1^T; \quad \text{and} \quad \hat{\psi}_q = \nabla \psi_q x_1^T \quad (3.51)$$

Where the subscript 1 denotes the first approach,  $x_1$  is the set of unknown coefficients,  $N$  is the number of the simulation data points. The letters with a hat notation represent estimated values and the letters with no hat notation are the values of the FE simulation data. For the optimization problem formulation of the WFSM, there is only one constraint as that kind of machine may might exhibit negative saliency  $L_d > L_q$  and positive  $L_d < L_q$  at different operating points. Therefore the only constraint to be considered is the fact that the magnetizing field inductance  $L_{mf}$  is positive. Recalling (2.88), the constraint is then formulated in terms of the linear magnetizing coefficient, as  $l_{dq001} > 0$ .

The second approach is based on the alternative set of flux-linkage expressions (2.82) and (2.83). Here the optimization process is divided in two steps. The first step focuses on the identification of coefficients for a constant  $i_{f_h}$  value using the expressions (2.79) and (2.80).

$$f_{2a}(x_h) \Big|_{i_{f_h}} = \sum_{k=1}^N \left[ (\psi_d(i_{d_k}, i_{q_k}) - \hat{\psi}_d(i_{d_k}, i_{q_k}))^2 + (\psi_q(i_{d_k}, i_{q_k}) - \hat{\psi}_q(i_{d_k}, i_{q_k}))^2 \right] \\ \text{with,} \quad \hat{\psi}_d = \nabla \psi_d x_h^T; \quad \text{and} \quad \hat{\psi}_q = \nabla \psi_q x_h^T \quad (3.52)$$

in (3.52) the subscript  $2_a$  represents the first step of the second approach and  $x_h$  is the subset of coefficients valid for the given field current  $i_{f_h}$ . Similarly to the constraints in the first approach, for this set of objective functions, the only constraint to consider is the positive value of  $l_{dq00} > 0$ , which relates directly to the rotor field flux-linkage. The second step is dedicated to the final identification of the coefficients only with respect to  $i_f$  according to the polynomial structure in (2.81). For each set of coefficients  $l_{dq(i)(k)}$  and  $l_{qd(i)(k)}$  the following objective function is defined:

$$f_{2_b}(l_h) \Big|_{i_{f_h}} = \sum_{h=1}^{N_f} \left( l_{()() (i)(k)}(i_{f_k}) - \widehat{l}_{()() (i)(k)}(i_{f_k}) \right)^2 \quad (3.53)$$

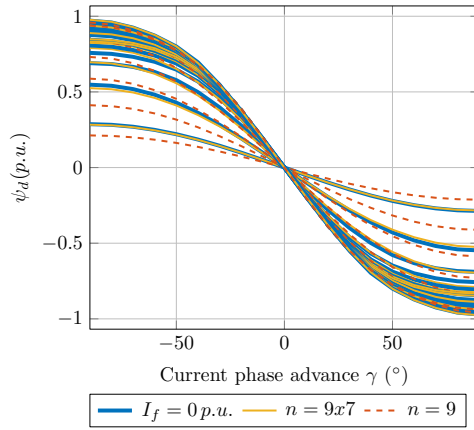
with,  $\widehat{\psi}_d = \nabla \psi_d l_h^T$ ;      and       $\widehat{\psi}_q = \nabla \psi_q l_h^T$

where the subscripts  $(i)(k)$  represent the dq-axes current powers of the associated coefficient and  $l_h$  is the set of coefficients that describe the field current dependency of coefficient  $l_{()() (i)(k)}$ .

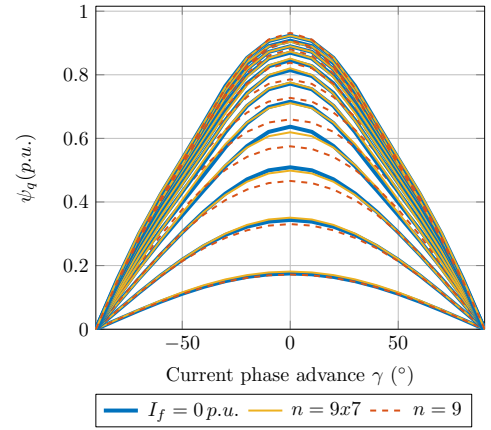
The polynomial degree  $n = 9$  was selected to describe the dq-axes current dependency of the flux-linkages. This was the result of a strong non-linear characteristics of the flux-linkages. In approach 2, the polynomial degree  $n_f$  to describe each coefficient was set to 7. With a total number of 11 sets of flux-linkage data at different  $i_f$  values, a subset of 8 field current values was sufficient to represent with satisfactory accuracy the coefficients identified for each of the 11 operating points.

Fig. 3.20 summarizes the results with the two approaches. Three subsets are displayed to cover the whole field current range. The red curves ( $n = 9$ ) represent the first approach which is based on (3.51) and the yellow ones ( $n = 9 \times 7$ ) correspond to the second approach, which consists of the two step identification according to (3.52) and (3.53). The first approach cannot describe correctly the flux-linkages for all operating conditions, specially maximum field current value. This is more evident in Fig. 3.20e, where estimate of the d-axis flux-linkage at negative  $\gamma$  values and high phase current deviates the most.

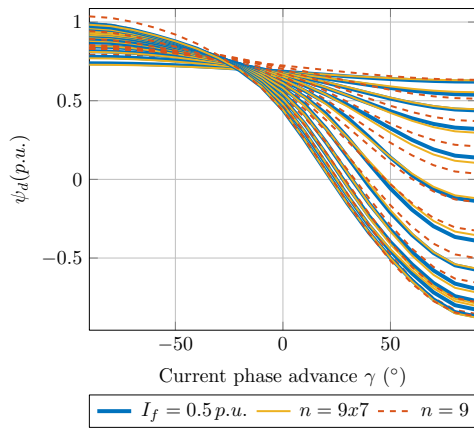
### 3 Flux-Linkage Model Parameter Identification



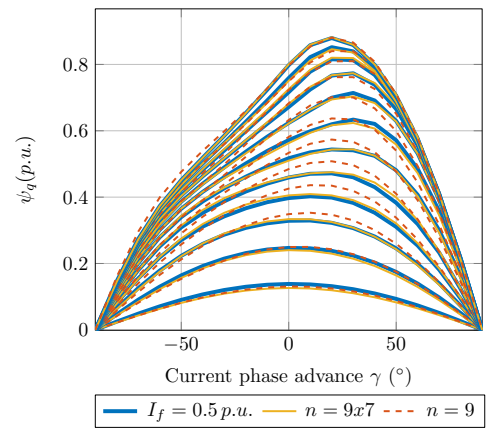
(a) D-axis flux-linkage at  $i_f = 0 p.u.$



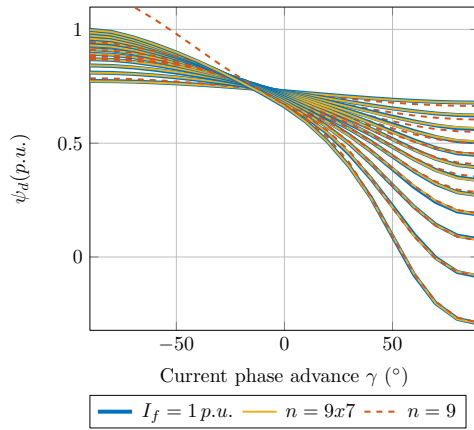
(b) Q-axis flux-linkage at  $i_f = 0 p.u.$



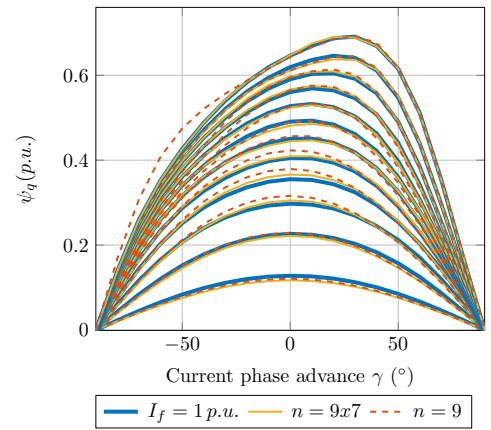
(c) D-axis flux-linkage at  $i_f = 0.5 p.u.$



(d) Q-axis flux-linkage at  $i_f = 0.5 p.u.$



(e) D-axis flux-linkage at  $i_f = 1 p.u.$

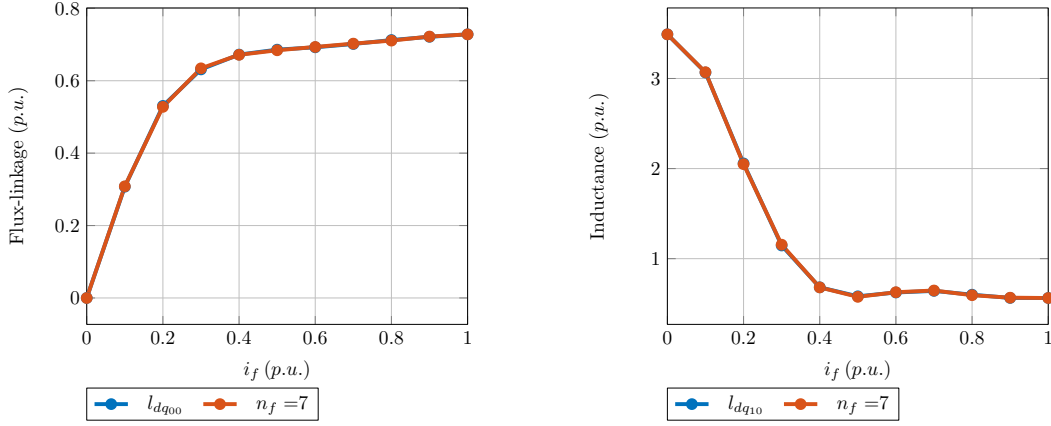


(f) Q-axis flux-linkage at  $i_f = 1 p.u.$

**Figure 3.20:** Flux-linkages at increasing current for different  $i_f$  values.

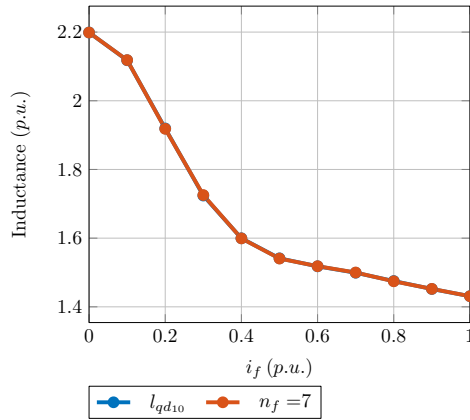
### 3.4 Offline Identification of WFSMs: FEA Simulation Data

The deviations observed at maximum phase current can be explained with Runge's phenomenon [58]. At high polynomial degrees, the approximated curves start to oscillate around the edge of the interpolated interval. This effect wasn't evident with the PMSM as the polynomial degrees were lower. In addition to this, the oscillations were mitigated by using constrained optimization and minimizing the least squares to find the coefficients [58]. Conversely, there is only one constraint for the objective function (3.51) and the polynomial has three variables.



(a) Rotor flux-linkage vs.  $i_f$ .

(b) Small signal d-axis inductance vs.  $i_f$ .



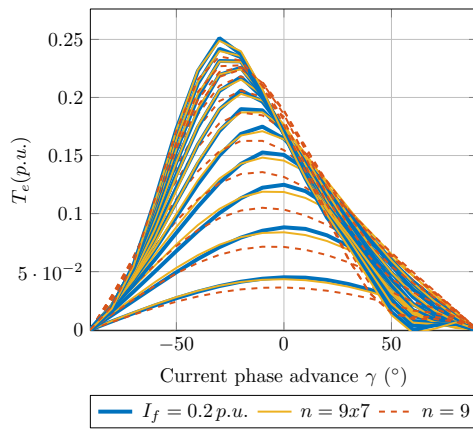
(c) Small signal q-axis inductance vs.  $i_f$ .

**Figure 3.21:** Coefficients for different  $i_f$  values.

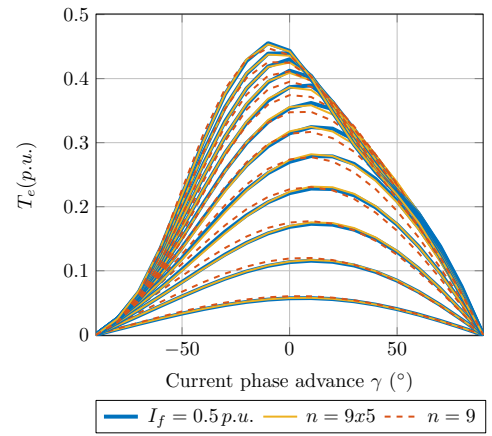
On the other hand, the curves with the second approach show no oscillations. The identification problem was divided in two steps, reducing the effective degree of complexity of the formulated polynomial. This means, the first step considers a reduced set of data with two variables, namely  $i_d$  and  $i_q$  and the second one identifies the coefficients

### 3 Flux-Linkage Model Parameter Identification

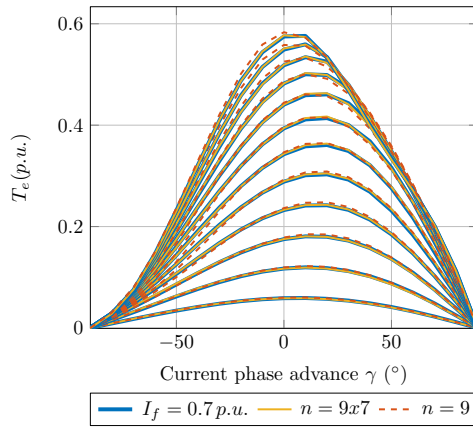
of a polynomial with only one variable  $i_f$  from the set of coefficients obtained in the first step. This piece-wise optimization leads to a better approximation accuracy. Fig. 3.21 depicts the three most representative coefficients,  $l_{dq00}$  which correspond to the biasing DC flux-linkage produced by the rotor field current,  $l_{dq10}$  is the small signal d-axis inductance and  $l_{dq10}$  the small signal q-axis inductance. Those coefficients were identified using the general formulation (2.81) to describe their dependency on  $i_f$  as can be seen in Fig 3.21. Additionally, a few aspects can be derived from the coefficients dependency on  $i_f$ . The saturation seen at mid  $i_f$  values of the rotor dc flux-linkage in Fig. 3.21a is a good indication of the limits of the design in terms of the definition of maximum field current. Fig. 3.21b and 3.21c offer a first insight into the saliency of the machine, which at lower  $i_f$  values is negative and in the upper mid region of  $i_f$  becomes positive.



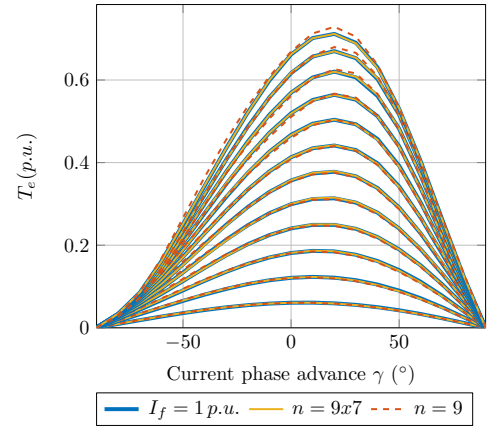
(a) D-axis flux-linkage at  $i_f = 0.2 p.u.$



(b) Q-axis flux-linkage at  $i_f = 0.5 p.u.$



(c) D-axis flux-linkage at  $i_f = 0.7 p.u.$



(d) Q-axis flux-linkage at  $i_f = 1 p.u.$

**Figure 3.22:** WFSM flux-linkages at increasing current for different  $i_f$  values.

### 3.4 Offline Identification of WFSMs: FEA Simulation Data

Fig. 3.22 show the torque at different field current values, where the first hint of the saliency seen in the coefficients  $l_{dq10}$  and  $l_{qd10}$  can be confirmed. The maximum torque moves from negative to positive  $\gamma$  values at increasing  $i_f$ . Besides the better accuracy of the second approach observed in Fig. 3.20, the analytical description of the flux-linkages opens the door for a minimization of the number of simulation points. Instead of defining small current steps to improve the resolution of the curves, specially the torque curve, the flux-linkage expressions can be used to obtain a better resolution in order to capture, for example, the maximum torque.

The magnetizing inductance  $L_{mf}$ , main driver of the torque generation, is obtained according to (2.87) using only the second approach. Fig. 3.23 shows the dependency of  $L_{mf}$  with respect to  $i_q$  at increasing  $i_f$ .

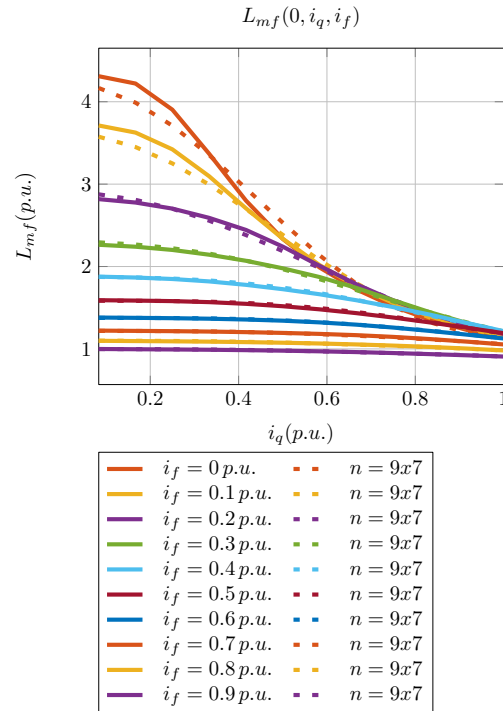


**Figure 3.23:** WFSM magnetizing inductance  $L_{mf}$  vs  $i_q$ .

Similarly, the dq-axes inductances were obtained based on (2.88) and (2.89). Fig. 3.24 depict the inductances with respect to the d- and q-axis currents at increasing field current. It is worth to note, that once a flux is produced by the rotor coil, the d-axis inductance becomes asymmetric with respect to  $i_d$ , which is in line with the asymmetry seen at the PMSM of section 3.3.2. In that case, there is a permanent flux excitation coming from the rotor magnets. Conversely, at the absence of the rotor biasing flux, the d-axis inductance is symmetric like the q-axis inductance with respect the d- and q-axis currents respectively. Another important aspect is the saturation effect caused by the

### 3 Flux-Linkage Model Parameter Identification

rotor flux. The inductance value decreases at increasing  $i_f$ , indicating a saturation in the magnetic circuit of the machine.

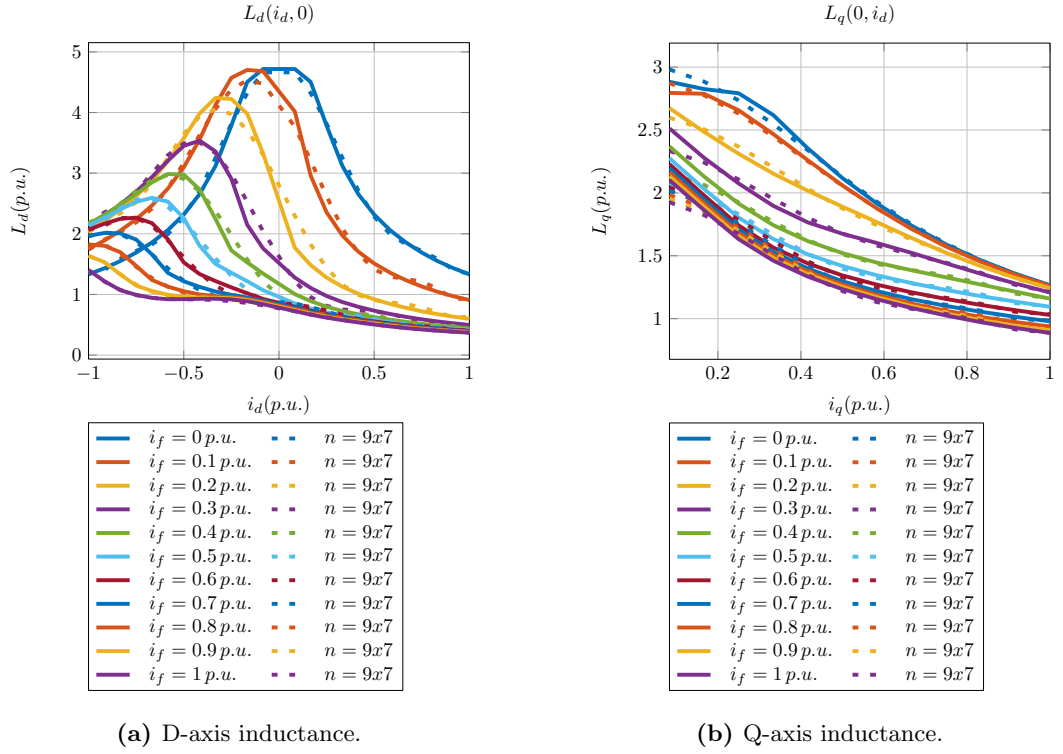


**Figure 3.24:** WFSM absolute inductances at different  $i_f$  values.

To finalize this section, the torque constant is evaluated according to (2.95) at different  $i_f$  values. The behavior of  $K_t$  in Fig. 3.25 confirms the expected dependency of the saturation with respect to the currents  $i_q$  and  $i_f$ . The torque constant is described with two groups of terms. The first one represents only the contribution of  $i_f$  and the second one the mutual coupling between  $i_f$  and  $i_q$ . What Fig. 3.25 shows is the expected strong dependency of  $K_t$  with respect  $i_f$ , as it is torque generating variable. In addition to this, a high mutual coupling between  $i_f$  and  $i_q$  is observed at low  $i_f$  values, but once the magnetic circuit is relatively saturated by the flux generated by the rotor, the mutual saturation effect diminishes.

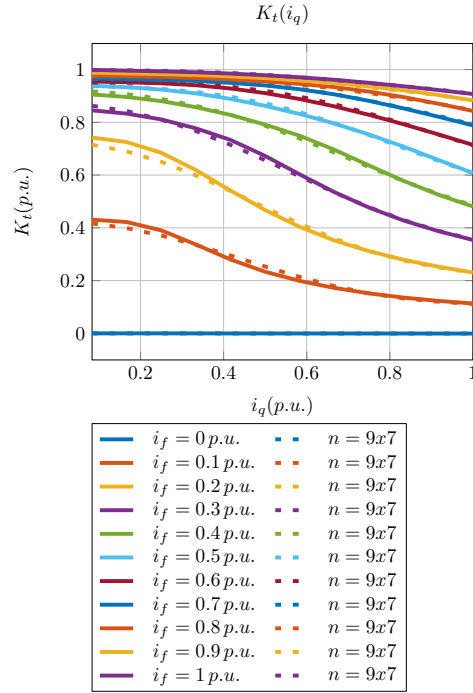


**Figure 3.25:** WFSM torque constant at different  $i_f$  values.

This section presented a comparison of two approaches to describe the flux-linkages of a WFSM. The machine used to illustrate the applicability of the expressions derived in section 2.4 exhibited highly non-linear flux-linkage curves, leading to the use of a high polynomial degree. The second approach, which split the identification process in two steps, showed excellent results in handling three variables. The description of the flux-linkages in an analytical form delivered an insight into the behavior observed through all the curves presented in this section.

## 3.5 Offline Identification: Experimental Data

### 3.5.1 Constant Magnet Temperature

As mentioned in section 3.1.2, for the experimental parameter identification, the flux-linkages need to be obtained indirectly from the machine voltages. But there are still two options to consider, as the parameter identification is going to be carried out offline and online. For the offline identification there are almost no constraints in terms of machine excitation, amount of data and quality of the measured signals. On the other hand, the online approach has certain limitations with regards of the machine excitation, torque measurement availability and measured signal quality. These limitations will be analyzed closely in chapter 6. As for the optimization procedure itself, it is still valid for both options. The equations and the parameters to be constrained remain the same, the

### 3 Flux-Linkage Model Parameter Identification

difference relies on the QP solver to be used and the constraints values. This section will focus only on the offline parameter identification using experimental data as proposed by the author of this project in [1]. Furthermore, the formulation of the optimization problem will serve as the foundation for the online estimation scheme presented in chapter 6.

In addition to dq-axes voltages, the electromagnetic torque is going to be used as additional source of information, as it implies no extra effort to obtain and process the readings or measurement of a torque sensor on the bench. The dq-axes voltages (2.9) and electromagnetic torque (2.13) are used to describe the machine. As a consequence, the polynomial terms of (2.28) and (2.30) are involved in all three equations. Therefore, the objective function will be the combination of all three equations in the following form for a polynomial degree  $n$  and a set of  $N$  data points:

$$f_n(x) = \sum_{k=1}^N \left[ (u_{dk} - \hat{u}_{dk})^2 + (u_{qk} - \hat{u}_{qk})^2 + (T_{ek} - \hat{T}_{ek})^2 \right] \quad (3.54)$$

with,  $\hat{u}_d = \nabla u_d x^T$ ;  $\hat{u}_q = \nabla u_q x^T$  and  $\hat{T}_e = \nabla T_e x^T$

where  $x$  represents the vector of unknown parameters and the letters with hat notation correspond to estimated signal values and without hat notation measured data. The voltage and torque expressions are formulated for a polynomial degree  $n$  in terms of flux-linkages, average winding resistance  $R_s$  and rotor electrical speed  $\omega_r$  as:

$$u_d(i_d, i_q) \Big|_n = R_s i_d - \omega_r \psi_q(i_d, i_q) + \dot{\psi}_d(i_d, i_q) \quad (3.55)$$

$$u_q(i_d, i_q) \Big|_n = R_s i_q + \omega_r \psi_d(i_d, i_q) + \dot{\psi}_q(i_d, i_q) \quad (3.56)$$

$$T_e(i_d, i_q) \Big|_n = \frac{3}{2} p (\psi_d(i_d, i_q) i_q - \psi_q(i_d, i_q) i_d) \quad (3.57)$$

The optimization problem can then be defined in the following form:

$$\begin{aligned} \text{Minimize} \quad & Q(x) = \frac{1}{2} x^T G x + g^T x \\ \text{with,} \quad & \psi_{m_{min}} < \psi_m < \psi_{m_{max}} \\ & L_{d_{min}} < l_{dq10} < L_{d_{max}} \\ & L_{q_{min}} < l_{qd10} < L_{q_{max}} \\ & R_{s_{min}} < R_s < R_{s_{max}} \\ \text{where,} \quad & G = \nabla u_d \nabla u_d^T + \nabla u_q \nabla u_q^T + \nabla T_e \nabla T_e^T \\ & g = -2u_d \nabla u_d - 2u_q \nabla u_q - 2T_e \nabla T_e \end{aligned} \quad (3.58)$$

where the limits for the inequality constraints are obtained from the FEA simulation results obtained in the previous chapter.

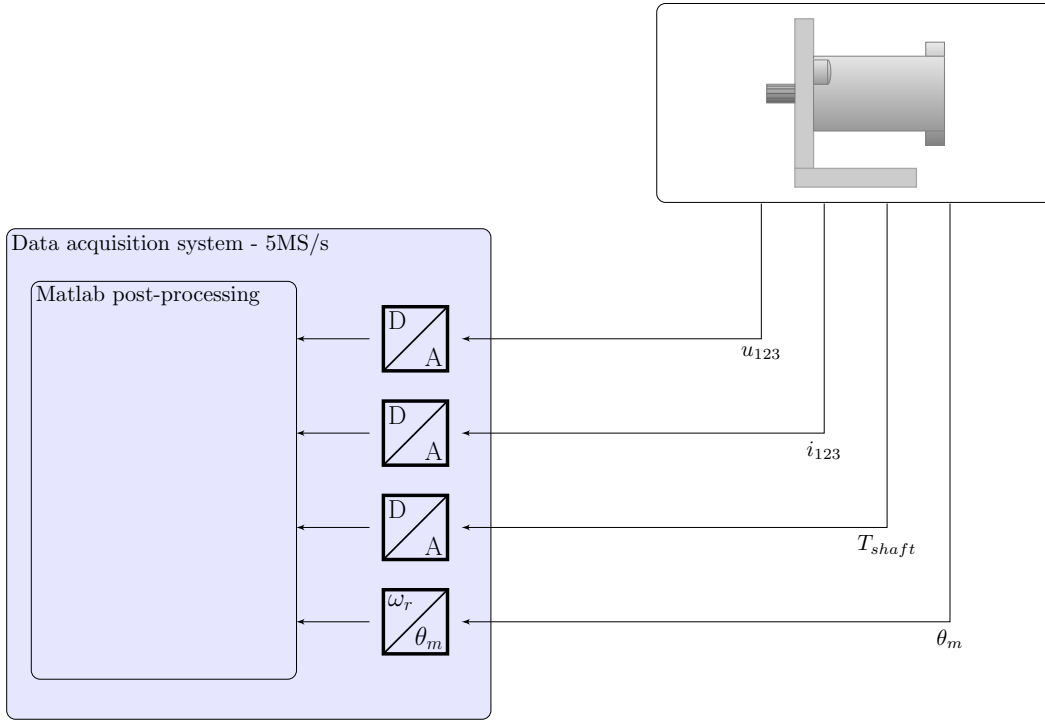


**Figure 3.26:** Testrig setup.

The experimental identification procedure is based on the method proposed by the author of this work in [1]. As illustrated in Fig. 3.26, the machine terminal voltage signals  $u_{123}$ , phase currents  $i_{123}$ , the shaft torque  $T_{shaft}$  and the mechanical rotor position  $\theta_m$  are sampled at the same time to perform the parameter identification. With the rotor position information, rotor speed and the dq-axes voltage and current signals can be obtained. In order to capture the inverter nonlinear effects, all the signals are sampled at a rate of  $5\text{ MS/s}$  considering the Pulse-width modulation (PWM) switching frequency of  $20\text{ kHz}$ . In addition to this, the inverter's dead time of  $800\text{ ns}$  can be captured with the resulting sampling time of  $200\text{ ns}$ . To fully cover one quadrant of operation, the machine speed is held constant to a value below base speed. In that way, the phase current can be set for any combination of  $i_d$  and  $i_q$ . A series of current ramps at constant phase advance angles are set as shown in Fig. 3.27. As the winding resistance and the permanent flux-linkage are temperature dependent. The current excitation is applied for a short period compared to the thermal time constants of the machine. The selected ramp duration was  $3.2\text{ s}$ , which for the machines in question lead to winding temperature rises of less than  $1^\circ\text{K}$ . The measurements were carried out at a room temperature of  $22^\circ\text{C}$ .

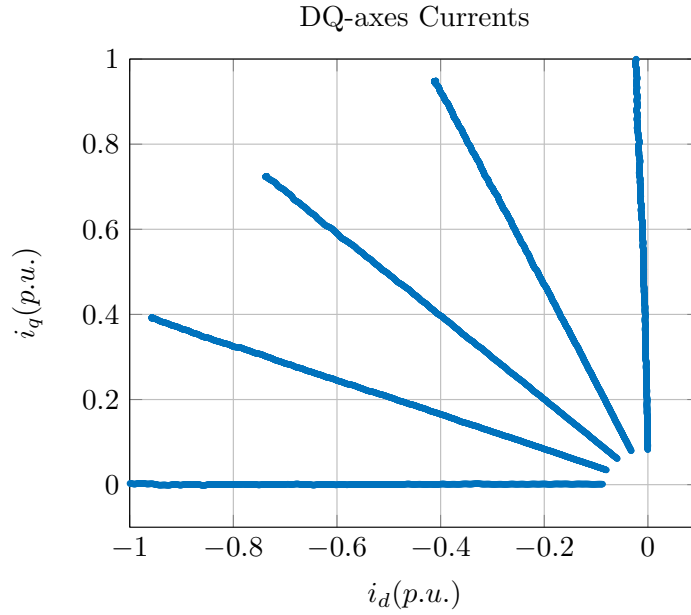


**Figure 3.27:** Test current ramps

As a post-processing step, the terminal voltages and phase currents are transformed into the rotor reference frame applying the Park transformation. The dq-axes quantities are afterwards low-pass filtered, avoiding in that way unwanted signal phase shifting. The signals are filtered to extract the dc-component of the dq-axes signals, which contains the information of the fundamental frequency of the signals. Therefore, the harmonic components due to slotting and inverter switching can be attenuated. As a final step, the filtered signals  $u_d$ ,  $u_q$ ,  $i_d$ ,  $i_q$ ,  $T_e$  and  $\omega_r$  are used to form the matrix  $G$  and the vector  $g$  in (3.58) to solve the optimization problem.

To demonstrate the validity of the proposed method, the three machines listed in table 3.4 were considered: an IPMSM, a Surface Mounted Permanent Magnet Synchronous Machine (SMPMSM) and an Outer Rotor Permanent Magnet Synchronous Machine (ORPMSM).

**Table 3.4:** Machine to be identified

	<i>IPMSM</i>	<i>SMPMSM</i>	<i>ORPMSM</i>
<i>Nominal Torque</i>	4.6 Nm	4.9 Nm	2.5 Nm
<i>Peak output power</i>	600 W	400 W	250 W
<i>Number of pole pairs</i>	4	7	7
<i>Nominal voltage</i>	12 V	12 V	48 V

### 3.5 Offline Identification: Experimental Data

The three machines of table 3.4 present also different characteristics such as large saliency (IPMSM and ORPMSM), high magnetic saturation (ORPMSM) and small saliency (SMPMSM). In the case of the SMPMSM, the saliency should be then reflected in the coefficients. As it is expected that the linear dq-axes inductances are close to each other, then the coefficients  $l_{dq_{10}}$  and  $l_{qd_{10}}$  should be quite similar. The selected measurement speed for the IPMSM and SMPMSM was 900 *rpm* and for the ORPMSM the speed was 800 *rpm*.

To assess the effectiveness of the proposed flux-linkage expressions, the degree of agreement of the estimated voltage and torque signals will be verified with the CoD as it was done with the FEA simulation data. In addition to this, four key machine parameters will be compared against the identified ones: the dc average winding resistance  $R_s$ , the permanent magnet flux-linkage  $\psi_m$  and the linear dq-axes inductances. Where  $R_s$  is measured directly with a 4-terminal sensing measurement and the permanent magnet flux-linkage  $\psi_m$  is derived from the induced bmf voltage. The linear inductances are obtained from a line-to-line impedance measurement at low current amplitude (0.04 *p.u.* peak). The imaginary part of the impedance corresponds to the inductance and over one electrical revolution the maximum and minimum values represent the q-axis and d-axis inductances respectively. As the measurement speed of the IPMSM and SMPMSM is 900 *rpm*, the corresponding bmf voltage was measured at that speed and the inductances at a electrical frequency of 60 Hz for the 4-pole pair IPMSM and at 105 Hz for the 7-pole pair SMPMSM. Similarly, the bmf voltage of the ORPMSM was measured at 800 *rpm* and the inductances at 93 Hz.

The identified machine parameters are listed in tables 3.5, 3.6 and 3.7 for a polynomial degree  $n = 3$ . The identified parameters of the IPMSM and the SMPMSM exhibit a maximum deviation of 1.26% with respect to the measured parameters, whereas the ORPMSM shows a maximum deviation at the linear d-axis inductance ( $l_{dq_{10}}$ ) of 2.96%. The closeness of identified parameters to measured ones confirms the correlation of the polynomial approach with the machine magnetic characteristics.

**Table 3.5:** IPMSM Linear Parameters

<i>4-pole pair IPMSM</i>		<i>Measured</i>	<i>Identified</i>	<i>dev.</i>
<i>Winding resistance</i>	$R_s$	12.58m $\Omega$	12.45m $\Omega$	-1.26%
<i>Permanent flux linkage</i>	$\psi_m$	6.415mV.s	6.411mV.s	-0.07%
<i>D-axis inductance</i>	$l_{dq_{10}}$	56.52 $\mu$ H	56.30 $\mu$ H	-0.39%
<i>Q-axis inductance</i>	$l_{qd_{10}}$	70.31 $\mu$ H	70.73 $\mu$ H	0.61%

### 3 Flux-Linkage Model Parameter Identification

**Table 3.6:** SMPMSM Linear Parameters

<i>7-pole pair SMPMSM</i>		<i>Measured</i>	<i>Identified</i>	<i>dev.</i>
<i>Winding resistance</i>	$R_s$	9.92m $\Omega$	9.8m $\Omega$	-1.15%
<i>Permanent flux linkage</i>	$\psi_m$	4.15mV.s	4.14mV.s	-0.12%
<i>D-axis inductance</i>	$l_{dq_{10}}$	77.01 $\mu$ H	76.23 $\mu$ H	-1.01%
<i>Q-axis inductance</i>	$l_{qd_{10}}$	77.82 $\mu$ H	78.32 $\mu$ H	0.64%

**Table 3.7:** ORPMSM Linear Parameters

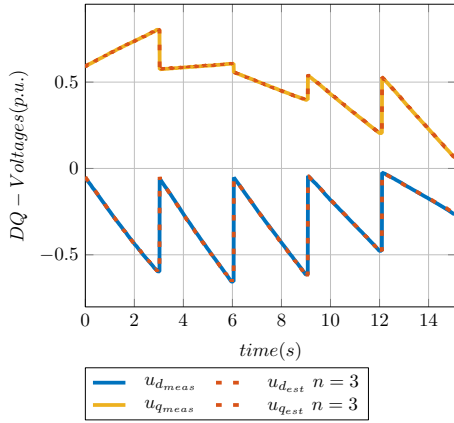
<i>7-pole pair ORPMSM</i>		<i>Measured</i>	<i>Identified</i>	<i>dev.</i>
<i>Winding resistance</i>	$R_s$	63.42m $\Omega$	62.76m $\Omega$	-1.05%
<i>Permanent flux linkage</i>	$\psi_m$	8.11mV.s	8.16mV.s	0.64%
<i>D-axis inductance</i>	$l_{dq_{10}}$	104.4 $\mu$ H	107.49 $\mu$ H	2.96%
<i>Q-axis inductance</i>	$l_{qd_{10}}$	146.36 $\mu$ H	146.81 $\mu$ H	0.31%

The identified cross-saturation parameters listed in table 3.8 offer a deeper look into the machine's characteristics, as most of the coefficients of the ORPMSM are one two order of magnitude larger than the ones of the IPMSM and the SMPMSM. This means that in the region where the machines were identified the ORPMSM exhibits larger magnetic saturation and cross-coupling effects.

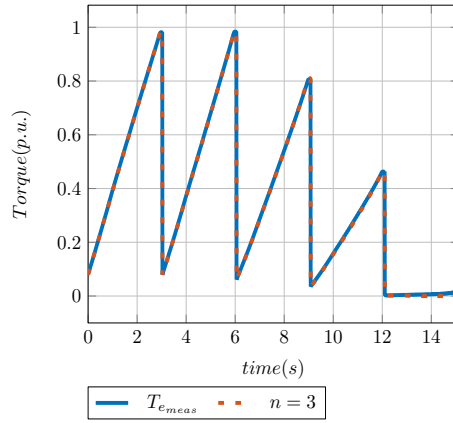
**Table 3.8:** identified cross-saturation parameters

	<i>IPMSM</i>	<i>SMPMSM</i>	<i>ORPMSM</i>
$l_{dq_{20}}$	-28.06nH/A	-83.38nH/A	-3.07 $\mu$ H/A
$l_{dq_{30}}$	-0.05fH/A <sup>2</sup>	-0.47nH/A <sup>2</sup>	-19.26nH/A <sup>2</sup>
$c_{dq_{01}}$	-30.37nH/A	-35.04nH/A	-1.06 $\mu$ H/A
$c_{dq_{11}}$	-0.74nH/A <sup>2</sup>	-0.54nH/A <sup>2</sup>	-32.94nH/A <sup>2</sup>
$l_{qd_{30}}$	-0.15nH/A <sup>2</sup>	-0.26nH/A <sup>2</sup>	-0.24nH/A <sup>2</sup>

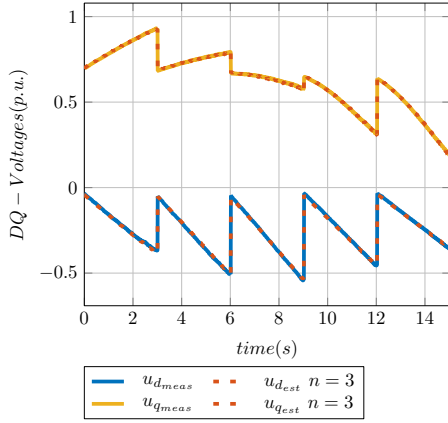
Fig. 3.28a and 3.28b show the estimated voltages and torque signals against the measured values for the different current ramps of Fig. 3.27 for the IPMSM, which shows a rather linear behavior. Conversely, the dq-axes voltages of the ORPMSM exhibit a nonlinear trajectory as shown in Fig. 3.28c.



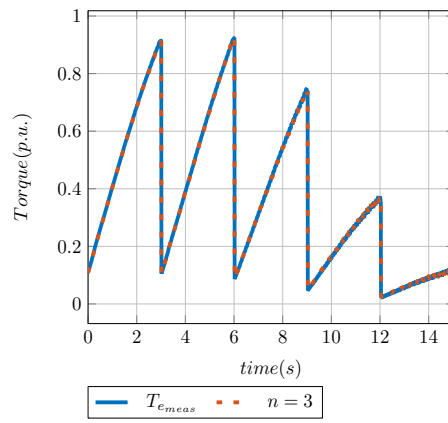
(a) DQ-Voltages of the IPMSM.



(b) Torque of the IPMSM.



(c) DQ-Voltages of the ORPMSM.



(d) Torque of the ORPMSM.

**Figure 3.28:** Estimated signals.

The electromagnetic torque was obtained by subtracting the shaft torque obtained at the same rotor speed to eliminate the influence of the mechanical and iron losses on the identification. With regards of the iron losses this is just an approximation as only the open circuit losses were subtracted and the losses originated in the different operating points might differ, however the measurement speed lays below base speed making iron losses to be small and the loss variations for the various operating points small as well. The curves in Fig. 3.28 depict the target signals used in the optimization's objective function and approximated voltage and torque expressions for  $n = 3$ . Another key aspect to assess the accuracy of the flux-linkage expressions, is the torque constant.  $k_t$  is obtained from the measured torque signal at zero advance current angle  $\gamma = 0^\circ$ .

### 3 Flux-Linkage Model Parameter Identification

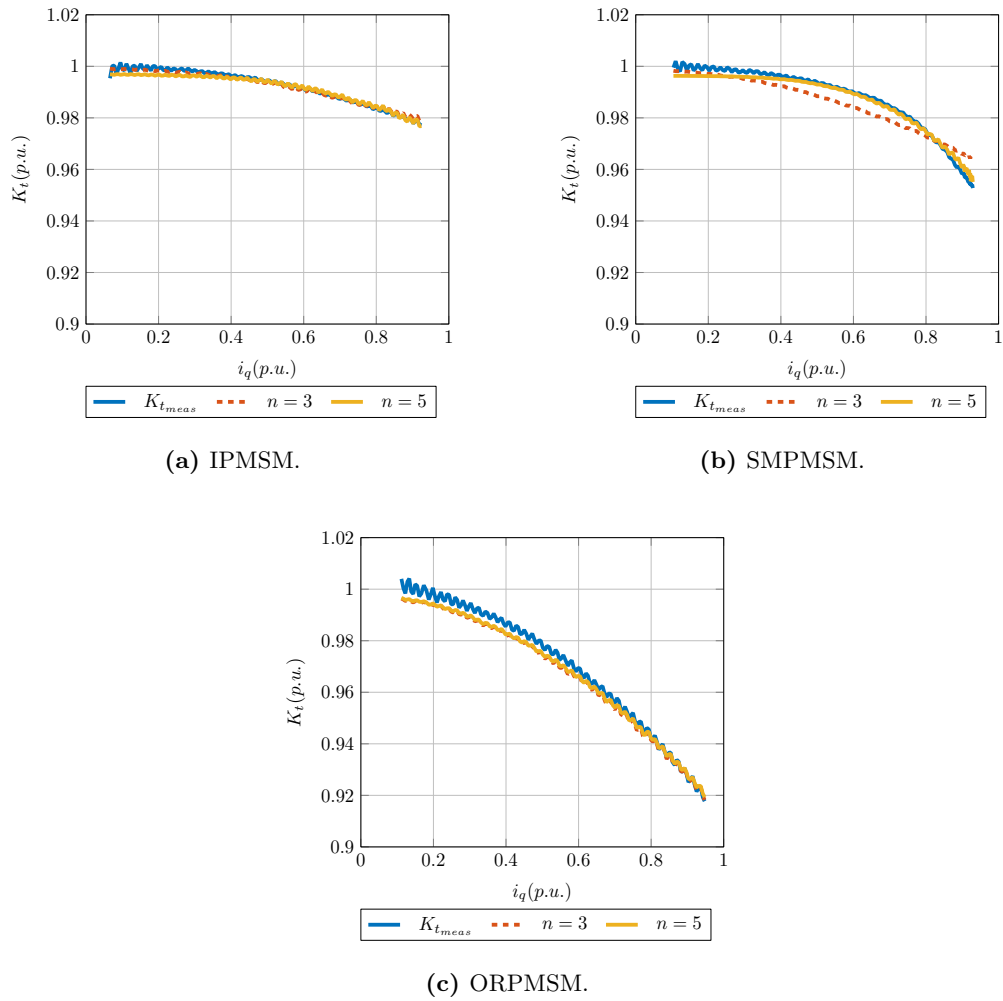


**Figure 3.29:** Torque constant.

The blue line in Fig. 3.29a represents the measured  $K_t$ , where it is worth to note that the machine is not quite saturated showing only about 2% reduction at the maximum measured current. The machine exhibits in this case a non-linear behavior that can be described with  $n = 3$ . On the other hand as shown in Fig.3.29b, the higher saturation of roughly 5% can be accurately described with  $n = 5$ . The form of non-linear relationship of  $K_t$  with respect  $i_q$  is better captured with that polynomial degree. This is actually the key aspect, the form of the non-linear behavior determines the proper polynomial degree. The outer rotor PMSM is a good example of high saturation, 8%, and low polynomial order. For this machine  $n = 3$  is more than sufficient to capture both maximum saturation and curve trend.

**Table 3.9:** CoD

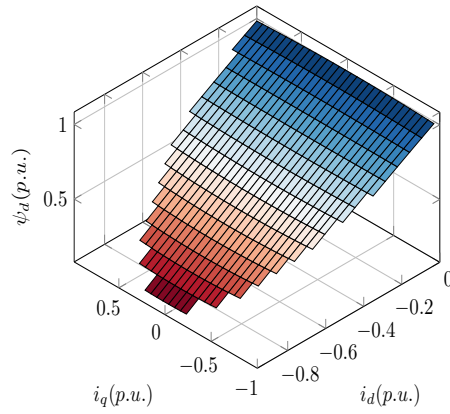
	$n = 3$	$n = 5$
<i>IPMSM</i>	0.9999519	0.9999626
<i>SMPMSM</i>	0.9999321	0.9999648
<i>PMSM</i>	0.9999417	0.9999459

In addition to the aspects analyzed so far, the CoD values in table 3.9 provide also an indication of the agreement of the different polynomial degrees. According to the CoD values of the *IPMSM*, the values achieved with  $n = 3$  and  $n = 5$  are very close. Consequently the overall agreement of the approximation with both polynomial should be similar. This is then reflected in the closeness of the  $K_t$  curves shown in Fig. 3.29a for both polynomial degrees. Similarly, the CoD values obtained for the outer rotor *PMSM* are also pretty close, leading to nearly identical  $K_t$  curves in Fig. 3.29c. On the other hand, the CoD values of *SMPMSM* exhibit the largest deviation with  $CoD_3 = 0.9999321$  and  $CoD_5 = 0.9999648$ , which is reflected in Fig. 3.29b as well, where the curve with  $n = 5$  shows a significant better agreement than with  $n = 3$ .

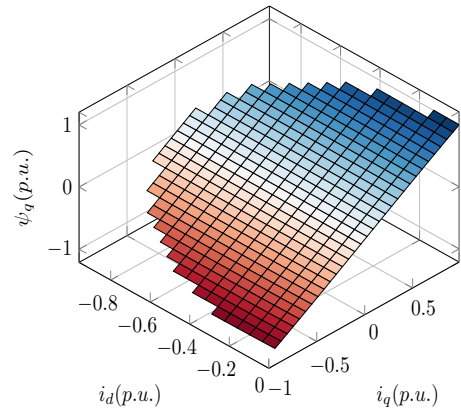
The correlation of the CoD value with the approximated curves is actually expected as the CoD provides a measure through the optimization residuals, nevertheless it is important to make a link between the absolute value of the CoD and the agreement obtained with the model at key characteristics such as  $K_t$ ,  $R_s$ ,  $\psi_m$  and the linear or small signal inductances. With that link in mind the selection of the optimal polynomial degree can be done considering the aspects addressed so far.

After evaluating the agreement achieved with the polynomials, the resulting flux-linkage expressions can be then used to evaluate the machine. The main objective of the identification procedure is to obtain the dq-axes flux-linkages. One key aspect to remember, is the fact that the flux-linkages are present in the dq-axes voltages as shown in (3.55) and (3.56). This means that if  $R_s$  is correctly identified, what is then left, are just the flux-linkages. The good agreement of the  $R_s$  identification could be then proved in tables 3.5, 3.6 and 3.7. In addition to this, the agreement with the measured linear parameters, inductances and  $\psi_m$ , and the ability to capture the nonlinear behavior of  $K_t$ , are very good indicators for a high degree of confidence on the resulting flux-linkages.

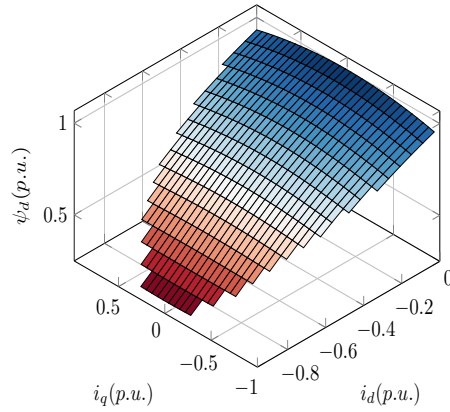
### 3 Flux-Linkage Model Parameter Identification



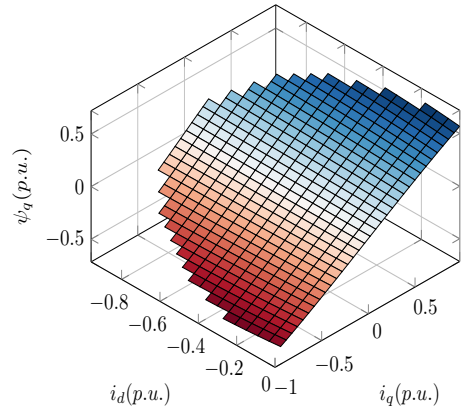
(a) D-axis flux-linkage - IPMSM.



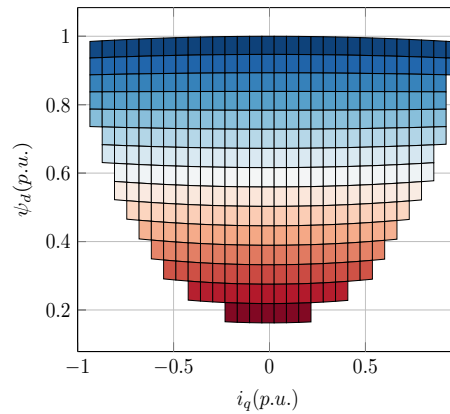
(b) Q-axis flux-linkage - IPMSM.



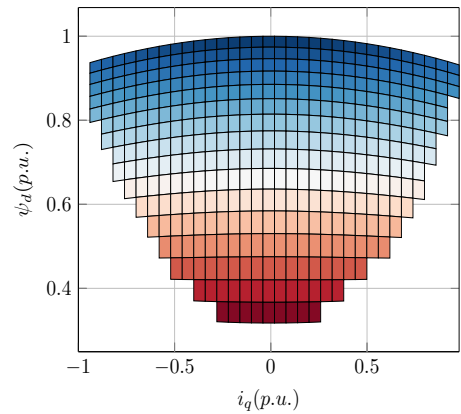
(c) D-axis flux-linkage - outer rotor PMSM.



(d) Q-axis flux-linkage - outer rotor PMSM.



(e) IPMSM: saturation effect on  $\psi_d$  due to  $i_q$ .



(f) Outer rotor PMSM: saturation effect on  $\psi_d$  due to  $i_q$ .

**Figure 3.30:** Identified flux-linkage surfaces.

### 3.5 Offline Identification: Experimental Data

Two representative examples of flux-linkages are shown in Figs. 3.30: the *IPMSM*, a machine that exhibits low torque constant saturation and the outer rotor *PMSM* has more pronounced saturation with respect to  $i_q$ . This saturation aspect is then observable in the d-axis flux-linkage surfaces plotted in Fig. 3.30e and 3.30f, where the decrease of the flux-linkage by increasing  $i_q$  is evident in Fig. 3.30f, the flux-linkage of the outer rotor *PMSM*.

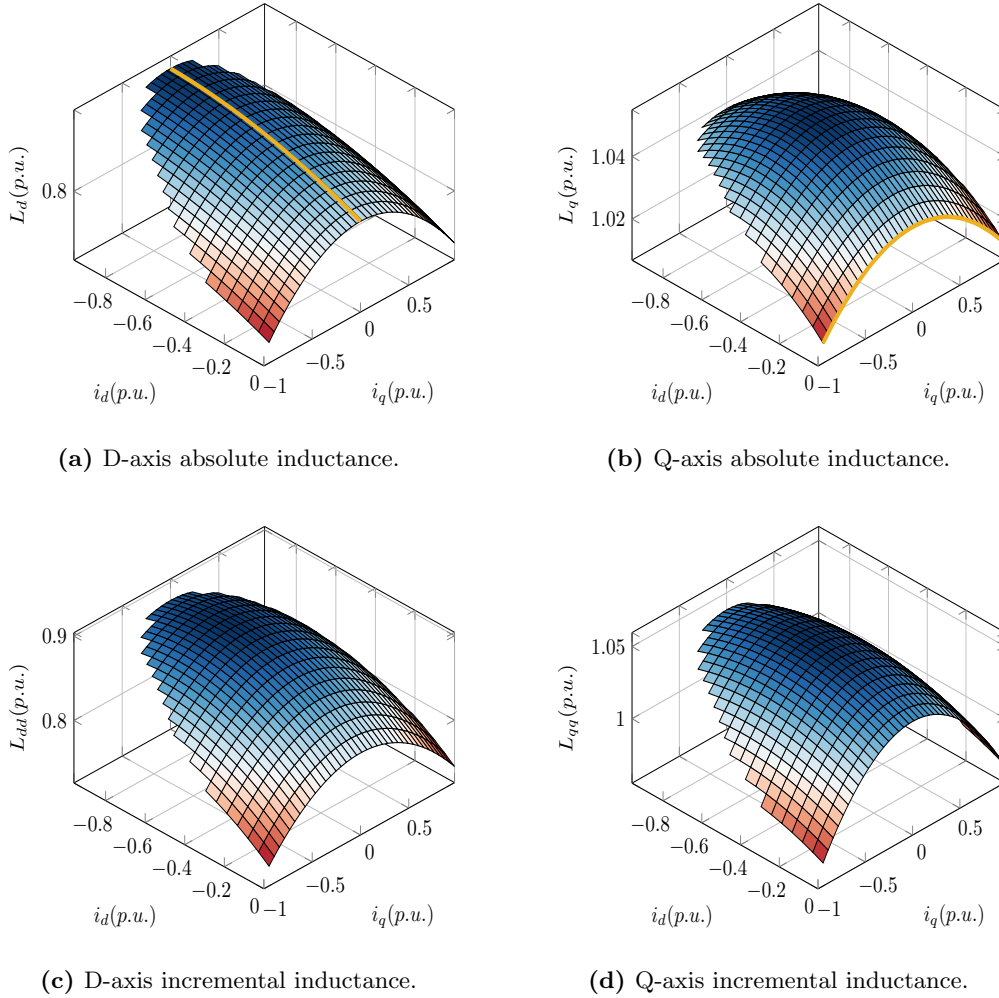


**Figure 3.31:** 4-pole pair IPMSM Inductances.

Additionally, the inductances are an immediate byproduct of the flux-linkages expression, as they can be derived analytically from the flux-linkage expressions according to (2.41), (2.43), (2.45) and (2.45). Fig. 3.31 shows the absolute and incremental inductances of the *IPMSM*. Contrary to  $K_t$ , the inductances of this machine exhibit certain

### 3 Flux-Linkage Model Parameter Identification

saturation or current dependency. The cross-coupling of  $L_d$  is specially interesting, as the d-axis current dependency is much lower than the q-axis current. This makes the cross-coupling effect relevant and at the same time it should not be neglected, which denotes the relevance of the consideration of the nonlinear effects in such a machine.

Despite the larger  $\psi_d$  saturation of the outer rotor PMSM, the d-axis inductance surface has a small cross-coupling with respect  $i_q$  as shown in Fig. 3.32a and 3.32c. This differs from the more coupled behavior exhibited by the d-axis inductance of the IPMSM in Fig. 3.31a. However  $L_d$  presents higher  $i_d$  dependency that in the case of the IPMSM. Conversely the q-axis inductances in both machines show a similar trend with respect to self and mutual coupling.

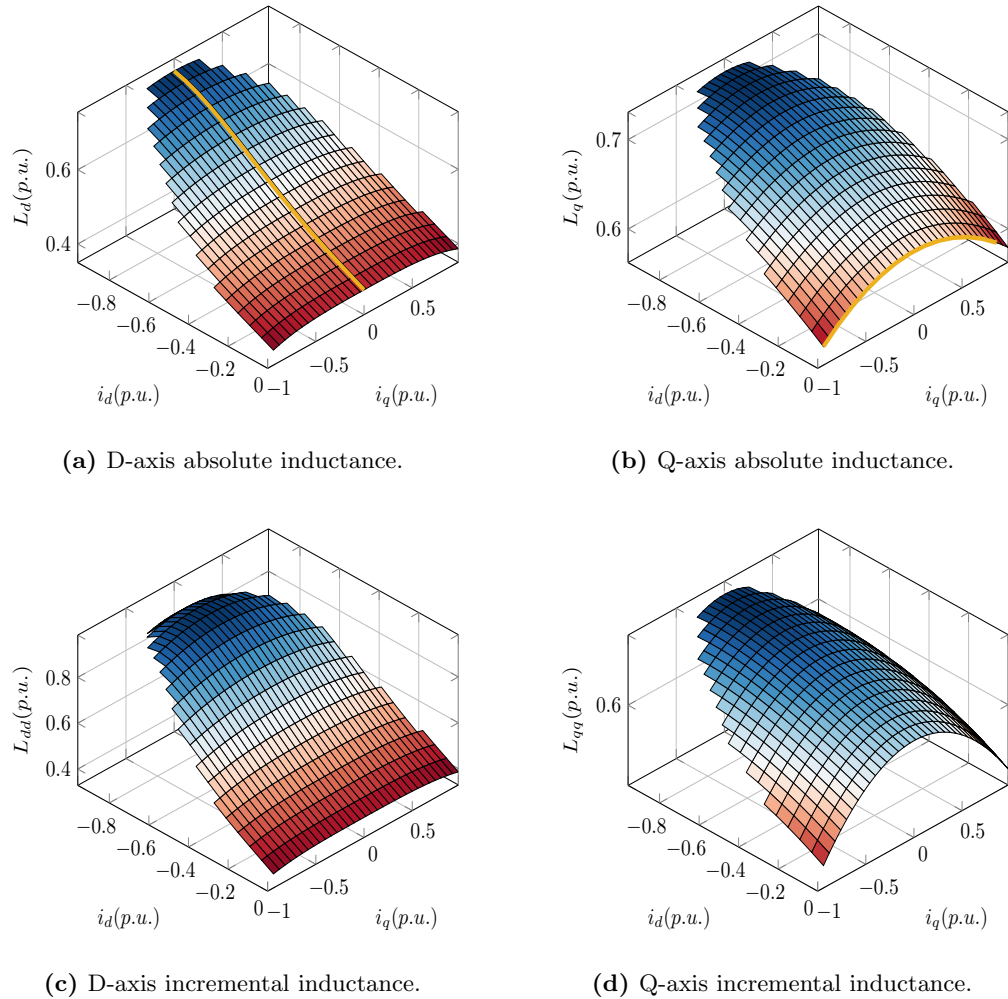


**Figure 3.32:** 7-pole pair outer rotor PMSM Inductances.

This section dealt with the experimental determination of the dq-axes flux-linkage of various machines, where a simple hardware setup was presented to capture voltage, current, torque and rotor position signals. The coefficients of the dq-voltages and torque expressions based on the flux-linkage polynomials (2.38) and (2.39) were determined by performing a minimization of the sum of least-squares with constrained optimization. In addition to this, it was shown that coefficients of the proposed expressions relate with good accuracy to key machine parameters such as  $\psi_m$  and the small signal dq-axes inductances. Moreover the nonlinear characteristic of the torque constant could be represented with good agreement depending on the polynomial degree used. Furthermore, the use of the CoD gave more insight into the agreement with the different polynomial degrees.

#### 3.5.2 Magnet Temperature Variation

This section considers the identification of the flux-linkage coefficients for different magnet temperatures. In a real application the machine is designed to operate under certain environmental and working conditions. The machine could be operated at ambient temperatures several degree Celsius above room temperature ( $21^\circ C$ ) or it could work under high load for long periods of time which can lead to an overall increment of the machine temperature components, including magnets and windings coils. For an online identification of  $\psi_m$  and the average winding resistance  $R_s$ , the involvement of the flux-linkage in the voltage equations, (3.55) and (3.56), means that any variation on  $\psi_m$  affects both d- and q- axis voltages. A characterization for different magnet temperatures or permanent flux-linkage values can help to assess the impact of such variation on the online estimation of the parameters of question.

In section 3.5.1 the main focus laid on the identification of the coefficients at room temperature. The magnet temperature was held constant by running fast current ramps. This means that  $\psi_m$  remained constant and the obtained flux-linkage coefficients were valid for that flux-linkage value. Recalling section 3.3.4, the dependency of the flux-linkages on  $\psi_m$  can be described according to (2.61) and (2.62). A similar approach as with the FEA data is then taken, where three  $\psi_m$  values are chosen to find the coefficients of the flux-linkage expressions. These are  $22^\circ C$ ,  $54^\circ C$  and  $82^\circ C$ . They correspond in *p.u.* to values of  $\psi_m = [1 \quad 0.97 \quad 0.94]$ .

The test setup remained similar to the one presented in the previous section. However, the only modification was the introduction of a box to isolate the machine from the ambient in order to avoid external temperature disturbances. By demanding high currents, the machine magnets can be heated up to the desired temperature. The magnet temperature was obtained indirectly by measuring the bmf voltage and with the help of the magnet's temperature coefficient. A 4-pole pair IPMSM was used for the identification which was provided with thermocouples in the windings in order to control the winding temperature for each current ramp for the identification.

### 3 Flux-Linkage Model Parameter Identification

The identification procedure of the previous section, 3.5.1, was applied to the measured data at each temperature. As the final output of this procedure are the flux-linkages, they can be used directly to obtain the coefficients of the expressions that consider the dependency of  $\psi_m$ . The three sets of dq-axes flux-linkage data are summarized in (3.59), where  $n = 5$  was selected to capture the nonlinear effects in a compromise of accuracy and numerical efficiency, as the analysis done so far on this machine, whether FEA or experimental, have shown that  $n = 5$  deliver satisfactory results.

$$\begin{array}{l}
 \psi_{d_5}(i_d, i_q) \Big|_{\psi_m=1 \text{ p.u.}} \quad \psi_{q_5}(i_d, i_q) \Big|_{\psi_m=1 \text{ p.u.}} \\
 \psi_{d_5}(i_d, i_q) \Big|_{\psi_m=0.97 \text{ p.u.}} \quad \psi_{q_5}(i_d, i_q) \Big|_{\psi_m=0.97 \text{ p.u.}} \\
 \psi_{d_5}(i_d, i_q) \Big|_{\psi_m=0.94 \text{ p.u.}} \quad \psi_{q_5}(i_d, i_q) \Big|_{\psi_m=0.94 \text{ p.u.}}
 \end{array} \quad (3.59)$$

The sets of dq-axes flux-linkages in (3.59) are shown in Fig. 3.33. As a visual aid, only the flux-linkage curves corresponding to a few current ramps are plotted in order to show the effect that the magnet temperature or the variation of  $\psi_m$  has on the origin of each set of dq flux-linkages, as it moves along with the change of  $\psi_m$ .

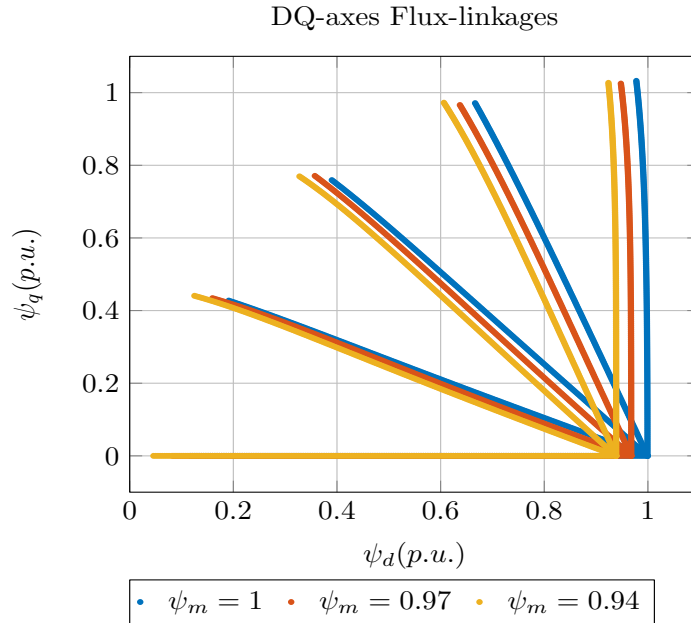


**Figure 3.33:** DQ-axes flux-linkages

As shown in section 3.3.4, the coefficients of the expressions for  $\psi_d(i_d, i_q, \psi_m)$  and  $\psi_q(i_d, i_q, \psi_m)$  can be obtained with the following quadratic programming problem :

$$\begin{aligned}
 f_n(x) = & \\
 & \sum_{k=1}^N \left[ (\psi_d(i_{d_k}, i_{q_k}, \psi_{m_k}) - \widehat{\psi}_d(i_{d_k}, i_{q_k}, \psi_{m_k}))^2 + (\psi_q(i_{d_k}, i_{q_k}, \psi_{m_k}) - \widehat{\psi}_q(i_{d_k}, i_{q_k}, \psi_{m_k}))^2 \right] \\
 & \text{with,} \quad \widehat{\psi}_d = \nabla \psi_d x^T; \quad \text{and} \quad \widehat{\psi}_q = \nabla \psi_q x^T
 \end{aligned} \tag{3.60}$$

Where  $x$  is the set of unknown coefficients,  $N$  is the number of the data points,  $n$  is the polynomial degree and  $\psi_{m_k}$  represent the three values of  $\psi_m$  indicated in (3.59). The letters with a hat notation represent estimated values and the letters with no hat notation are the values of the identified flux-linkage data. The constrained optimization problem can be then formulated in the following form:

$$\begin{aligned}
 \text{Minimize} \quad Q(x) &= \frac{1}{2} x^T G x + g^T x \\
 \text{with,} \quad l_{dq100} &> 0 \quad \text{and} \quad l_{qd100} > 0 \\
 \text{where,} \quad G &= \nabla \psi_d \nabla \psi_d^T + \nabla \psi_q \nabla \psi_q^T \\
 g &= -2\psi_d \nabla \psi_d - 2\psi_q \nabla \psi_q
 \end{aligned} \tag{3.61}$$

Due to the good agreement achieved with  $n = 5$  at constant magnet temperature in 3.3.4, the QP-problem (3.61) with objective function (3.60) is then solved for  $n = 5$  as well. The identified coefficients listed in table 3.10 show the impact of the magnetic saturation caused by  $\psi_m$  on the linear inductances represented by the coefficients  $l_{dq10x}$  and  $l_{qd10x}$ .

**Table 3.10:** IPMSM linear signal inductance coefficients

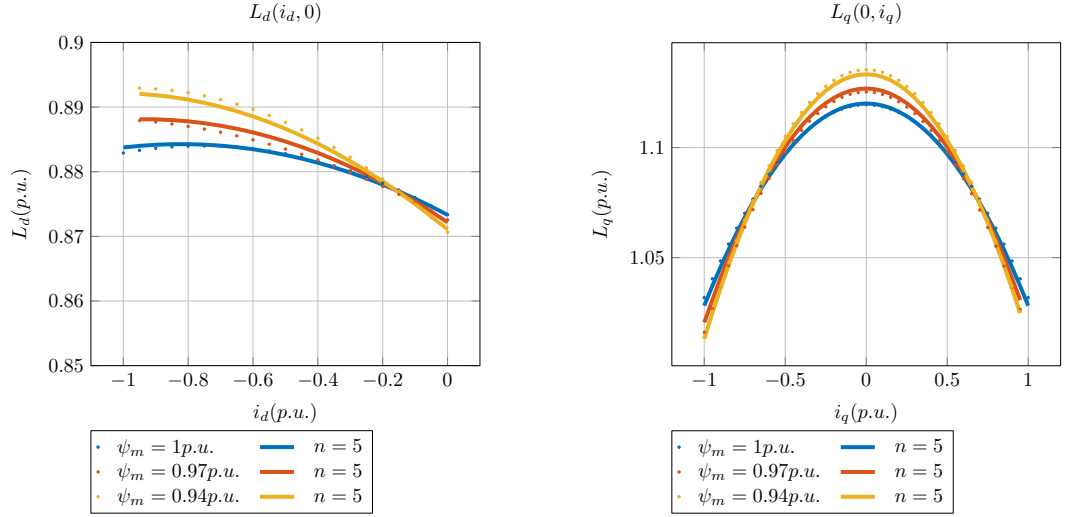
<i>extended coefficients</i>	
$l_{dq100}$	$61.75 \mu H$
$l_{dq102}$	$-0.0914 H/Wb^2$
$l_{dq104}$	$0.0022 H/Wb^4$
$l_{qd100}$	$85.03 \mu H$
$l_{qd102}$	$-0.2974 H/Wb^2$
$l_{qd104}$	$0.0033 H/Wb^4$

These coefficients can be traced back to  $l_{dq10}$  and  $l_{qd10}$  in the inductance expressions (2.41) and (2.43) that only consider the current effects at a certain  $\psi_m$ . As a result of the extension of the flux-linkage expressions, new coefficients appear to represent the effects of  $\psi_m$ . To illustrate this, the coefficients  $l_{dq10x}$  and  $l_{qd10x}$  are rearranged to form  $l_{dq10}$  and  $l_{qd10}$  with respect  $\psi_m$ :

$$\begin{aligned}
 l_{dq10}(\psi_m) &= l_{dq100} + l_{dq102} \cdot \psi_m^2 + l_{dq104} \cdot \psi_m^4 \\
 l_{qd10}(\psi_m) &= l_{qd100} + l_{qd102} \cdot \psi_m^2 + l_{qd104} \cdot \psi_m^4
 \end{aligned} \tag{3.62}$$

### 3 Flux-Linkage Model Parameter Identification

What (3.62) is expressing, is the fact that the coefficients of flux-linkage expressions identified at a constant  $\psi_m$  are a function of  $\psi_m$  itself. The plots in Fig. 3.34 show the agreement between the identified data at each magnet temperature and the flux-linkage model coefficients identified with all the data.



(a) Absolute d-axis inductance.

(b) Absolute q-axis inductance.

**Figure 3.34:** IPMSM - Inductances at different magnet temperatures

Finally Fig. 3.35 and 3.36 summarizes the sets of dq-axes flux-linkages used in the objective function (3.60) compared with the flux-linkages derived from the expressions with the identified coefficients.

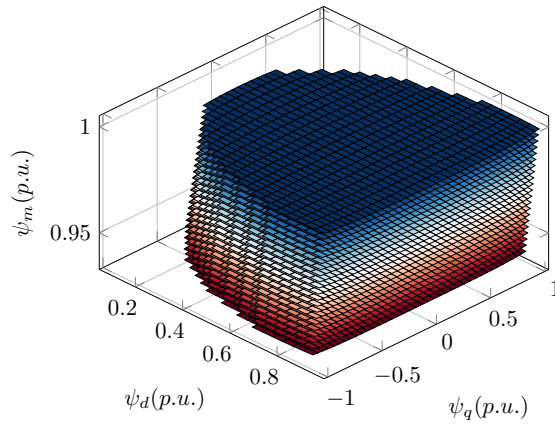
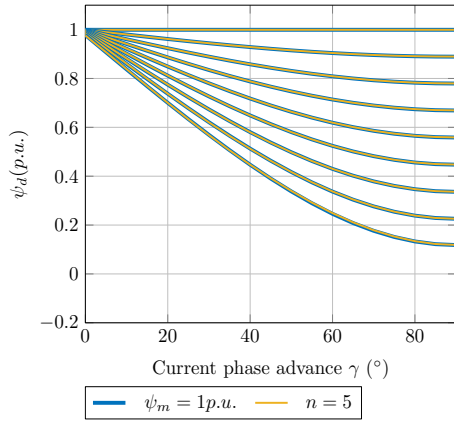
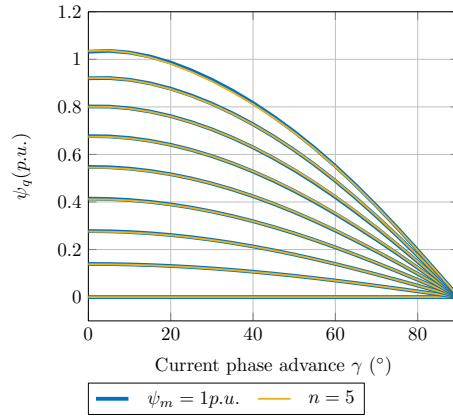


**Figure 3.35:** DQ-axes flux-linkages at different magnet temperatures.

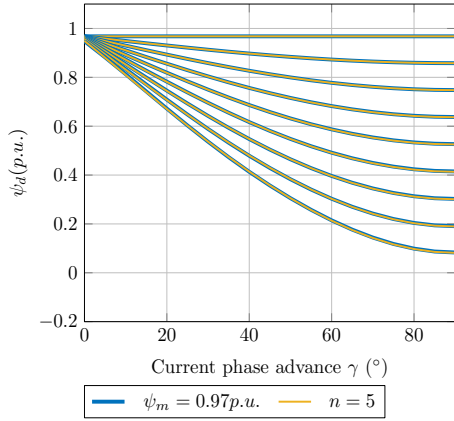
### 3.5 Offline Identification: Experimental Data



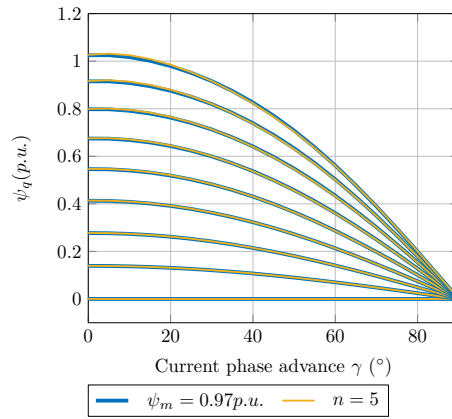
(a) D-axis flux-linkage at  $\psi_m = 1p.u..$



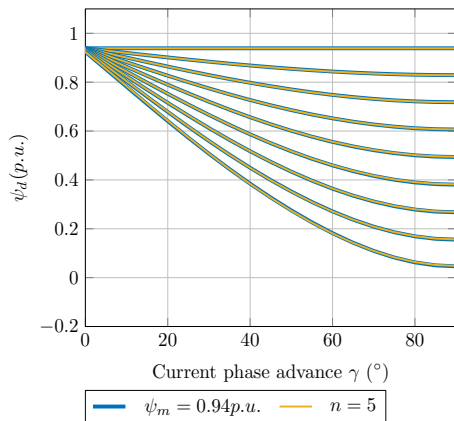
(b) Q-axis flux-linkage at  $\psi_m = 1p.u..$



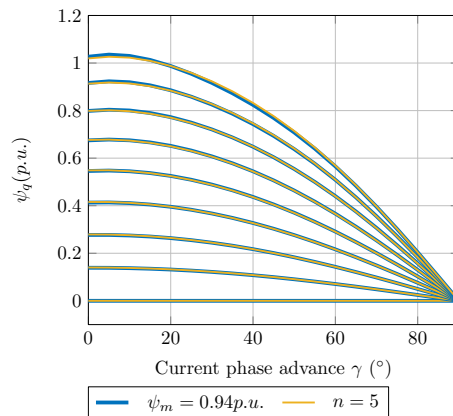
(c) D-axis flux-linkage at  $\psi_m = 0.97p.u..$



(d) Q-axis flux-linkage at  $\psi_m = 0.97p.u..$



(e) D-axis flux-linkage at  $\psi_m = 0.94p.u..$



(f) Q-axis flux-linkage at  $\psi_m = 0.94p.u..$

**Figure 3.36:** Flux-linkages at increasing current for different  $\psi_m$ .

### 3 Flux-Linkage Model Parameter Identification

This section showed how to characterize or describe the flux-linkages of a 4-pole pair IPMSM with respect to the permanent magnet flux-linkage or indirectly as a function of the magnet temperature. This is the next level of high fidelity modeling, where not only the nonlinear magnetic effects were captured but the dependency on permanent magnet flux-linkage variations were introduced. Finally, such model can be used to improve or complement a model used for an online parameter identification, specially the coefficients concerning the linear inductances  $l_{dq_{10x}}$  and  $l_{qd_{10x}}$  as they are the dominant coefficients driven by the dq-axes currents. The use of a polynomial degree 5 delivered a good agreement with the target flux-linkages for the different magnet temperatures enabling the consideration of the effects of magnet temperature on the dq-axes flux-linkages.

In addition to the theoretical treatment given to the machine model in chapter 2, a fast and simple measurement procedure was presented to identify the polynomials coefficients experimentally, where a model based approach was used to obtain the dq-axes flux-linkage and winding resistance without previous knowledge of the latter as typically proposed in the literature [4, 33]. At a constant speed, current ramps with a duration of 3.6s were proposed to characterize one quadrant of the machine. In a post-processing step the polynomials coefficients were determined showing a high degree of correspondence with key machine parameters such as the small signal dq-axes inductances, the open circuit bmf and DC-winding resistance.

## 4 Considering Electromagnetic Losses

Electromagnetic power loss plays a significant role in the operation of the machine, as losses can be regarded as heat sources that have a direct impact on temperature dependent parameters like the winding resistance or the permanent magnet flux-linkage. Those can be resistive loss in the windings or core loss in the stator and rotor. In general terms the iron losses are a function of flux-density and frequency [14], which depends on the core materials properties. This chapter will go through the relevant loss sources and its modeling in order to capture its effects for a thermal model of a PMSM and an extension of the dq-axes voltage equations to consider the iron losses. The latter serves as an extension of the flux-linkage expressions  $\psi_d(i_d, i_q)$  and  $\psi_q(i_d, i_q)$  to improve the machine model for the online identification.

### 4.1 Resistive Losses

One of the main heating sources in the PMSMs are the copper Joule losses. The associated resistance of each phase winding in the machine will generate the following losses:

$$P_{winding} = R_s \cdot I_{rms}^2 \quad (4.1)$$

where in (4.1),  $R_s$  represents the winding resistance of one machine phase and  $I_{phase_{rms}}$  root mean square (rms) value of the phase current. Assuming a balanced system, with symmetric phase resistances, the total resistive loss of a three phase PMSM can then be written in terms of the phase resistance and the current peak value in following form:

$$P_{resistive} = \frac{3}{2} R_s \cdot I_{peak}^2 \quad (4.2)$$

The formulation of the total resistive losses in terms of the peak current value is convenient, as the current vector length in the dq-frame,  $I_{peak} = \sqrt{i_d^2 + i_q^2}$ , corresponds to the phase current peak value. This leads to the formulation of the resistive loss expressed in dq-axes terms of (4.3).

$$P_{resistive} = \frac{3}{2} R_s (i_d^2 + i_q^2) \quad (4.3)$$

### 4.2 Iron Losses

After Joule losses the core loss contributes importantly to the machine losses. The core losses are the losses in the sheets in the stator and rotor of the machine. As these sheets are commonly made of electrical steel their losses in this work will be regarded as iron

losses. In classical theory the losses in ferromagnetic materials are composed of hysteresis and eddy-current losses, where the hysteresis loss is the result of the resistance of the material to change its magnetic state. On the other hand, Eddy current losses appear at the presence of space harmonics in the stator ampere-conductor distribution and winding current's time harmonics produced for example by the PWM operation [35, 14].

This section will deal with the modeling of the iron losses in order to establish an equivalent model to be used as a complement to the online parameter estimation algorithm, in that way the robustness of the estimation with respect to the rotor velocity can be improved.

#### 4.2.1 Iron Losses Model

The Hysteresis loss is defined as the loss per cycle of the enclosed B-H loop as expressed by Steinmetz [59]. The resultant power loss is proportional to the frequency and to the flux density raised to a power  $n$ , commonly referred to the Steinmetz constant. Depending on the material this exponent can be in the range 1.3 – 2.6. The Steinmetz equation is then formulated in the following form:

$$P_{hy} = C_{hy} B^\alpha f \quad (4.4)$$

Where  $C_{hy}$  is a coefficient,  $B$  is the flux density,  $f$  is the frequency and  $\alpha$  is the Steinmetz coefficient. Besides the hysteresis losses, the classical losses play an important role in the whole core losses. The induced currents generated by the emf in the stator produce losses proportional to the electrical resistivity of the material in question. These losses are the Eddy current losses which are proportional to the square of the flux density and to the square of the frequency as expressed in the following equation:

$$P_{eddy} = C_{eddy} (B \cdot f)^2 \quad (4.5)$$

Where  $C_{eddy}$  is a coefficient,  $B$  is the flux density and  $f$  is the frequency. The Iron-Losses play a significant role when the rotor speed is relatively high. On the other hand, hysteresis loss and Eddy-current loss are additional heat sources that contributes to thermal behavior of the machine. In addition to the consideration of the classical core losses and the hysteresis losses, there has been proposed another core losses structure. Bertotti [60] explains in a detailed way the physical meaning of the excess losses which are associated to the classical losses. He then proposes a power losses separation where exponents of the individual terms are fixed in the following manner:

$$P_{iron} = C_{hy} B^\alpha f + C_{exc} (B \cdot f)^{1.5} + C_{eddy} (B \cdot f)^2 \quad (4.6)$$

where  $C_{exc}$  is the excess loss coefficient according to [60].

The machine's shaft torque is the sum of the contributions of the electromagnetic torque, viscous and Coulomb friction in the following form:

$$T_{shaft} = T_e - k_c \cdot \text{sign}(\omega_m) - k_v \omega_m - T_{iron} \quad (4.7)$$

where  $k_c$  and  $k_v$  are the Coulomb and viscous friction coefficients respectively,  $T_e$  the electromagnetic torque and  $T_{iron}$  the torque generated by the core losses. The shaft torque expression can be used to write the shaft output power. The mechanical power  $P_m$ , as in Fig. 4.1, can be expressed in terms of torque  $T$  and angular velocity  $\omega_m$  as shown in (4.8).

$$P_m = T \cdot \omega_m \quad (4.8)$$

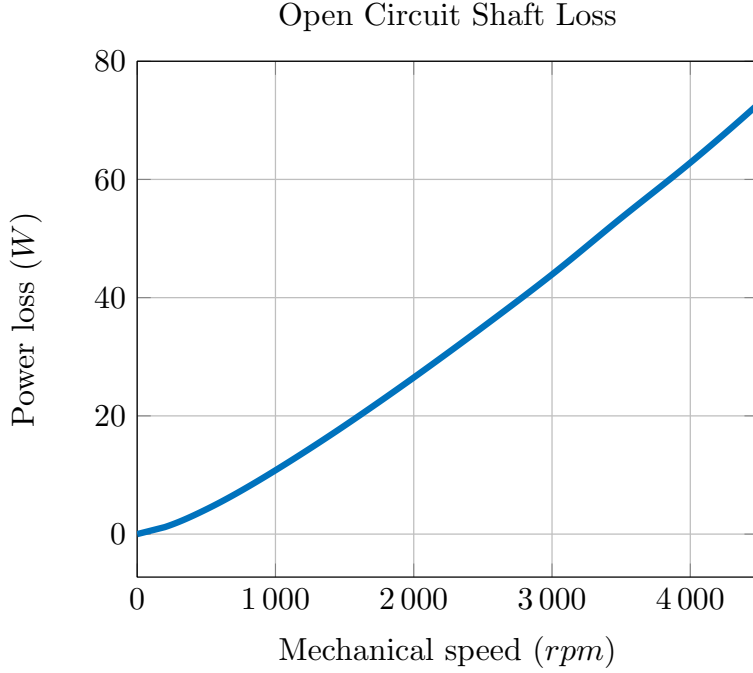


**Figure 4.1:** IPMSM open circuit shaft loss

At the same time  $f_e$ , the fundamental frequency acting in the magnetic circuit, can be used to express the angular velocity as:

$$\omega_m = \frac{2\pi \cdot f_e}{p} \quad (4.9)$$

where  $p$  is the number of pole pairs. Finally, the total output power can then be written according to (4.8), using (4.7) and replacing (4.9) in (4.6) as:

$$P_{shaft} = T_e \omega_m - \text{sign}(\omega_m) \cdot k_c \omega_m - k_v \omega_m^2 - k_{hy} \omega_m - k_{exc} \omega_m^{1.5} - k_{eddy} \omega_m^2 \quad (4.10)$$

The loss coefficients  $k_{hy}$ ,  $k_{exc}$  and  $k_{eddy}$  are the result of expressing the iron losses in terms of angular velocity instead of electrical frequency. In (4.10) the power loss due to coulomb friction  $\text{sign}(\omega_m) \cdot k_c \cdot \omega_m$  is proportional to  $\omega_m$  as the hysteresis loss term

#### 4 Considering Electromagnetic Losses

$k_{hy} \cdot \omega_m$ . Similarly, the viscous loss term and the eddy currents terms share the same speed dependency  $\omega_m^2$ , making a separation of those terms parting from the overall losses difficult.

Therefore, the experimental identification of these losses needs to be carried out in a way that the mechanical losses can be captured separately from the electromagnetic losses. This can be done, either with machines without magnets, so that the magnetic circuit isn't biased and therefore no iron losses are present or considering the electric power balance to identify only core losses.

In [61] and [17] it is proposed the modeling and characterization of the iron-losses, where the hysteresis losses and Eddy current losses are determined for open and short circuit conditions, which corresponds magnetically speaking to a magnetizing and demagnetizing path in the machine. The open circuit measurement should help to characterize the iron losses coming from the torque generating flux and the short circuit should capture the losses seen in the path where the d-axis flux acts. They are combined and scaled to the permanent magnet flux-linkage. The losses are determined for the losses structure of (4.6). This is a compelling approach as the open and the short circuit measurements are simple procedures, the challenging part is the separation of the mechanical losses e.g. bearing losses and the iron losses. By extracting the magnets is possible to capture only the mechanical losses and in that way a clean losses separation is possible. The open circuit loss  $P_{iron}^{OC}$  and the short circuit loss  $P_{iron}^{SC}$  are then formulated in a similar manner as in (4.6) but in terms of  $\psi$  which corresponds to a flux-density  $B$ . In addition to this, as reported by the authors in [62] and [63], it is a good approximation to assume  $\alpha = 2$  in the hysteresis loss term. The resulting loss expressions are then formulated as:

$$P_{iron}^{OC}(\psi_m) = a_{hy}f_e + a_{exc}f_e^{1.5} + a_{eddy}f_e^2 \quad (4.11)$$

$$P_{iron}^{SC}(\psi_{d_0}) = b_{hy}f_e + b_{exc}f_e^{1.5} + b_{eddy}f_e^2 \quad (4.12)$$

where  $f_e$  is the electric frequency,  $\psi_{d_0}$  is the flux-linkage produced by the d-axis current in the short-circuit case,  $\psi_m$  is the open circuit permanent magnet flux-linkage, the loss coefficients  $a$  and  $b$  are obtained from the short circuit and open circuit operating points, this means that they are derived from driving the machine at a constant magnetic flux density.

The iron losses at open circuit (4.11) are driven by the flux density generated by the magnets. In this case the flux-linkage remains constant and it is used as a reference value which is then scaled for the different load conditions for given dq-axes flux-linkage values with vector length  $\psi = \sqrt{\psi_d^2 + \psi_q^2}$ . Furthermore, the frequency  $f_e$  can be expressed in terms of the rotor velocity  $\omega_r$  in the following form:

$$P_{iron}^{OC}(\psi) = a_{hy} \cdot \frac{\omega_r}{2\pi} \cdot \left( \frac{\psi}{\psi_m} \right)^2 + a_{exc} \cdot \left( \frac{\psi}{\psi_m} \cdot \frac{\omega_r}{2\pi} \right)^{1.5} + a_{eddy} \cdot \left( \frac{\psi}{\psi_m} \cdot \frac{\omega_r}{2\pi} \right)^2 \quad (4.13)$$

$$\text{with :} \quad \omega_r = 2\pi f_e \quad \text{and} \quad \psi = \sqrt{\psi_d^2 + \psi_q^2}$$

Similarly, the short circuit iron losses can be written referenced to the d-axis flux-linkage  $\psi_{d_{SC}}$ :

$$P_{iron}^{SC}(\psi_{d_0}) = b_{hy} \cdot \frac{\omega_r}{2\pi} \cdot \left( \frac{\psi_{d_0}}{\psi_{d_{SC}}} \right)^2 + b_{exc} \cdot \left( \frac{\psi_{d_0}}{\psi_{d_{SC}}} \cdot \frac{\omega_r}{2\pi} \right)^{1.5} + b_{eddy} \cdot \left( \frac{\psi_{d_0}}{\psi_{d_{SC}}} \cdot \frac{\omega_r}{2\pi} \right)^2 \quad (4.14)$$

$$\text{with:} \quad \omega_r = 2\pi f_e \quad \text{and} \quad \psi_{d_0} = \psi_d - \psi_m$$

Where in (4.14),  $\psi_{d_{SC}}$  represents the d-axis flux-linkage produced by  $i_d$  for the calculation of the reference losses  $P_{iron}^{SC}$ . The iron losses can be included in the dq-axes equivalent circuit of the machine in the form of resistors, it is based on the electrical power balance equation, the input power  $P_{in}$  equals the resistive loss  $P_{resistive}$ , iron losses  $P_{iron}$  and the power generated by the electromagnetic torque  $P_e$  and angular velocity:

$$P_{in} = P_{resistive} + P_{iron} + P_e \quad (4.15)$$

By (4.3) in (4.15), the resistive losses and the electromagnetic power  $P_e$  can brought together in terms of the dq-axes voltages and currents. It can then be rewritten in the following way:

$$P_{in} = \frac{3}{2} \cdot (u_d \cdot i_d + u_q \cdot i_q) + P_{iron} \quad (4.16)$$

The iron losses can be fitted in form of a resistor,  $R_m$  in both d- and q-axis as shown in Fig. 4.2. In the literature it has been modeled with different degrees of accuracy, starting with the simple approach where only the eddy current losses are modeled as reported in [64]. More detailed approaches as proposed in [62] and [63] consider the hysteresis and eddy current losses in the calculation of the equivalent loss resistance  $R_m$ . The authors of [65] go further and differentiate between the d- and q-axis iron loss resistors and modeling them as two different components. Based on the findings showed in [61], where iron losses for a magnetizing and demagnetizing path are considered as in (4.11) and (4.12), the equivalent loss circuit needs to be extended. In order to do the model extension, (4.13) and (4.14) are replaced in the electric power equation (4.16) leading to the following expression:

$$P_{in} = \frac{3}{2} \left[ R_s \cdot (i_d^2 + i_q^2) + \omega_r \cdot (\psi_d \cdot i_{qm} - \psi_q \cdot i_{dm}) + \frac{2}{3} \left( P_{iron}^{OC}(\psi) + P_{iron}^{SC}(\psi_{d_0}) \right) \right] \quad (4.17)$$

To obtain the equivalent loss resistors it is needed the final connection to the dq-axes voltage equations:

$$\begin{aligned} u_d &= R_s i_d - \omega_r \psi_q \\ u_q &= R_s i_q + \omega_r \psi_m + \omega_r \psi_{d_0} \end{aligned} \quad (4.18)$$

Where the terms  $\omega_r \psi_q$ ,  $\omega_r \psi_m$  and  $\omega_r \psi_{d_0}$  are considered voltage sources that have an associated loss resistor. This can be clearly seen when looking at the two rearranged iron loss equations for OC and SC, (4.19) and (4.20). They lead to an equivalent model

#### 4 Considering Electromagnetic Losses

where there is a magnetizing loss resistor  $R_m$  in the dq-axes voltages and a demagnetizing loss resistor  $R_d$  only in the q-axis voltage circuit:

$$\frac{2}{3} \cdot P_{iron}^{OC} = \frac{2}{3} \underbrace{\left( \frac{a_{hy}}{2\pi\psi_m^2\omega_r} + \frac{a_{eddy}}{(2\pi\psi_m)^2} + \frac{a_{exc}}{(2\pi\psi_m)^{1.5} \cdot \sqrt{\psi \cdot \omega_r}} \right)}_{\frac{1}{R_m}} \cdot (\psi_d^2 + \psi_q^2) \cdot \omega_r^2 \quad (4.19)$$

$$\frac{2}{3} \cdot P_{iron}^{SC} = \frac{2}{3} \underbrace{\left( \frac{b_{hy}}{2\pi\psi_{dSC}^2\omega_r} + \frac{b_{eddy}}{(2\pi\psi_{dSC})^2} + \frac{b_{exc}}{(2\pi\psi_{dSC})^{1.5} \cdot \sqrt{\psi_{dSC} \cdot \omega_r}} \right)}_{\frac{1}{R_d}} \cdot \psi_{d0}^2 \cdot \omega_r^2 \quad (4.20)$$

(4.19) and (4.20) can be written in terms of  $R_m$  and  $R_d$  respectively as:

$$P_{iron}^{OC} = \frac{3}{2} \left( \frac{(\psi_d \cdot \omega_r)^2}{R_m} + \frac{(\psi_q \cdot \omega_r)^2}{R_m} \right) \quad (4.21)$$

$$\text{with: } \psi_d = \psi_m + \psi_{d0}$$

$$P_{iron}^{SC} = \frac{3}{2} \frac{(\psi_{d0} \cdot \omega_r)^2}{R_d} \quad (4.22)$$

which is the sum of the power dissipation of two resistors driven by two voltage sources. This means that there is a loss resistor  $R_m$  connected to the voltage source  $\omega_r(\psi_m + \psi_{d0})$  and another resistor with the same value attached to  $-\omega_r\psi_q$ , which are the voltage sources in the dq-axes equations in (4.18). The equivalent dq-axes circuit with new loss resistors based on (4.21),(4.22) and (4.18) can be seen in Fig. 4.2.

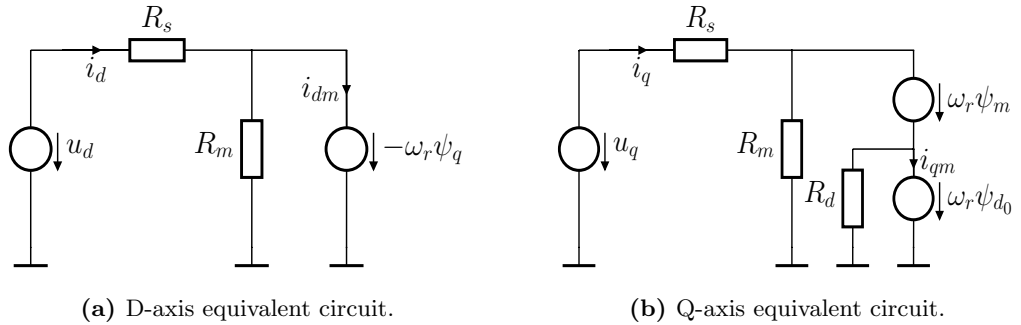


**Figure 4.2:** Voltage model considering iron losses

After having introduced the loss resistors into the dq-axes equivalent circuit, the remaining aspect is the definition of the single loss contributions for the two resistors,

which are divided in hysteresis, eddy current and excess losses. This can be done with (4.19) and (4.20), which for  $R_m$  results in the following terms:

$$\frac{1}{R_m} = \frac{1}{R_{m_{hy}}} + \frac{1}{R_{m_{eddy}}} + \frac{1}{R_{m_{exc}}} \quad (4.23)$$

where,

$$R_{m_{hy}} = \frac{3\pi\psi_m^2\omega_r}{a_{hy}} \quad R_{m_{eddy}} = \frac{6(\pi\psi_m)^2}{a_{eddy}} \quad R_{m_{exc}} = \frac{3(2\pi\psi_m)^{1.5}\sqrt{\psi \cdot \omega_r}}{2a_{exc}} \quad (4.24)$$

For  $R_d$  applies the same treatment:

$$\frac{1}{R_d} = \frac{1}{R_{d_{hy}}} + \frac{1}{R_{d_{eddy}}} + \frac{1}{R_{d_{exc}}} \quad (4.25)$$

where,

$$R_{d_{hy}} = \frac{3\pi\psi_{dSC}^2\omega_r}{b_{hy}} \quad R_{d_{eddy}} = \frac{6(\pi\psi_{dSC})^2}{b_{eddy}} \quad R_{d_{exc}} = \frac{3(2\pi\psi_{dSC})^{1.5}\sqrt{\psi \cdot \omega_r}}{2b_{exc}} \quad (4.26)$$

The set of equations shown in (4.23), (4.24), (4.25) and (4.26) define a way to model the iron losses in the machine, the parameters in those expressions such as the loss coefficients  $a$  and  $b$  can be derived either from FEA simulation results or from measurements. Where the experimental approach requires a way to isolate the mechanical losses from the electromagnetic losses. To address this issue, in the next section a method to identify the value of loss resistors  $R_m$  and  $R_d$  is presented.

#### 4.2.2 Iron Loss Resistance Identification

One interesting aspect of this way of modeling the iron losses in the dq-voltage model is that the losses could be obtained from other source, other than externally measuring the machine's torque over speed. The losses characterization doesn't remain strictly to torque-speed measurements in open and short circuit conditions. As already mentioned, in the case of the measured losses, the main obstacle is the separation of the mechanical losses and the iron losses, which would require the a machine without magnets. But if the equivalent model in Fig. 4.2 is taken into account, the iron losses can be identified in the form of the loss resistors parting from the machine input power. To perform the identification of the losses from the input power, an expression for the input power needs to be derived. This expression is then used to identify the unknown iron losses resistances from measured input power data. From the equivalent model in Fig. 4.2, an expression for the total input power losses can be derived, but it has to be in terms of known signals or variables, as the magnetizing currents  $i_{dm}$  and  $i_{qm}$  can not be obtained by a direct measurement. To facilitate the analysis, the dq-axes voltages can be written according to (4.18) in terms inductances instead of flux-linkages as:

$$u_d = R_s i_d - \omega_r L_q i_{qm} \quad (4.27)$$

$$u_q = R_s i_q + \omega_r (\psi_m + L_d i_{dm}) \quad (4.28)$$

#### 4 Considering Electromagnetic Losses

Similarly, according to the equivalent circuit in Fig.4.2, the dq-axes currents can be written in terms of the magnetizing currents as:

$$i_d = i_{dm} - \frac{\omega_r L_q i_{qm}}{R_m} \quad (4.29)$$

$$i_q = i_{qm} + \frac{\omega_r \psi_m}{R_m} + \frac{\omega_r L_d i_d}{R_d} \quad (4.30)$$

According to (4.29) and (4.30), the magnetizing current  $i_{qm}$  can be expressed in the following form:

$$i_{qm} = \frac{1}{1 + \frac{\omega_r^2 L_d L_q}{R_m} \left( \frac{1}{R_m} + \frac{1}{R_d} \right)} \left( i_q - \frac{\psi_m \omega_r}{R_m} - i_d L_d \omega_{elec} \left( \frac{1}{R_m} + \frac{1}{R_d} \right) \right) \quad (4.31)$$

where (4.31) can be simplified assuming that :

$$\frac{\omega_r^2 L_d L_q}{R_m} \left( \frac{1}{R_m} + \frac{1}{R_d} \right) \ll 1 \quad (4.32)$$

which in the case of machines with reasonable core losses means that the order of magnitude of the inductances is much smaller than the one of the resultant loss resistance:

$$\omega_r^2 L_d L_q \ll R_m \cdot (R_m || R_d) \quad (4.33)$$

For example in the case of the IPMSM, the inductances are in the order of  $56 - 70 \mu H$  and foreseeing loss resistance values in the order of  $> 1 \Omega$ , it is reasonable to assume that the inequality (4.33) holds, leading to the following approximation:

$$1 + \frac{\omega_r^2 L_d L_q}{R_m} \left( \frac{1}{R_m} + \frac{1}{R_d} \right) \approx 1 \quad (4.34)$$

The magnetizing current  $i_{qm}$  in (4.31) can be then rewritten as:

$$i_{qm} \approx i_q - \frac{\psi_m \omega_r}{R_m} - i_d L_d \omega_r \left( \frac{1}{R_m} + \frac{1}{R_d} \right) \quad (4.35)$$

Consequently, replacing (4.35) in (4.29) results in the magnetizing d-axis current  $i_{dm}$  to be:

$$i_{dm} \approx i_d + \frac{\omega_r L_q i_q}{R_m} - \frac{\omega_r^2 \psi_m L_q}{R_m^2} - \frac{\omega_r^2 L_d L_q i_d}{R_m} \left( \frac{1}{R_m} + \frac{1}{R_d} \right) \quad (4.36)$$

Now that the magnetizing currents are expressed in terms of known variables, the q-axis voltage expression can be formulated as:

$$u_q = i_q R_s + \omega_r \psi_m \left( 1 - \frac{\omega_r^2 L_q L_d}{R_m^2} \right) + \omega_r L_d i_d \left( 1 - \frac{\omega_r^2 L_q L_d}{R_m} \left( \frac{1}{R_m} + \frac{1}{R_d} \right) \right) + \frac{\omega_r^2 L_d L_q i_q}{R_m} \quad (4.37)$$

The expression (4.37) exhibits terms in the same form as in the inequality (4.33) making it possible to simplify it under the approximation (4.34) in the following fashion:

$$u_q = i_q R_s + \omega_r (\psi_m + L_d i_d) + \frac{\omega_r^2 L_d L_q i_q}{R_m} \quad (4.38)$$

the d-axis voltage is obtained by replacing (4.35) into (4.27):

$$u_d = i_d R_s - \omega_r L_q i_q + \frac{\omega_r^2 L_q \psi_m}{R_m} + \omega_r^2 i_d L_d L_q \left( \frac{1}{R_m} + \frac{1}{R_d} \right) \quad (4.39)$$

At this point, it is then possible to formulate the input power using the voltage expressions and the currents giving as a result the following :

$$P_{in} = \frac{3}{2} \left[ (i_d^2 + i_q^2) R_s + \omega_r (i_q \psi_m + (L_d - L_q) i_d i_q) + \frac{\omega_r^2 (\psi_m L_q i_d + L_d L_q (i_d^2 + i_q^2))}{R_m} + \frac{\omega_r^2 L_d L_q i_d^2}{R_d} \right] \quad (4.40)$$

Parting from (4.40), it is then possible identify the resistances  $R_m$  and  $R_d$ . This can be done with the corresponding current excitation and speed. If the flux-linkage is maintained constant and the speed is varied, the resulting input power curves will only change with respect to the electrical velocity. By using the identified flux-linkage model parameters in table 3.10 for a 4-pole pair IPMSM, it is then possible to formulate  $P_{in}$  in terms only two unknown variables namely,  $R_m$  and  $R_d$ . The known terms can be extracted from the input power to reduce the problem only to the iron loss terms as in:

$$P_{iron} = \frac{3}{2} \left[ \frac{\omega_r^2 (\psi_m L_q i_d + L_d L_q (i_d^2 + i_q^2))}{R_m} + \frac{\omega_r^2 L_d L_q i_d^2}{R_d} \right] \quad (4.41)$$

where the loss resistors are defined in the following manner to model the hysteresis and Eddy current loss components as:

$$R_{loss} = (R_{hysteresis_0} \cdot \omega_r) || R_{eddy} \quad (4.42)$$

the iron loss resistor as defined in 4.42 describes both losses as parallel connected resistors with the hysteresis loss resistance depending on the electrical velocity in order to model the direct proportionality of the hysteresis loss to the electrical frequency. The two resistors connected in parallel can be represented in terms of the equivalent admittances as:

$$R_{loss} = \frac{1}{\frac{1}{R_{hysteresis_0} \cdot \omega_r} + \frac{1}{R_{eddy}}} = \frac{1}{\frac{Y_{hysteresis_0}}{\omega_r} + Y_{eddy}} \quad (4.43)$$

Expressing the hysteresis loss and eddy current loss components in terms of admittance facilitates mathematically the formulation of the iron loss equation as it brings the unknown variables to be multipliers. As the goal is to determine those resistance it is simpler to formulate the minimization problem in a manner that the variables are

#### 4 Considering Electromagnetic Losses

multipliers. Consequently, the two resistors  $R_m$  and  $R_d$  are decomposed in to four admittances in the following form:

$$Y_{m_{hy}} = \frac{1}{R_{m_{hy}}} = \frac{1}{R_{m_{hy0}} \cdot \omega_r} = \frac{Y_{m_{hy0}}}{\omega_r} \quad (4.44)$$

$$Y_{d_{hy}} = \frac{1}{R_{d_{hy}}} = \frac{1}{R_{d_{hy0}} \cdot \omega_r} = \frac{Y_{d_{hy0}}}{\omega_r} \quad (4.45)$$

$$Y_{m_{eddy}} = \frac{1}{R_{m_{eddy}}}; \quad Y_{d_{eddy}} = \frac{1}{R_{d_{eddy}}} \quad (4.46)$$

Replacing (4.23), (4.25), (4.44), (4.45) and (4.46) in (4.41) leaves the iron loss expression in the final form:

$$P_{iron} = \frac{3}{2} \left[ \left( \frac{Y_{m_{hy0}}}{\omega_r} + Y_{m_{eddy}} \right) \cdot (\omega_r^2 (\psi_m L_q i_d + L_d L_q (i_d^2 + i_q^2))) + \left( \frac{Y_{d_{hy0}}}{\omega_r} + Y_{d_{eddy}} \right) \cdot (\omega_r^2 L_d L_q i_d^2) \right] \quad (4.47)$$

Following the same approach as in the previous chapter, the loss admittance can be obtained by minimizing the sum of the quadratic error of the iron loss expression (4.41) as:

$$f_{iron}(x) = \sum_{k=1}^N [(P_{iron} - \hat{P}_{iron})^2] \quad (4.48)$$

where,

$$\hat{P}_{iron} = \nabla P_{iron} x^T$$

$$x = [Y_{m_{hy0}} \ Y_{m_{eddy}} \ Y_{d_{hy0}} \ Y_{d_{eddy}}]$$

Where  $f_{iron}$  is the objective function and  $N$  is the number of the data points. The letters with a hat notation represent estimated values and the letters with no hat notation are the values of the identified data. The constrained optimization problem can be then formulated in the following form as the loss admittances are positive:

$$\begin{aligned} \text{Minimize} \quad & Q(x) = \frac{1}{2} x^T G x + g^T x \\ \text{with,} \quad & Y_{m_{hy0}} > 0 & Y_{m_{eddy}} > 0 \\ & Y_{d_{hy0}} > 0 & Y_{d_{eddy}} > 0 \end{aligned} \quad (4.49)$$

where,

$$G = \nabla P_{iron} \nabla P_{iron}^T$$

$$g = -2 P_{iron} \nabla P_{iron}$$

The optimization process is then performed as defined in (4.49), using the input power data depicted in Fig. 4.3a. A low phase current value, 0.5 p.u., was selected for the different speed ramps at phase advance angles of 25°, 45°, 65° and 90°. A low current magnitude makes the iron loss to have more weight in the input power than by choosing

a large current magnitude [66]. In addition, the machine behaves linearly up to this current magnitude, which facilitates the calculation of the inductances. By covering different advance angles a quadrant is covered for each current magnitude guaranteeing enough information to identify the loss resistors.

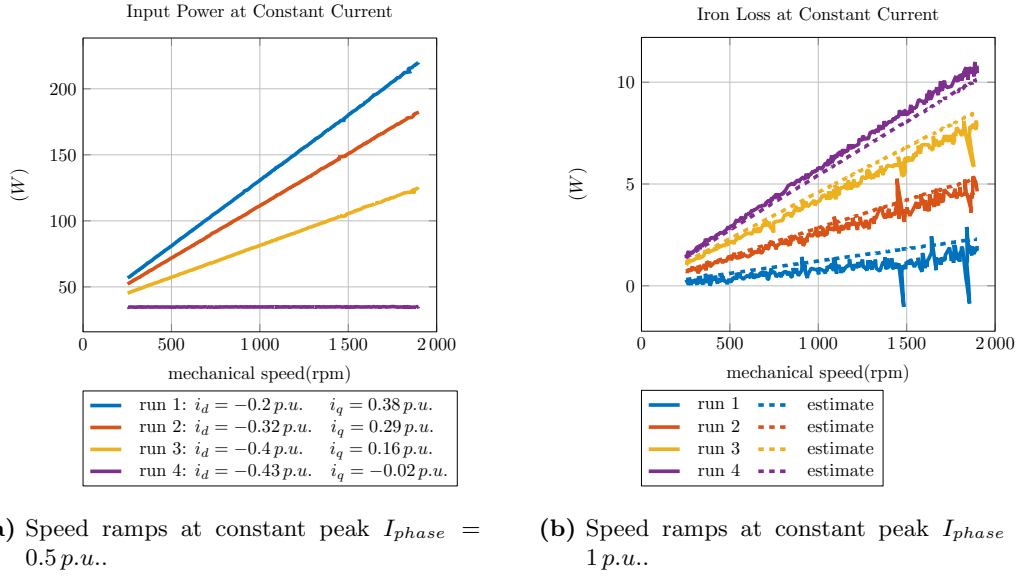


**Figure 4.3:** 4-pole pair IPMSM input power measurement.

The identified loss resistance values are summarized in table 4.1, with a coefficient of determination of  $Cod = 0.9624$ . Considering the ratio between input power, Fig 4.3a and the iron losses in Fig 4.3, the resulting approximation error is sufficient to model the iron losses with an average error less than 10%. However, the agreement displayed in Fig 4.3 indicates that the modeling assumption of constant loss resistance isn't completely true, nevertheless for a practical implementation in an embedded system the approximation accuracy obtained with this assumption is very satisfactory.

**Table 4.1:** IPMSM loss resistances with PWM based excitation

	<i>Loss resistance</i>
$R_{m_{hy0}}$	$3.26 \text{ m}\Omega \cdot \text{s/rad}$
$R_{m_{eddy}}$	$7.83 \Omega$
$R_{d_{hy0}}$	$0.39 \text{ m}\Omega \cdot \text{s/rad}$
$R_{d_{eddy}}$	$7.18 \Omega$

With the iron loss model represented by the loss resistances in table 4.1, it is then possible to obtain the mechanical losses in the machine by subtracting the estimated

#### 4 Considering Electromagnetic Losses

open circuit iron losses. By recalling (4.10), the mechanical losses can be written as:

$$\text{sign}(\omega_m) \cdot k_c \omega_m + k_v \omega_m^2 = P_{\text{shaft}} - P_{\text{iron}} \quad (4.50)$$

where the coefficients  $k_c$  and  $k_v$  are calculated similarly to the loss resistance by the minimization of the least-square error. The resulting coefficients are listed in table 4.2.

**Table 4.2:** IPMSM mechanical loss coefficients

<i>Loss coefficient</i>	
$k_c$	26.2 mNm
$k_v$	0.25 $\mu\text{Nm} \cdot \text{s}$

Once the iron and mechanical losses are known, the shaft loss measurement can be decomposed in the different contributions as shown in Fig. 4.4a. Furthermore, the core losses can be plotted separately as well as Fig. 4.4b.

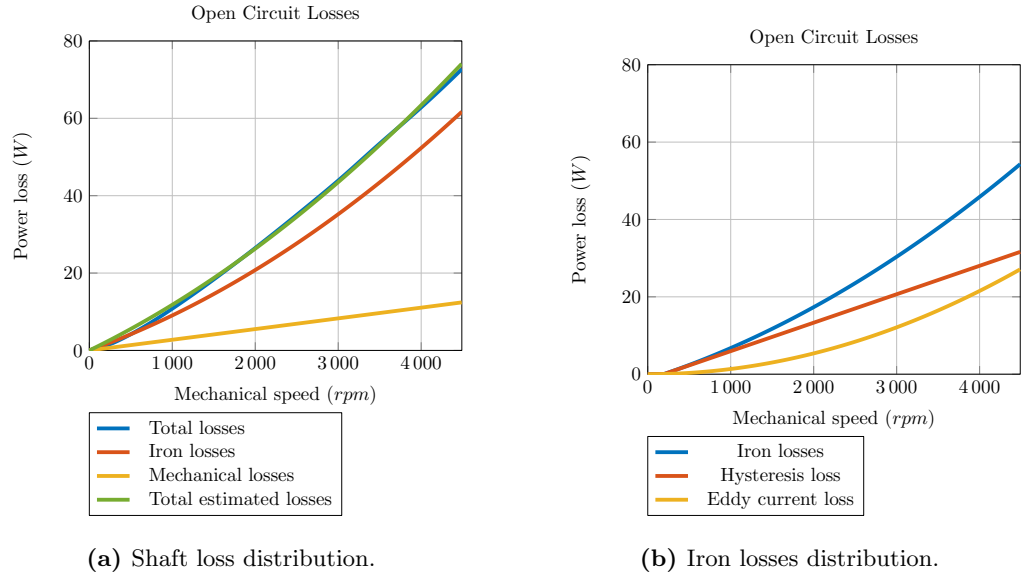


**Figure 4.4:** IPMSM open circuit shaft loss.

Finally, after separating mechanical and electromagnetic losses, the measured open circuit shaft loss is then expressed as the sum of the iron losses and friction losses, where the former are represented by the loss resistors in table 4.1 and the friction losses are obtained through the coefficients in table 4.2.

To fully characterize the machine in the operating regions of interest, power loss maps can be generated from the equivalent model. Moreover the hysteresis and Eddy current loss components can be normalized, where the hysteresis loss is divided by  $f_e$  and the

Eddy current loss by  $f_e^2$ . Fig. 4.5 depicts these two loss maps of the IPMSM using the flux-linkage model obtained in section 3.5.1.

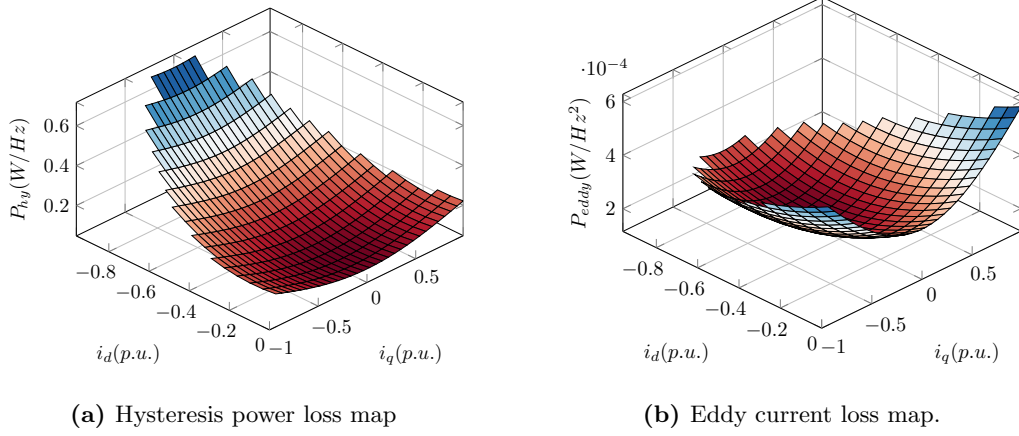


**Figure 4.5:** 4-pole pair IPMSM loss maps.

Conversely the loss map at a given rotor speed can be determined. As depicted in Fig. 4.6a, the per-unit total iron loss at 900 *rpm* is significantly small compared to the one at 4500 *rpm*, making for instance more convenient the identification of the flux-linkage at low speeds. On the other hand is it crucial to consider the iron loss effects at increasing rotor speed as they become larger, hence impacting the machine overall input power and an online parameter identification.

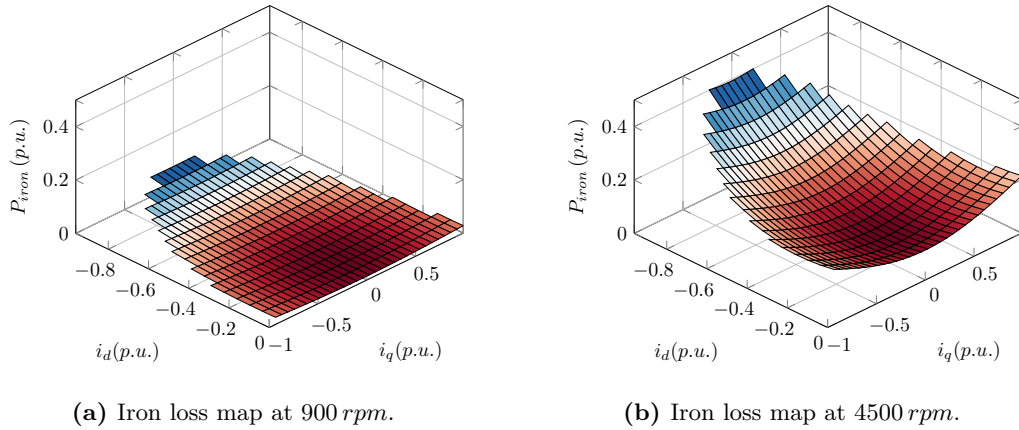


**Figure 4.6:** 4-pole pair IPMSM iron loss maps.

This chapter focused on the identification of the machine core losses, the iron losses were modeled with a modified loss resistor arrangement to include the demagnetization

#### *4 Considering Electromagnetic Losses*

loss according to the proposed method described in [61] in the equivalent dq-axes circuit. Moreover the iron loss resistance values were determined with the help of this equivalent circuit. As a final step, the mechanical loss coefficients were obtained from an open circuit shaft loss measurement by subtracting the corresponding iron losses. Finally, the core loss model will be used to model the power loss heat sources in the thermal model in chapter 5 and also to improve the fidelity of the machine model for the online parameter identification.

## 5 Motor Thermal Model

One key aspect projected in this work for a robust online parameter identification is the use of a thermal machine model to enhance the online estimation algorithm at every operating condition of the machine. The rationale behind this, is the limitation that online estimation algorithms may encounter. If it is a passive algorithm, which uses measured signals as a result of the current operating point, then there is a big risk that the operating point in terms of current and voltage magnitude and speed aren't sufficient to perform a proper parameter identification. As an example if the speed is close to zero it is not possible to obtain the flux-linkages with enough precision.

Conversely, if the main target is to supervise the temperature of key components inside the machine such as the phase windings and the magnets, a thermal model alone presents its limitations if additional information isn't available. If the system is started on "warm" conditions, where the elements of interest possess a undefined start temperature, much different than the reference or ambient temperature, the thermal model will indicate or estimate the wrong temperature of these elements for a certain period of time. In the case that additional information is available, let's say, winding resistance or permanent magnet flux-linkage estimation, the temperature coefficient of the copper or magnet could be used to do a direct estimate of the temperature of these components to correct the initial temperature values of the thermal model.

### 5.1 Thermal Modeling

The model of the thermal characteristics in a machine can be performed in different manners. It can be as complex and detailed as numerical analysis such as FE analysis or computational fluid analysis (CFD) or it can be described analytically in terms of the materials properties of the machine and its geometry. Where the analytical approach can be quite accurate or simplified through the use of lumped parameter thermal-network (LPTN) as shown by the authors of [67] and [68].

#### 5.1.1 Lumped Parameter Modeling

From the different methods to model the thermal behavior of the components of a machine, the lumped parameter approach is a simple and good alternative for embedded systems as shown by Mellor and Turner in [10]. The main idea is to model the heat transfer in the machine using elements equivalent to the ones of an electrical network, such as resistors, voltage sources or capacitors, as shown in table 5.1:

**Table 5.1:** Equivalent thermal to electrical elements

<i>Component</i>	<i>Thermal units</i>	<i>Electrical units</i>
<i>R</i>	$^{\circ}\text{C}/\text{W}$	$\Omega$
<i>C</i>	$\text{J}/^{\circ}\text{C}$	<i>F</i>
<i>Voltage source</i>	$^{\circ}\text{C}$	<i>V</i>
<i>Current source</i>	<i>W</i>	<i>A</i>

The heat sources in the thermal network are modeled by current sources as shown in table 5.1. There are three types of heat sources in the machine: the Joule losses, the core losses and the mechanical losses. The resistive losses can be obtained from the winding resistance and the current flowing through it. In addition to this, the temperature coefficient of the copper needs to be taken into account as the resistance will vary with the temperature as well. (4.3) describes the resistive power loss as a function of the winding temperature:

$$P_{resistive} = \frac{3}{2}R_{s_0} \left[ 1 + tempco_{cu}(T_{winding} - T_0) \right] (i_d^2 + i_q^2) \quad (5.1)$$

where  $R_{s_0}$  is the average winding resistance,  $tempco_{cu}$  is the temperature coefficient of the copper,  $T_{winding}$  is the average winding temperature and  $T_0$  the reference temperature at which  $R_{s_0}$  holds. The expression in (5.1) represents the average power losses as the heating process inside the machine is not homogeneous, certain parts of the windings wire will develop different temperatures. Therefore additional nodes are introduced to capture a more accurate thermal behavior. Typically the end windings, the end part of the winding coils, are modeled with their own nodes.

The core losses are additional heat sources in the machine due to the hysteresis and Eddy current losses addressed in chapter 4. The iron losses depend on the machine's operating point with regards of the dq-axis currents but the permanent magnet flux-linkage  $\psi_m$  as well. The resulting expression of the losses is then written in terms of the currents and  $\psi_m$  as:

$$P_{iron} = \frac{3}{2} \left[ \frac{\omega_r^2 \cdot (\psi_m(T_{magnet}) \cdot L_q i_d + L_d L_q (i_d^2 + i_q^2))}{R_m} + \frac{\omega_r^2 L_d L_q i_d^2}{R_d} \right] \quad (5.2)$$

where the iron loss resistors are defined as in (4.23) and (4.25) and  $\psi_m$  is magnet temperature dependent according to (2.55) as:

$$\psi_m(T_{magnet}) = \psi_{m_{T_0}} [1 + tempco_{magnet}(T_{magnet} - T_0)] \quad (5.3)$$

The term  $tempco_{magnet}$  is the equivalent temperature coefficient of the permanent flux-linkage,  $\psi_{m_{T_0}}$  is the flux-linkage obtained at the reference temperature  $T_0$  and  $T_{magnet}$  is the average magnet temperature.

On the other hand, the mechanical losses, Coulomb and viscous friction losses, are modeled with the coefficients  $k_c$  and  $k_v$  as per (4.10) to provide additional the heat sources representing bearing and windage losses in the thermal network. The thermal network loss sources are then summarized as:

**Table 5.2:** Power loss sources

<i>Resistive losses</i>	$P_{resistive}$
<i>Iron losses</i>	$P_{hy} + P_{eddy}$
<i>Mechanical losses</i>	$P_{coulomb} + P_{viscous}$

The next step is then to define the calculation of the values of the passive elements in the network, which are the thermal resistors and thermal capacitors values.

The equivalent elements in table 5.1 depict the process of various types of heat transfer, such as conduction, convection and radiation. For instance, the thermal resistances can be obtained according to geometry of the materials in place. The thermal resistance due to the conduction of heat is defined as the transfer rate of heat between two points [69]:

$$R_{cond} = \frac{T_1 - T_2}{q} = \frac{l}{k \cdot A} \quad (5.4)$$

where  $T_1$  and  $T_2$  are the temperatures at the points of interest in the material,  $q$  is the conduction heat rate,  $l$  is the path length,  $A$  the corresponding area and  $k$  is the material's thermal conductivity. Similarly, the convection thermal resistance depends on the materials geometry as:

$$R_{conv} = \frac{1}{h \cdot A} \quad (5.5)$$

in this case  $h$  represents the convection heat transfer coefficient of the material in question. Finally the associated thermal resistance to the thermal radiation between surfaces is expressed in the same way as the one due to convection:

$$R_{rad} = \frac{1}{h_r \cdot A} \quad (5.6)$$

where  $h_r$  is the radiation heat transfer coefficient between surfaces. In addition to the thermal resistances that can be determined for certain parts in the machine of known geometry and thermal characteristics, the thermal contact resistance needs to be considered as well. The interfacing between materials surfaces involves a combination of heat transfer due to conduction in the areas in contact and due to convection or radiation across gaps that may be present. Finally, the remaining passive element, the thermal capacitance, will depend on the mass density and volume of the material in question.

An example of a thermal network can be seen in Fig. 5.1, where a LPTN of a 4 pole pair IPMSM is displayed. The thermal network was created with commercial software *MotorCAD*. The nodes of the thermal network in Fig. 5.1 represent the temperature

## 5 Motor Thermal Model

in different sections of the machine. Therefore a detailed thermal network can end up having a large amount of nodes which would make the model not suitable for an embedded application.

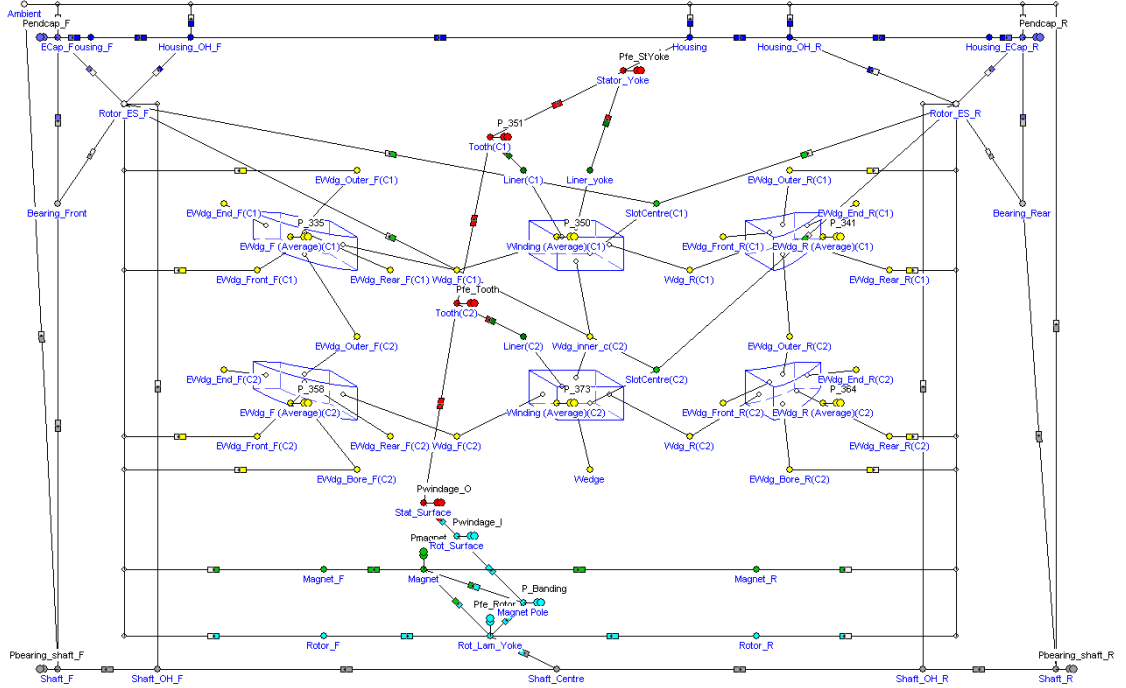


Figure 5.1: MotorCAD - 4 pole pair IPMSM thermal network

Depending on the fidelity level expected of the model, the number of nodes and elements can be significantly large. This implies that the accuracy of the temperature estimation or modeling is directly dependent on the number of network nodes, as pointed out in [68]. Which means that for a target group of temperatures in the machine, an additional set of nodes may be required to increase the model's order, in that way the accuracy or quality of the estimated temperature in the target nodes can be improved as shown in [70] and [71]. To summarize, a deep knowledge of all materials and geometry of the different components in a machine are required to calculate and build the thermal network. This is time consuming and it could require additional measurements to characterize for example the contact thermal resistances between the different materials surfaces inside the machine. Furthermore, for a high fidelity model, the addition of intermediate nodes could be necessary [71].

## 5.2 Modeling Approach

There are two main objectives in this work regarding the thermal model of the machine. The first one is the derivation of a high fidelity thermal model that can be used for a sys-

tem simulation in conjunction with the flux-linkage based high fidelity machine model. This goal was set to facilitate the design of the online parameter identification algorithm by creating a multi-physics model that covers the inverter, the machine's torque generation and the machine thermal behavior.

The second a most important objective is the generation of a simple thermal model that can be used in an embedded system to assist and enhance an online parameter estimation algorithm. As seen in the previous section, deep knowledge of the machine geometry and materials properties would be necessary for the creation of an analytical thermal model of the machine. The intention of this work is to propose a modeling approach where a thermal network can be derived, without special knowledge of the machine and that is simple enough to be implemented in an embedded system. In other words a model reduction methodology, with the intention to apply it, when possible, to an existent high fidelity thermal model.

### 5.2.1 Model Reduction

In order to have a consistent workflow where there is a high fidelity model that can be used for simulation and design purposes on a personal computer and a simple model that can be implemented on a micro-controller, the concept of model reduction arises. It is a way to generate a simplified model for online purposes. A simple model can be derived from complex models, lets say, thermal networks with a high number of nodes as shown in [70]. Additionally to this, if the model reduction technique is chosen properly, it can serve as means to derive a high fidelity thermal model from FE simulation results or measurements. Besides a FE thermal model or an existing complex thermal network, the physical machine can be considered a high fidelity model itself, where the temperature of selected places is known, through sensors and the heat sources are known as well. This aspect is going to be explored and exploited in order to present a simple way to obtain a lumped parameter thermal model of a PMSM. By simple is meant that the machine itself can be considered as a black box, the geometry of the machine and material knowledge aren't needed, simplifying the effort necessary to generate the thermal network. The model reduction technique can be applied actually twice; the first time to derive the high fidelity model from FE data or measurements and the second time to obtain a simplified model for use in an embedded system.

So far the concept of thermal network has been mentioned in general terms, but as pointed out with table 5.1, there is an equivalence to resistive networks. This means that Kirchhoff's circuit laws apply to the thermal network. With that in mind the lumped parameter thermal network can be formulated in the following form:

$$C \cdot \dot{T} = -G \cdot T + P_l \quad (5.7)$$

where  $C$  is the thermal capacitance matrix,  $T$  is a vector containing the temperature value of each node,  $G$  is the conductance matrix and matrix  $P_l$  is the power loss in the machine. Fig. 5.2 shows a simple thermal network where  $T_a$  is the ambient temperature,

## 5 Motor Thermal Model

$C_{th}$  is the thermal capacitance,  $R_{th}$  is the thermal resistance and  $P$  represents the power losses.

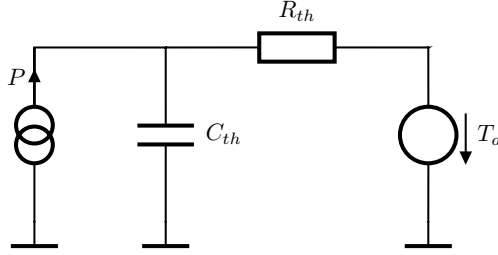


**Figure 5.2:** Example of a simple LPTN.

The conductance matrix is defined as the inverse of the thermal resistance matrix  $R$ . The thermal resistance matrix is built to describe the power exchange between nodes in the network or in an equivalent way the thermal conductance  $G_{th}$ , as:

$$P_{ij} = \frac{T_i - T_j}{R_{th_{ij}}} = G_{th_{ij}} \cdot (T_i - T_j) \quad (5.8)$$

Each resistor in the network could be connected to any other node in the network, making  $R$  a square and symmetrical matrix with  $R_{th_{ij}} = R_{th_{ji}}$ . The elements  $R_{th_{ii}}$  are the equivalent resistance at the corresponding node conversely the conductance  $G_{th_{ii}}$  is the sum of all conductances between node  $i$  and the remaining nodes in the network. For this reason, the formulation in terms of conductance is much more convenient as the matrix can be easily formed.

The thermal network of the size of Fig. 5.1 consists of more than 50 nodes. This is the result of a high fidelity model, where many sections of the machine are modeled to create a more accurate model. At this point, a complex model would be available and the remaining task would be the generation of a simple model, that can capture certain target temperatures with acceptable accuracy and that can be implemented in an embedded system considering the computational cost of running it online.

With respect to reduced models, there are approaches where the model is already formulated in a reduced form due to previous experience with the machine in question as reported in [72] and [73]. In [70] the lumped parameter thermal network approach is expressed in its mathematical form according to (5.7) with the objective to obtain a reduced model parting from a complex network. The proposed model reduction focuses on the frequency domain where (5.7) is transformed into its Laplace representation, where the frequency domain is obtained by setting  $s = j\omega$ . Afterwards, the matrices are divided in association with target nodes and the remaining nodes. Through this separation the heat source matrix  $\mathbf{P}_l$  becomes complex, at which the imaginary parts

are neglected in order to simplify the final model. Finally it was shown that the selection of additional nodes beside the target nodes was decisive to improve the reduced model accuracy. On the other hand, the authors in [71] undertook a similar approach by analyzing the model reduction problem from the Laplace perspective and encountering the same mathematical issue of inverting the model matrices in the Laplace domain. For that reason, a transfer function approach was adopted to formulate the reduced model. Ladder network structures were proposed to model interaction between power loss sources and the nodes of interest. Where the order of the proposed ladder networks were increased in certain nodes to improve the model accuracy.

A common aspect on the aforementioned methods is the need for an additional treatment to the reduced models to achieve the desired performance. However there is a key aspect that is worth to recognize, which is the fact that the network reduction obtained mathematically from the steady state perspective delivers an equivalent model with no approximation or decreased accuracy. The steady state form of the network (5.7) can be written as by letting the temperature derivatives to be zero:

$$P_l = G \cdot T \quad (5.9)$$

it gets reduced to a merely resistive network with power sources. It can be then rewritten in terms of the target temperatures and the remaining ones as:

$$\begin{bmatrix} P_{l_1} \\ P_{l_2} \end{bmatrix} = \begin{bmatrix} G_{11} & G_{12} \\ G_{21} & G_{22} \end{bmatrix} \cdot \begin{bmatrix} T_1 \\ T_2 \end{bmatrix} \quad (5.10)$$

where  $T_1$  refers to the target temperature nodes and  $T_2$  to the ones that will be excluded from the reduced model. (5.10) can be rearranged to get an expression only in terms of the target temperature nodes  $T_1$  as:

$$P_{l_1} - G_{12} \cdot G_{22}^{-1} \cdot P_{l_2} = \left( G_{11} - G_{12} \cdot G_{22}^{-1} \cdot G_{21} \right) \cdot T_1 \quad (5.11)$$

at this point one remark needs to be made, the left side terms of (5.11) consider that each node in the network is fed with a power loss source. In reality this is not the case, as already shown in table 5.2 there is a limited number of power losses sources which won't be present in all nodes of a large thermal network. For this reason, those nodes are considered as target nodes due to its relevance in the excitation of the thermal network. Hence, the temperature nodes with subscript  $(1)$  group the nodes with associated power sources and the ones with subscript  $(2)$  temperature nodes with power sources. Therefore the power loss term  $P_{l_2}$  can be set to zero, thus reducing (5.11) in the following form:

$$P_{l_1} = \left( G_{11} - G_{12} \cdot G_{22}^{-1} \cdot G_{21} \right) \cdot T_1 \quad (5.12)$$

The conductance matrix of the reduced model can be then obtained from the parent conductance matrix as:

$$G_r = G_{11} - G_{12} \cdot G_{22}^{-1} \cdot G_{21} \quad (5.13)$$

## 5 Motor Thermal Model

Finally, the steady-state equation of the reduced model results in:

$$P_{l_1} = G_r \cdot T_1 \quad (5.14)$$

For steady-state conditions, the reduced model (5.14) delivers an exact solution, the main resistive network in (5.9) was divided in two groups to obtain mathematically the equivalent conductance (5.13) of the nodes of interest. The reduced model conductance matrix will be of the same form as the thermal resistance matrix  $R$ , square and symmetric with  $G_{r_{ij}} = G_{r_{ji}}$ , taking then the following form:

$$G_r = \begin{bmatrix} G_{r_{11}} & G_{r_{12}} & \cdots & G_{r_{1n}} \\ G_{r_{21}} & G_{r_{22}} & \cdots & G_{r_{2n}} \\ \vdots & \vdots & \ddots & \vdots \\ G_{r_{n1}} & G_{r_{n2}} & \cdots & G_{r_{nn}} \end{bmatrix} \quad (5.15)$$

The conductance matrix (5.15) depicts a network where all nodes are interconnected with each other through the conductances  $G_{r_{ij}}$  and elements in the diagonal  $G_{r_{ii}}$  are defined as:

$$G_{r_{ii}} = - \sum_{j=1}^n G_{r_{ij}} \quad \text{with} \quad j \neq i \quad (5.16)$$

Returning to the dynamic formulation of the temperature, the reduced model is formulated as the steady state equivalent resistive network  $G_r$  with associated power losses  $P_{l_r} = P_{l_1}$  and node capacitance matrix  $C_r$ :

$$C_r \cdot \dot{T} = -G_r \cdot T_r + P_{l_r} \quad (5.17)$$

where the vector  $T_r$  contains the target temperatures. The capacitance matrix  $C_r$  represents the thermal capacitances associated to each node. The elements in  $C_r$  denote a capacitance between every node and one with respect to the reference point.

$$C_r = \begin{bmatrix} C_{11} & C_{12} & \cdots & C_{1n} \\ C_{21} & C_{22} & \cdots & C_{2n} \\ \vdots & \vdots & \ddots & \vdots \\ C_{n1} & C_{n2} & \cdots & C_{nn} \end{bmatrix} \quad (5.18)$$

Consequently, the capacitances  $C_{ii}$  represent the self capacitance of the node with respect to the network reference. The mutual capacitances linking each node  $C_{ij}$  contribute to the dynamic characteristics of the network. Moreover, they can be used to increase the model's order, as the authors in [70] propose that those capacitances adopt a negative value to improve the model's performance. Despite the direct relationship between the thermal resistances with the ones of the parent model with their physical corresponding physical meaning. Matrix  $C_r$  represents the equivalent capacitances at each node in a purely mathematical sense. As they help to model the dynamic behavior of the thermal network and they don't have a physical meaning. At this point the only unknown element in (5.17) is the thermal matrix (5.18), which should be identified using temperature

data of each target node derived from the parent model.

The validity of the reduction process was tested with the machine thermal model of Fig. 5.1, which consist of a lumped parameter thermal model of 66 nodes, of which only 12 nodes have power sources associated to them. The reduced model shall contain nodes of interest, such as the winding and magnet temperature, moreover the nodes with power sources associated to them are also considered in order to avoid unnecessary simplifications. Coincidentally, the target nodes have power sources as well, which leaves the node count at 12 in addition to the ambient temperature node. Therefore the network is reduced down to 13 nodes.

In order to achieve the most reduced form of the thermal network, the mutual capacitances  $C_{ij}$  are assumed to be zero. This assumption is justify based on the findings presented in [70] and [71], where the reduced network was modified in order to increase the models order. However, a key factor stated by [70] was the introduction of additional key temperature nodes to improve the model's performance. The addition of nodes is an intuitive approach and doesn't require the modification of the network elements with new arrangements.

Based on the assumption that each thermal node has a capacitance referred to reference as shown in Fig. 5.2, this capacitance should be the node's dominant thermal capacitance, consequently the linking capacitances between nodes as per (5.18) should contribute to the high frequency or highly dynamic response [70]. Hence, neglecting the mutual capacitances might have a negative impact on the model's order which at the same time can be compensated by introducing additional nodes to the reduce model. The advantage of this modeling approach is its simplicity in terms of implementation. Finally, the capacitance matrix  $C_r$  takes then the following form:

$$C_r = \begin{bmatrix} C_1 & 0 & \dots & 0 \\ 0 & C_2 & \dots & 0 \\ \vdots & \vdots & \ddots & \vdots \\ 0 & 0 & \dots & C_n \end{bmatrix} \quad (5.19)$$

The reduced network with 13 nodes takes then the general form displayed in Fig. 5.3, where each node is connected to the other nodes through a thermal resistor according to the conductance matrix  $G_r$ , each node besides the ambient temperature node has a capacitance connected to the reference point as per matrix  $C_r$  in (5.19) and as mentioned before those nodes are also fed with a power loss source.

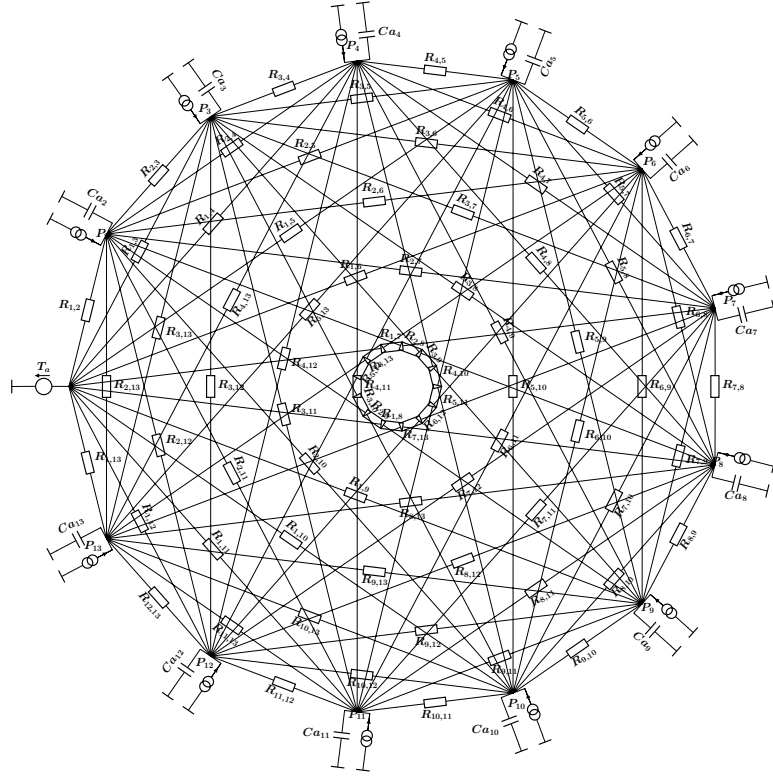


**Figure 5.3:** General thermal network for 13 nodes.

As the conductances of the parent model are known, the thermal conductances of the reduced network in Fig. 5.3 are determined directly using (5.13). On the other hand, the thermal capacitances are obtained using simulated temperature profiles. Based on (5.17), the differential equation that involves the capacitance of the  $n$ -th node can be formulated as:

$$P_{l_n} = C_n \cdot \frac{dT_n}{dt} + G_{r_{n1}} \cdot T_1 \dots + G_{r_{nn}} \cdot T_n \dots + G_{r_{nm}} \cdot T_m \quad (5.20)$$

where  $m$  is the total number of nodes of the network,  $T_{()}$  are the node temperatures and  $P_{l_n}$  is the power loss source associated to the node  $n$ . If each node temperature  $T_{()}$  is known, (5.20) would only have one unknown variable namely  $C_n$ , as  $\frac{dT_n}{dt}$  can be calculated from  $T_n$ . With this in mind, for a set of simulated temperature profiles, the capacitance of each node can be then obtained by minimizing the following objective function:

$$f_{thermal}(x) = \sum_{n=1}^N \left[ (P_{l_n} - \hat{P}_{l_n})^2 \right] \quad (5.21)$$

where,  $\hat{P}_l = \nabla P_l \cdot x^T$

Where  $f_{thermal}$  is the objective function and  $N$  is the number of the data points. The letters with a hat notation represent estimated values and the letters with no hat notation are the values of the identified data. Similarly as in previous sections, the quadratic programming is used for the possibility to limit the solution to positive thermal capacitances.

$$\begin{aligned}
 \text{Minimize} \quad & Q(x) = \frac{1}{2}x^T Gx + g^T x \\
 \text{with,} \quad & C_n > 0 \\
 \text{where,} \quad & G = \nabla P_l \nabla P_l^T \\
 & g = -2P_l \nabla P_l
 \end{aligned} \tag{5.22}$$

The flowchart in Fig. 5.4 summarizes the steps taken towards the reduction of the parent model.

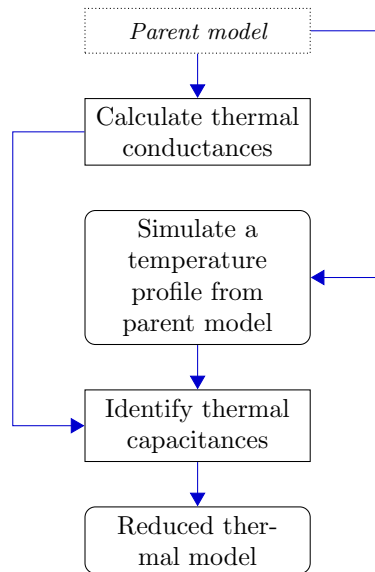


**Figure 5.4:** Thermal model reduction.

The optimization problem formulated in (5.21) and (5.22) delivers then the capacitance values to finally complete the reduced thermal network of Fig. 5.5.

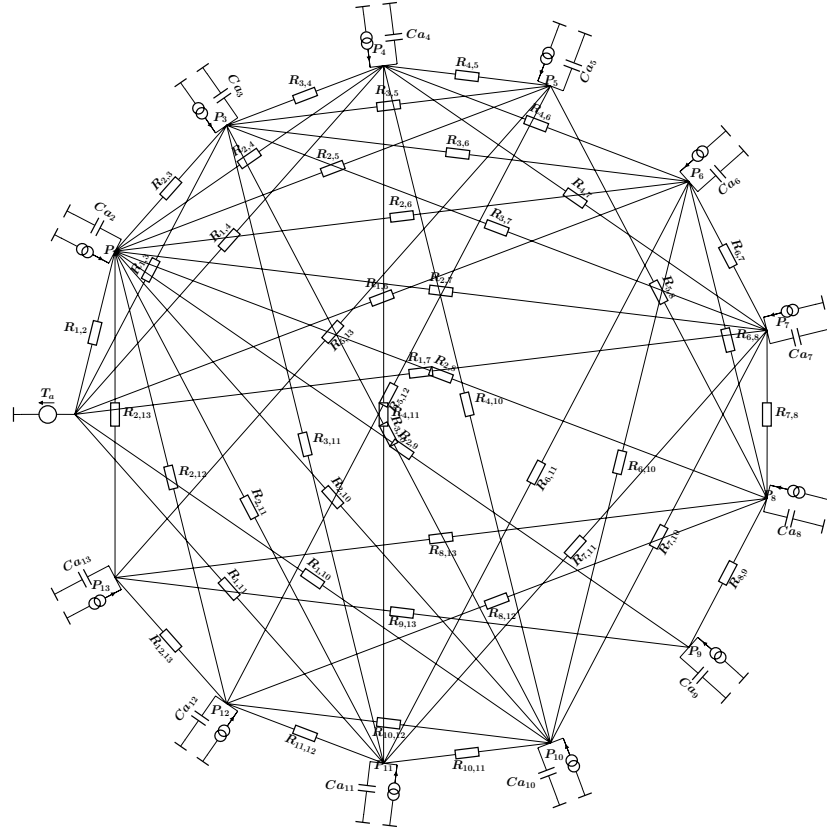
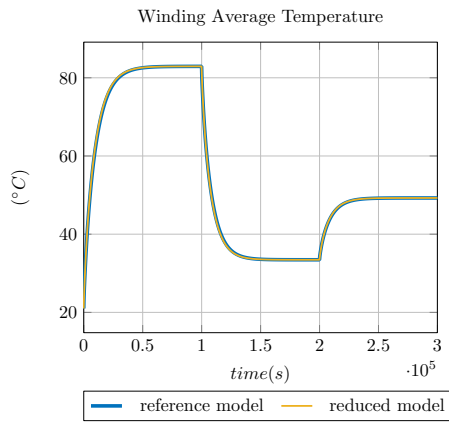


**Figure 5.5:** Reduced thermal network from parent MotorCAD model.

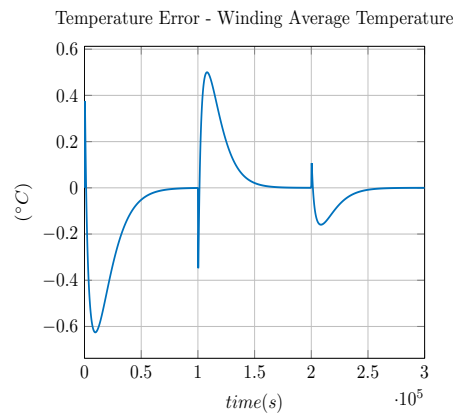
In principle, the conductance reduction according to (5.13) leads to an interconnection between all the nodes, which translates into thermal resistances connecting each node with all the remaining nodes of the network as already shown in Fig. 5.3. However, the resulting network in Fig. 5.5 exhibits less thermal resistors as in the generic formulation of 13 nodes in Fig. 5.3. For large thermal resistance values<sup>1</sup>, the resistance was approximated to an infinite value, leading in that way to a even more simplified form of the network. Additionally, each node except for the ambient temperature node  $T_a$  has a thermal capacitance that contributes to model the dynamic behavior of the thermal network.

The temperature of the average winding resistance and magnet are shown in Fig. 5.6, moreover they are compared against the simulated temperature obtained with the reference model or parent model.

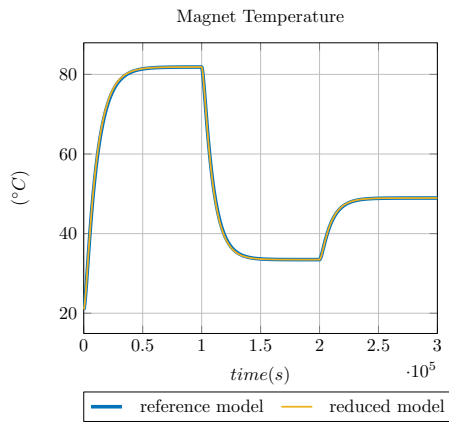
<sup>1</sup>Thermal resistors with values larger than  $100k$  K/W were removed from the network.



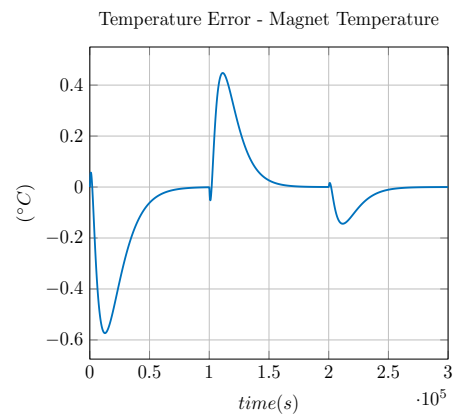
(a) Temperature at node 3



(b) Temperature deviation at node 3.



(c) Temperature at node 8



(d) Temperature deviation at node 8

**Figure 5.6:** Reduced model temperature.

In Fig. 5.6b and 5.6d the error in steady state is zero due to the exact calculation of the conductance matrix from the parent model and the thermal capacitances obtained through the optimization process provide deviations below  $0.7^{\circ}C$ . These deviation can be observed for all the remaining nodes as depicted in Fig. 5.7

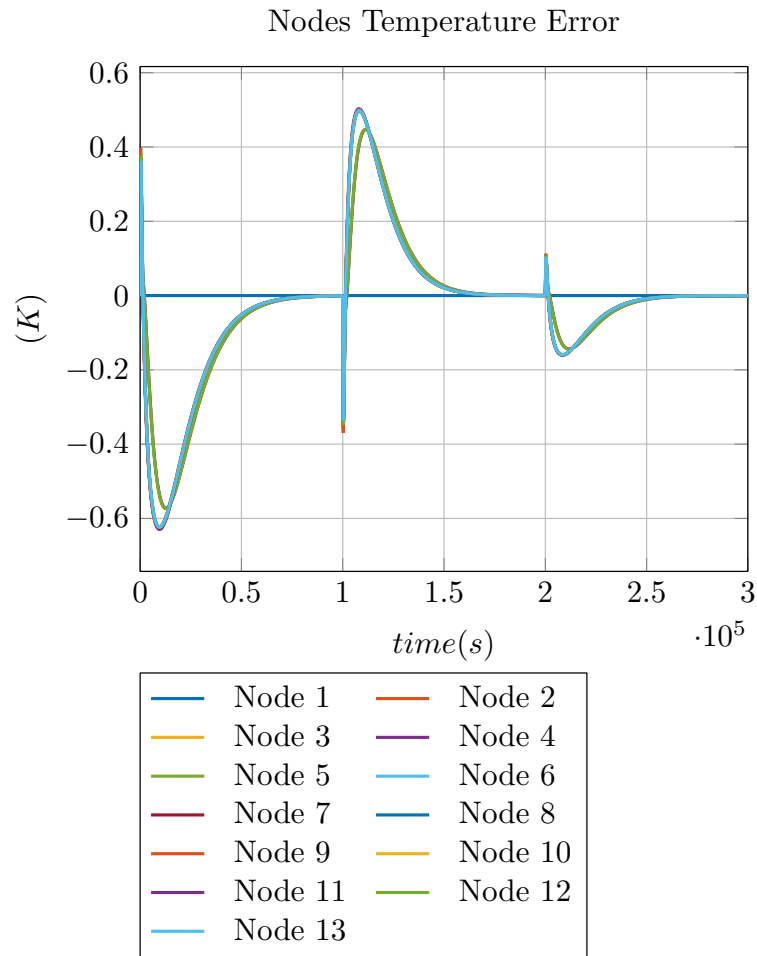


**Figure 5.7:** Reduced temperature deviations of all nodes.

For the given test profiles the reduced model was able to predict the different node temperatures with deviations below  $0.7^{\circ}C$ , moreover the steady state temperature error achieved for all the nodes is close to zero due to the direct reduction of the resistive network from the parent model.

The two step model reduction could be successfully performed on the example model presented in Fig. 5.1, where a reduced model consisting of a thermal resistive network and thermal capacitances associated to each node was obtained as presented in Fig. 5.5. Furthermore, the interconnection of each node through resistances with the rest of the nodes can be used as a generic start point for the formulation of the reduced thermal network. Besides the possibility to reduce a known large thermal network into a simpler one, a real machine can be directly modeled. Temperature sensors can be placed in many sections inside a machine to capture the temperature behavior in the

regions of interest. The generic network structure for  $n$ -nodes, i.e. Fig 5.3, can be used in combination with the measured temperatures to fit the corresponding elements of the network. Following that idea, a high fidelity thermal model of the machine could be created without knowledge of the geometry and characteristics of the materials in the machine. Similarly, a reduced thermal model with a small set of nodes could be generated from the measurements as well.

### 5.2.2 Thermal Model Parameter Identification

This section will address the proposed approach to generate a thermal network based on measurements. The target network according to (5.20) is determined with respect to the nodes of interest; the ones where the relevant power loss sources are present and the nodes of interest. The main objective is to estimate the average winding and magnet temperatures. The machine considered in further steps is the IPMSM used in section 3.5.1 with characteristics listed in table 2.1. K-type thermocouples sensors were placed in the machine as illustrated in Fig. 5.8. Additional sensors were placed to obtain the ambient and test rig base plate temperatures. Moreover, the machine was placed in a chamber to isolate it from any air flow disturbance and to guarantee consistent and repeatable measurements.

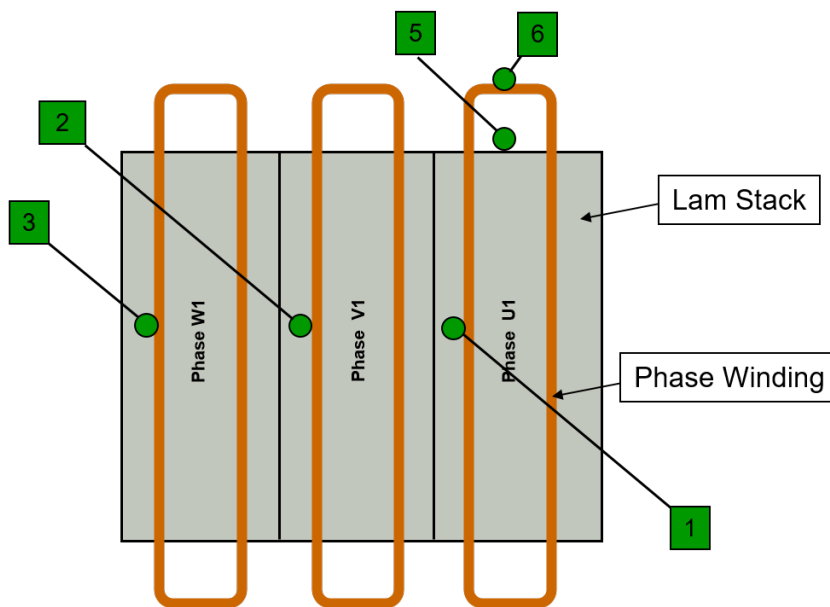


**Figure 5.8:** Thermo couples positions.

The average value of the measured mid-point temperatures of phases  $U$ ,  $V$  and  $W$ , positions 1, 2 and 3 in Fig. 5.8, is used to generate the average winding temperature value. The final thermal network is ultimately defined to estimate the average winding and magnet temperatures. Additional key nodes, such as the machine housing, motor base plate and the chamber temperature, are included in order to increase the model's

## 5 Motor Thermal Model

order. These nodes are located along the path between the windings and the magnets to the ambient temperature completing the modeling of the thermal behavior of the whole machine setup. Table 5.3 and Fig. 5.9 summarize the different sections of the setup that should be modeled in the thermal network.

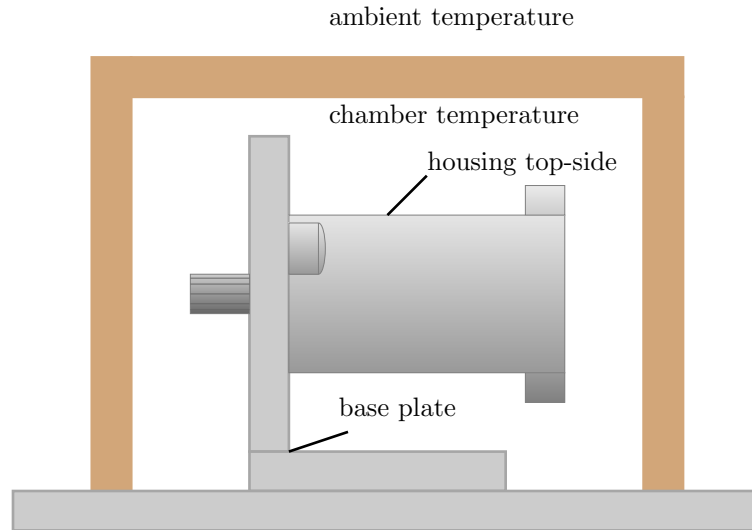


**Figure 5.9:** Test rig - thermal couples positions .

**Table 5.3:** Thermal network nodes mapping

<i>Name</i>	<i>Node</i>
base plate	1
chamber temperature	2
machine housing top-side	3
average winding temperature	4
average magnet temperature	5
ambient temperature	6

As shown in Fig. 5.5 and according to (5.18), each node has an associated thermal capacitance except for the ambient temperature node, which is the reference node. As for the heat sources, only nodes 4 and 5 will have one source, as they are directly related to the iron losses and Joule losses. The network identification procedure is described in the flow chart 5.10, where the first step involves the measurement of the corresponding temperatures.

Once the nodes or places of interest are defined, the model identification is performed in two steps. The first step considers only the steady state conditions, where the conduc-

tance matrix  $G_r$  is determined. The second focuses on the identification of the thermal capacitance of each node.

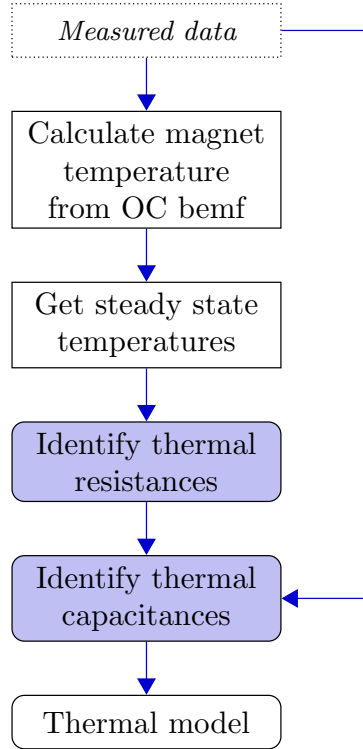


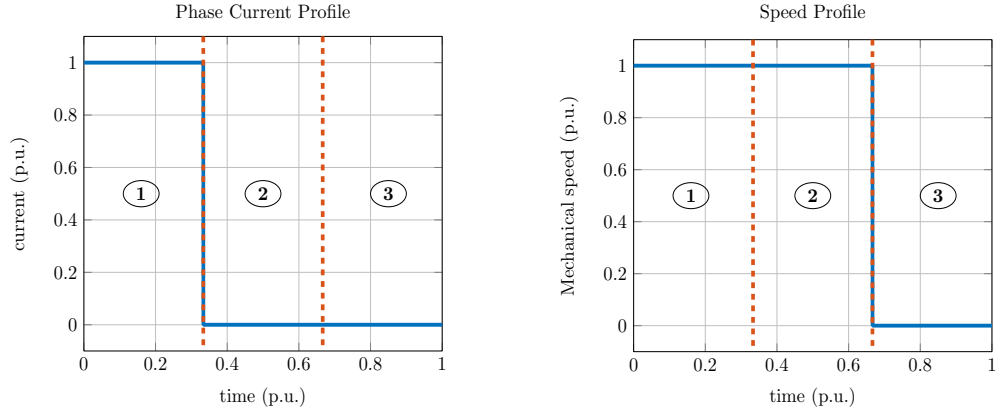
**Figure 5.10:** Thermal model identification.

The flowchart of Fig. 5.10 describes in general terms the procedure used to identify the equivalent thermal network from measured data. The latter is generated through a series of current and speed profiles. Analogue to a charge and discharge profile in an electric circuit, the machine is excited with different phase current values at a given rotor speed for a time period sufficient to reach a temperature steady state as shown in Fig. 5.11.

Three regions result from the phase current and speed profiles defined in Fig. 5.11a and 5.11b. The first region intends to generate enough heat to produce a temperature change in the nodes of interest that depends on the heat sources, which are represented by the winding Joule losses and the iron losses. On the other hand, the second region represents phase where the winding Joule losses are switched off and only the iron losses are generating heat as the rotor is still spinning. Finally the third region represents the cool down phase the machine will tend to reach the reference temperature value. To summarize, the three regions serve to isolate the different aspects of the thermal

## 5 Motor Thermal Model

network, such as the operation of the machine under load conditions, the effects of the open circuit iron losses and the passive cool down phase.



(a) Phase current test profile.

(b) Mechanical speed test profile

**Figure 5.11:** Measured data profile.

As there isn't a sensor available to obtain the magnets temperature, it is determined through an indirect measurement. The magnet temperature dependency of  $\psi_m$  is used to calculate indirectly temperature variations.  $\psi_m$  is derived from the bemf voltage at open circuit in the second profile part of Fig. 5.11 where the machine is not energized but the rotor is still be driven at constant speed. The deviation of  $\psi_m$  with respect to the room temperature value is used to calculate the delta temperature in the magnets. The *NdFeB* magnets used in the machine have a  $B_r$  temperature coefficient  $\alpha$  of  $-0.11\%/^{\circ}C$ . The average magnet temperature is then obtained in the following form:

$$T_{magnet} = \frac{1}{\alpha} \left( \frac{\psi_m(T)}{\psi_m(T_0)} - 1 \right) + T_0 \quad (5.23)$$

The temperature values at the end of the first profile region are used to obtain the thermal resistances, as the time duration of the first region is defined to reach steady state conditions. At this point it is important to remark, that some thermal resistances in the machine will vary with the rotor speed. The air flow in the air-gap affects the convective heat flow between rotor and stator [74], therefore a speed dependency of the resistance values associated to the magnet temperature node is expected. The lowest rotor speed is chosen to start with the thermal resistance identification in order to take into account the speed dependency of the resistances at increasing speed. The speed is set to 100rpm because at that speed the bemf voltage is large enough to obtain a decent estimation of the magnet temperature given the resolution of the data acquisition system used.

After having defined the test profile, the remaining part is to determine the amount of data required to identify the thermal network elements. The measured data is generated

according to the size of the thermal network, as the number of unknown conductances in  $G_r$  is given by (5.24):

$$N_{res} = \frac{n \cdot (n - 1)}{2} \quad (5.24)$$

where  $n$  is the number of nodes in the network and  $N_{res}$  the number of unknown conductances. The relationship in (5.24) is derived from the fact that the conductance matrix  $G_r$  is symmetric and the diagonal is the sum of the row elements according to (5.16). The measured data of one profile delivers  $n$  temperature values, which correspond to the nodes in the network. In the case of a 6-nodes thermal network the number of unknown elements is  $N_{res} = 15$ , therefore, the data of at least three sets<sup>2</sup> of measurements is required to recollect sufficient node temperature values. As a consequence of the minimum required amount of data, phase current values from 20A up to 45A in steps of 5A were set to generate enough data to solve the optimization problem of the conductance identification. Table 5.4 summarizes the operating points of the profiles used to identify the thermal elements of matrix  $G_r$ .

**Table 5.4:** Operating point of profiles according to definition in Fig. 5.11

<i>Phase current</i>	<i>Speed</i>
20 A	100 rpm
25 A	100 rpm
30 A	100 rpm
35 A	100 rpm
40 A	100 rpm
45 A	100 rpm

Opposed to the steps taken to derive a reduced thermal network from a complex model, the conductances need to be identified instead of being direct calculated. This is done by means of least squares based on the thermal node equation (5.20) but assuming thermal steady state, which means that the derivative of the node temperature is zero. The steady state can then be described as:

$$P_{l_n} = G_{r_{n1}} \cdot T_{1\dots} + G_{r_{nn}} \cdot T_{n\dots} + G_{r_{nm}} \cdot T_m \quad (5.25)$$

---

<sup>2</sup>One measurement set corresponds to the steady temperature of 6 nodes for one profile or operating condition, in order to have at least 15 different temperatures values, the temperature at three different profiles needs to be capture to obtain  $3 \cdot 6 = 18$  temperatures.

## 5 Motor Thermal Model

where  $m$  is the total number of nodes of the network and  $n$  is the  $n$ -th node. The expression in (5.25) is the basis for the formulation of the objective of the minimization problem:

$$f_{thermal}(x) = \sum_{n=1}^N \left[ (P_{l_n} - \hat{P}_{l_n})^2 \right] \quad (5.26)$$

where,  $\hat{P}_l = \nabla P_l \cdot x^T$

Where  $f_{thermal}$  is the objective function and  $N$  is the number of measured temperature values obtained from the profiles in table 5.4. The letters with a hat notation represent estimated values and the letters with no hat notation are the values of the identified data. Similarly as in previous sections, quadratic programming is used and the solution is limited to positive thermal conductances.

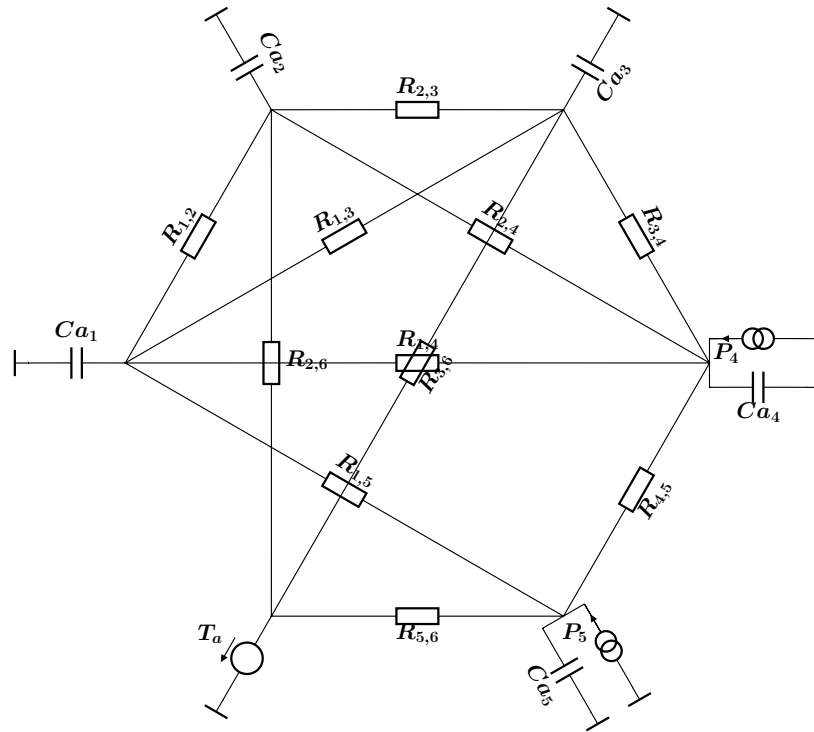


**Figure 5.12:** Thermal network.

Fig. 5.12 shows thermal network that results from solving the minimization problem. Similarly to the reduced model derived from the 66 nodes model in the previous section, the thermal resistors with values larger than  $100 \text{ kK/W}$  were removed from the final network. However the network elements are not completely identified, as the thermal capacitances associated to the nodes are still unknown. Following the steps illustrated in Fig. 5.10, the next procedure is the identification of the capacitances now that the

thermal conductances of the network are available. For this step, the same temperature node formulation, (5.20), of the previous section is employed and the same objective function, (5.21), as well. As the number of capacitances to be determined is the number of network nodes minus the reference node, the data of one profile is sufficient to identify them. So the selection criteria is the run with more signal excitation, which in the case of the profiles listed in table 5.4 refers to the profile with the highest phase current, 45 A.

The verification of the identified parameters was performed in Matlab/Simulink, where the thermal network is modeled in a state-space representation:

$$\dot{T}_r = C_r^{-1} \cdot (-G_r \cdot T_r + P_{l_r}) \quad (5.27)$$

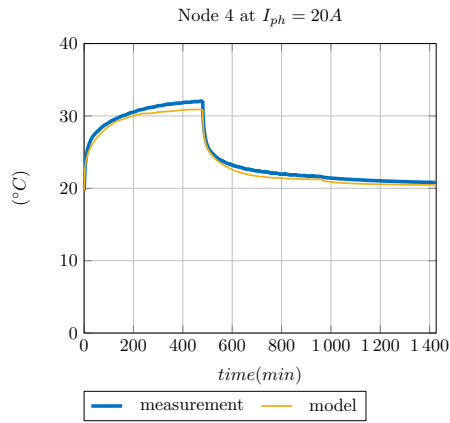
where  $T_r$  represents the target temperatures,  $C_r$  the identified capacitance matrix,  $G_r$  the equivalent admittance matrix and  $P_{l_r}$  the power losses. Additionally, the room temperature winding losses  $P_{r0}$ , which are part of  $P_{l_r}$ , are updated according to the copper temperature coefficient in the following form:

$$P_{resistive} = P_{r0} \left[ 1 + tempco_{cu}(T_{winding} - T_0) \right] \quad (5.28)$$

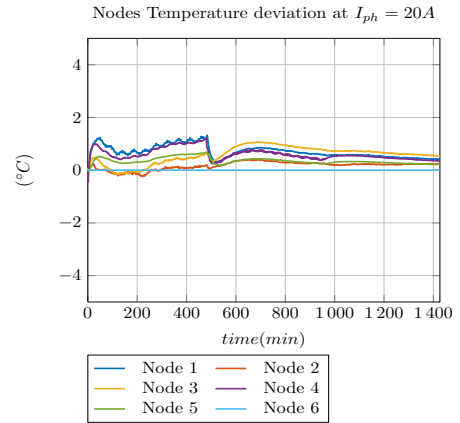
A recollection of the simulation results can be seen in Fig. 5.13 where the measured average winding temperature, node 4, is plotted with the estimated temperature of the thermal network and the deviation of the temperature estimates for all nodes is presented. The highest temperature deviation is observed at the profile with 45 A with values around  $\pm 2.5^\circ C$ , specially the deviations at the time mark of 500 min evidences the resistive network accuracy. However, the limitations of the reduced model are evident when looking at the dynamic sections of the profile where the error increases.

The identified thermal elements of the network in Fig. 5.12 are valid for 100 rpm as the rotor speed influences the heat flow between rotor and stator. The consideration of speed dependent effects are captured with additional measurements at different speeds. As already mentioned, the speed variation of thermal conductances happens between the magnet temperature node and the rest of the nodes, as it represents the air flow in the air-gap, therefore the conductances associated to the magnet temperature (node 5) are unknown parameters for the given speed and the remaining ones remain constant with the value identified in the previous step at 100 rpm.

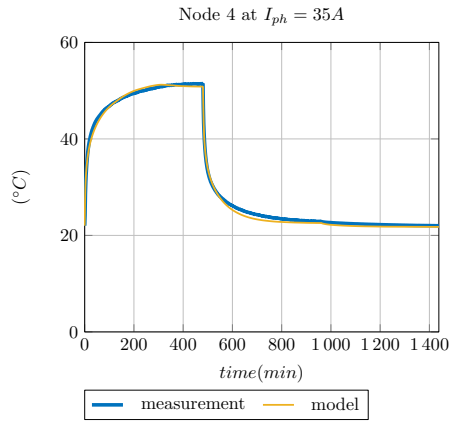
## 5 Motor Thermal Model



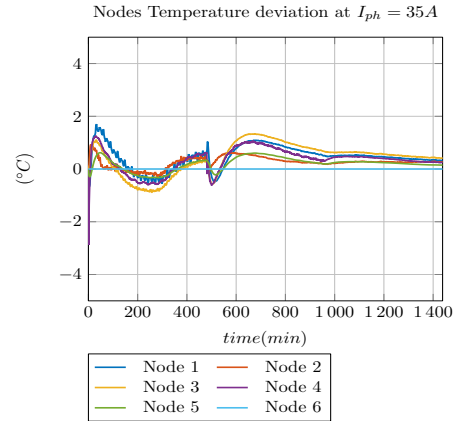
(a) Average winding temperature.



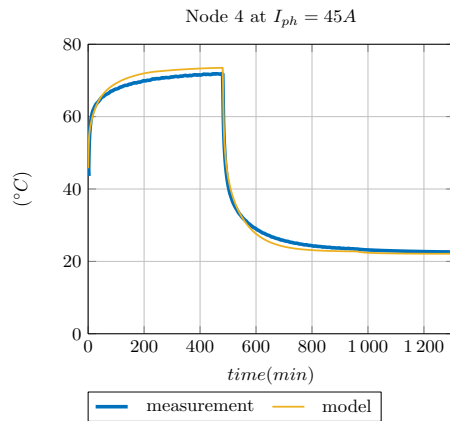
(b) Temperature deviations.



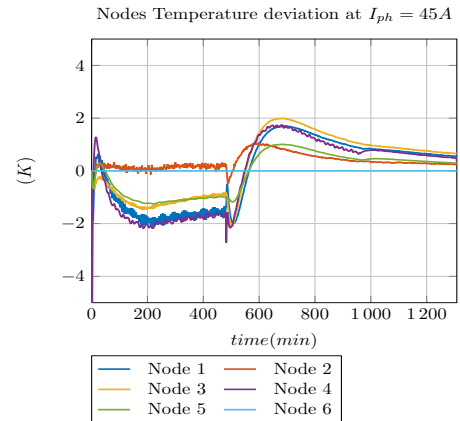
(c) Average winding temperature.



(d) Temperature deviations.



(e) Average winding temperature.



(f) Temperature deviations.

**Figure 5.13:** Reduced model temperature.

Fig. 5.14 summarizes the two step process to obtain the thermal network elements.

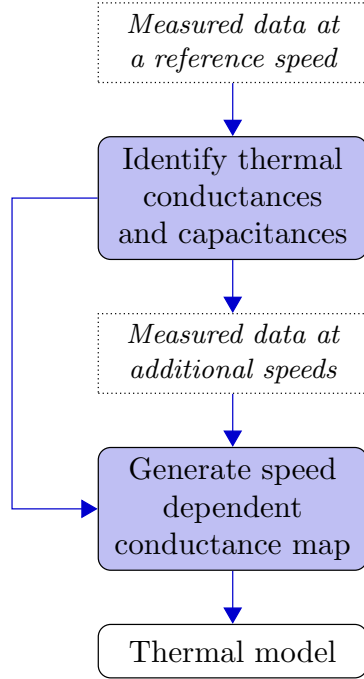


**Figure 5.14:** Thermal model identification for several rotor speeds.

The profiles used for the conductance identification for different speeds are listed in table 5.5.

**Table 5.5:** Operating point of profiles for speed dependent terms.

<i>Phase current</i>	<i>Speed</i>
50 A	700 rpm
35 A	1000 rpm
50 A	1300 rpm
20 A	2000 rpm

The conductance values at a given speed are interpolated using the values obtained from the identification procedure shown in flowchart 5.14. The speed dependent conductances associated to node 5 were saved as a look-up table that depends on the current speed as:  $G_{r_{5m}}(w_{rpm})$ , where  $m$  is the  $m$ -th node and  $w_{rpm}$  the mechanical speed in revolutions per second. Fig. 5.15 shows an example of the thermal resistance dependency on the rotor mechanical speed.

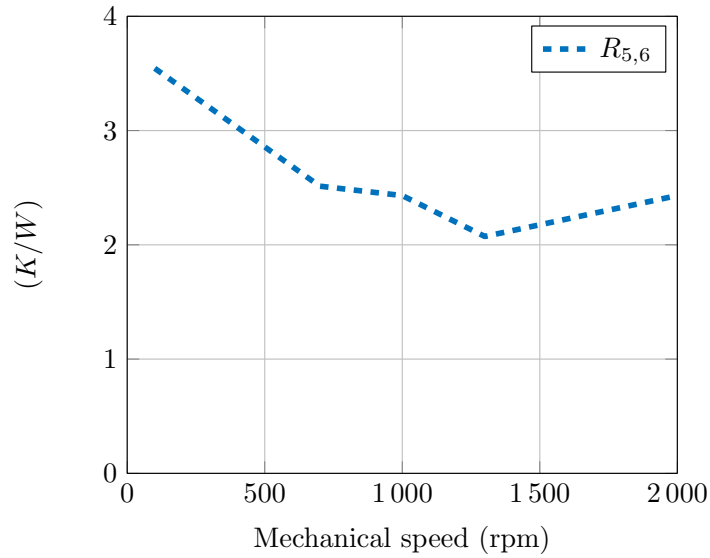


**Figure 5.15:** Speed dependent thermal resistance.

To summarize, the thermal network consist of a set of thermal capacitances  $C_n$  which were identified with the data obtained from profiles listed in table 5.4, the thermal conductances  $G_{r_{nm}}$  were identified with that data as well but they are mainly valid for  $100\text{ rpm}$ . In a second step, the speed dependency of the magnet node related conductances is addressed by generating additional data from profiles at different speeds as shown in table 5.5. The subset of conductances  $G_{r_{5m}}$  form a map that depends on the machine speed.

The validation of the thermal network is performed with two types of test profiles. The first one, shown in Fig. 5.16, focuses on different load scenarios ranging from no load to maximum load with different time duration.

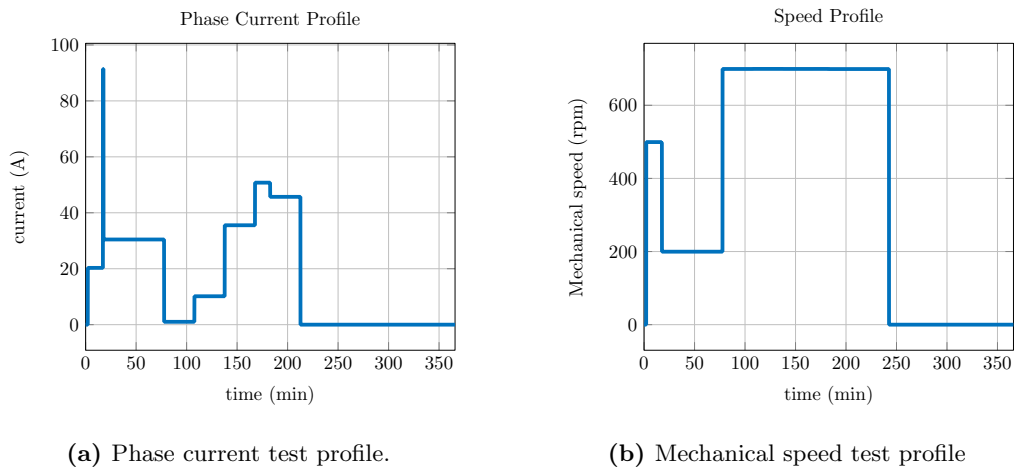


Figure 5.16: Test profile 1.

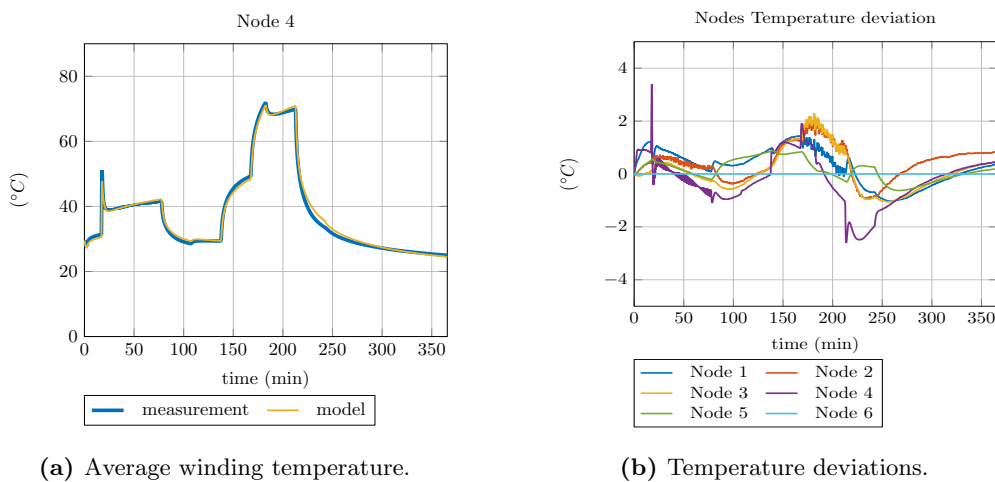
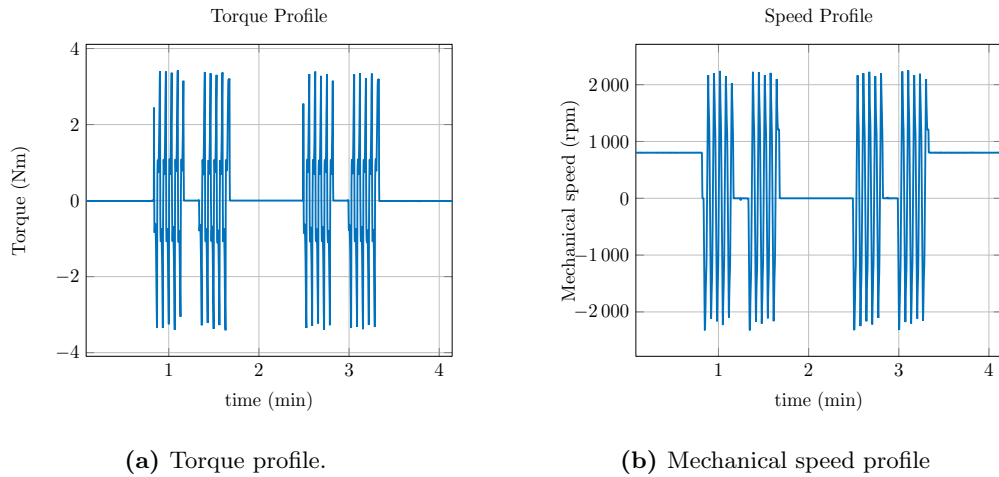


Figure 5.17: Reduced model temperature.

The initial conditions of the thermal network in the Simulink model were set to the ones of the measurement for each node. The corresponding temperature deviations and exemplary average winding temperature estimation can be appreciated in Fig. 5.17. The thermal network can predict the temperatures of interest with a maximum error of  $3.4^{\circ}\text{C}$  at the most dynamic part of the profile.

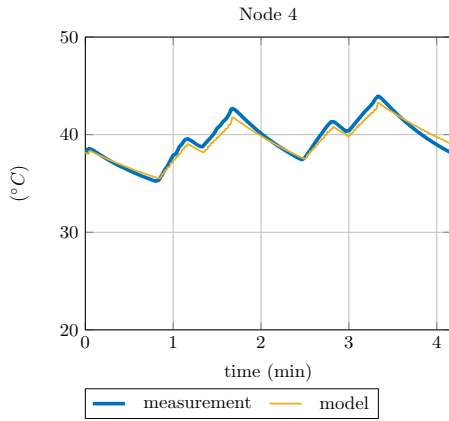
The next validation test intends to cover real operating conditions of the application where the machine is being used. The torque and speed profiles illustrated in Fig. 5.18 are an example of a typical Electric Power Steering (EPS) system parking cycle profile.



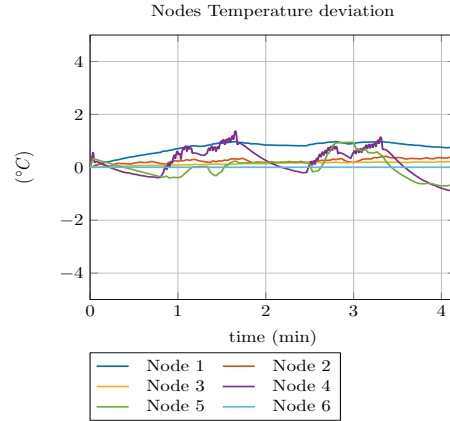
**Figure 5.18:** Steering park cycle profile.

The load torque and speed have changes rapidly between negative and positive values building a highly dynamic excitation. Moreover, in the first 50s of the profile the machine is driven at constant speed with no load in order to calculate the initial average magnet temperature from the bmf voltage. In the same fashion, the last 50s of the profile are used to obtain the end value magnet temperature. Finally, the initial conditions of each temperature node were set to match the initial state of the measured temperatures.

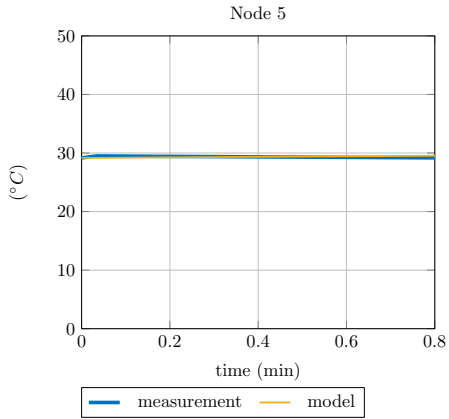
Fig. 5.19 summarizes the key aspects of the thermal model performance for the profile of Fig. 5.18. Although the profile is highly dynamic it has a short loading duration, leading to a small temperature rise on magnets and windings. Nevertheless, the average winding temperature reflects seamlessly the profile regions with and without torque load as shown in Fig. 5.19a. The maximum temperature deviation observed occurs at node 4 (winding temperature) with an underestimation of  $1.37^{\circ}C$ , conversely the magnet temperature remains almost unchanged for the duration of the profile, which can be observed in the two temperature close-ups in Fig. 5.19c and 5.19d.



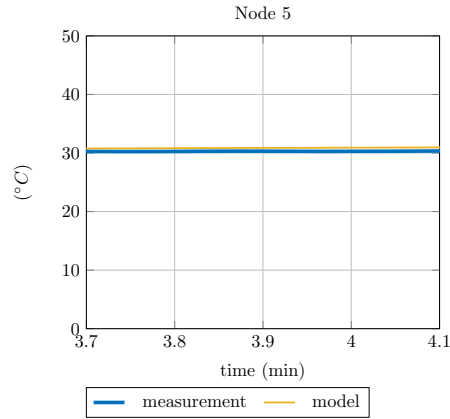
(a) Average winding temperature.



(b) Temperature deviation at node 3.



(c) Close-up of initial section of the average magnet temperature profile.



(d) Close-up of final section of the average magnet temperature profile.

**Figure 5.19:** Reduced model temperature.

It is important to notice that the node temperatures shown in Fig. 5.19 start at a higher value than the  $21^{\circ}\text{C}$  room temperature of the previous results. For the exercise of validating the model, it is reasonable to set the thermal network to the same initial conditions of the reference data, however in a real application this might not be possible. In the specific case considered in this work, a EPS system, the thermal network would be implemented in an embedded system, where normal operation conditions involve long periods of time without any activity of the machine. It is then quite possible to encounter scenarios where the system starts to operate at any environmental conditions from  $-40^{\circ}\text{C}$  to  $85^{\circ}\text{C}$  due to the proximity of the EPS system to the combustion engine or simply due to the seasonal temperature variations, winter or summer to name an example. This problematic is an issue for thermal models in general that lack of any feedback

on the initial temperatures. As in the application considered in this work, there is no thermal sensor inside the machine, it is not possible to initialize the thermal network, this could lead to large temperature estimation errors. A solution for this issue is the topic of the next chapter, where the average winding resistance and permanent magnet flux-linkage are estimated online in order to derive the corresponding temperature rises to update the node temperatures of the thermal network identified in this chapter.

A reduced modeling method was proposed to generate a machine thermal model without the knowledge of the machine's geometry or materials characteristics. The proposed approach was applied to an existing complex LPTN model or measured data. Where the for a 66 nodes LPTN a maximum temperature deviation of  $0.7^{\circ}C$  was achieved with a 13-nodes reduced network. Furthermore, using the generic formulation of the reduced model, a 6-nodes network was obtained directly from measured temperature data. The effects of the heat flow speed dependency in the rotor air-gap were considered and different machine load profiles were used to validate the model. It delivered a maximum temperature of  $3.4^{\circ}C$  at different test profiles.

## 6 Online Parameter Estimation

The initial chapters of this work presented a method to model synchronous machines and how to parameterize that model from FE data or measurements, how to obtain and include the iron loss in the machine model and the previous chapter focused on the thermal modeling of the machine. This final chapter will present the conjunction of all these pieces in order to come up with an online parameter estimation scheme.

In addition to that, as shown with the experimental identification, constrained optimization has the potential to make the identification robust compared to an unbounded one. Therefore the online parameter identification based on QP will be discussed in this chapter as well. The hardware used consist of a custom made inverter and the SoC board ZedBoard<sup>1</sup> which offers the flexibility to develop model based solutions in Matlab/Simulink and enables the possibility to simulate and test the algorithms beforehand. Table 6.1 summarizes the key aspects of the inverter used.

**Table 6.1:** Power electronics key figures.

nominal DC-link voltage	12V
rated phase current	160A
PWM switching frequency	20kHz

### 6.1 Hardware Setup

Continuing with the methodology adopted through all this work, the PMSM machine model used for the online parameter identification is based on the rotor reference frame voltage equations (2.9), the dq-axes flux-linkage expressions presented in (2.38)-(2.39) and the iron loss model illustrated Fig. 4.2. The resulting voltage expressions with consideration of the dynamic behavior are formulated in the following form:

$$u_d = R_s \cdot i_d - \omega_r \cdot \psi_q(i_{d_m}, i_{q_m}) + \dot{\psi}_d(i_{d_m}, i_{q_m}) \quad (6.1)$$

$$u_q = R_s \cdot i_q + \omega_r \cdot \psi_d(i_{d_m}, i_{q_m}) + \dot{\psi}_q(i_{d_m}, i_{q_m}) \quad (6.2)$$

where subscript  $m$  indicates the magnetizing currents that result after considering the iron loss effects. Expressions (6.1) and (6.2) define then the required data to implement the online parameter estimation. The rotor reference frame quantities and the rotor speed are the signals needed for the estimation algorithm. As for the phase currents, they are available through current sensors placed in the machine phase terminals in the

<sup>1</sup>see Appendix A.3 for a more detailed description of the hardware system used.

## 6 Online Parameter Estimation

power electronics printed circuit board (PCB). Similarly, the rotor speed is captured through an optical encoder attached to the machine shaft. At last, the voltages are typically estimated through models that use the demanded dq-axes voltages and the DC-link voltage as inputs. Nevertheless, the models need to be adjusted to include the nonlinear characteristics of the VSI. On top of that, additional effects come into play, as the inverter temperature affects the nonlinear behavior of the VSI as reported in [75]. This nonlinear effects are typically characterized offline [76] to be used later in the embedded system. On the other hand, a direct measurement of the phase voltages can be implemented with a few passive electronic components. Furthermore, the advantage of a voltage measurement is that all the VSI nonlinear effects, and temperature influences are captured in the measurement. For these reasons and together with the goal of a robust estimation, the voltage measurement option is preferred in this work.

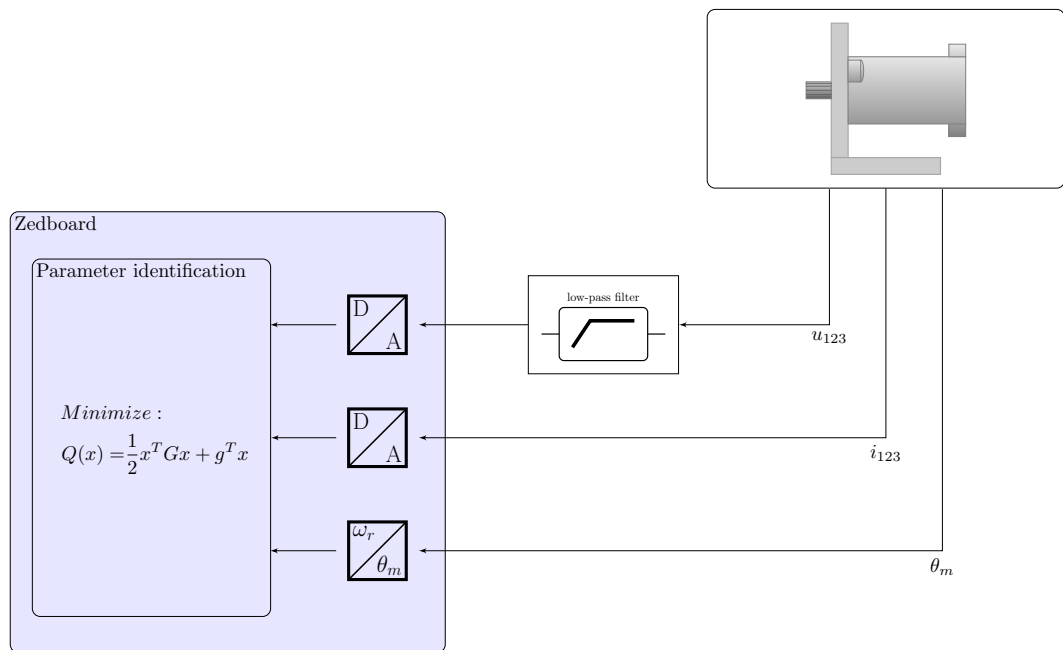


**Figure 6.1:** Hardware setup.

The main task in the voltage measurement setup is the extraction of the voltage signal associated to fundamental frequency of operation of the machine. The PWM based voltages are driven contain a large amount of harmonic distortion due to the nature of the constant switching between the DC-link voltage and ground, this reduces the tasks to a low-pass filter, which is intended to reject the high frequency harmonic content of the voltage signals. Therefore a second order low-pass filter was chosen, as shown Fig. 6.2 which consist only of passive elements making it an attractive and low cost solution.

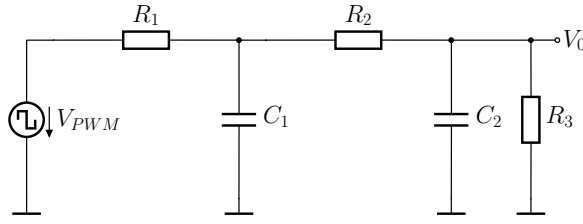


**Figure 6.2:** Second order low-pass filter.

A second order low-pass filter was selected in a trade of simplicity and voltage ripple minimization. The filter can be then designed according to specific conditions of the application, firstly the machine speed range of operation and the PWM switching frequency,  $f_{PWM}$ , need to be taken into account to define the cut-off frequency. Fig. 6.2 depicts the low-pass filter circuit used for each of the three phase terminal voltages. The transfer function of the filter can be easily described in the Laplace domain as shown in (6.3).

$$H(s) = \frac{R_3}{s^2 C_1 C_2 R_1 R_2 R_3 + s(C_1 R_1 (R_2 + R_3) + C_2 R_3 (R_1 + R_2)) + (R_1 + R_2 + R_3)} \quad (6.3)$$

where symbol  $s$  represents the Laplace operator variable and  $H(s)$  denotes the transfer function in question. The frequency response is then set in the way that the frequency at  $3dB$  of attenuation is one decade apart from  $f_{PWM}$ , which means  $2kHz$  for  $f_{PWM}=20kHz$ . The resulting normalized Bode diagram in Fig. 6.3a shows then an attenuation of  $31dB$  at  $20kHz$ . The final values of the resistors and capacitors are listed in table 6.2.

**Table 6.2:** Loss-pass filter values.

$R_1$	$100\text{ k}\Omega$
$R_2$	$4.2\text{ k}\Omega$
$R_3$	$560\ \Omega$
$C_1$	$10\text{ nF}$
$C_2$	$100\text{ nF}$

The maximum mechanical speed of the application is  $7000\text{ rpm}$ , which traduces in  $466\text{ Hz}$  for the 4-pole pair machine. The cut-off frequency of  $2\text{ kHz}$  is then far enough to avoid excessive attenuation of the signal's fundamental frequency as can be appreciated in Fig. 6.3a.

## 6 Online Parameter Estimation

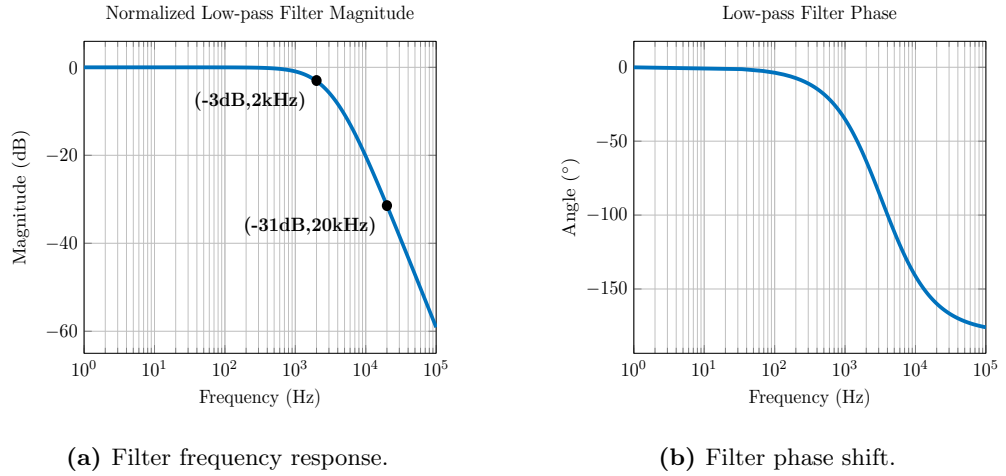


**Figure 6.3:** Filter's Bode diagram.

However, the phase shift produced by the filter on the input signal has a big impact on the voltage signals, once they are transformed in to the rotor reference frame (2.7). As illustrated in Fig. 6.4 the additional phase angle  $\Delta\theta$  compromise the real value of the dq-axes components of the voltage vector, leading to deviations on the online parameter identification.

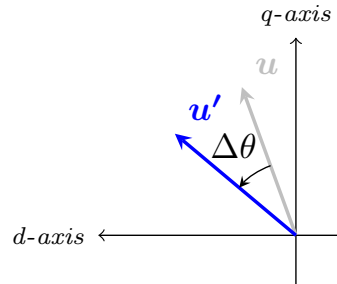


**Figure 6.4:** Filter phase shift of the voltage signals.

The frequency dependent phase shift of Fig. 6.3b can be used to express it in the form of a group delay as:

$$t_{delay} = \frac{\Delta\theta}{\omega} \quad \text{with} \quad \omega = 2\pi f \quad (6.4)$$

where the transport delay time  $t_{delay}$  remains almost constant for frequency values below the cut-off frequency and specially for frequencies up to  $466\text{ Hz}$  as can be observed in Fig. 6.5.

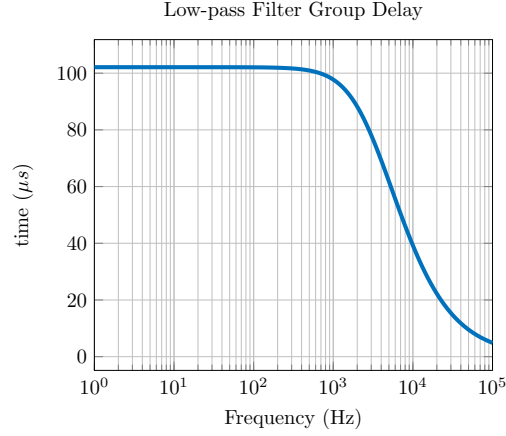


**Figure 6.5:** Low-pass filter group delay.

Being the transport delay constant for the frequency range of interest enables an easy form to compensate the phase shift expected in the filtered voltage signals. The transport delay can be easily calculated from the transfer function (6.3), when parting from the phase shift by replacing the Laplace operator  $s$  by  $j\omega$ :

$$\Delta\theta = \angle H(j\omega) \quad (6.5)$$

Further development of (6.5) leads then to :

$$\Delta\theta = \arctan \frac{\omega(C_1R_1(R_2 + R_3) + C_2R_3(R_1 + R_2))}{R_1 + R_2 + R_3 + \omega^2(C_1C_2R_1R_2R_3)} \quad (6.6)$$

As the transport delay is almost constant in the frequency range of interest and to keep the things simple, the phase shift can be then calculated towards zero frequencies, leading to the following simplified expression:

$$\Delta\theta \approx \frac{\omega(C_1R_1(R_2 + R_3) + C_2R_3(R_1 + R_2))}{R_1 + R_2 + R_3} \quad (6.7)$$

To obtain the transport delay<sup>2</sup> (6.7) is replaced in (6.4):

$$t_{delay} \approx \frac{(C_1R_1(R_2 + R_3) + C_2R_3(R_1 + R_2))}{R_1 + R_2 + R_3} \quad (6.8)$$

<sup>2</sup> The transport delay value obtained with (6.8) was cross-checked with the voltage step response of the filter in question. The measurement results are shown in Appendix A.5.

## 6 Online Parameter Estimation

Finally, for the online parameter estimation, the phase shift of the filtered voltage signals can be compensated with the knowledge of the transport delay in the following form:

$$\begin{bmatrix} u_d \\ u_q \end{bmatrix} = \begin{bmatrix} \cos(t_{delay} \cdot \omega_r) & -\sin(t_{delay} \cdot \omega_r) \\ \sin(t_{delay} \cdot \omega_r) & \cos(t_{delay} \cdot \omega_r) \end{bmatrix} \cdot \begin{bmatrix} u'_d \\ u'_q \end{bmatrix} \quad (6.9)$$

where the primed symbols represent the filtered voltages and  $\omega_r$  the electrical angular rotor frequency.

The second aspect to consider is the attenuation produced by the filter, which can be regarded as small but it is still an additional source of error for the online estimation. In the same way as with the phase shift calculation, it can be obtained analytically from the filter's transfer function (6.3) as:

$$|H(j\omega)| = \frac{R_3}{\sqrt{(R_1 + R_2 + R_3 - \omega^2 C_1 C_2 R_1 R_2 R_3)^2 + (\omega(C_1 R_1 (R_2 + R_3) + C_2 R_3 (R_1 + R_2)))^2}} \quad (6.10)$$

The attenuation factor is simply formulated with respect to the DC gain of the filter and the angular rotor frequency in the following form:

$$A_{tt_{factor}} = \frac{\sqrt{(R_1 + R_2 + R_3 - \omega_r^2 C_1 C_2 R_1 R_2 R_3)^2 + (\omega_r(C_1 R_1 (R_2 + R_3) + C_2 R_3 (R_1 + R_2)))^2}}{R_1 + R_2 + R_3} \quad (6.11)$$

the correction factor  $A_{tt_{factor}}$  is then saved in the embedded processor in the form of look-up table. The resulting attenuation factor for the filter of parameters 6.2 is shown in Fig. 6.6, where the voltage vector  $\vec{u}$  is corrected around 1.2% at 5000rpm.

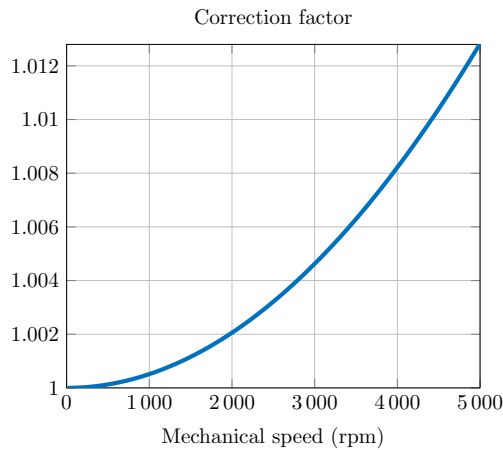


**Figure 6.6:** Compensation factor for the voltage attenuation

This section addressed a way to get hold of the machine voltage signals for an online parameter estimation. Instead of the conventional approach of modeling the inverter non-linear characteristics to estimate the dq-axes voltages, a simple passive low-pass filter was proposed to accurately capture the non-linear behavior contained in the voltage signals. Furthermore, the two side effects produced by the filter, frequency dependent phase shift and magnitude attenuation, were thoroughly addressed. Moreover correction factors such as the transport delay  $t_{delay}$  and the magnitude compensation factor  $A_{tt_{factor}}$  were analytically calculated minimizing the characterization effort of such filter approach.

## 6.2 Parameter Identification

The required signals to perform the online parameter identification have been considered and a filter stage for the machine's terminal voltages has been introduced, where the attenuation and phase shift imposed on the voltage signals were analyzed as well. The following step is then to define the parameter identification scheme and for that purpose the machine is modeled by expressions (6.1) and (6.2) in a generic way. In addition, the approach presented in section 2.2.1 provides a tool to describe the non-linear behavior of the flux-linkages. Therefore, the online usage of the flux-linkage expressions is completely aligned with the initial steps where FEA simulation data and test rig measurements were used to obtain the coefficients or parameters of flux-linkage expressions based on (2.38) and (2.39). Consequently, the machine<sup>3</sup> used in this section underwent an offline identification procedure in order to determine the appropriate polynomial degree for the flux-linkage expressions and to obtain reference values for the polynomial coefficients. It is then the machine that was characterized at different magnet temperatures in section 3.5.1. It was also shown that an appropriate polynomial degree for the machine was  $n = 3$ . As a result the dq-axes voltage equations (6.1) and (6.2) can be written in terms of the flux-linkage expressions (2.38) and (2.39) for  $n = 3$  as:

$$\begin{aligned}
 u_d = R_s i_d - \omega_r i_{q_m} & \underbrace{\left( l_{qd10} + l_{qd30} i_{q_m}^2 + c_{dq01} i_{d_m} + \frac{c_{dq11} i_{d_m}^2}{2} \right)}_{L_q(i_{d_m}, i_{q_m})} \\
 & + \underbrace{\left( l_{dq10} + 2l_{dq20} i_{d_m} + 3l_{dq30} i_{d_m}^2 + \frac{c_{dq11} i_{q_m}^2}{2} \right)}_{L_{dd}(i_{d_m}, i_{q_m})} \frac{di_{d_m}}{dt} + \underbrace{\left( c_{dq01} i_{q_m} + c_{dq11} i_{d_m} i_{q_m} \right)}_{L_{dq}(i_{d_m}, i_{q_m})} \frac{di_{q_m}}{dt}
 \end{aligned} \tag{6.12}$$

<sup>3</sup>specification data of the machine can be found in appendix A.2

$$\begin{aligned}
 u_q = & R_s i_q + \underbrace{\omega_r \left( \psi_m + \frac{c_{dq01} i_{qm}^2}{2} \right)}_{\psi_m(i_{qm})} + \underbrace{\omega_r i_{dm} (l_{dq10} + l_{dq20} i_{dm} + l_{dq30} i_{dm}^2 + \frac{c_{dq11} i_{qm}^2}{2})}_{L_d(i_{dm}, i_{qm})} \\
 & + \underbrace{(c_{dq01} i_{qm} + c_{dq11} i_{dm} i_{qm})}_{L_{qd}(i_{dm}, i_{qm})} \frac{di_{dm}}{dt} + \underbrace{(l_{qd10} + 3l_{qd30} i_{qm}^2 + c_{dq01} i_{dm} + \frac{c_{dq11} i_d^2}{2})}_{L_{qq}(i_{dm}, i_{qm})} \frac{di_q}{dt}
 \end{aligned} \tag{6.13}$$

In addition to the steady state flux-linkage terms, the voltage expressions (6.12) and (6.13) incorporate terms to describe the dynamic behavior of the voltages such as the incremental self and mutual inductances. Due to the analytical formulation of the flux-linkages an expression for the incremental inductances can be obtained according to (2.11) as indicated under the braces in (6.12) and (6.13). On the other hand, the iron loss effects are also included in the voltage formulation in the form of magnetizing currents  $i_{dqm}$  which are derived from the equivalent loss resistors obtained in section 4.2.2. The equivalent circuit get then extended based on (6.12) and (6.13) as depicted in Fig. 6.7.

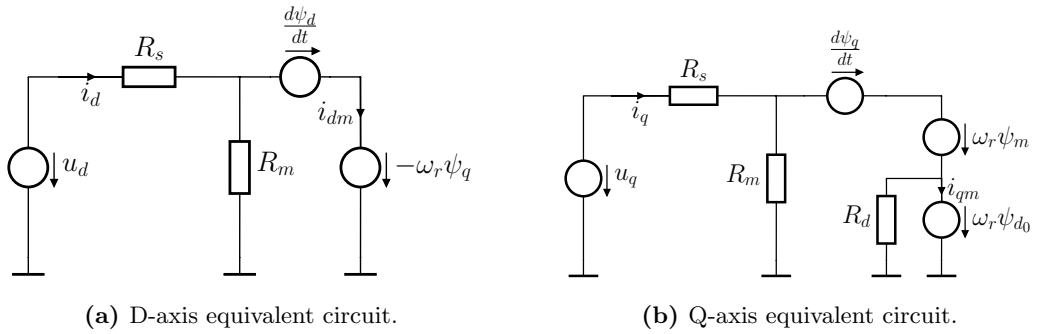


**Figure 6.7:** Voltage model considering iron losses

### 6.2.1 Optimization Solver

The parameter identification carried out in chapter 3 was based on least-square minimization by means of QP optimization, initially for FEA simulation data and in a second step the identification was performed using measured data. For practical reasons, the QP optimizer used in both methods was the built-in Matlab function *quadprog*. However, for an implementation in an embedded system, the QP algorithm should be fast and suitable for real-time applications.

Early QP methods like Online Active Set Strategy (qpCOMP), based on nonsmooth equations/successive quadratic programming, showed to be robust and fast compared to other contemporary solvers [77, 78] despite being implemented in *C* there are no

available files of the solver, as the implementation of such algorithm isn't within the scope of this work, it was discarded. On the other hand the interior-point based solver Online Active Set Strategy (OOQP) [79] is an algorithm intended for object-oriented designs. Even though the solver package offers interfaces to different software platforms including Matlab, porting the  $C++$  code into  $C$  is also not an option. In contrast to the previous solvers, Online Active Set Strategy (qpOASES) is an active set based method [80] which is available in  $C$ , furthermore its use in areas such as model predictive control was reported as well. Similarly, the method Operator Splitting Quadratic Program (OSQP) is a solver based on the alternating direction method of multipliers (ADMM) which delivers high accuracy solutions at low computational cost [81]. It is available in the  $C$  language and suitable for embedded code generation as demonstrated in [82]. In addition to this, the authors of the method carried out a benchmark against several open-source and commercial available QP solvers demonstrating the excellent performance of OSQP compared to the other methods. Furthermore OSQP outperformed qpOASES in that benchmark in terms of less failure rate, as qpOASES wasn't able to solve several test problems. However the authors in [81] emphasize that the method ADMM in OSQP leads inherently to reduced accuracy compared to interior-point based methods like qpOASES but at the same time OSQP can deal with larger problems and a more number of constraints than qpOASES. Finally OSQP was the selected method to solve the online parameter identification problem in question.

### 6.2.2 Solver Performance

To evaluate the fitness of OSQP for the end application two aspects were considered, accuracy and execution time in the target platform. The accuracy was assessed by looking at the relative deviation of the solution with respect to *quadprog* when using measured data. This was done with the data set obtained for the offline identification of IPMSM<sup>4</sup> presented in section 3.5.1. The deviation in percentage of each coefficient with respect the values obtained with *quadprog* is listed in table 6.3. The comparison was performed in Matlab but the version of OSQP was a  $C$  compiled one, which is exact the same version that can be integrated in the target development environment.

---

<sup>4</sup> details of the solver settings and the values of the identified coefficients can be found in Appendix A.4

**Table 6.3:** IPMSM - identified coefficients relative deviation

Parameter	%
$R_s$	$-1.78e-6$
$\psi_m$	$1.62e-5$
$l_{dq10}$	$4.46e-4$
$l_{qd10}$	$-6.8e-6$
$l_{dq20}$	$-15.4e-3$
$l_{dq30}$	$-30.8e-3$
$c_{dq01}$	$4.11e-4$
$c_{dq11}$	$3.41e-4$

It is important to notice that the values delivered by OSQP differ in a small magnitude, below thirty thousandth of one percent. Therefore the proposed solver can be used without concerns of accuracy reduction<sup>5</sup>. Moreover, as a consequence of the overall insignificant deviations, the fitness of the model doesn't get compromised. This is verified through the CoD in table 6.4 as well.

**Table 6.4:** IPMSM - Coefficient of determination

	CoD
<i>quadprog</i>	0.999921532634165
OSPQ	0.999921532634197

As already mentioned, the embedded system used is a ZedBoard. This is a SoC solution with an advanced RISC machines (ARM) processor connected to Xilinx-FPGA, where the development environment is Matlab/Simulink in conjunction with Xilinx/Vivado to automatically generate the code that should run on the Zedboard. The *C* code of the solver OSQP is allocated in the ARM processor part, whereas the motor control, PWM generation, encoder unit and ADCs were implemented in the field-programmable gate array (FPGA) part as illustrated in Fig. 6.8. The main function responsible for the communication with external devices, the drive state machine<sup>6</sup> is allocated in the ARM processor

<sup>5</sup>comparisons with data sets of other machines are presented in Appendix A.4 as well

<sup>6</sup>The drive state machine monitors any fault in the hardware and motor control configuration.

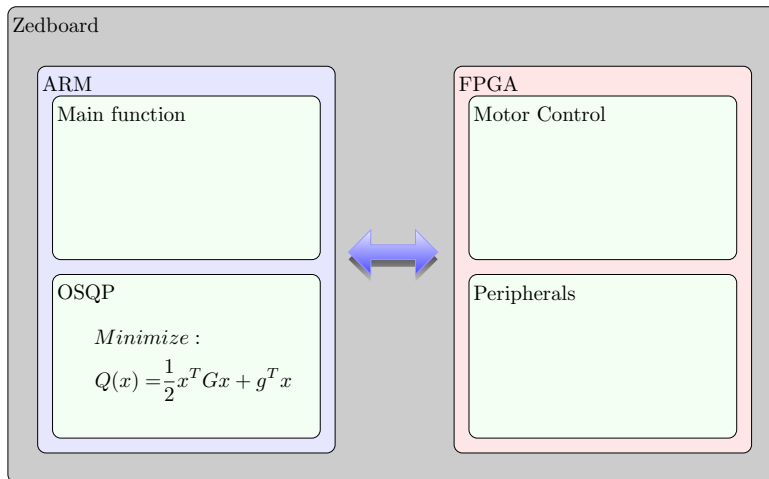


**Figure 6.8:** Software setup.

In order to assess the computational cost of OSQP in the Zedboard, the data used in the previous step were imported into Simulink. For the time measurement two scenarios were considered. The first one was normal operation, which is defined as the time elapsed for one identification and the second one was truncated operation where the maximum number of iterations to solve the problem is reached. The latter was created by manipulating the input in a way that the gradient data differs significantly from the original values.

**Table 6.5:** OSQP - computational time duration

Scenario	average time
normal operation	2.62ms
max. iterations	4.74ms

The average time observed when the maximum number of iterations was reached in table 6.5 is a good indication that the solver itself can be used for the intended purpose as 4.74ms leaves plenty of room for the online identification algorithm. The rationale behind this relies on the fact that the thermal constant of the temperature dependent parameters in the voltage equations (6.12) and (6.13) are much larger than 4.74ms. The profiles in Fig. 5.13 used to parameterize the thermal model evidenced thermal constants in the order of hours, whereas for fast transients as in Fig. 5.17 winding temperature changes were observed in the magnitude of seconds, furthermore data time resolution in the order of hundred of milliseconds was more than sufficient to represent rapid changes in temperature of Fig. 5.19. Therefore an execution period of the QP solver task of 20ms leaves plenty of room for additional overhead and it is still fast enough that the

temperature dependent parameters can be considered constant for several consecutive execution periods.

### 6.3 Identification Algorithm

Similar to the offline parameter identification presented in section 3.5.1, the QP solver is used to minimize a sum of squared errors of the dq-axes voltage signals as :

$$f(x) = \sum_{k=1}^N \left[ (u_{d_k} - \hat{u}_{d_k})^2 + (u_{q_k} - \hat{u}_{q_k})^2 \right] \quad (6.14)$$

with,  $\hat{u}_d = \nabla u_d x^T$ ;  $\hat{u}_q = \nabla u_q x^T$

where the  $N$  represents the number of data points available and the objective function in (6.14) is used to formulate the optimization problem as well in the following form:

$$\begin{aligned} \text{Minimize} \quad & Q(x) = \frac{1}{2} x^T G x + g^T x \\ \text{with,} \quad & \psi_{m_{min}} < \psi_m < \psi_{m_{max}} \\ & L_{d_{min}} < l_{dq10} < L_{d_{max}} \\ & L_{q_{min}} < l_{dq10} < L_{q_{max}} \\ & R_{s_{min}} < R_s < R_{s_{max}} \end{aligned} \quad (6.15)$$

$$\begin{aligned} \text{where,} \quad & G = \nabla u_d \nabla u_d^T + \nabla u_q \nabla u_q^T \\ & g = -2u_d \nabla u_d - 2u_q \nabla u_q \end{aligned}$$

where the matrix  $G$  and vector  $g$  are inputs to the OSQP solver. In the QP problems solved so far, these two inputs were calculated just once using the available data. However the optimization problem described by (6.14) and (6.15) shall be solved every 20ms as defined in the previous section. This yields two options, the use of an input buffer with a length  $N$  or a scheme where  $G$  and  $g$  are calculated recursively from the last input data points. The former is equivalent to the offline approach with a finite set of data and the latter refers to a recursive filter structure. The memory and computational cost of the first option makes it not an adequate solution for an online algorithm, whereas the second one requires less memory space and offers possibility to average the input values. The proposed filter scheme is then depicted in Fig. 6.9, the task called *QP interface* filters the input data to obtain  $G$  and  $g$  with the same filter structure and coefficients  $b_0$  and  $b_1$ .

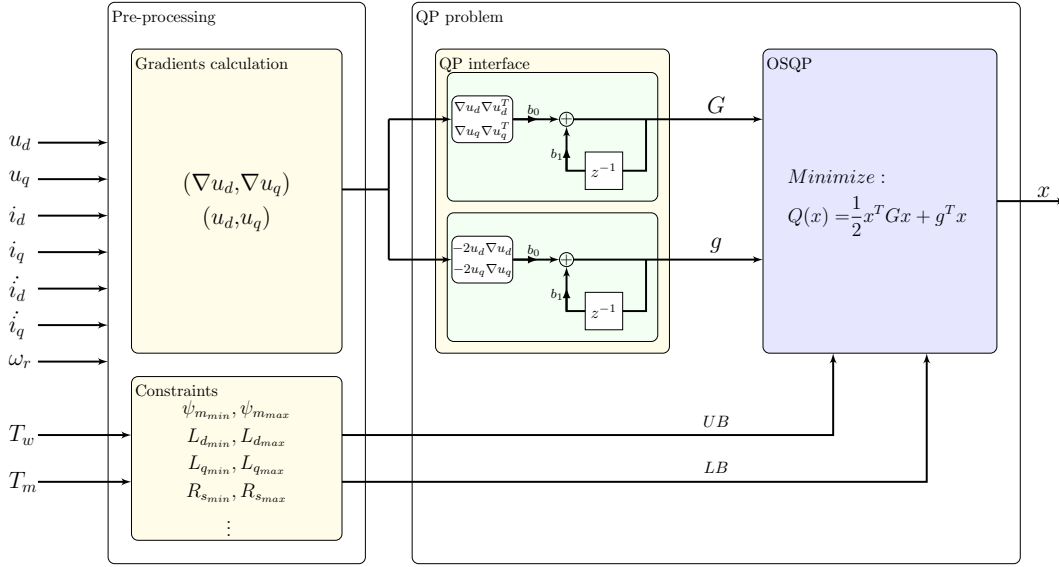


Figure 6.9: Identification block diagram.

The algorithm architecture depicted in Fig. 6.9, recollects the elements studied and used so far. It is a QP based approach which seeks to minimize recursively the sum of dq-axes voltage squared errors, while the solution space is constrained by upper and lower boundaries of the target parameters represented by  $UB$  and  $LB$  respectively. It is completely aligned with the previous steps based on FEA data and measured data in terms of flux-linkage modeling and parameters.

### 6.3.1 Dynamic Constraints

As shown in Fig. 6.9, besides the already mentioned inputs  $G$  and  $g$ , the OSQP solver also expects the constraints  $UB$  and  $LB$ , which define the valid solution range for each target parameter in the solution vector  $x$ . If the constraints are ignored when solving the optimization problem it then gets reduced to a mere least squared minimization problem as already discussed in section 3.1.1. However the constraints offer the possibility to improve the robustness of the identification for all the machine's operating range.

One of the main issues with a passive parameter identification is the signal's information, for example at decreasing rotor speeds, the flux-linkage terms  $\psi_d \omega_r$  and  $\psi_q \omega_r$  will tend to zero. Similarly, the phase resistance voltage drops  $R_s i_d$  and  $R_s i_q$  will tend to zero at decreasing phase current as well. During the machine's operation, certain working regions are critical to obtain an accurate estimation, due to the low magnitude of the machine voltage that cannot be properly captured by the system's ADC. Therefore a minimum voltage magnitude for the resistive terms and for the speed dependent terms is required. Likewise a minimum current magnitude  $I_{min}$  is introduced to guarantee a

significant voltage value of the resistive terms in the dq-axes voltage equations. On the other hand, the flux-linkage terms are rotor speed dependent, for that reason a minimum rotor speed  $\omega_{r_{min}}$  is introduced as well.

The keen reader would notice that the valid regions according to the current or rotor speed don't necessarily occur at the same time. Therefore scenarios where the rotor speed is below  $\omega_{r_{min}}$  but the current is above  $I_{min}$  and vice-versa are plausible. In the former case only the winding resistance identification would be reliable and in the latter  $\psi_m$  could be estimated properly. In order to backup the identification algorithm in those two scenarios, two dynamic constraints are introduced as proposed in Fig. 6.10, the first one for  $R_s$  and the second one for  $\psi_m$ . They are dynamic because the constraints are given by tolerance bands that depend either on  $I_{min}$  or  $\omega_{r_{min}}$ . Therefore, in the corresponding invalid regions, the value of  $R_s$  or  $\psi_m$  is fixed through the tight tolerance band, as the input signals quality in an invalid region might lead to reduced accuracy. Nevertheless, the simple action of fixing the parameter's value doesn't improve the estimation but if the parameter in question is derived from other source, performance and robustness of the identification algorithm can be enhanced, more on this aspect is discussed in section 6.4.

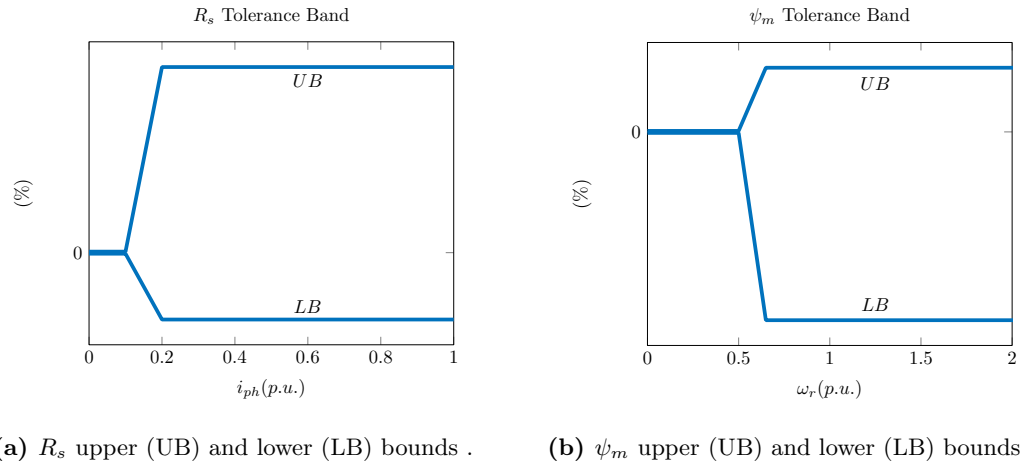


**Figure 6.10:** Example of dynamic tolerance bands.

## 6.4 Hybrid Identification Scheme

In the specific case of the identification of  $R_s$  active methods like the ones using signal injection [29, 30, 7] exhibit a clear advantage, as the resistive voltage drop is actively generated by the injected signal enabling an identification of  $R_s$  even at the absence of the dq-axes currents of the fundamental frequency. However it is important to note that advantage can be eclipsed by the additional noise created by the imposed high frequency signal. On the other hand, the proposed method seeks to use the information provided

by the machine thermal model discussed in chapter 5 to backup the estimation of  $R_s$  and  $\psi_m$  in the invalid regions of operation. The average winding temperature is used to update the corresponding winding resistance and in the case of invalid rotor speed region,  $\psi_m$  is derived from the average magnet temperature, as illustrated in Fig. 6.11.

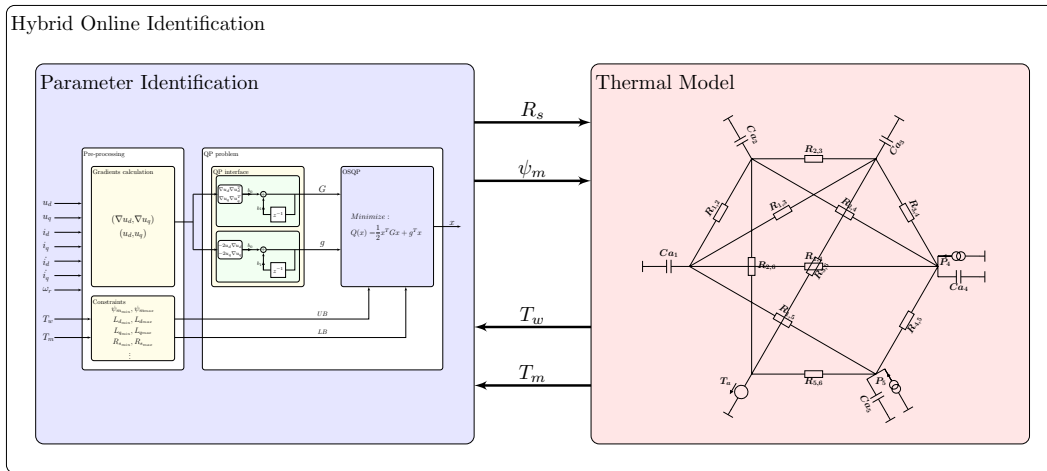
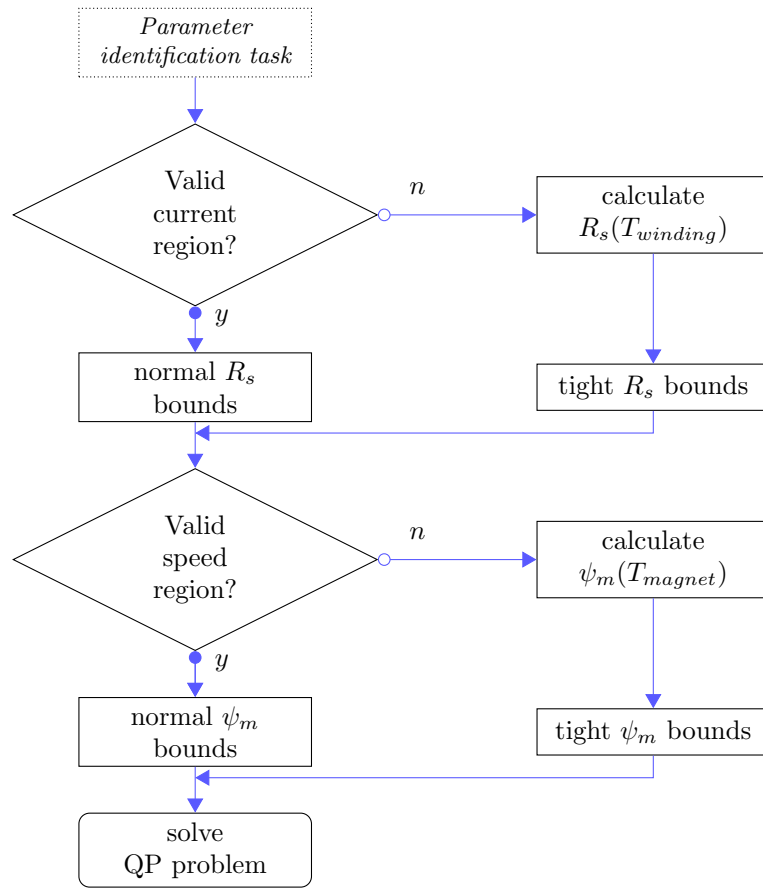


Figure 6.11: Identification block diagram.

The average winding temperature  $T_w$  and the average magnet temperature  $T_m$  are used to calculate the winding resistance or permanent flux-linkage, in addition their bounds are set to a minimum as shown in Fig. 6.10 in order to set them as constant parameters and solve the QP problem for the remaining parameters, as explained in the flow chart in Fig. 6.12.



**Figure 6.12:** Identification block diagram.

Conversely the winding or magnet temperature are updated while the machine is operating in corresponding valid regions, this helps to improve the thermal model's estimation and also to correct these temperature nodes in case the thermal model has been initialized with the incorrect temperature. This is a plausible scenario when the system has been inactive for long periods of time and external factors affect the machine temperature. The flow chart in Fig. 6.13 describes then the update procedure of  $T_m$  and  $T_w$ .

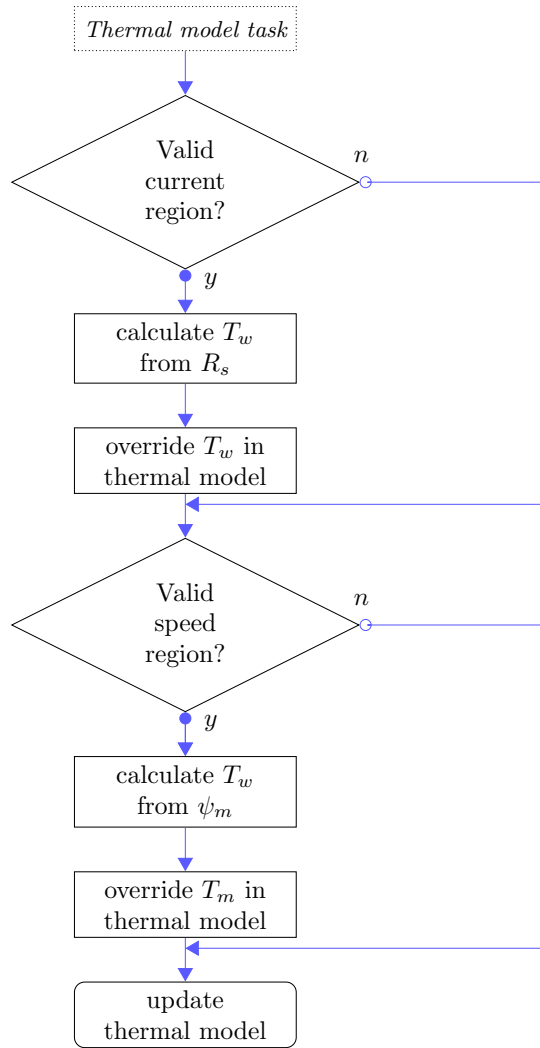


**Figure 6.13:** Temperature nodes update.

A scheme to backup the online parameter estimation of  $R_s$  and  $\psi_m$  has been established, however the remaining parameters or coefficients in (6.12) and (6.13) need to be considered as well. The biasing effect of the permanent magnet flux-linkage on the overall flux-linkages was presented in section 3.3.4 and the corresponding experimental determination of the associated model coefficients was introduced in section 3.5.2 as well. This machine characterization enables the analysis of the possible variations of the flux-linkage coefficients with respect to  $\psi_m$  due to manufacturing tolerances or temperature effects. According to (2.61) and (2.62), for  $n = 5$ , the coefficients with subscript  $l_{dq10x}$  and  $l_{qd10x}$  depict  $\psi_m$  dependency of the main coefficients  $l_{dq10}$  and  $l_{qd10}$  as:

$$\begin{aligned}
l_{dq_{10}}(\psi_m) &= l_{dq_{100}} + l_{dq_{102}} \cdot \psi_m^2 + l_{dq_{104}} \cdot \psi_m^4 \\
l_{qd_{10}}(\psi_m) &= l_{qd_{100}} + l_{qd_{102}} \cdot \psi_m^2 + l_{qd_{104}} \cdot \psi_m^4
\end{aligned} \tag{6.16}$$

where in (6.16), the upper and lower limits of  $l_{dq_{10}}$  and  $l_{qd_{10}}$  can be determined with respect to  $\psi_m$  for an identified machine. In the case of the IPMSM identified in section 3.5.2, the extreme variations of  $\psi_m$  are given by manufacturing tolerances, defined per specification at  $\pm 5\%$ , and temperature effects. The latter is defined according to the magnet's maximum operating temperature and temperature coefficient<sup>7</sup>, leading to the following variation range of the key parameters:

**Table 6.6:** IPMSM - coefficients expected variation with respect to  $\psi_m$

$n = 3$	min.	max.
$\psi_m$	-18.36%	7.04%
$l_{dq_{10}}$	-0.94%	2.16%
$l_{qd_{10}}$	-2.45%	5.61%

The variation ranges of the parameters in table 6.6 can be used directly as the constraints of the QP problem. Interestingly, the narrow variation range for the parameter  $l_{dq_{10}}$  can be interpreted as virtual fixation of the parameter with respect to the remaining ones. This narrow variation band which is due in part to the biasing effect of the magnet's flux on the core was already seen in the inductance plots in Fig. 3.17 and 3.18 when the extension of the flux-linkage expressions to consider the dependency of  $\psi_m$  was presented.

## 6.5 Algorithm Simulation

The evaluation of the hybrid identification scheme is performed at simulation level using the steering cycle profile from section 5.2.2. As shown in Fig. 6.14 the profile covers different operating regions, where the resistance or flux-linkage cannot be identified properly and even where no identification is possible at all.

<sup>7</sup>see table A.1 for detailed machine data.

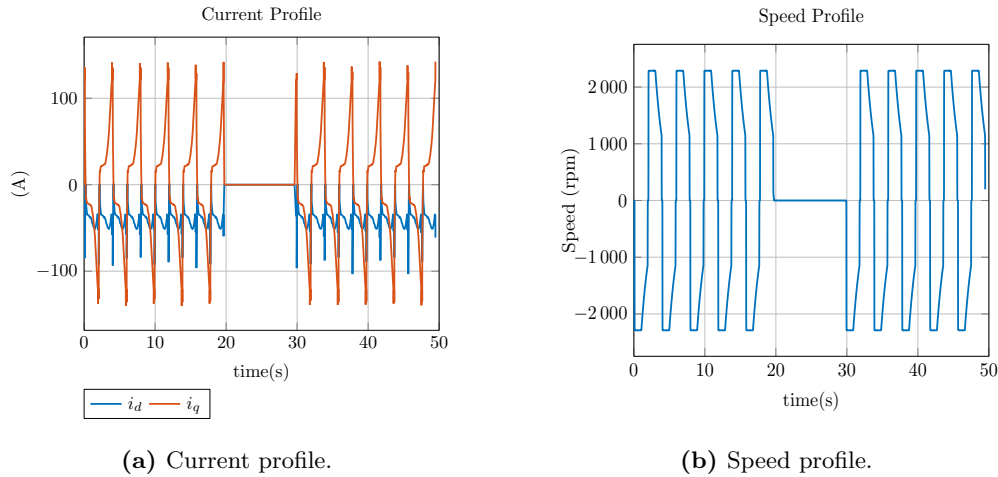


**Figure 6.14:** Steering Cycle.

With respect to the simulation model, the machine model used was based on the extended flux-linkage model of the IPMSM described in section 3.5.2. This model not only describes the flux-linkages in an accurate fashion but also considers the temperature effects on the flux-linkage itself, which is directly tied to the magnet temperature. Moreover a machine thermal model including the nodes of the three phase winding temperatures was coupled to the machine model in order to recreate the whole system.

The dq-voltage signals can be correctly estimated despite the highly dynamic nature of the profile as can be seen in Fig. 6.15.

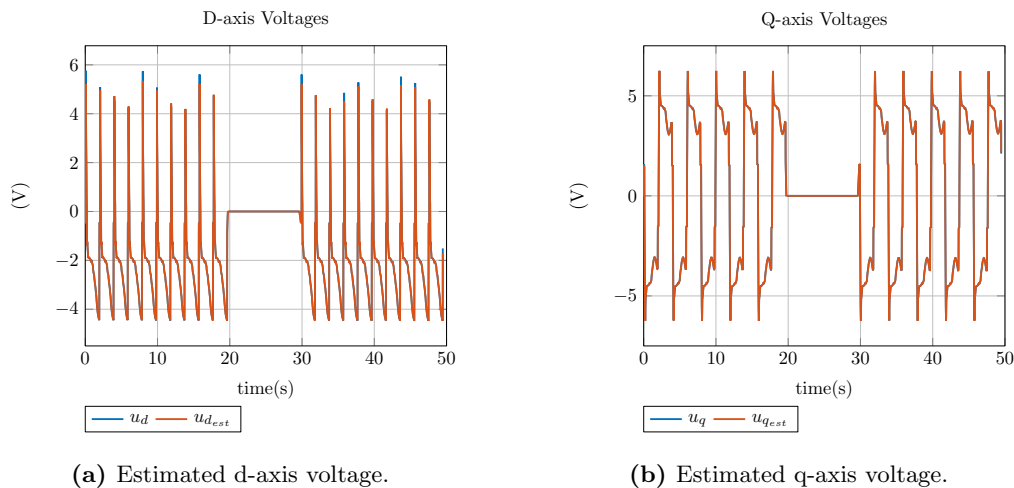
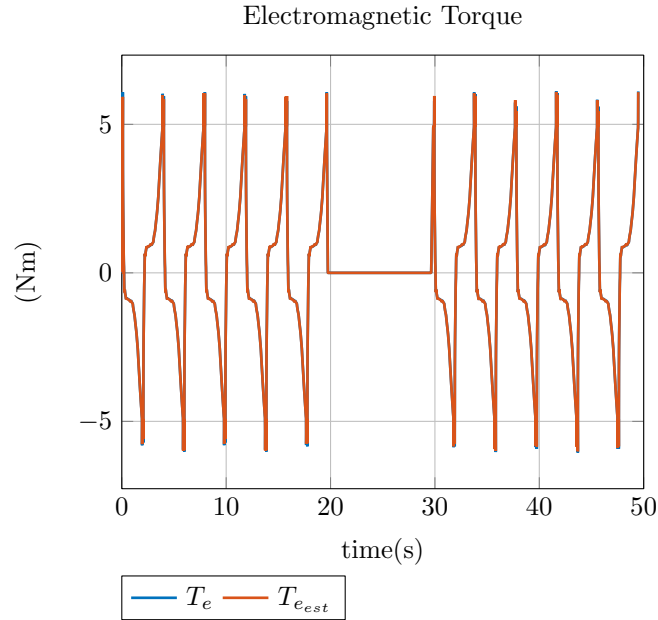


**Figure 6.15:** Simulated steering park cycle - voltage signals.

## 6 Online Parameter Estimation

In a similar manner, the agreement achieved with the estimated electromagnetic torque can be observed in Fig. 6.16.

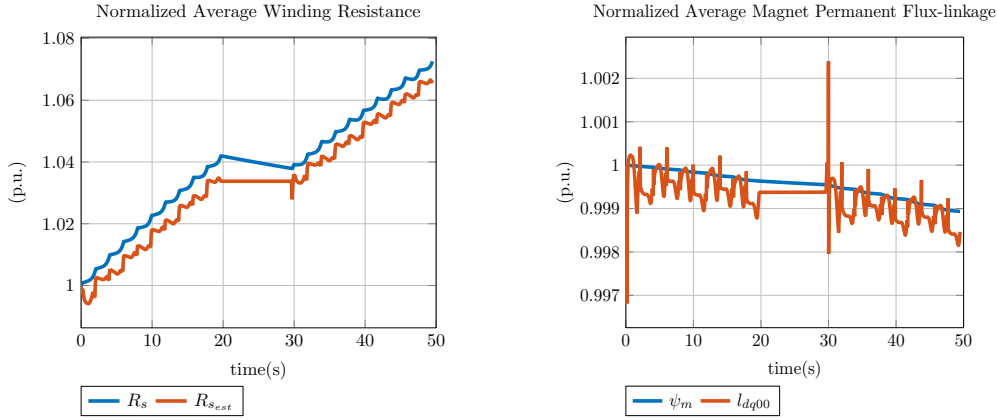


(a) Estimated d-axis voltage.

**Figure 6.16:** Simulated steering park cycle -torque signals.

In particular it is important to remember the almost static nature of the flux-linkage expressions parameters, as the only time variant parameters are  $R_s$  and  $\psi_m$ . Although they vary slowly with the associated machine temperatures, these two parameters can be considered constant for the time span of  $20ms$  used to solve the QP problem. Nevertheless, quantization errors introduced by the analogue to digital converter (ADC)s resolution, the signals ripple created by the PWM's switching pattern are responsible for the deviations of  $R_s$  and  $\psi_m$  observed in Fig. 6.17. However, despite all these error sources, the deviation for  $R_s$  is smaller than 0.8% and for  $\psi_m$  it is even below 0.3%.

The identified resistance and permanent flux-linkage in Fig. 6.17 evidenced the ability of the algorithm to follow the thermal effects on these parameters, but also effectiveness of the hybrid scheme, where despite of having profile regions with insufficient or no excitation the identification algorithm was able to provide a close estimate of the parameters in question.



(a) Average winding temperature estimation. (b) Average magnet temperature estimation.

**Figure 6.17:** Simulated temperature estimation.

As stated in the flow chart of Fig. 6.13, the corresponding winding and magnet temperatures are derived either from the thermal model itself or the temperature dependent parameters. The latter is formulated in terms of the associated temperature coefficients and reference values as:

$$T_{winding} = \frac{1}{\beta} \cdot \left( \frac{R_s(T)}{R_s(T_0)} - 1 \right) + T_0 \quad (6.17)$$

$$T_{magnet} = \frac{1}{\alpha} \cdot \left( \frac{\psi_m(T)}{\psi_m(T_0)} - 1 \right) + T_0 \quad (6.18)$$

where  $\beta$  and  $\alpha$  are the temperature coefficients of copper and the magnet material respectively,  $T_0$  is the reference temperature, and the symbols  $R_s(T)$  and  $\psi_m(T)$  represent the parameter values at a the temperature  $T$ . From (6.17) and (6.18), the impact of the deviation of the estimated parameter can be calculated. In particular the parameter with the smallest temperature coefficient will suffer large temperature variations. For this reason, the expected parameter errors are expressed in terms of a given temperature deviation and the copper and magnet temperature coefficients values are replaced in (6.17) and (6.18) producing the following expressions:

$$\Delta T_{winding} = 254 \cdot \frac{\Delta R}{R_{s0}} \quad (6.19)$$

$$\Delta T_{magnet} = 909 \cdot \frac{\Delta \psi}{\psi_{m0}} \quad (6.20)$$

As a result, expressions (6.19) and (6.20) shows that for the same deviations  $\frac{\Delta R}{R_{s0}}$  and  $\frac{\Delta \psi}{\psi_{m0}}$ , the magnet temperature development is 3.57-times larger than the winding one. Consequently, errors in the estimation of  $\psi_m$  will have a larger impact on the magnet

## 6 Online Parameter Estimation

temperature deviation than the impact of the estimation errors of  $R_s$  on the winding temperature. This is relevant, for the minimum rotor speed threshold design and to realize that the parameter estimation errors need to be small in order to obtain satisfactory temperature estimations, at least for this work a band of  $\pm 5^\circ\text{C}$  is considered as acceptable.

Finally, Fig. 6.18 shows that the winding and magnet temperatures could be tracked with high closeness to the expected values. This simulation of the online estimation algorithm provides an idea of the effectiveness of the hybrid scheme to deliver an reliable estimate regardless of the machine's operating conditions.

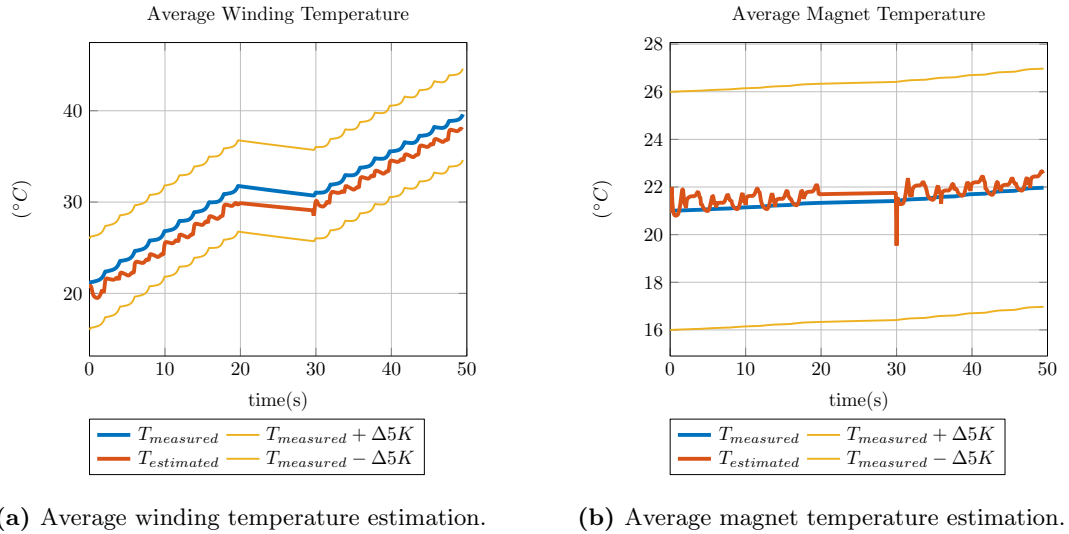


Figure 6.18: Online temperature estimation.

## 6.6 Online Estimation

This section shall discuss the performance of the online parameter identification algorithm on the test bench. As the embedded system used supports model based code generation, the algorithm's evaluation was realized in the same environment as the simulation of the algorithm but in the form of a hardware in the loop (HIL) setup.

### 6.6.1 Unbalanced Phase Resistance

The concept of average winding resistance relies on the fact that each of the three phase resistances possess the same value. However, in reality this is not the case, because of manufacturing tolerances, asymmetric thermal behavior or fault conditions. In addition to this, the machine could be connected to the inverter via long harness cables, which

at the same time could lead to asymmetric resistances. Winding resistance variations between phases due to manufacturing tolerances can be actually managed through a design specification. On other scenarios where the machine is loaded at still stand for longer periods of time can lead to asymmetric temperature development, producing an imbalance among the phase resistances. Consequently, assuming that each phase resistance is a variable on its own, it leads to a resistance matrix in the dq-reference in the following form:

$$\mathbf{R} = \begin{bmatrix} R_{dd} & R_{dq} \\ R_{qd} & R_{qq} \end{bmatrix} \quad (6.21)$$

where in (6.21), the sub-indexes  $d$  or  $q$  refers to the associated dq-axes currents. Furthermore the elements of this matrix can be expressed in terms of the winding resistances and the rotor position. For the sake of simplicity, the average winding resistance  $R_s$  is defined as:

$$R_s = \frac{R_1 + R_2 + R_3}{3} \quad (6.22)$$

The sub-indexes 1, 2, 3 represent the corresponding winding phases. Expression (6.22) is used then to formulate the elements of (6.21) in the following:

$$R_{dd} = R_s + \frac{(2R_1 - R_2 - R_3)}{6} \cos(2\omega_r t) \quad (6.23)$$

$$R_{qq} = R_s + \frac{(2R_1 - R_2 - R_3)}{6} \sin(2\omega_r t) \quad (6.24)$$

$$R_{dq} = R_{qd} = \frac{(R_2 + R_3 - 2R_1)}{6} \sin(2\omega_r t) - \frac{\sqrt{3}(R_2 - R_3)}{6} \cos(2\omega_r t) \quad (6.25)$$

Where  $\omega_r t$  is the formulation in time of the rotor position  $\theta$ . As a result, two types of terms arise, a constant component in the resistors (6.23) and (6.24) which is the expected average resistance  $R_s$  and a dynamic component with twice the electrical frequency of the machine. The latter becomes critical at low speeds and large resistance asymmetries, however these terms could be used to assess the health of the machine windings, in case of a faulty condition. In addition to this, under normal conditions, these rotor angle dependent components can be filter out, minimizing its ripple on the estimated value of  $R_s$ .

## 6 Online Parameter Estimation

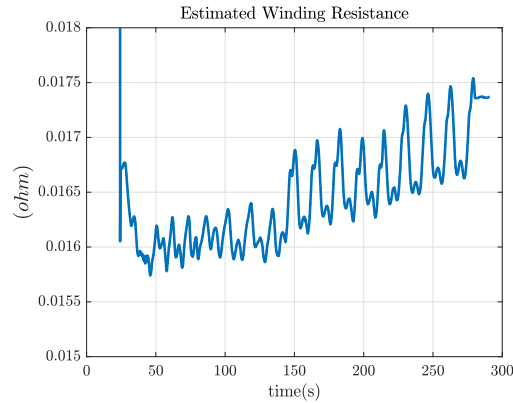


**Figure 6.19:** Effects of asymmetric winding resistance.

Fig. 6.19 depicts the identified  $R_s$  at the presence of asymmetric machine harness resistance for different speeds. Typically in a real application, the winding resistance balance will be kept as small as possible, i.e.  $< 2.5\%$ , for that reason a small ripple can be expected and its attenuation can be easily done with a low-pass filter. However, a degradation of winding or harness resistance could be detected through a larger ripple or a large increase of  $R_s$ .

### 6.6.2 Test Profiles

The same test profile from the previous section was used to evaluate the algorithm on the test bench, however the profile was modified to include twice the steering cycle, with a long pause between them to recreate a warm start at the second cycle as shown in Fig. 6.20. Two machine temperature scenarios were analyzed, mid and high magnet temperature range. With the first steering cycle a cold start of identification is recreated to evaluate the ability of the algorithm to track the machine's temperature after a system reset or initialization. The second cycle seeks to recreate again a warm start of the algorithm.

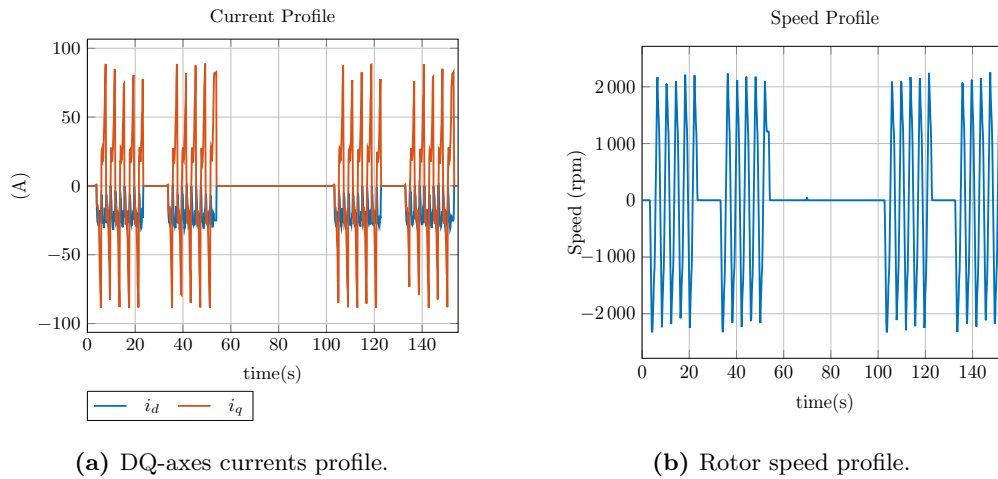


**Figure 6.20:** Steering park cycle profile.

The first measurement was performed at a magnet temperature around  $36^\circ\text{C}$ . The machine was previously loaded to achieve the expected magnet temperature, implying a preheating of the windings as well. Fig. 6.21 summarizes the winding and magnet temperature profiles, where the red curves represent the estimated values of the hybrid temperature model, the blue ones the measured temperatures<sup>8</sup>

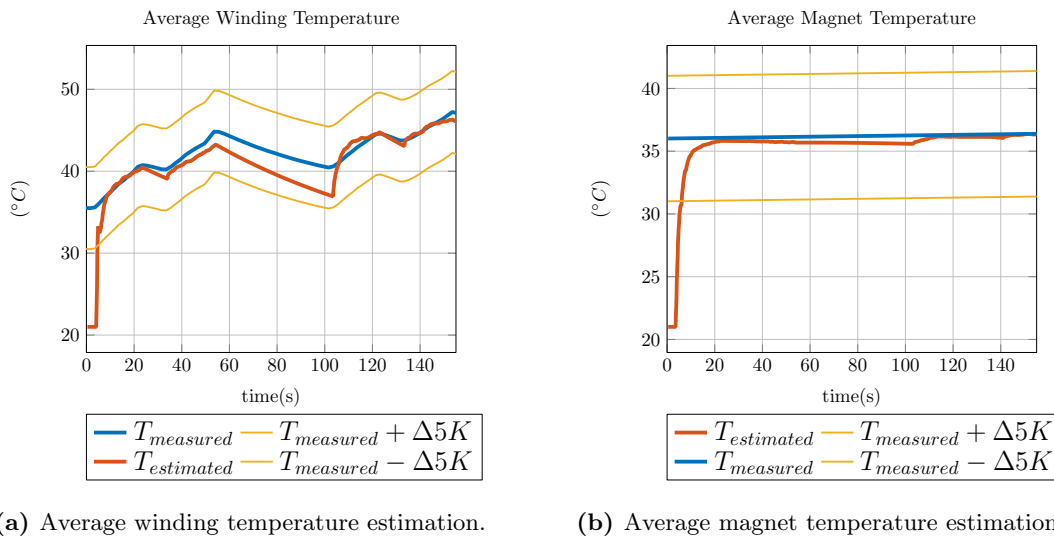


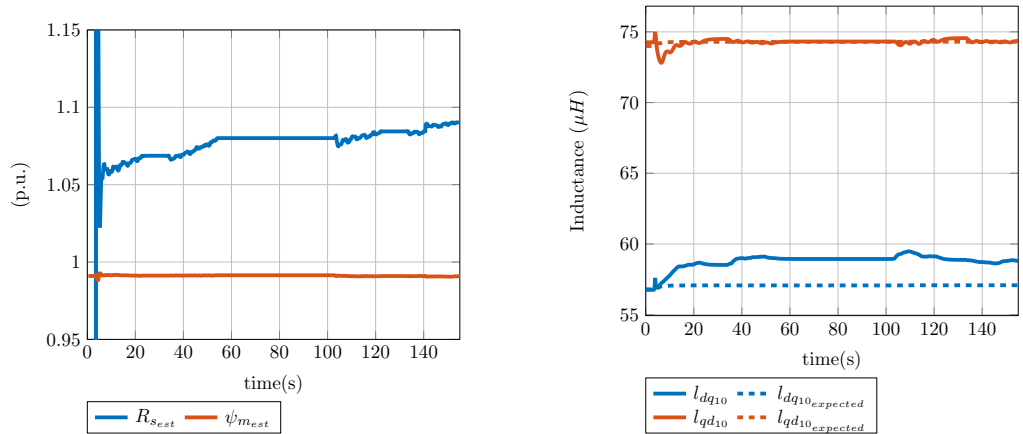
**Figure 6.21:** Online temperature estimation.

<sup>8</sup>The magnet temperature was obtained indirectly by measuring the bmf-voltage as is chapter 5.

## 6 Online Parameter Estimation

The hybrid model was able to correct the temperature values to the actual ones once the operating conditions permitted the activation of the parameter identification algorithm. In addition to this the temperature correction lead to small temperature deviations, below  $\pm 5^\circ C$ . Nevertheless, the major deviation that can be observed occurs in the pause between 60s-100s, where the thermal model is running the estimation alone as the online parameter estimation is inactive due to the lack of machine excitation. The temperature deviations appears because only the winding and magnet nodes were updated with actual temperature values and the remaining nodes started with the default initial condition of  $21^\circ C$ . For that reason the winding temperature node, which has a better thermal contact to the remaining nodes is being driven rapidly again to the cooler temperatures.

Consequently, the online parameter estimation algorithm was able to track variations of  $R_s$  and  $\psi_m$  as can be seen in Fig. 6.22a. The main coefficients that describe the inductances  $l_{dq10}$  and  $l_{qd10}$  could be estimated with a high degree of closeness to the values obtained experimentally in the offline identification<sup>9</sup>. The dotted lines in Fig. 6.22b depict the expected coefficient values considering its  $\psi_m$  dependency according to 6.16 and the solid lines the identified values. On the one hand  $l_{qd10}$  matched closely the expected value, however the coefficient  $l_{dq10}$  was off by nearly 3.5% which can be explained in part due to the relatively small magnitude of the d-axis current in the steering cycle profile, which is below 30A and combined with the ADC resolution and associated noise it could lead to current signals errors.



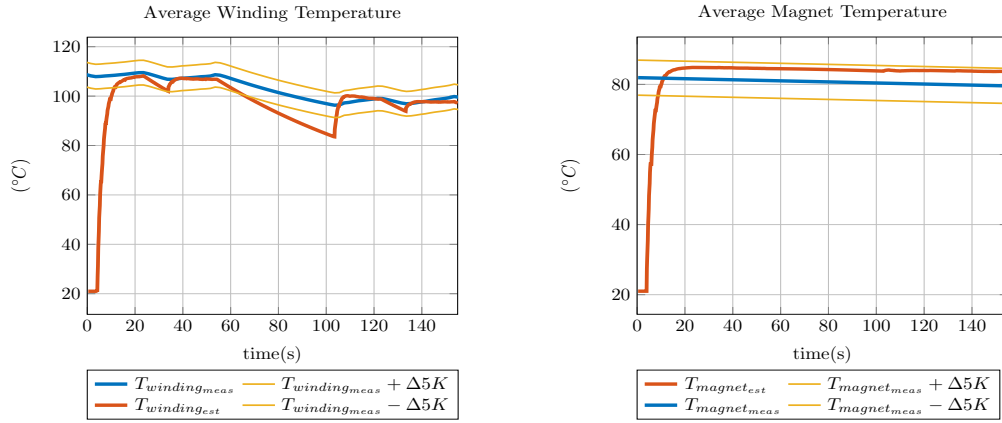
(a) Average winding resistance and permanent magnet flux. estimation.

(b) Linear inductance coefficients.

**Figure 6.22:** Identified parameters.

<sup>9</sup>This is the PMSM machine used to present the offline identification in section 3.5.1 and it was also the example machine employed in section 3.5.2 to present the offline identification with consideration of variations  $\psi_m$ .

A similar picture can be observed with the second test profile, where the magnet temperature was driven up to  $81^\circ\text{C}$  and the winding temperature around  $115^\circ\text{C}$ . The hybrid thermal model can again update the node temperatures successfully to the actual values as depicted in Fig. 6.23. Similarly to the previous case, the biggest temperature deviation lays in the long pause between cycles due to the same reasons, but in this case the rate of temperature decrease is pronounced as the remaining nodes are nearly  $80^\circ\text{C}$  "cooler". However once the machine is excited again in the second cycle, around 100s, the winding temperature gets corrected again.



(a) Average winding temperature estimation. (b) Average magnet temperature estimation.

**Figure 6.23:** Online temperature estimation.

On the other hand the magnet temperature shows a maximum deviation of  $4^\circ\text{C}$ , which could be related to the small d-axis current leading to deviations in the d-axis inductance estimates, that at the same time affects the estimation of  $\psi_m$ .

$$\psi_d = \psi_m + i_d L_d(i_d, i_q) \quad (6.26)$$

A small error as 1% in the estimation of  $l_{dq10}$  leads in this case to a correction of  $4^\circ\text{C}$  in the estimated magnet temperature deviation as illustrated in Fig. 6.24.

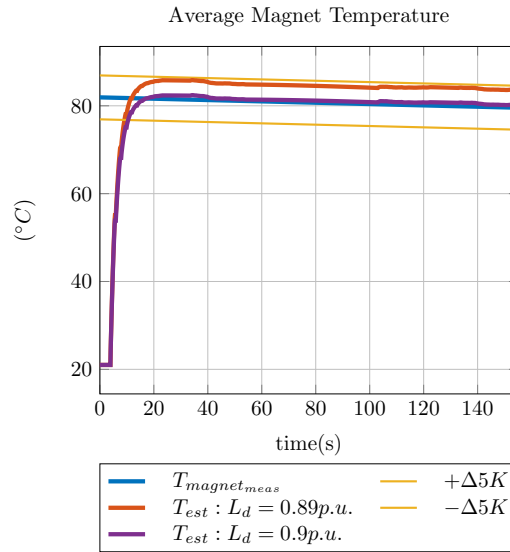
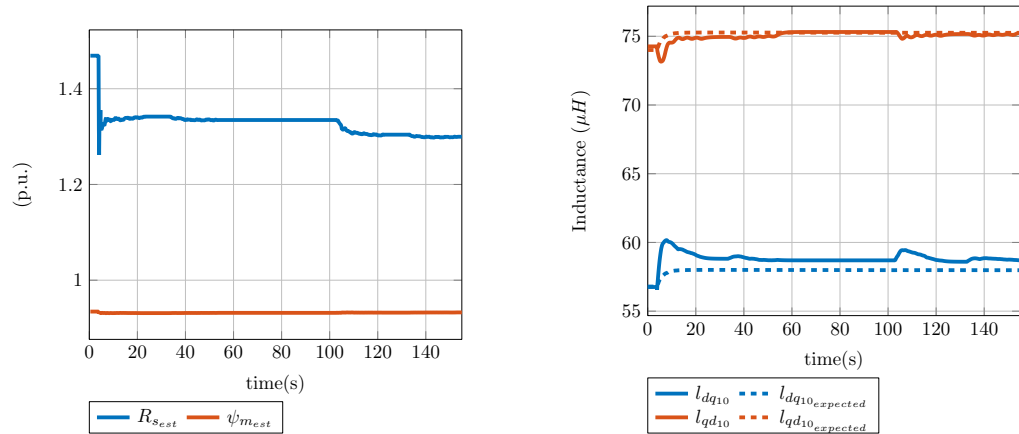


Figure 6.24: Effects of  $L_d$  on magnet temperature estimation.

Finally the main identified parameters are presented in Fig. 6.25, where the cool down trajectory of the winding resistance is observed and the nearly constant magnet temperature as well. With a similar behavior, the identified coefficients  $l_{dq10}$  and  $l_{qd10}$  also track the indirect effects caused by the magnet temperature, which had reduced the value of  $\psi_m$  leading to a small increase of those two coefficients, as displayed in Fig. 6.25.



(a) Average winding resistance and permanent magnet flux. estimation.

(b) inductance coefficients.

Figure 6.25: Identified parameters.

Specially in the coefficient  $l_{qd10}$  it was clear that the parameter identification could track the temperature dependency as shown in the close up in Fig. 6.26.

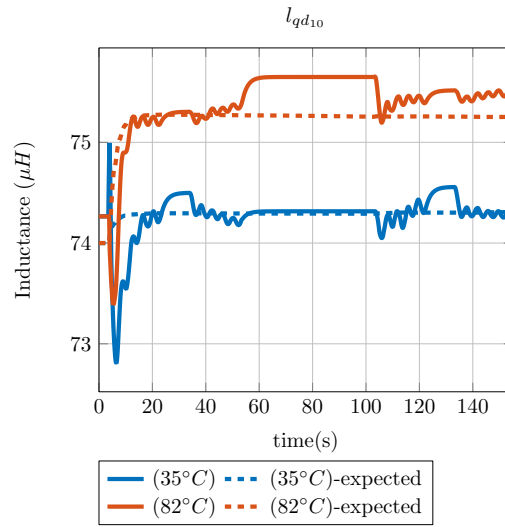
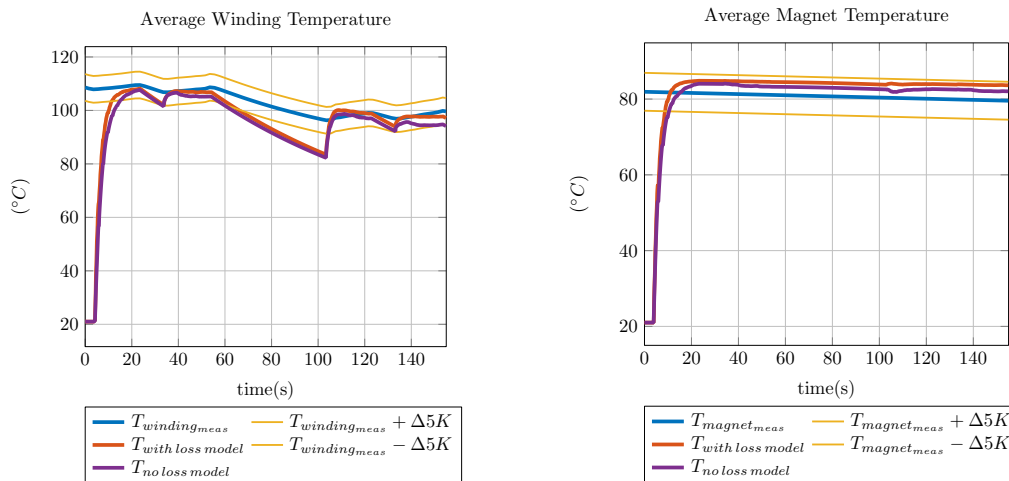


**Figure 6.26:** Temperature dependency of  $l_{qd10}$ .

The iron loss model presented in Chapter 4 was required for the thermal network power source modeling and it is part of the equivalent dq-axes voltage model used for the online identification as proposed in Fig. 6.7. The impact of the iron loss model on the temperature estimation is depicted in Fig. 6.27.



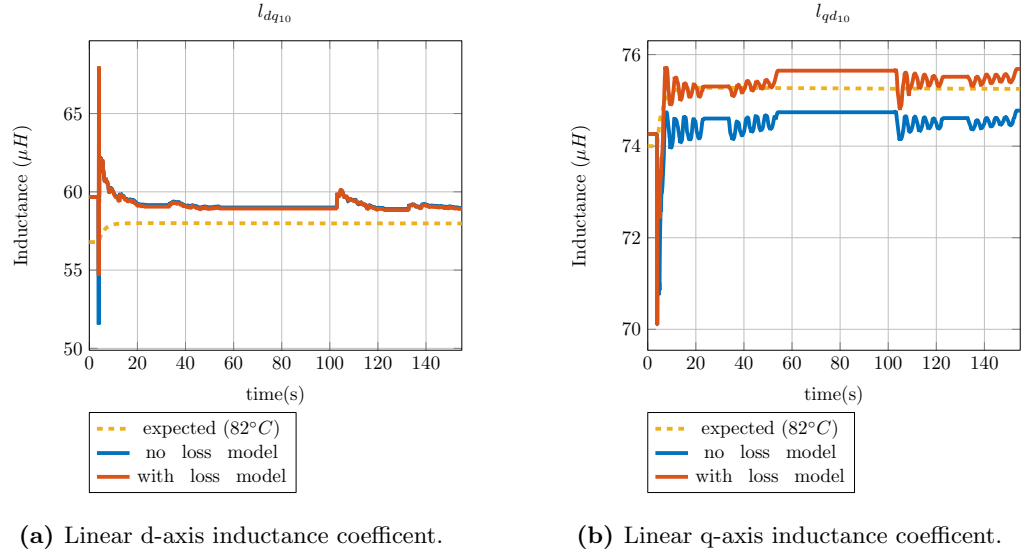
(a) Average winding temperature estimation.

(b) Average magnet temperature estimation.

**Figure 6.27:** Online estimation with and without iron loss model

## 6 Online Parameter Estimation

It can be observed in Fig. 6.27a a negative impact on the predicted winding temperature, specially at the end of the cycle the deviation increases. Conversely, the estimated magnet temperature without iron loss model is now closer to the expected temperature depicted with the blue curve, with an improvement of  $1.6^\circ\text{C}$ . However, this deviation corresponds to  $0.176\%$  of change in  $\psi_m$ , which is fairly small.



(a) Linear d-axis inductance coefficient.

(b) Linear q-axis inductance coefficient.

**Figure 6.28:** Online estimation with and without iron loss model

A closer look to the linear inductance coefficients  $l_{dq10}$  and  $l_{qd10}$  delivers additional information to the impact of the iron loss model on the parameter identification. On the one hand side, as shown in Fig. 6.28a, the identification of coefficient  $l_{dq10}$  without iron loss model was nearly unaffected by it. As the maximum demanded d-axis current during the cycle does not exceed  $30\text{ A}$ , its contribution to  $\psi_d$  is small compared to  $\psi_m$ . As  $i_d$  would need to reach:

$$i_{dsc} = \frac{\psi_m}{L_d(i_d, i_q)} \quad (6.27)$$

to achieve a flux-linkage value equal to  $\psi_m$ . Therefore, under these operating conditions the identification of  $l_{dq10}$  is less affected to the impact of the iron loss model than  $\psi_m$ . On the other hand, the estimation of the q-axis linear inductance coefficient suffered a reduction of around  $1\%$  as shown in Fig. 6.28b, which is the most perceptible deviation of the four estimates displayed in Fig. 6.27. From the author's perspective, the iron loss model is worthwhile, as it helps to improve the average winding temperature estimation and the coefficient  $l_{qd10}$ , despite of having little impact on the estimation of the magnet temperature and coefficient  $l_{dq10}$ .

### 6.6.3 Unconstrained Identification

The proposed hybrid parameter estimation scheme is not subjected to one identification method. Returning to the summary delivered in section 3.1.1.1, it was remarked the advantage of the RLS algorithm due to its low computational cost. This evident benefit specially in embedded applications is supported by its popularity in the literature [2, 29, 83]. However, the essential difference with respect to the QP algorithm is the possibility to define parameter constraints. The formulation of the RLS problem is done to minimize the sum of the squared errors of the dq-axes voltages as well:

$$\begin{aligned}\hat{x}(k) &= \hat{x}(k-1) + \gamma(k) [y(k) - \varphi^T(k)\hat{x}(k-1)] \\ \gamma(k) &= \frac{1}{\varphi^T(k)P(k-1)\varphi(k) + \lambda} P(k-1)\varphi(k) \\ P(k) &= \frac{1}{\lambda} (I - \gamma(k)\varphi^T(k))P(k-1)\end{aligned}\quad (6.28)$$

with,

$$\varphi(k) = \begin{bmatrix} \nabla u_{d_k} \\ \nabla u_{q_k} \end{bmatrix}^T \quad \text{and} \quad y(k) = \begin{bmatrix} u_{d_k} \\ u_{q_k} \end{bmatrix}$$

where  $\lambda$  is the forgetting factor, which determines the weight of past values. The computational time duration of the algorithm presented in (6.28) was evaluated in the same way as the QP solver with the software setup of Fig. 6.8 in the Zedboard environment. This means that the RLS algorithm was implemented in the ARM processor as well. The resulting average execution time was  $123.96\mu s$ , which confirmed the expected low computational cost of such method, opening then the option of running the algorithm at faster rates compared to the QP solver, even  $1ms$  would be an option. Consequently, two algorithm setups with the parameters of table 6.7 were evaluated.

**Table 6.7:** RLS algorithms setups

Setup Name	$\lambda$	$T_{execution}$
RLS 1	0.99998	$1ms$
RLS 2	0.9998	$20ms$

The first remarkable aspect can be seen in Fig. 6.29, on the one hand the average magnet temperature can be estimated by the variant RLS 1 and QP in the range of  $\pm\Delta 5K$ , as shown in Fig. 6.29b, on the other hand RLS 2 is able to deliver a closer estimate of the winding temperature than RLS 1 as depicted in Fig. 6.29a. However, overall the temperature estimates of the QP solver outperforms both RLS algorithms.

## 6 Online Parameter Estimation

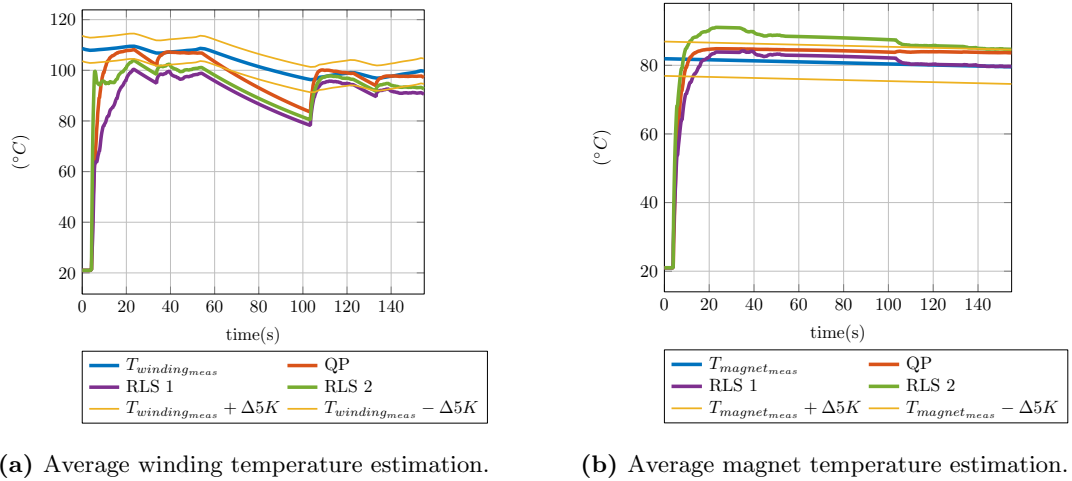


**Figure 6.29:** Online temperature estimation.

A look into the coefficients  $l_{dq10}$  and  $l_{qd10}$  provides some insights into the source of the estimates differences. Fig. 6.30a shows how both RLS estimates of  $l_{dq10}$  drift over time, while the expected value should remain quite constant due to its permanent magnet flux dependency. Conversely, the QP based approach presents a constant trend being only affected by the transitions between valid and invalid signal regions and an offset. In addition, both RLS estimates of  $l_{qd10}$  show an offset and a small drift as well, as illustrated in Fig. 6.30b. All these effects indicate the limited estimation capabilities of both RLS algorithms when dealing with many unknown parameters.

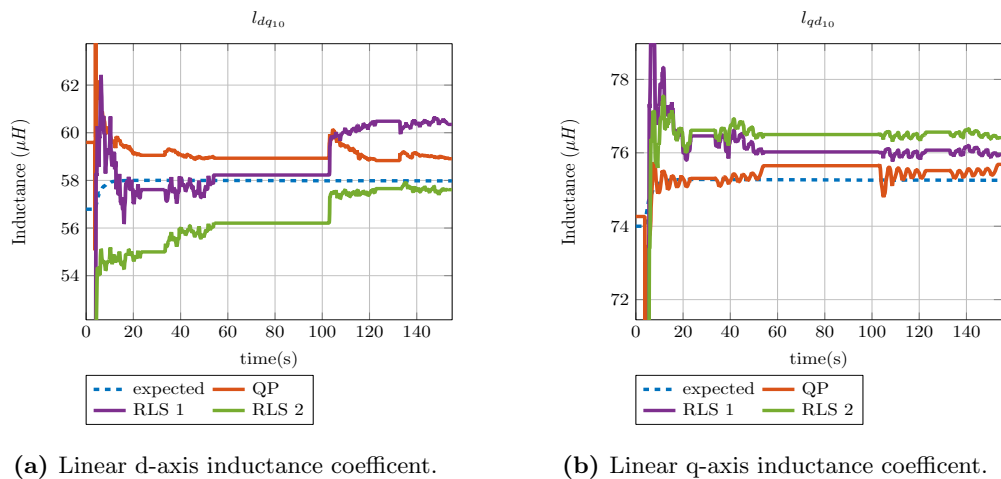


**Figure 6.30:** Online temperature estimation.

The proposed approach based on a  $QP$  solver was able to deliver consistent and accurate results with respect to the expected values, furthermore the presented parameter identification runs at a low execution rate reducing the computational burden.

The polynomial based machine model presented in chapter 2 was used as the foundation of an online parameter identification scheme of a PMSM, which was based on voltage and current signals of the fundamental frequency. The machine's non-linear effects are then described in the form of polynomials with constant coefficients and in conjunction with a recursive estimation scheme provides a solution to the rank deficient problem. Regardless of the load conditions, the coefficients that describe the flux-linkage's cross-coupling and saturation effects remain constant, therefore by recollecting the data of several different operating points a full-rank solution to the estimation problem could be found. Consequently, the temperature dependent parameters such as the winding resistance and the permanent flux-linkage were treated as constant values for short periods of time compared to the machine's thermal time constant. As a result, the parameter variation due to the average winding and rotor magnets temperatures could be tracked. In order to account for the speed dependent iron losses that interact with the flux-linkages, two equivalent loss resistors were employed, the first one representing the magnetizing losses associated to the dq-axes flux-linkages and the second one representing the demagnetizing losses associated to the current dependent d-axis flux-linkage terms. Moreover, the online parameter identification algorithm was backed up by a machine's thermal model. This hybrid setup provided a solution to the limitations of both estimation methods. Firstly, the proposed hybrid approach delivers parameter estimates at any operating condition of the machine, as the thermal model takes over the estimation of the average winding and magnet temperatures when the machine doesn't have enough excitation in terms of phase currents or rotor speed. The average winding resistance and permanent magnet flux-linkage values are then derived from the corresponding estimated temperatures. Secondly, the parameter estimates, when the machine is operating in regions with proper excitation, are used to update the thermal model's winding and magnet temperatures in case the identification algorithm is started at an initial thermal condition different of the real machine temperatures.



# 7 Conclusions

## 7.1 Summary

In this work a hybrid online parameter estimation scheme was presented. Firstly, a polynomial based nonlinear machine model was introduced. This approach allowed the description of the saturation and cross-coupling effects of the dq-axes flux-linkages. Moreover, the polynomial's structure was simplified considering the symmetry properties of the machine's flux-linkages and the energy conservation law. The proposed flux-linkage expressions described the saturation of the torque constant caused by the q-axis current, as well as the cross-coupling due to the dq-axes currents in the absolute and incremental inductances. To model the magnet temperature impact on the flux-linkages, the proposed expressions were extended to consider the permanent magnet flux-linkage as a third variable, enabling the representation of the inductances or the electromagnetic torque with respect to the magnet temperature. In a similar manner, the mentioned approach was also applied to machines with constant field excitation like Wound Field Synchronous Machines (WFSM), where instead of permanent magnets, the rotor has field windings that produce the necessary magnetic flux to emulate the permanent magnets. Because of the highly nonlinear magnetic behavior over the whole range of operation of such machines, a new polynomial structure was proposed to improve the accuracy of the flux-linkage expressions. The derived flux-linkage expressions were validated using FEA simulation data of an IPMSM and a WFSM, the former machine was simulated at different magnet  $B_r$  values to emulate various magnet temperatures. Afterwards, a fast and simple measurement procedure was presented to identify the coefficients of the proposed expressions on the test bench. This experimental validation was carried out on three types of PMSMs: an inner rotor SMPMSM, an IPMSM, and an outer rotor SMPMSM. Additionally, the extended model that considers the permanent magnet flux-linkage as a third variable, was validated with measured data of the IPMSM at different magnet temperatures. Aiming to the main objective of this work, namely the online parameter identification of PMSMs, the proposed flux-linkage expressions offered a solution to the rank deficient issue reported in the literature. Where the traditional formulation of the inductances as a value determined by the instantaneous operating point leads to approaches that require the solution of a underdetermined system of equations. The proposed polynomials described the dq-axes current dependency of the flux-linkages, hence the polynomial's coefficients remain constant at any current condition. For this reason, over several operating points, the resulting system of equations becomes overdetermined with a unique solution. However, this is only valid for periods of time at constant magnet and winding temperatures.

## 7 Conclusions

As a following step, it was acknowledged that the formulation of the flux-linkages in terms of dq-axes currents needed to be complemented to account for additional effects caused by iron losses and machine temperature. By modeling the iron losses, the frequency dependency of the flux-linkage polynomial's coefficients could be reduced, leaving them constant with respect to the machine's speed. For that purpose, an equivalent dq-axes voltage circuit with two sets of resistors modeling the iron losses of the magnetizing and demagnetizing path. Each set consisting of resistors representing the hysteresis and the eddy current losses. One set of resistors models the iron losses of the magnetizing path and the second one the demagnetizing path. The determination of the resistors was performed experimentally on the already characterized IPMSM, which was designated as the target machine to be used for the online parameter identification.

The estimation of the permanent magnet flux-linkage and the average winding resistance delivers indirectly the temperature in the magnets and windings. Hence, the temperature estimates provided by a machine's thermal model would enable the calculation of the mentioned parameters as well. By running both estimation algorithms in parallel, a hybrid online parameter identification can be arranged, where both algorithms complement each other. Therefore, the derivation of a machine thermal model was presented in chapter 5. The aim was to obtain a thermal model that could be implemented in an embedded system. For that reason a model reduction approach was presented, which does not require the knowledge of the machine's geometry or its material's properties. The proposed model reduction method was based on a mathematical simplification of resistive networks in order to find an equivalent network with a reduced set of nodes and thermal capacitances associated to those target nodes to achieve the desired dynamic response. The model reduction method was validated using simulation data of a large thermal network and measured temperature data of the IPMSM. With the use of the simulation data, the effectiveness of the reduced resistive network could be demonstrated, as well as the dynamic response of the thermal network with the associated thermal capacitances. Moreover, the measured data was used to validate the proposed method by considering a set of operating points at different load conditions and machine speeds. The latter was modeled by saving the thermal resistances as a speed dependent map. The resulting 6-node thermal network achieved a good agreement in steady state, at dynamic load conditions including different machine speeds.

The final chapter of this work, introduced the hybrid online parameter setup, that comprised the equivalent dq-axes voltage circuit, which is based on the flux-linkage expressions of chapter 2 and the thermal model of the IPMSM. This hybrid arrangement sought to provide a solution to the limitations of each estimation method. Firstly, the proposed hybrid approach delivers parameter estimates at any operating condition of the machine, as the thermal model takes over the estimation of the average winding and magnet temperatures when the machine doesn't have enough excitation in terms of phase currents or rotor speed. The average winding resistance and permanent magnet flux-linkage values are then derived from the corresponding estimated temperatures. On the other hand, when the machine is operating in regions with proper excitation,

the machine's parameter estimates are used to update the thermal model's winding and magnet temperatures. Additionally, in order to enhance the parameter estimation algorithm, a constrained optimization method was proposed to dynamically bound the machine parameters according to the operating conditions. For instance, when the machine speed or the phase currents are too low to provide enough information to obtain an estimate. The capabilities of the proposed identification algorithm were shown using a profile containing dynamic load and still stand conditions. The hybrid setup was presented with the help of simulation data and the already mentioned profile. Afterwards, the proposed method was tested experimentally considering two types of warm start conditions. The parameter estimates of the average winding resistance and permanent magnet flux-linkage provided sufficient information to correct the temperature in the corresponding nodes of the thermal network to the actual temperature values. Then, the performance of the hybrid algorithm was shown considering two different types of identification algorithms, namely the proposed constrained optimization and a classical recursive least-squares algorithm. The latter was outperformed by the constrained optimization, which delivered overall better agreement at the estimation of average winding and magnet temperatures, as well as the small signal dq-axes inductances estimation.

## 7.2 Future Work

Some aspects dealt in this work could served as a starting point for further analysis. The flux-linkage expressions introduced throughout chapter 2 provided a model based on the fundamental frequency of the machine. However, harmonic components due to slotting and nonlinearities in the electromagnetic circuit are present in the flux-linkages. An extension of the proposed flux-linkage expressions to consider harmonics components is the natural step towards a complete nonlinear machine model. In another perspective, the demand for fault tolerant systems has brought the attention to new machine topologies such as multiplex machines. Where dual three phase machines are used in order to fulfill requirements of torque availability after a fault condition. The electromagnetic coupling between winding sets is an important factor for the simulation of the torque capability after a fault has occurred. Hence, the extension of the flux-linkage expressions presented in this work to model multiplex and multi-phase machines would provide a high fidelity machine model to investigate torque capability, torque ripple and phase current development at several fault scenarios. In the case of multi-phase machines, an extension of the flux-linkage expressions to include the influence of the zero sequence current would be convenient.

The proposed online parameter identification scheme can also be extended to incorporate monitoring and diagnostic features of the machine. Due to the constrained optimization performed to estimate the machine parameters, fault conditions such as open phase winding or failures of the inverter's switching elements could be monitored with the help of the proposed parameter identification algorithm. In the sense of condition monitoring, the polynomial's coefficients could provide information related to degradation of the magnets or the magnetic circuit over time. Due to the analytical nature of the

## 7 Conclusions

flux-linkage expressions, maximum torque per ampere or field-weakening strategies can be implemented for an online usage. These algorithms can be formulated as optimization problems which can be described mathematically with additional direct information such as the derivatives of the flux-linkages with respect to the dq-axes currents. As a final example, for torque controlled applications, the nonlinear description of the flux-linkage in analytical form can be used to linearize the torque output.

# Bibliography

- [1] L. Ayala, A. Schwinn, D. Moule, and R. Kennel, "Modelling the flux-linkage in permanent magnet synchronous machines," in *2019 IEEE International Electric Machines Drives Conference (IEMDC)*, May 2019, pp. 112–118.
- [2] S. J. Underwood and I. Husain, "Online parameter estimation and adaptive control of permanent-magnet synchronous machines," *IEEE Trans. Ind. Electron.*, vol. 57, no. 7, pp. 2435–2443, July 2010.
- [3] B. G. Park, R. Y. Kim, and D. S. Hyun, "Fault diagnosis using recursive least square algorithm for permanent magnet synchronous motor drives," in *8th International Conference on Power Electronics - ECCE Asia*, May 2011, pp. 2506–2510.
- [4] K. M. Rahman and S. Hiti, "Identification of machine parameters of a synchronous motor," *IEEE Trans. Ind. Appl.*, vol. 41, no. 2, pp. 557–565, March 2005.
- [5] S. Kuehl and R. M. Kennel, "Measuring magnetic characteristics of synchronous machines by applying position estimation techniques," *IEEE Trans. Ind. Appl.*, vol. 50, no. 6, pp. 3816–3824, Nov 2014.
- [6] A. D. Pizzo, I. Spina, U. Schaefer, and L. T. Beti, "A parameter estimation method for on-line failure detection in permanent magnet ac-brushless motors having current-dependent parameters," in *8th IEEE Symposium on Diagnostics for Electrical Machines, Power Electronics Drives*, Sept 2011, pp. 258–264.
- [7] J. Bonifacio, N. Amann, and R. Kennel, "Online full-parameter identification strategy for ipmsm using voltage signal injection," in *2018 20th European Conference on Power Electronics and Applications (EPE'18 ECCE Europe)*, Sep. 2018, pp. P.1–P.7.
- [8] K.-H. Kim, S.-K. Chung, G.-W. Moon, I.-C. Baik, and M.-J. Youn, "Parameter estimation and control for permanent magnet synchronous motor drive using model reference adaptive technique," in *Industrial Electronics, Control, and Instrumentation, 1995., Proceedings of the 1995 IEEE IECON 21st International Conference on*, vol. 1, Nov 1995, pp. 387–392 vol.1.
- [9] M. Yoshimi, M. Hasegawa, and K. Matsui, "Parameter identification for ipmsm position sensorless control based on unknown input observer," in *2010 IEEE Symposium on Industrial Electronics and Applications (ISIEA)*, Oct 2010, pp. 383–388.

## Bibliography

- [10] P. H. Mellor and D. R. Turner, "Real time prediction of temperatures in an induction motor using a microprocessor," *Electric Machines & Power Systems*, vol. 15, no. 4-5, pp. 333–352, dec 1988.
- [11] B. Boazzo and G. Pellegrino, "Model-based direct flux vector control of permanent-magnet synchronous motor drives," *IEEE Transactions on Industry Applications*, vol. 51, no. 4, pp. 3126–3136, July 2015.
- [12] G. Pellegrino, R. Bojoi, and P. Guglielmi, "Impact of the motor magnetic model on direct flux vector control of interior pm motors," in *IECON 2011 - 37th Annual Conference of the IEEE Industrial Electronics Society*, Nov 2011, pp. 1879–1884.
- [13] G. Pellegrino, B. Boazzo, and T. M. Jahns, "Magnetic model self-identification for pm synchronous machine drives," *IEEE Transactions on Industry Applications*, vol. 51, no. 3, pp. 2246–2254, May 2015.
- [14] R. Krishnan, *Permanent Magnet Synchronous and Brushless DC Motor Drives*. CRC Press, 2010.
- [15] I. Jeong, B. Gu, J. Kim, K. Nam, and Y. Kim, "Inductance estimation of electrically excited synchronous motor via polynomial approximations by least square method," *IEEE Transactions on Industry Applications*, vol. 51, no. 2, pp. 1526–1537, March 2015.
- [16] D. Hwang and B.-G. Gu, "Field current control strategy for wound-rotor synchronous motors considering coupled stator flux linkage," *IEEE Access*, vol. 8, pp. 111 811–111 821, 2020.
- [17] J. Goss, P. H. Mellor, R. Wrobel, D. A. Staton, and M. Popescu, "The design of ac permanent magnet motors for electric vehicles: A computationally efficient model of the operational envelope," in *6th IET International Conference on Power Electronics, Machines and Drives (PEMD 2012)*, March 2012, pp. 1–6.
- [18] J. Goss, M. Popescu, D. Staton, R. Wrobel, J. Yon, and P. Mellor, "A comparison between maximum torque/ampere and maximum efficiency control strategies in ipm synchronous machines," in *2014 IEEE Energy Conversion Congress and Exposition (ECCE)*, Sep. 2014, pp. 2403–2410.
- [19] A. Kiltbau and J. Pacas, "Parameter-measurement and control of the synchronous reluctance machine including cross saturation," in *Conference Record of the 2001 IEEE Industry Applications Conference. 36th IAS Annual Meeting (Cat. No.01CH37248)*, vol. 4, Sep. 2001, pp. 2302–2309 vol.4.
- [20] M. Pacas and R. Morales, "A predictive torque control for the synchronous reluctance machine taking into account the magnetic cross saturation." IEEE, 2005.
- [21] A. Kiltbau and J. Pacas, "Appropriate models for the control of the synchronous reluctance machine," in *Conference Record of the 2002 IEEE Industry Applications*

- Conference. 37th IAS Annual Meeting (Cat. No.02CH37344)*, vol. 4, Oct. 2002, pp. 2289–2295 vol.4.
- [22] P. Pescetto and G. Pellegrino, “Sensorless magnetic model and pm flux identification of synchronous drives at standstill,” in *2017 IEEE International Symposium on Sensorless Control for Electrical Drives (SLED)*, Sep. 2017, pp. 79–84.
- [23] S. A. Odhano, P. Pescetto, H. A. A. Awan, M. Hinkkanen, G. Pellegrino, and R. Bojoi, “Parameter identification and self-commissioning in ac motor drives: A technology status review,” *IEEE Transactions on Power Electronics*, vol. 34, no. 4, pp. 3603–3614, April 2019.
- [24] O. Scaglione, M. Markovic, and Y. Perriard, “On-line parameter estimation for improved sensorless control of synchronous motors,” in *2012 XXth International Conference on Electrical Machines*, Sept 2012, pp. 2229–2237.
- [25] S. Moreau, R. Kahoul, and J. P. Louis, “Parameters estimation of permanent magnet synchronous machine without adding extra-signal as input excitation,” in *2004 IEEE International Symposium on Industrial Electronics*, vol. 1, May 2004, pp. 371–376 vol. 1.
- [26] L. Liu, D. A. Cartes, and W. Liu, “Particle swarm optimization based parameter identification applied to pmsm,” in *2007 American Control Conference*, July 2007, pp. 2955–2960.
- [27] X. Xi, X. Qingsong, T. Jun, T. Peigen, and W. Guohong, “An improved method of interior permanent magnet synchronous motor parameter identification based on particle swarm optimization,” in *2013 15th European Conference on Power Electronics and Applications (EPE)*, Sept 2013, pp. 1–9.
- [28] A. Balamurali, A. Mollaeian, S. M. Sangdehi, and N. C. Kar, “Parameter identification of permanent magnet synchronous machine based on metaheuristic optimization,” in *2015 IEEE International Electric Machines Drives Conference (IEMDC)*, May 2015, pp. 1729–1734.
- [29] Q. Liu and K. Hameyer, “A fast online full parameter estimation of a pmsm with sinusoidal signal injection,” in *2015 IEEE Energy Conversion Congress and Exposition (ECCE)*, Sept 2015, pp. 4091–4096.
- [30] G. Feng, C. Lai, K. Mukherjee, and N. C. Kar, “Current injection-based online parameter and vsr nonlinearity estimation for pmsm drives using current and voltage dc components,” *IEEE Transactions on Transportation Electrification*, vol. 2, no. 2, pp. 119–128, June 2016.
- [31] S. Ichikawa, M. Tomita, S. Doki, and S. Okuma, “Sensorless control of permanent-magnet synchronous motors using online parameter identification based on system identification theory,” *IEEE Trans. Ind. Electron.*, vol. 53, no. 2, pp. 363–372, April 2006.

## Bibliography

- [32] P. B. Chi-Thuan Cao, “Verfahren und vorrichtung zur momentenregelung eines elektromotors in einem steer-by-wire-lenksystem,” Germany patentde DE1 010 873B42 007.02.15, Feb., 2007.
- [33] S. Kuehl, P. Landsmann, and R. M. Kennel, “Bivariate polynomial approximation of cross-saturated flux curves in synchronous machine models,” in *2012 IEEE International Energy Conference and Exhibition (ENERGYCON)*, Sept 2012, pp. 219–224.
- [34] C. K. J. A. E. Fitzgerald and S. D. Umans, *Electric machinery*. Boston, Mass: McGraw-Hill, 2003.
- [35] J. R. Hendershot and T. Miller, *Design of Brushless Permanent-Magnet Motors*. Motor Design Books LLC, 2010.
- [36] T. J. E. Miller, *Brushless permanent-magnet and reluctance motor drives*. Clarendon Press, 1993.
- [37] T. M. Apostol, *Calculus, Multi-Variable Calculus and Linear Algebra with Applications*. John Wiley & Sons, 1969.
- [38] S. P. K. O. W. Krause, Steven Pekarek, *Analysis Electric Machinery and Drive Systems*. John Wiley and Sons, 2013. [Online]. Available: [https://www.ebook.de/de/product/19579645/krause\\_steven\\_pekarek\\_sudhoff\\_paul\\_krause\\_oleg\\_wasynczuk\\_analysis\\_electric\\_machinery\\_3e.html](https://www.ebook.de/de/product/19579645/krause_steven_pekarek_sudhoff_paul_krause_oleg_wasynczuk_analysis_electric_machinery_3e.html)
- [39] D. C. Herbert H. White, *Electromechanical Energy Conversion*, J. Wiley and Sons, Eds., 1959.
- [40] R. D. Schultz and L. Zhao, “Coenergy based transient model of interior permanent synchronous machines.” *IEEE*, oct 2015.
- [41] N. Bianchi and S. Bolognani, “Magnetic models of saturated interior permanent magnet motors based on finite element analysis,” in *Conference Record of 1998 IEEE Industry Applications Conference. Thirty-Third IAS Annual Meeting (Cat. No.98CH36242)*. IEEE, 1998.
- [42] J. A. Walker, D. G. Dorrell, and C. Cossar, “Flux-linkage calculation in permanent-magnet motors using the frozen permeabilities method,” *IEEE Transactions on Magnetics*, vol. 41, no. 10, pp. 3946–3948, Oct 2005.
- [43] D. Hanselman, *Brushless permanent magnet motor design*. Lebanon, Ohio: Magna Physics Publishing, 2006.
- [44] S. Trout, “Material selection of permanent magnets, considering thermal properties correctly,” in *Proceedings: Electrical Insulation Conference and Electrical Manufacturing and Coil Winding Conference (Cat. No.01CH37264)*. IEEE, 2001.

- [45] S. Liu and G. Kuhl, “Temperature coefficients of rare earth permanent magnets,” *IEEE Transactions on Magnetics*, vol. 35, no. 5, pp. 3271–3273, 1999.
- [46] A. M. Technologies. (2010, Jan.) Understanding and using reversible temperature coefficients. [Online]. Available: <https://www.arnoldmagnetics.com/resources/technical-publications>.
- [47] O. Nelles, *Nonlinear System Identification*. Springer, 2001.
- [48] M. M. Rolf Isermann, *Identification of Dynamical Systems*. Springer-Verlag GmbH, 2011. [Online]. Available: [https://www.ebook.de/de/product/10052164/rolf\\_ismann\\_marco\\_muenchhof\\_identification\\_of\\_dynamical\\_systems.html](https://www.ebook.de/de/product/10052164/rolf_ismann_marco_muenchhof_identification_of_dynamical_systems.html)
- [49] W. SUN and Y.-X. YUAN, *OPTIMIZATION THEORY AND METHODS Nonlinear Programming*, P. M. Pardalos and D.-Z. Du, Eds. Springer, 2006, vol. 1.
- [50] M. Bartholomew-Biggs, *Nonlinear Optimization with Engineering Applications*. Springer-Verlag GmbH, 2008. [Online]. Available: [https://www.ebook.de/de/product/12470277/michael\\_bartholomew\\_biggs\\_nonlinear\\_optimization\\_with\\_engineering\\_applications.html](https://www.ebook.de/de/product/12470277/michael_bartholomew_biggs_nonlinear_optimization_with_engineering_applications.html)
- [51] C. K. Chui, *Kalman filtering : with real-time applications*. Berlin: Springer, 2009.
- [52] O. Wallscheid and J. Boecker, “Design and identification of a lumped-parameter thermal network for permanent magnet synchronous motors based on heat transfer theory and particle swarm optimisation,” in *2015 17th European Conference on Power Electronics and Applications (EPE'15 ECCE-Europe)*, Sept 2015, pp. 1–10.
- [53] J. Kennedy and R. Eberhart, “Particle swarm optimization,” in *Neural Networks, 1995. Proceedings., IEEE International Conference on*, vol. 4, Nov 1995, pp. 1942–1948 vol.4.
- [54] T. Apostol, *Calculus, One-Variable Calculus with an Introduction to Linear Algebra*. John Wiley & Sons, 1967.
- [55] C. R. Rao, *Linear Statistical Inference and its Applications*. John Wiley and Sons, 2001. [Online]. Available: [https://www.ebook.de/de/product/3606626/rao\\_linear\\_statistical\\_inference\\_2e\\_p.html](https://www.ebook.de/de/product/3606626/rao_linear_statistical_inference_2e_p.html)
- [56] T. O. Kvalseth, “Cautionary note about R2,” *The American Statistician*, vol. 39, no. 4, pp. 279–285, nov 1985.
- [57] S. L. Kellner and B. Piepenbreier, “General pmsm d,q-model using optimized interpolated absolute and differential inductance surfaces,” in *2011 IEEE International Electric Machines Drives Conference (IEMDC)*, May 2011, pp. 212–217.
- [58] L. Trefethen, *Approximation Theory and Approximation Practice*, 01 2013.

## Bibliography

- [59] C. P. Steinmetz, "On the law of hysteresis," *Transactions of the American Institute of Electrical Engineers*, vol. IX, no. 1, pp. 1–64, jan 1892.
- [60] G. Bertotti, "General properties of power losses in soft ferromagnetic materials," *IEEE Transactions on Magnetics*, vol. 24, no. 1, pp. 621–630, jan 1988.
- [61] P. H. Mellor, R. Wrobel, and D. Holliday, "A computationally efficient iron loss model for brushless ac machines that caters for rated flux and field weakened operation," in *2009 IEEE International Electric Machines and Drives Conference*, May 2009, pp. 490–494.
- [62] M. Popescu, D. G. Dorrell, and D. M. Ionel, "A study of the engineering calculations for iron losses in 3-phase AC motor models," in *IECON 2007 - 33rd Annual Conference of the IEEE Industrial Electronics Society*. IEEE, 2007.
- [63] T. Ishikawa and Y. Matsumoto, "Efficiency optimization for an IPMSM considering eddy-current and hysteresis losses," in *2020 International Conference on Electrical Machines (ICEM)*. IEEE, aug 2020.
- [64] N. Urasaki, T. Senjyu, and K. Uezato, "A novel calculation method for iron loss resistance suitable in modeling permanent-magnet synchronous motors," *IEEE Transactions on Energy Conversion*, vol. 18, no. 1, pp. 41–47, mar 2003.
- [65] S. L. Kellner, M. Seilmeier, and B. Piepenbreier, "Impact of iron losses on parameter identification of permanent magnet synchronous machines," in *2011 1st International Electric Drives Production Conference*. IEEE, sep 2011.
- [66] F. Fernandez-Bernal, A. Garcia-Cerrada, and R. Faure, "Determination of parameters in interior permanent-magnet synchronous motors with iron losses without torque measurement," *IEEE Transactions on Industry Applications*, vol. 37, no. 5, pp. 1265–1272, Sep. 2001.
- [67] D. Gerling and G. Dajaku, "Thermal calculation of systems with distributed heat generation," in *Thermal and Thermomechanical Proceedings 10th Intersociety Conference on Phenomena in Electronics Systems, 2006. IThERM 2006*. IEEE, 2006.
- [68] A. Boglietti, A. Cavagnino, D. Staton, M. Shanel, M. Mueller, and C. Mejuto, "Evolution and modern approaches for thermal analysis of electrical machines," *IEEE Transactions on Industrial Electronics*, vol. 56, no. 3, pp. 871–882, March 2009.
- [69] F. Incropera, *Fundamentals of heat and mass transfer*. Hoboken, NJ: John Wiley, 2007.
- [70] M. Broussely, Y. Bertin, and P. Lagonotte, "Reduction and optimisation of thermal models using kirchhoff network theory," *International Journal of Thermal Sciences*, vol. 42, no. 8, pp. 795–804, aug 2003.

- [71] N. Jaljal, J. Trigeol, and P. Lagonotte, “Reduced thermal model of an induction machine for real-time thermal monitoring,” *IEEE Transactions on Industrial Electronics*, vol. 55, no. 10, pp. 3535–3542, Oct 2008.
- [72] T. Huber, W. Peters, and J. Boecker, “A low-order thermal model for monitoring critical temperatures in permanent magnet synchronous motors,” in *7th IET International Conference on Power Electronics, Machines and Drives (PEMD 2014)*, April 2014, pp. 1–6.
- [73] A. Boglietti, E. Carpaneto, M. Cossale, and A. L. Borlera, “Stator thermal model for short-time thermal transients,” in *2014 International Conference on Electrical Machines (ICEM)*. IEEE, sep 2014.
- [74] D. A. Howey, P. R. N. Childs, and A. S. Holmes, “Air-gap convection in rotating electrical machines,” *IEEE Transactions on Industrial Electronics*, vol. 59, no. 3, pp. 1367–1375, March 2012.
- [75] N. Pothi, S. Premrudeepreechacharn, and C. Rakpenthai, “Voltage losses compensation using artificial neural network for estimation nonlinear characteristic of switches,” in *2007 7th International Conference on Power Electronics and Drive Systems*, Nov 2007, pp. 1015–1019.
- [76] S. Wiedemann and R. M. Kennel, “Accurate self-identification of inverter nonlinear effects in ac drives,” in *PCIM Europe 2018; International Exhibition and Conference for Power Electronics, Intelligent Motion, Renewable Energy and Energy Management*, June 2018, pp. 1–70.
- [77] S. C. Billups and M. C. Ferris, “QPCOMP: A quadratic programming based solver for mixed complementarity problems,” *Mathematical Programming*, vol. 76, no. 3, pp. 533–562, mar 1997.
- [78] J.-S. Pang and S. A. Gabriel, “NE/SQP: A robust algorithm for the nonlinear complementarity problem,” *Mathematical Programming*, vol. 60, no. 1-3, pp. 295–337, jun 1993.
- [79] E. M. Gertz and S. J. Wright, “Object-oriented software for quadratic programming,” *ACM Transactions on Mathematical Software*, vol. 29, no. 1, pp. 58–81, mar 2003.
- [80] H. J. Ferreau, C. Kirches, A. Potschka, H. G. Bock, and M. Diehl, “qpOASES: a parametric active-set algorithm for quadratic programming,” *Mathematical Programming Computation*, vol. 6, no. 4, pp. 327–363, apr 2014.
- [81] G. Banjac, P. Goulart, B. Stellato, and S. Boyd, “Infeasibility detection in the alternating direction method of multipliers for convex optimization,” *Journal of Optimization Theory and Applications*, vol. 183, no. 2, pp. 490–519, aug 2019.

## *Bibliography*

- [82] G. Banjac, B. Stellato, N. Moehle, P. Goulart, A. Bemporad, and S. Boyd, “Embedded code generation using the OSQP solver,” in *2017 IEEE 56th Annual Conference on Decision and Control (CDC)*. IEEE, dec 2017.
- [83] Y. Xu, U. Vollmer, A. Ebrahimi, and N. Parspour, “Online estimation of the stator resistances of a PMSM with consideration of magnetic saturation,” in *2012 International Conference and Exposition on Electrical and Power Engineering*. IEEE, oct 2012.

# A Appendix

## A.1 Taylor's Theorem for Multi-variable Functions

For a  $n$  differentiable function  $f(x)$  it can find a polynomial  $P(x)$  with the same  $n$  derivatives around the point  $x = a$  in the form:

$$P(a) = f(a), \quad P'(a) = f'(a), \quad \dots, \quad P^{(n)}(a) = f^{(n)}(a), \quad (\text{A.1})$$

the polynomial of degree  $n$  that fulfills (A.1) has the following form:

$$P(x) = \sum_{k=0}^n c_k x^k \quad (\text{A.2})$$

where the coefficients  $c_k$  are determined based on (A.1) as:

$$c_k = \frac{f^{(k)}(a)}{k!} \quad (\text{A.3})$$

Finally, (A.3) leads to the Taylor polynomial:

$$P(x) = \sum_{k=0}^n \frac{f^{(k)}(a)}{k!} (x - a)^k \quad (\text{A.4})$$

Now  $f(x)$  can be approximated by  $P(x)$  with an error  $E_n(x, a) = f(x) - P(x)$  according to Taylor's theorem [54]:

$$f(x) = \sum_{k=0}^n \frac{f^{(k)}(a)}{k!} (x - a)^k + E_n(x, a) \quad (\text{A.5})$$

the error function or remainder can be written in terms of the  $n + 1$  derivative as<sup>1</sup>:

$$E_n(x, a) = \frac{f^{(n+1)}(c)}{(n+1)!} (x - a)^{n+1} \quad (\text{A.6})$$

where  $c$  is located between  $x$  and  $a$ .

The Taylor polynomial (A.4) can also be extended to multi-variable functions with  $\mathbf{x}^T = [x_1 \ x_2 \ \dots \ x_m]$  in the following manner:

---

<sup>1</sup>More information on the theorem's proof and the error function can be found in [54]

## A Appendix

$$P(\mathbf{x}) = f(\mathbf{a}) + \sum_{i=1}^m \frac{\partial f}{\partial x_i}(\mathbf{a})(x_i - a_i) + \frac{1}{2} \sum_{i=1}^m \sum_{j=1}^m \frac{\partial^2}{\partial x_i \partial x_j}(\mathbf{a})(x_i - a_i)(x_j - a_j) + \dots \quad (\text{A.7})$$

In the case of Taylor's formula, the second order approximation is expressed as :

$$f(\mathbf{x}) = f(\mathbf{a}) + (\mathbf{x} - \mathbf{a})^T \nabla f(\mathbf{a}) + \frac{1}{2} (\mathbf{x} - \mathbf{a})^T H(\mathbf{a})(\mathbf{x} - \mathbf{a}) + E_2(\mathbf{x}, \mathbf{a}) \quad (\text{A.8})$$

where  $E_2(\mathbf{x}, \mathbf{a})$  is the Taylor remainder for the second order polynomial and  $H$  is the Hessian matrix that contains the second partial derivatives of  $f$ :

$$H = \begin{bmatrix} \frac{\partial^2 f}{\partial x_1^2} & \frac{\partial^2 f}{\partial x_1 x_2} & \cdots & \frac{\partial^2 f}{\partial x_1 x_m} \\ \frac{\partial^2 f}{\partial x_2 x_1} & \frac{\partial^2 f}{\partial x_2^2} & \cdots & \frac{\partial^2 f}{\partial x_2 x_m} \\ \vdots & \vdots & \ddots & \vdots \\ \frac{\partial^2 f}{\partial x_m x_1} & \frac{\partial^2 f}{\partial x_m x_2} & \cdots & \frac{\partial^2 f}{\partial x_m^2} \end{bmatrix} \quad (\text{A.9})$$

The approximation of the function  $f$  is then defined by the polynomial degree  $n$  of  $P(x)$  and the corresponding partial derivatives which permit the calculation of the unique polynomial coefficients as defined in (A.1). However when  $n$  is large the calculation of the partial derivatives becomes laborious, therefore another method to obtain the polynomial coefficients is preferred. The least-square approximation [37] seeks to find a polynomial of degree  $n$  with the smallest possible mean-square error for the interval  $[ab]$  of an integrable function  $f(x)$ :

$$\int_b^c |f(x) - P(x)|^2 dx \quad (\text{A.10})$$

under the premise of the minimization of the polynomial error, the polynomial structure of (A.7) can be adopted and instead of using the partial derivatives, coefficients can be used. This implies then that  $f(x) \approx P(x)$ , furthermore it is important to notice that the Hessian matrix  $H$  is symmetric since  $\frac{\partial^2 f}{\partial x_i \partial x_j} = \frac{\partial^2 f}{\partial x_j \partial x_i}$ , which permits a simplification in the formulation of the polynomial structure with unique terms. The second order approximation of a function  $f$  with two variables  $\mathbf{x}^T = [x_1 \ x_2]$  around  $\mathbf{a} = (0, 0)$  based on (A.7) and replacing the partial derivatives and constants by coefficients takes the following form:

$$P(\mathbf{x}) = c_{00} + c_{10}x_1 + c_{01}x_2 + c_{20}x_1^2 + c_{11}x_1x_2 + c_{02}x_2^2 \quad (\text{A.11})$$

where the subscripts in  $c_{ij}$  represent the power of the variables  $x_1$  and  $x_2$  respectively. In the case of two variables, based on (A.11), the generalization of a  $n$  degree polynomial  $P(x_1, x_2)$  can be expressed as:

$$P(\mathbf{x}) = \sum_{i=0}^n \sum_{j=0}^i c_{(i-j)(j)} x_1^{(i-j)} x_2^{(j)} \quad (\text{A.12})$$

The formulation of (A.12) guarantees that the combination of variables  $x_1$  and  $x_2$  with their respective power it is not repeated. Similarly the second order polynomial for three variables  $\mathbf{x}^T = [x_1 \ x_2 \ x_3]$  with unique variable combinations can be written as:

$$P(\mathbf{x}) = c_{000} + c_{100}x_1 + c_{010}x_2 + c_{001}x_3 + c_{200}x_1^2 + c_{110}x_1x_2 + c_{101}x_1x_3 + c_{011}x_2x_3 + c_{020}x_2^2 + c_{002}x_3^2 \quad (\text{A.13})$$

Keeping the convention of (A.11), the subscripts in  $c_{ijk}$  represent the power of the variables  $x_1$ ,  $x_2$  and  $x_3$  respectively. The generalization of (A.13) for a function with three variables is then formulated as:

$$P(\mathbf{x}) = \sum_{i=0}^n \sum_{j=0}^i \sum_{k=0}^{n-i} c_{(i-j)(j)(k)} x_1^{(i-j)} x_2^{(j)} x_3^{(k)} \quad (\text{A.14})$$

At this point the least-square approximation for a given interval is determined by minimizing the mean-square error (A.10). However in the case of discrete function, the sum of the least-squares for a given set of data points is:

$$\text{minimize} \quad \sum_{i=0}^m (f(\mathbf{x}_i) - P(\mathbf{x}_i))^2 \quad (\text{A.15})$$

## A.2 Test Machines

The machine referred as IPMSM in this work corresponds to a machine with following room temperature characteristics:

**Table A.1:** 4-pole pair IPMSM.

Nominal voltage	12V
rated phase current	140 A
Max. speed	7000 rpm
pole pairs	4
$K_e$	43.86 mV.s/rad
phase resistance	10.76 mΩ
$L_d$	55.77 μH @ 60Hz
$L_q$	72.86 μH @ 60Hz
Magnets operating temperature	-40°C to 180°C
Magnet's temperature coefficient	-0.11%/°C

### A.3 Hardware Implementation

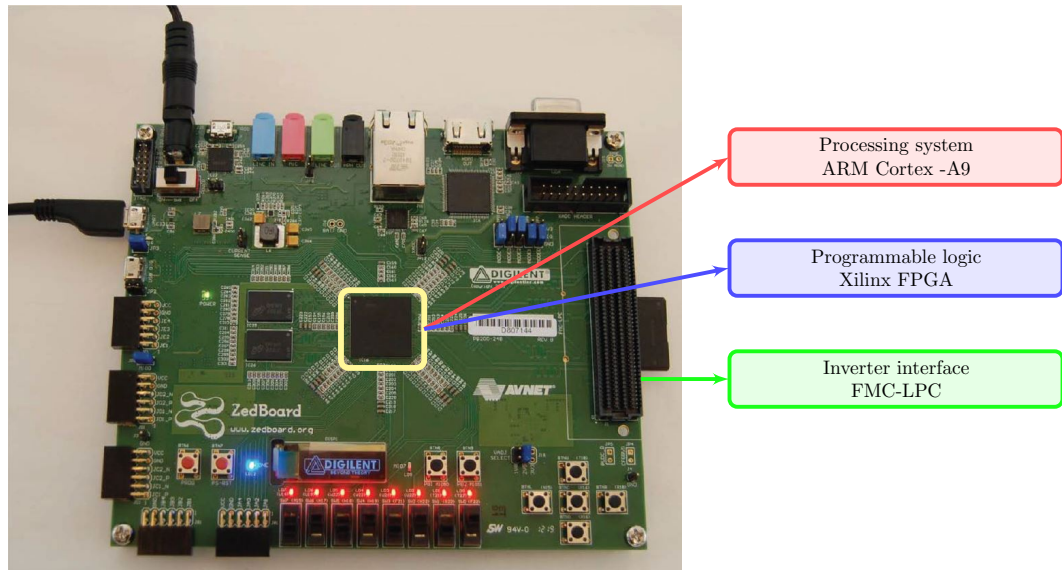


Figure A.1: Avnet ZedBoard.

Table A.2: Avnet ZedBoard SoC.

Nominal voltage	12V
<i>Xilinx SoC</i>	Zynq-7000 SoC XC7Z020-CLG484-1
processing system	ARM Cortex-A9 MPCore
FPGA	Xilinx Artix-7

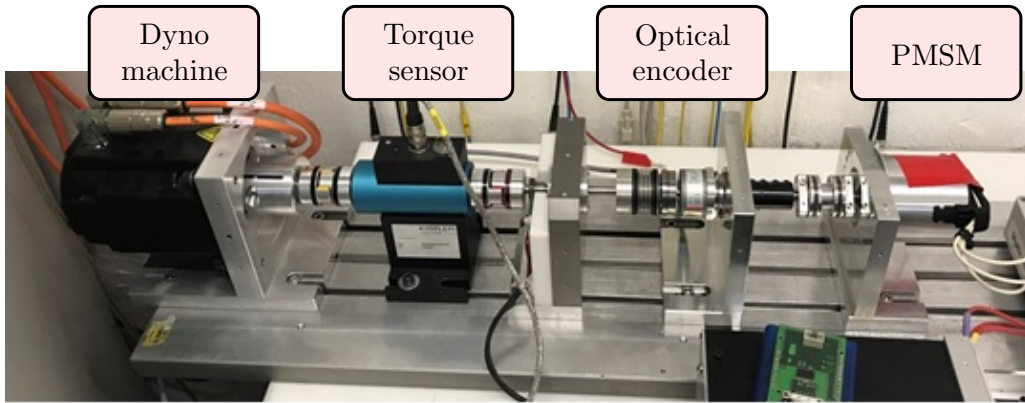


Figure A.2: Testrig setup

Table A.3: Test rig setup.

Dyno machine	Kollmorgen
Torque sensor	Kistler 0.5Nm/5Nm
Optical encoder	Kuebler 8142

## A.4 OSQP Algorithm

The performance comparison of OSQP and the Matlab function *quadprog* was done using the optimization problem of section 3.5.1, which seeks to minimize the voltage and torque signals error using measured data. The identified set of coefficients used for the performance evaluation and online parameter identification in chapter 6 are listed in the following table:

Table A.4: IPMSM - identified coefficients

$n = 3$	
$R_s$	$11.01m\Omega$
$\psi_m$	$6.32mV.s$
$l_{dq10}$	$54.71\mu H$
$l_{qd10}$	$72.86\mu H$
$l_{dq20}$	$-56.74nH/A$
$l_{dq30}$	$-0.24nH/A^2$
$c_{dq01}$	$-20.66nH/A$
$c_{dq11}$	$-0.33nH/A^2$
$l_{qd30}$	$-0.72nH/A^2$

**Table A.5:** OSQP settings.

Parameter	
sigma	$1 \cdot 10^{-12}$
eps abs	$1 \cdot 10^{-9}$
eps rel	$1 \cdot 10^{-9}$
eps prim inf	$1 \cdot 10^{-12}$
eps dual inf	$1 \cdot 10^{-12}$
scaling	24
check termination	2

## A.5 Terminal Voltage Measurement

The transport delay of the filter in Fig. 6.2 was obtained based on the resistor and capacitor values listed in table 6.2 with equation (6.8). However, the resulting transport delay  $t_{delay} = 102.1\mu s$  was validated through a direct measurement. The step response of the low pass filter was measured and fitted to an expected waveform of second order as shown in Fig. A.3 where the expression  $V(t)$  is the general formulation in time to the Laplace transfer-function (6.3). The time constants  $\tau_1$  and  $\tau_2$  are related to the impedance associated to the capacitors  $C_1$  and  $C_2$  in Fig. 6.2 as shown in (6.8). The average transport delay  $t_{delay} = \tau_1 + \tau_2$  obtained was  $t_{delay} = 103.7\mu s$ .

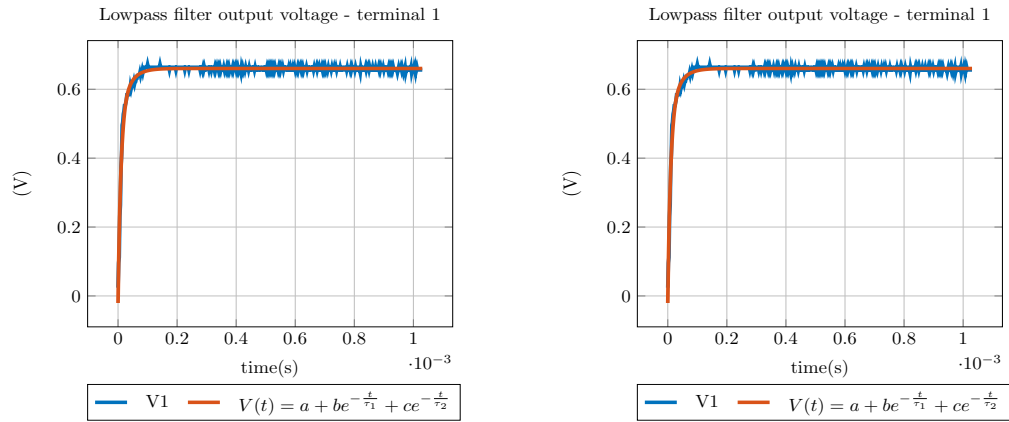


**Figure A.3:** Filter characterization.